Dipl.-Ing. Klemens Kranawetter, BSc

Modelling, Simulation and Control of Highly Dynamic Automotive Test Bed Components

DOCTORAL THESIS

to achieve the university degree of

Doktor der technischen Wissenschaften

submitted to

Graz University of Technology

Supervisors

Univ.-Prof. Dipl.-Ing. Dr. techn. Martin Horn

Institute of Automation and Control

Priv.-Doz. Dipl.-Ing. Dr. techn. Robert Bauer

KS Engineers

Graz, July 2019

Eidesstattliche Erklärung

Ich erkläre an Eides statt, dass ich die vorliegende Arbeit selbstständig verfasst, andere als die angegebenen Quellen/Hilfsmittel nicht benutzt, und die den benutzten Quellen wörtlich und inhaltlich entnommenen Stellen als solche kenntlich gemacht habe. Das in TUGRAZonline hochgeladene Textdokument ist mit der vorliegenden Arbeit identisch.

Graz, am 2. Juli 2019 Klemens Kranawetter

Datum Unterschrift

Statutory Declaration

I declare that I have authored this thesis independently, that I have not used other than the declared sources/resources, and that I have explicitly marked all material which has been quoted either literally or by content from the used sources. The text document uploaded to TUGRAZonline is identical to the present doctoral thesis.

Graz, 2019-July-2nd Klemens Kranawetter

Date Signature

Abstract

The rapid advancement of today's technology requires the employed testing equipment to progress at high rates, too. Particularly in the automotive industry, trends as the electrification of the powertrain, autonomous driving, and the demand to measure an automobile's real-driving emissions pose substantial challenges to the involved test beds. In this context, the present thesis aims to contribute to a further development of automotive testing systems, by addressing a series of control engineering problems from this field.

The first topic to be dealt with concerns the modelling of test bed drive lines. It is found that the task of mathematically describing a drive line, such that the rotary resonances can be predicted accurately, is an all but trivial problem, especially when modifications of the real setup are to be investigated in simulation first. It turns out that large inertias, like that of an electrical dynamometer, need to be interpreted as distributed-parameter systems in order to obtain satisfying simulation results.

The two subsequently covered topics share a common plot: For hydrodynamic couplings and for elements containing mechanical backlash, it became apparent that most of the modelling approaches found in current literature suffer from several deficiencies, especially in the considered control-oriented setting. For each component a new modelling strategy is developed, which significantly improves on the achieved simulation quality.

Furthermore, the present thesis addresses the question of suppressing undesired torque oscillations. Also in this regard, it is found that many of the published concepts to overcome this highly relevant impediment suffer from drawbacks that restrict their practical applicability under the considered circumstances. A novel scheme to compensate for a system's resonances and to suppress undesired oscillations is thus derived.

Lastly, a control problem form an entirely different physical domain is discussed: the control of charge air and fuel gas pressure on a test bed for large bore gas engines. It is demonstrated that the application of simple but effective model based techniques allows to strongly enhance the performance of the controllers for these important pneumatic quantities.

The majority of insights, findings and ideas that are presented in this work were validated by the means of measured experimental data, obtained on several different test beds.

Zusammenfassung

Der rasche Fortschritt moderner Technologie erfordert eine ebenso zügige Weiterentwicklung der eingesetzten Prüftechnik. Vor allem in der Automobilindustrie führen Trends wie die Elektrifizierung des Antriebsstranges oder die Messung von Emissionen im praktischen Fahrbetrieb zu signifikanten prüftechnischen Herausforderungen. In diesem Kontext versucht die gegenständliche Arbeit zur Verbesserung von automotiven Prüfständen beizutragen, und behandelt mehrere regelungstechnische Probleme aus diesem Themenfeld.

Das erste Kapitel widmet sich der Modellierung von Prüfstandsantriebssträngen. Es stellt sich heraus, dass deren mathematische Beschreibung eine höchst nichttriviale Problemstellung darstellt, insbesondere wenn die Änderung von rotatorischen Resonanzen nach Modifikation des realen Stranges in der Simulation vorhergesagt werden soll. Es wird gezeigt, dass Strangelemente mit großer Trägheit als verteilt-parametrische Objekte aufgefasst werden müssen, um realistische Simulationsergebnisse zu erzielen.

Die Behandlung der zwei anschließenden Problemstellungen folgt einer beinahe identen Handlung: Sowohl für hydrodynamische Kupplungen als auch für Elemente mit mechanischem Wellenspiel lässt sich erkennen, dass viele der in der Literatur verfügbaren Ansätze zur mathematischen Modellierung Nachteile aufweisen – vor allem im regelungstechnischen Kontext. Aus diesem Grund werden für die genannten Komponenten neue Modellierungsstrategien entwickelt, die die erzielbare Simulationsqualität stark verbessern.

Darüber hinaus wird die Thematik unerwünschter Drehmomentschwingungen im Antriebsstrang diskutiert. Auch in diesem Punkt stellt sich heraus, dass viele der in der aktuellen Literatur verfügbaren Kompensationsmethoden bei den gegebenen Problemstellungen nur beschränkt eingesetzt werden können. Aus diesem Anlass wird ein neues Schema zur Resonanz- und Schwingungskompensation abgeleitet.

Abschließend wird ein regelungstechnisches Problem aus einer gänzlich anderen physikalischen Domäne behandelt: Die Regelung von Ansaug- und Kraftstoffdruck an einem Prüfstand für Großgasmotoren. Es wird demonstriert wie mittels modellbasierter Methoden die Qualität der Regler dieser wichtigen Prüfstandsgrößen klar verbessert werden kann.

Der Großteil der nachfolgend präsentierten Ergebnisse wurde anhand von Messdaten validiert, die an mehreren unterschiedlichen Prüfständen gewonnen wurden.

Acknowledgements

This thesis presents the results of a research collaboration between the Institute of Automation and Control at Graz University of Technology and the company KS Engineers. Taking on and eventually mastering the challenges that led to this dissertation would not have been possible without the many friends and colleagues that accompanied me on this journey. I would like to sincerely thank each and every one of them. To some individuals I feel particularly indebted, however, and I wish to express my special appreciation to them:

First and foremost I would like to thank Dr. Wilfried Rossegger from KS Engineers for funding and supporting this collaboration throughout the past years. His background as a control engineer and his own love for the field provided an outstanding environment for this research. I also would like to express my sincere gratitude to the first of my doctoral fathers, Priv.-Doz. Dr. Robert Bauer from KS Engineers. His exceptional scientific and personal support remained unchanged throughout the work on this dissertation, and his wit and deep understanding of the oftentimes complex problems never failed to impress. I am particularly thankful for his patience when proofreading my drafts!

From the Institute of Automation and Control I would like to specifically thank my academic supervisor and second doctoral father, Prof. Dr. Martin Horn. Collaborating with him scientifically, teaching problem classes to one of his excellent lectures, and playing football on Friday evenings was a pleasure in all the years that I spent at his institute. Furthermore, I am grateful to all of my doctoral brothers and sisters from the institute, who spent countless hours to discuss my problems, cheered me up when progress was not so clearly visible, and proofed to me that undertaking a PhD dissertation was in fact a feasible problem.

I also would like to thank Prof. Dr. Klaus Janschek from TU Dresden, for his interest in my work, and his willingness to participate in my PhD project as an external examiner.

Above all, I would like to express my gratitude towards my non-scientific family: To my uncle Erwin, for the interesting discussions on many of the topics in this thesis. To my brilliant and wonderful sister Kathi, my loving mother Judith, and my caring father Reinhard; you are the best family that I could think of. And to my love Lena, who stood by me during the difficult times that unavoidably occur in the course of such a work, supported me whenever she could, and was so patient and understanding at all times.

Klemens Kranawetter

Contents

List of Figures

List of Tables

List of Abbreviations

CU	Control unit
DUT	Device-under-test
DFT	Discrete Fourier transform
BIBO	Bounded input – bounded output
EVO	Exhaust-valve-opening
FOC	Field-oriented control
FC	Frequency converter
HiL	Hardware-in-the-loop
ICE	Internal combustion engine
I/P	Current-to-pressure (converter)
IM	Induction machine
LTI	Linear time-invariant
LMS	Least-mean-squares
MCE	Multi-cylinder engine
PI	Proportional-integral (controller)
PWM	Pulse width modulation
R2R	Road-to-Rig
SISO	Single-input single-output
SCE	Single-cylinder engine

Glossary

Symbol	Definition	Unit
φ	Angular position	rad
ω	Angular velocity	rad/s
n	Rotational speed	rpm
T	Torque	Nm
I	Moment of inertia	$\mathrm{kg\,m^2}$
T_{airgap}	Airgap torque	Nm
T_{shaft}	Shaft torque	Nm
T_{shaft}	Shaft torque	Nm
$\hat{T}$	Magnitude of chirped torque signal	Nm
k	Stiffness coefficient	Nm/rad
c	Damping coefficient	Nm s/rad
f	Continuous time frequency	Hz
ν	Angular frequency	rad/s
ν_r	Angular resonance frequency	rad/s
ν_z	Angular frequency of transfer zero	rad/s
$\boldsymbol{u}$	Vector of phase voltages	V
$\boldsymbol{r}$	Vector of reference signals	-
$\boldsymbol{m}$	Vector of measured signals	-
k_P	Proportional gain	-
k_I	Integral gain	-
k_V	Feed through gain	-
k_F	Feed forward gain	-
τ_a	Actuator time constant	s
$\boldsymbol{x}_a$	State vector, absolute angles and velocities	-
$\boldsymbol{A}_a$	Dynamic matrix, absolute angles and velocities	-
$\boldsymbol{x}_d$	State vector, differential angles and velocities	-
$\boldsymbol{A}_d$	Dynamic matrix, differential angles and velocities	-
$\boldsymbol{x}_m$	State vector, absolute and differential angles and velocities	-
$\boldsymbol{A}_m$	Dynamic matrix, absolute and differential signals	-

Symbol	Definition	Unit
$\boldsymbol{x}_\varphi$	State vector, absolute angles	-
$\boldsymbol{K}_\varphi$	Stiffness matrix, absolute angles	-
$\boldsymbol{C}_\varphi$	Damping matrix, absolute angles	-
$\boldsymbol{x}_\Delta$	State vector, differential angles	-
$\boldsymbol{K}_\Delta$	Stiffness matrix, differential angles	-
$\boldsymbol{C}_\Delta$	Damping matrix, differential angles	-
k_{im}	Total stiffness, soft rotor	Nm/rad
c_{im}	Total damping, soft rotor	Nm s/rad
q_r	Spatial eigenfrequency	rad /m
α	Backlash gap	rad
A^+, A^-, A_0	Activation areas, phase-plane model	-
c_f	Additional backlash damping	Nm s/rad
k_{KV}	Stiffness Kelvin-Voigt model	Nm/rad
c_{KV}	Damping Kelvin-Voigt model	Nm s/rad
T_H	Hydraulic coupling torque	Nm
m_f	Oil mass flow	kg/s
ρ	Oil density	kg/m^3
p	Pressure	bar
β	Bulk modulus	bar
Re	Reynolds number	-
ν_0	Discrete notch frequency	-
r	Pole radius	-
T_d	Discretization time	s
x^*	Complex-conjugate of signal x	-
N	Number of signal samples considered for DFT	-
f_0	True signal frequency	Hz
X_0	True signal magnitude	-
w	Blackman window in time domain	-
Δk_{max}	DFT index error	-
p_{ch}	Charge air pressure	bar
p_g	Fuel gas pressure	bar
p_s	Supply pressure	bar
p_{amb}	Ambient pressure	bar
p_{ex}	Exhaust back pressure	bar
p_{cyl}	Cylinder pressure	bar
V_{cyl}	Cylinder volume	m^3
V_{d}	Displaced volume	m^3
ϑ_{cyl}	Cylinder temparature	°K
R	Specific gas constant	J/(K mol)
$A_{1,2}$	Effective flap areas	m^2

Symbol	Definition	Unit
N_r	Number of cylinder revolutions per combustion cycle	-
χ	Heat capacity ratio	-
$\mathrm{d}Q/\mathrm{d}t$	Wall heat flux	W
$\mathrm{d}m/\mathrm{d}t$	Change of cylinder mass	kg/s
h	Specific enthalpy	kJ/kg
Ψ	Flow function	-
q_e	Consumed engine air flow	kg/h
λ	Volumetric efficiency	-
q_q	Gas mass flow	kg/h
p_{res}	Reservoir pressure	bar
p_{mem}	Membrane pressure	bar
A_{mem}	Effective valve area, gas membrane	m^2
F_s	Spring force	N
F_p	Pressure force	N

To my parents Judith and Reinhard.

Chapter 1

Introduction

The development of cutting-edge technology requires advanced and sophisticated methods for testing. This simple but important truth appears to be more relevant now than it may have been in the past, particularly in view of the ever increasing complexity of today's technological systems [1–3]. In recent days, especially one branch of the economy stood out for a huge buzz that was created around its testing systems: the *automotive industry*. Not least due to the so-called *emissions scandal* in 2015, where it was found that many vehicles were equipped with software that would "activate emissions controls only during laboratory testing" [4], automotive test beds[1] became a fiercely and emotionally disputed topic – not only among experts in the field, but also in the broad public [5, 6]. At the latest at that point it was clear to a wider audience that the guidelines, methodologies, and also the engineering principles that underlie existing testing concepts have to adapt quickly and continuously to a rapidly changing environment. Addressing again the case of vehicle development, trends as the electrification of the powertrain, autonomous driving, and the demand to measure an automobile's real-driving emissions pose substantial challenges in that regard, not only to the suppliers of testing equipment, but also to the manufacturers of original equipment [7–12]. In that light, this thesis aims to contribute to the further advancement of automotive testing systems, by discussing several current *control engineering* problems from this field.

1.1 Focus and scope of this work

Despite a long-standing history of scientific work on automotive test beds [13, 14], the set of unsolved or not fully understood control problems in the area is growing steadily. In general, but even more so in the field of automotive testing, the question of whether a control problem can be solved successfully often depends strongly on the quality and availability of mathematical models for the involved system components. Some authors

[1] More specifically chassis-dynamometers for emission measurement.

even go as far as to classify the derivation of "reasonable mathematical models as the most important part of the entire analysis of control systems" [15]. Also this work is driven by a focus that puts the derivation of accurate, concise and control-oriented models first, to lay the ground for effective and successful controller design. It is the author's firm belief that in order to derive good controllers, the needs and peculiarities of the plant need to be identified in the first place. This calls for mathematical models that are complex enough to contain and point out the essential dynamical features of a system that is to be controlled, but at the same time simple enough not to obscure the picture and potentially distract from the crucial properties. For this reason, the famous saying

> *"As simple as possible, but not simpler!"*

is one of the guiding principles throughout this work. In that spirit, the questions of *modelling* drive lines, backlash and gear play, *suppressing* torque oscillations, and *controlling* the pressures of media such as intake air and fuel gas are treated thoroughly in this thesis, by placing a strong emphasis on deriving and analysing appropriate mathematical models for the involved system components.

1.2 Thesis objectives and contributions

The last paragraph of the previous section indicates that the present thesis considers a *rich and diverse basket of research questions*. However, all of the mentioned topics do share a common denominator, of which Fig. 1.1 presents a concrete example: The image depicts a

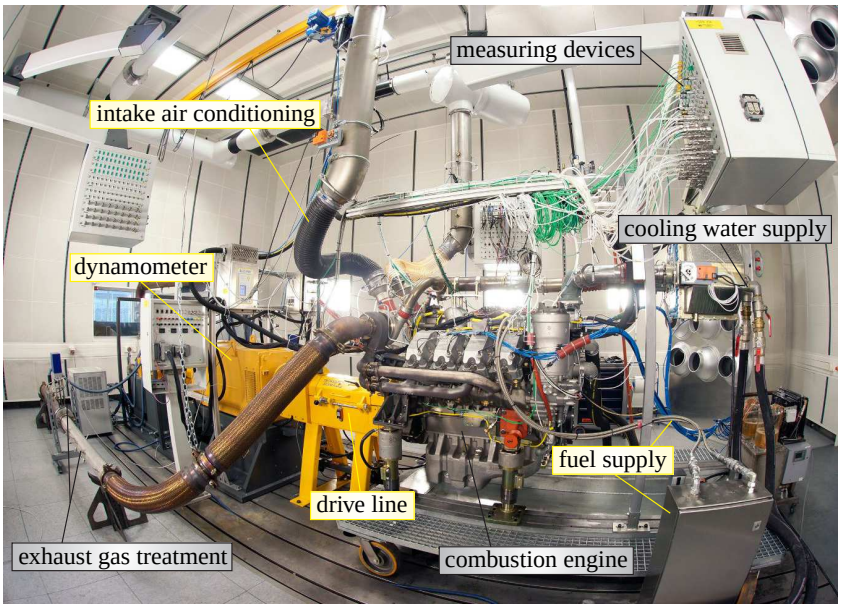

Figure 1.1: State-of-the-art combustion engine test bed.

state-of-the-art, high-end combustion engine test bed, which is employed to support the development process of engines for heavy-duty purposes. In essence, the tested combustion engine is connected mechanically to an electrical dynamometer, which allows to realise widespread mechanical load profiles. Additionally, the engine is supplied with specifically conditioned combustion air and fuel. Due to its excellent dynamical characteristics, this particular test rig may be used in a great variety of testing scenarios:

- The setup allows to perform *steady-state tests*, where torque and speed are demanded to remain constant throughout large sections of the test runs. Such tests are typically performed to optimize the combustion process of stationary engines [16], but also to investigate fatigue, wear, or the long term behaviour of the device-under-test.
- Another application that the considered test bed may be utilized for are *dynamic test cycles*. These trials are often normed by law, and frequently focus on the produced pollutants and exhaust gases [17, 18].
- Also highly dynamic, modern-day test runs are possible on the presented test stand. Therein, the interaction between components that are present in actual hardware with others that are represented in software is becoming more and more relevant [19–21]. A significant motivating factor behind this trend is the desire for increased flexibility: Components that are physically not available are replaced by mathematical real-time models, which allows for systematic testing at an early development stage ("front-loading" [22]). Such scenarios typically pose a significant challenge to the test rig, as it needs to respond to not only the device-under-test, but *also* to the demands of the acting real-time models.

Considering the complexity of the presented test bed, it does not surprise that a large number of physical quantities needs to be manipulated with great care in order to produce meaningful and substantial results. From a control engineering point of view, it turns out that controlling the variables that are connected to the yellow text boxes in Fig. 1.1 leads to particularly demanding challenges. Within these challenges, several questions were unanswered at the beginning of this work, which leads back to the beginning of this section, and completes the circle to the *rich basket of research topics* mentioned earlier on:

- In the test bed's drive line, which is considered to comprise also the rotor of the dynamometer, angular speed and torque have to precisely follow reference trajectories that may be the outcome of a normed testing procedure or a real-time computation. It became apparent that the typical and intuitive modelling approaches for the rotary behaviour of test bed drive lines do not suffice on many occasions, especially when the drive line's oscillatory resonances need to be predicted.

- It was found that the models for two important drive line components, i.e., elements containing gear play and hydrodynamic couplings, that are available in current literature frequently fail to produce satisfying results, too.
- It is well known that resonance oscillations can be a significant limiting factor in the control of angular speed and torque, which disturbs the involved controllers and prevents them from performing their tasks. In this regard, it was found that many of the existing and published methods to overcome undesired resonance oscillations suffer from several severe shortcomings in the given setting.
- Besides the mechanical quantities, the media that are supplied to the device-under-test must be conditioned to appropriately designed reference states. It turned out that controlling the pressures of, e.g., intake air and fuel gas in the setting of aggravated dynamical requirements is an unsolved problem in many applications.

The research project that is documented in this thesis allowed to work intensely on all of the points mentioned above, and led to the following findings and contributions:

- With regards to test bed drive lines, several different modelling approaches to reproduce its oscillatory behaviour were investigated. It was found that large inertias, which are for instance introduced into the drive line by the rotor of the electrical dynamometer, have to be interpreted as distributed-parameter systems in order to produce realistic simulation results.
- Considering the modelling of gear play, an extension of the established models was developed. In essence, the new model integrates damping that is present in phases without classical backlash contact into the established formalism that is found in current literature.
- For the case of hydrodynamic couplings, a new modelling approach was derived, where above all - and in contrast to existing approaches - the dynamical behaviour of the coupling's oil is taken into account explicitly.
- In response to the drawbacks of existing methods for resonance suppression, a new compensation scheme was developed, which relies on a novel frequency estimation method that employs Blackman-windowed signals and a series of checks on whether an oscillation is caused by one of the plant's resonances or by external excitation.
- In addition to the analysis of mechanical test bed parts, it was possible to investigate two important pneumatic subsystems, too. For the control of charge air and fuel gas pressure on a large bore single-cylinder gas engine test bed, it was demonstrated that the behaviour of typically employed controllers can be improved significantly by simple but effective model based techniques.

1.3 Structure of this work

The present thesis is structured in three parts:

The *first* and by pages largest one ("Modelling of Mechanical Components") spans over Chapters 2, 3, and 4, and is devoted to the modelling of mechanical test bed components. More specifically, Chapter 2 begins by motivating the importance of a detailed treatment of test bed drive lines, by explaining the employed experimental setups, and by discussing several important mathematical properties of the frequently used straight-chain-of-lumped-inertias models. A first crucial point of the chapter is a comparison between measured results and simulations obtained with one of these typical models. The presented comparison focusses on the systems' oscillatory resonances, and reveals a series of drawbacks of the considered model class. This assessment led to an investigation of especially the transfer zeros of multi-body systems, with the outcome of two alternative and to some degree bizarre topologies of lumped inertias. The unorthodox modelling approaches produce clearly improved results, but unfortunately lack of physical interpretability. Eventually, the chapter closes by introducing the class of distributed-parameter models especially for large members of a drive line, such as the rotors of the electrical dynamometers. The presented models can be explained intuitively and allow to produce highly satisfying simulation results. Chapter 3 continues by deriving a new model for backlash and gear play, a mechanical property that by some authors is characterized as the most important nonlinearity in modern drive systems. After discussing the test bed used for experimentation and reviewing the published modelling approaches, a new formalism is derived, which mainly consists of incorporating damping into phases that are free from classical backlash contact. A discussion of measured results concludes the chapter. The last mechanical object whose modelling is considered in this thesis are hydrodynamic couplings, the topic of Chapter 4. The latter commences by discussing this special type of coupling, and by pointing out the deficiencies of existing modelling approaches. In the following step, a novel model is developed, where the dynamical behaviour of the oil that moves inside the coupling is taken into account explicitly. The result is a second order, linear state-space model, which in spite of its simplicity significantly improves on the achieved modelling quality. The discussion of measured results obtained on a test bed whose drive line contains a hydrodynamic coupling substantiates this assessment, and closes Part I of the thesis.

The *second* part ("Control of Mechanical Components") of this work comprises solely Chapter 5, and considers the phenomenon of undesired torque oscillations in test bed drive lines. After analysing the root causes of growing torque oscillations from a control engineering point of view, the chapter continues by motivating the introduction of notch filters as an appropriate counter-measure. It is shown that the main unknowns in the process of parametrizing notch filters are the values of the plant's resonance frequencies. For several practical reasons, which are explained in the course of the chapter, it is desirable to find these frequencies online, in an adaptive manner. A review of published methods to do so uncovers several deficits of the existing concepts, which motivates the derivation of a novel

approach to detect a system's priorly unknown resonance frequencies. The proposed method combines what is known as discrete-Fourier-transform-interpolation with a series of criteria to tell external excitation from resonances as the sources for undesired oscillations. The chapter and with it Part II close by discussing the measured results of several experiments, which clearly point to the strengths and benefits of the proposed concept.

The *third* and last part ("Control of Air and Gas Pressure") of this work is covered by Chapter 6, and discusses the control of charge air and fuel gas pressure on a single-cylinder gas engine test bed. Improved pressure control had become indispensable on this particular testing system, in order to translate the demands of a hardware-in-the-loop system into action on the test rig. The hardware-in-the-loop system, which is discussed in the course of the chapter, too, represents the multi-cylinder engine that the tested single-cylinder engine is taken from. It is found that simple but effective model based strategies successfully solve the task of improving the dynamical behaviour of the considered pressures. Once again, a selection of measured results demonstrates the functionality of the presented ideas.

Part I

Modelling of Mechanical Components

Chapter 2

Drive Lines

The components of automotive drive lines interact through torque and angular speed. Consequently, these two quantities are at the root of many prominent concepts in automotive testing. On internal combustion engine ("ICE") test beds like the one shown in Fig. 2.1 (a), shaft torque and crank shaft speed frequently have to track specific reference trajectories, which may be part of a commissioning cycle or another normed testing procedure [23–25]. In order to successfully test transmissions like differential gears, both speed and torque must be controlled accurately, too. In the cases discussed in [26] and [27], one electrical machine is used to emulate the combustion engine by providing specific torque profiles, while two other machines are employed to regulate the speeds of the output cardan shafts. Moreover, also on highly complex testing systems like full-vehicle or road-to-rig ("R2R") test beds, speed and torque control is crucial. Figure 2.1 (b) presents an example of such a system. In order to reproduce the most extreme driving situations in consistency with reality, the test bed must respond to the vehicle with maximum dynamics. Again, the interaction between the device-under-test and its environment is rooted on speed and torque, which calls for the precise control of these variables [28–30].

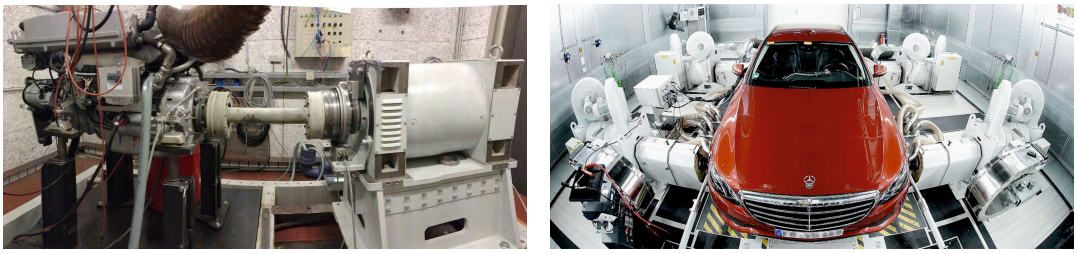

(a) Combustion engine test bed.

(b) R2R test bed.

Figure 2.1: Examplary test beds.

Controlling angular speed or torque in a test bed's drive line often turns out to be an exceptionally demanding problem, however. At its core, the situation is one of the classics

in control engineering: To achieve fast dynamics in the presence of disturbances, high-gain parameter settings are usually needed. High-gains, however, decrease the phase and magnitude margin, which may lead to poor performance and even stability problems.

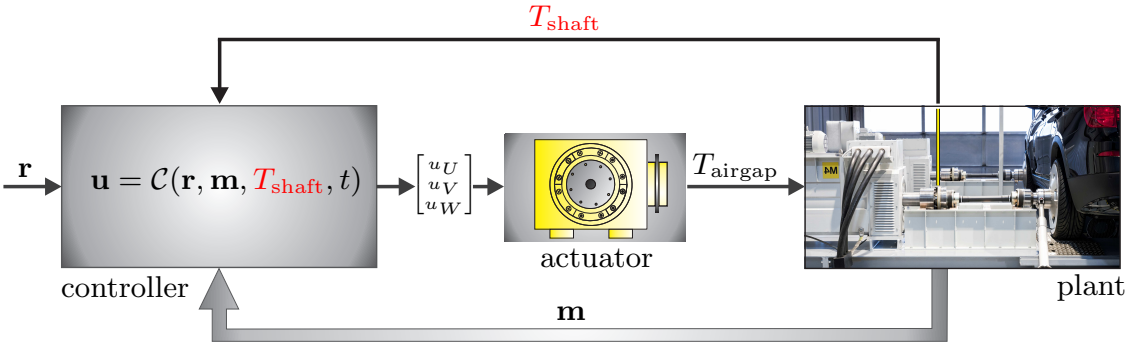

Figure 2.2: A typical scheme for speed or torque control.

For test beds like the ones presented in Figs. 2.1(a) and 2.1(b), the control loops for speed and torque frequently are similar to the structure shown in Fig. 2.2. The main components of the latter are the *drive line*, which constitutes the *plant* that is to be controlled, the *controller*, which comprises all the involved control algorithms ranging from speed or torque control to field-oriented-control and pulse-width-modulation ("PWM"), and the *actuator* or *dynamometer*, for which in this work only induction machines ("IMs") are considered. In Fig. 2.2, the vector $\boldsymbol{r}$ represents the reference values that are given to the controllers. Among others, the set points for speed and torque are two important elements of $\boldsymbol{r}$. The vector $\boldsymbol{m}$ comprises the measured variables. In the cases considered in this chapter, the speed of the dynamometer is measured by the means of a rotary encoder, and as shown in the *plant*-block, a torque measuring flange is part of the drive line to measure the transmitted shaft torque T_{shaft}. To emphasize its exceptional role[1] with regards to the dynamics of the system, T_{shaft} is not packed into $\boldsymbol{m}$. Besides speed and torque, especially the phase currents of the induction machine are three important measured quantities. The measured variables are passed on to a processor board[2] that is part of the frequency converter of the test bed. The board provides the hardware platform for all the control-related software, which in Fig. 2.2 is comprised in the block termed *controller*. In that sense, the expression

$$\boldsymbol{u} = C(\boldsymbol{r}, \boldsymbol{m}, T_{\text{shaft}}, t) \tag{2.1}$$

subsumes a significant number of controllers, observers, functional relations etc. The actual output of C is the vector of phase voltages $\boldsymbol{u} = [u_U, u_V, u_W]^T$, which can be set freely within its bounds by the means of a pulse-width-modulation scheme, and eventually leads to the airgap torque T_{airgap} that acts on the rotor of the dynamometer.

[1] This dependency is covered in detail in Chapter 5 of this work.

[2] In the test beds considered in this thesis, only products manufactured by dSPACE® with DS1006 or DS1005 processor boards are used. For details see [27, 31, 32].

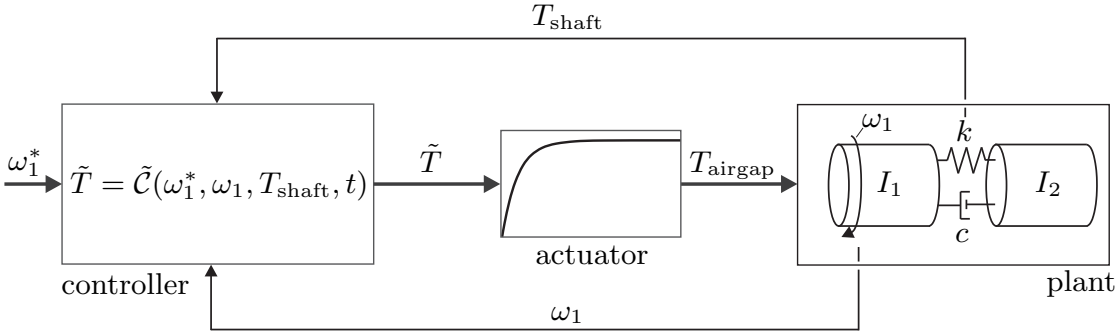

Figure 2.3: Strongly simplified representation of the considered control system.

To give an intuitive description of the problems associated with speed and torque control, some simplifications are made at this point, leading to the structure shown in Fig. 2.3. *Firstly*, the drive line is assumed to behave like a linear two mass oscillator. A possible description of the plant in the Laplace-domain is then given by

$$\begin{aligned} P_1(s) &:= \frac{T_{\text{shaft}}(s)}{T_{\text{airgap}}(s)} = \frac{1}{I_1} \cdot \frac{cs + k}{s^2 + c(\frac{1}{I_1} + \frac{1}{I_2})s + k(\frac{1}{I_1} + \frac{1}{I_2})} \qquad \text{and} \\ P_2(s) &:= \frac{\omega_1(s)}{T_{\text{airgap}}(s)} = \frac{1}{I_1} \cdot \frac{s + (cs + k)\frac{1}{I_2 s}}{s^2 + c(\frac{1}{I_1} + \frac{1}{I_2})s + k(\frac{1}{I_1} + \frac{1}{I_2})}, \end{aligned} \tag{2.2}$$

the transfer functions from T_{airgap} to T_{shaft} and ω_1, respectively. Therein, k, c, I_1 and I_2 denote stiffness, damping and rotary inertias of the two mass oscillator, respectively, and ω_1 stands for the measured angular velocity of I_1. *Secondly*, only the controllers for the mechanical variables in C are considered, which leads to the reduced system of controllers $\tilde{C}$, whose output is the desired control torque $\tilde{T}$. *Thirdly*, a classical PI-controller is assumed to be used for controlling the angular speed ω_1. In that case, also $\tilde{C}$ can be represented in the Laplace-domain, i.e.

$$\tilde{C}: \ \tilde{T}(s) = k_V T_{\text{shaft}}(s) + \frac{k_P s + k_I}{s}\left[\omega_1^*(s) - \omega_1(s)\right], \tag{2.3}$$

with k_I, k_P, k_V and ω_1^* as the integrator and proportional gain, the feed through gain and the set point for the angular speed, respectively. Especially the feed through path for T_{shaft} is an indispensable component in many applications, as the direct use of the measured shaft torque often is the quickest way to react to the device-under-test. *Fourthly* and lastly, the actuator is regarded as a first-order lag element. Under this assumption, the connection between controller output $\tilde{T}$ and airgap torque T_{airgap} can be expressed by

$$T_{\text{airgap}}(s) = \frac{1}{s\tau_a + 1}\tilde{T}(s), \tag{2.4}$$

where τ_a stands for the time constant of the first-order lag element. Combining these steps, the system can be analysed analytically, as especially the closed loop transfer function from

ω_1^* to ω_1 can be stated as

$$G_\omega(s) := \frac{\omega_1(s)}{\omega_1^*(s)} = \frac{k_P s^3 + (k_P \frac{c}{I_2} + k_I)s^2 + (k_P \frac{k}{I_2} + k_I \frac{c}{I_2})s + k_I \frac{k}{I_2}}{I_1\tau_a s^5 + (I_1 + I_1 c(\frac{1}{I_1} + \frac{1}{I_2})\tau_a)s^4 + (I_1 c(\frac{1}{I_1} + \frac{1}{I_2}) + I_1 k(\frac{1}{I_1} + \frac{1}{I_2})\tau_a - k_V c + k_P)s^3 + \\ + (I_1 k(\frac{1}{I_1} + \frac{1}{I_2}) - k_V k + k_P \frac{c}{I_2} + k_I)s^2 + (k_P \frac{k}{I_2} + k_I \frac{c}{I_2})s + k_I \frac{k}{I_2}}, \tag{2.5}$$

which allows a clear inspection of potential stability-related problems. Following Hurzwitz's criterion [33, 34], a necessary condition for BIBO-stability is that the parameters of the denominator must have the same sign. Since $I_1\tau_a$ is always positive, k_V, for instance, needs to fulfill

$$k_V < I_1(\frac{1}{I_1} + \frac{1}{I_2}) + \frac{k_P}{k}\frac{c}{I_2} + \frac{k_I}{k} \tag{2.6}$$

in order to allow the system to be BIBO-stable, among other conditions that also result from the application of the criterion. One can see clearly that large values for k_V have a destabilizing effect. As the parameters of the plant are usually not known exactly, may change over time, and in this consideration are associated with a two mass oscillator model that typically does not reflect the physical reality sufficiently well, finding the right controller setting often is an all but trivial problem. Figure 2.4 presents a possible consequence of violated stability conditions:

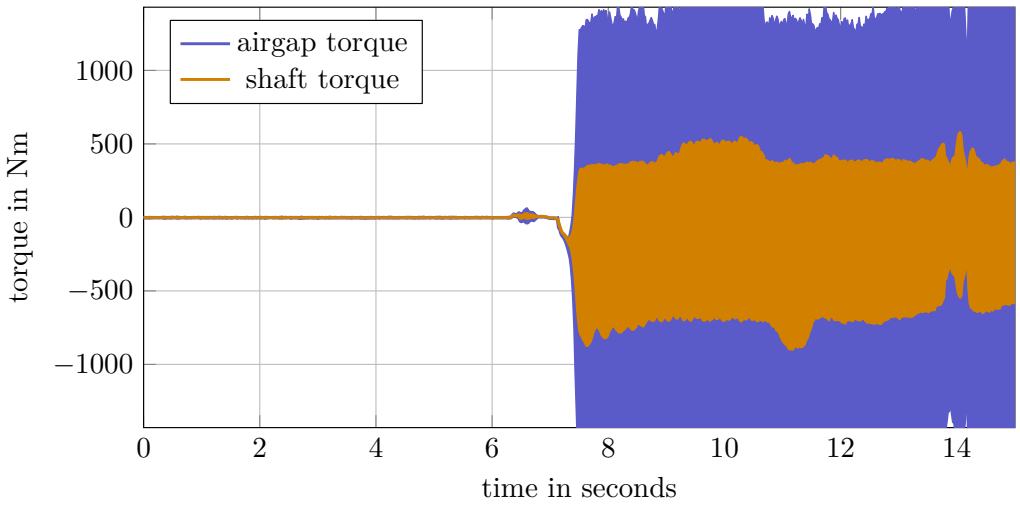

Figure 2.4: Undesired torque oscillation.

The plot displays the measured shaft and airgap torques during a test run on the test bed depicted in Fig. 2.2. Therein, both torques perform oscillations with magnitudes above 500Nm and a frequency close to 600Hz. As these situations in the worst case can lead to the destruction of test object, connecting shaft, or actuator, they must be avoided at any cost.

Unfortunately, the actual setup typically is more complex than the simplified abstraction shown in Fig. 2.3, and also the assumptions made for explanatory reasons only hold to a limited extent. Among the introduced simplifications, especially the behaviour of the drive line often turns out to be far from that of a simple two mass oscillator. Since accurate models typically are a crucial aid for gaining understanding about a system's stability bounds, the modelling of test bed drive lines like those presented is treated thoroughly in this chapter. The main results of this effort are presented in the following.

2.1 Experimental setup

In the course of this research, mainly the test beds depicted in Figs. 2.5 were used for trials. This section discusses both of these systems, and explains an important class of experiments.

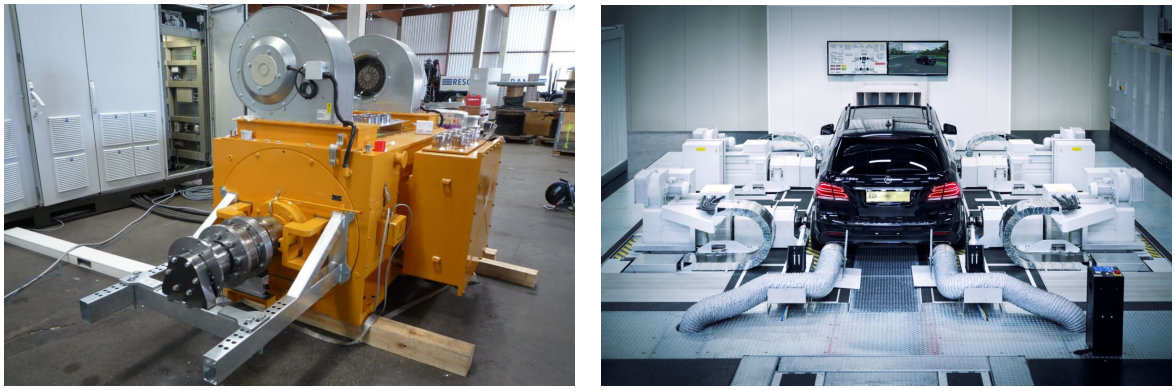

(a) Heavy-duty engine test bed.

(b) R2R full vehicle test bed.

Figure 2.5: Testing setups used for experimentation.

2.1.1 Heavy-duty engine test bed

The first experiments to target the modelling of test bed drive lines were conducted on the setup shown in Fig. 2.5(a). The arrangement is part of a test bed for heavy-duty combustion engines, and was available for testing during its pre-commissioning on the premises of KS Engineers. This circumstance explains the placement of machine and frequency converter (FC) in the centre of the assembly hall and the absence of a specimen. The actuator is an induction machine, which is covered in the orange housing in the centre of the picture. The upper left corner of Fig. 2.5(a) depicts the frequency converter of the test bed. The crucial segment of the FC from a control engineering perspective is the cabinet with the opened door, which contains the dSpace® processor board to execute the control-related

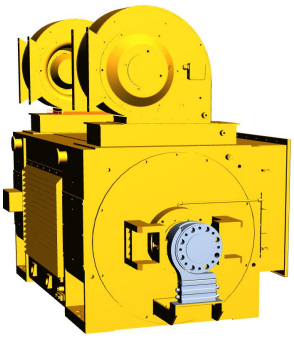

ELIN HKF145Z04		
power	kW	1400
speed	rpm	1337
torque	kNm	10
moment of inertia	kgm^2	23.9
current	A	1570
voltage	V	575
no. of pole pairs	–	2

Figure 2.6 & Table 2.1: Heavy-duty test bed: induction machine.

software C. As mentioned earlier, the output of C are the firing pulses for the transistor modules that adjust the voltages in the phases of the induction machine [35]. The phases are contained in the black cables on the left of the induction machine. The speed of the latter and the resulting shaft torque are measured by means of a rotary encoder and a torque measuring flange, respectively. The rotary encoder is mounted on the back of the machine, and hence is not visible in Fig. 2.5(a). The parameters of the most relevant components are listed in Tables 2.1, 2.2, 2.3 and 2.4.

HBM T12		
nominal torque	kNm	10
torsional stiffness	$MNm \cdot rad^{-1}$	7.9

Figure 2.7 & Table 2.2: Heavy-duty test bed: torque measuring flange.

Heidenhain ECN 413		
max. speed	rpm	15000
principle	–	sin-cos, optical incremental

Figure 2.8 & Table 2.3: Heavy-duty test bed: rotary encoder.

Heavy-duty test bed KS Engineers frequency converter		
power	MW	3.3
intermediate voltage	V	1000
control frequency	kHz	10
processor board	–	dSpace 1006

Figure 2.9 & Table 2.4: Heavy-duty test bed: frequency converter.

2.1.2 Road-to-rig test bed

The second test bed is the *road-to-rig* or *R2R* test bed shown in Fig. 2.5(b). Its purpose is to expose the tested vehicle precisely to the load conditions it would experience in real operation. In the present case, four electrical machines are employed for that objective. The presented R2R test bed was provided by KS Engineers as a second setup for experiments, after the heavy-duty test bed was shipped to the customer. For the experiments regarding the modelling of drive lines, the four axis were operated separately. By doing so, the setup in essence is equal to that of the heavy-duty test bed: The line is actuated by an induction machine, which is fed and controlled by the means of a highly dynamic frequency converter. Shaft torque and angular speed of the induction machine are measured with a torque measuring flange and a rotary encoder, respectively. The actual components, however, differ in certain aspects. Hence, the most important parameters are again listed in Tables 2.5, 2.6, 2.7 and 2.8.

HBM T12		
torque	kNm	5
torsional stiffness	MNm·rad^{-1}	4.6

Table 2.5: R2R test bed: torque measuring flange.

Heidenhain ECN 413		
max. speed	rpm	15000
principle	–	sin-cos, opt. inc.

Table 2.6: R2R test bed: rotary encoder.

Vascat MAC-QI 250P		
power	kW	376
speed	rpm	1123
torque	kNm	3.2
moment of inertia	kgm^2	3.3
current	A	715
voltage	V	400
no. of pole pairs	–	3

Table 2.7: R2R test bed: induction machine.

KS Engineers frequency converter		
power	MW	0.8
intermediate voltage	V	630
control frequency	kHz	10
processor board	–	dSpace 1005

Table 2.8: R2R test bed: frequency converter.

2.1.3 Chirp experiments

Chirp experiments consist of feeding chirped signals into a system of interest, where a "chirp" in this work is interpreted as a sinusoid with a linearly growing frequency. In the present context, the airgap torque T_{airgap} is interpreted as the plant's input. Hence, a chirp experiment in the following refers to an experiment where the actuator is demanded to

follow chirped torque profiles. Fig. 2.10 presents the result of one such experiment on the heavy-duty test bed. Due to high frequencies and little space for plotting, the signals appear as coloured areas, rather than sine-shaped oscillations.

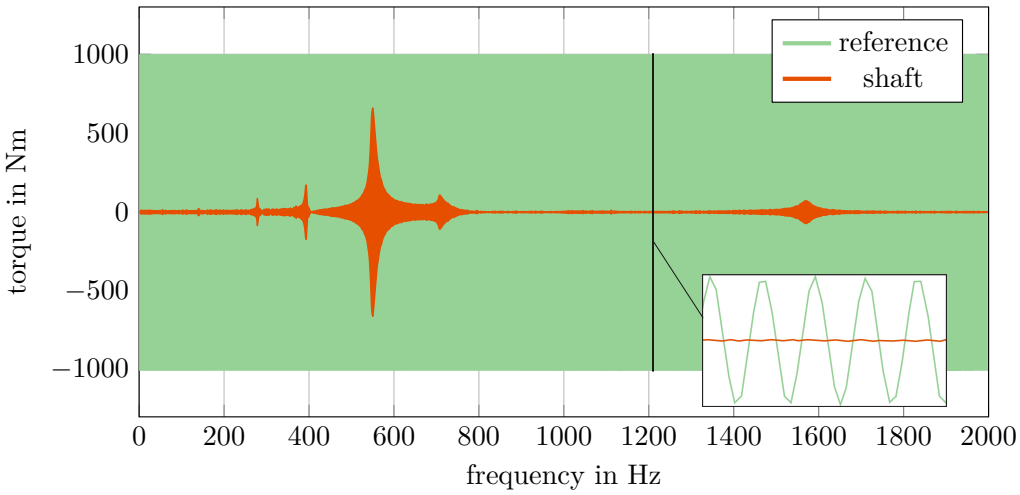

Figure 2.10: Chirp expirement on the heavy duty engine test bed.

The reference torque $\tilde{T}$ in this case may be expressed as

$$\tilde{T} = \hat{T} \cdot \sin\Big(\eta(t)\Big) = \hat{T} \cdot \sin\Big(\int_0^t \nu(t)\, d\tau\Big) = \hat{T} \cdot \sin\Big(2\pi \int_0^t \kappa\tau\, d\tau\Big), \tag{2.7}$$

with $\hat{T}$ as the sine wave's magnitude, η as the angular argument to the sine function, $\nu := \frac{\mathrm{d}}{\mathrm{d}t}\eta$ the frequency in radians, and κ as its linear growth rate. The other signals of interest, such as T_{airgap}, T_{shaft} or ω_1, result according the dynamics of the corresponding system. By the means of a chirp experiment, the assessment of a system's amplitude response and thus its resonance characteristics becomes possible immediately, as only the measured time-domain signals have to be inspected, without the need of additional computations. Moreover, the experiment itself does not require much preparation or prearrangement in the given settings. Therefore, much of the following analysis is based on insights gained by the means of chirp experiments.

2.2 Lumped structures

This section starts the discussion of drive line modelling, by presenting several ideas that are based on lumped inertias. The starting point of the analysis is the heavy-duty test bed discussed in Sec. 2.1.1, whose drive line was modified consecutively. Step by step, two flanges and a disk-pack coupling were added to the drive line. At each stage, numerous chirp experiments were conducted, of which three are shown in Figs. 2.11.

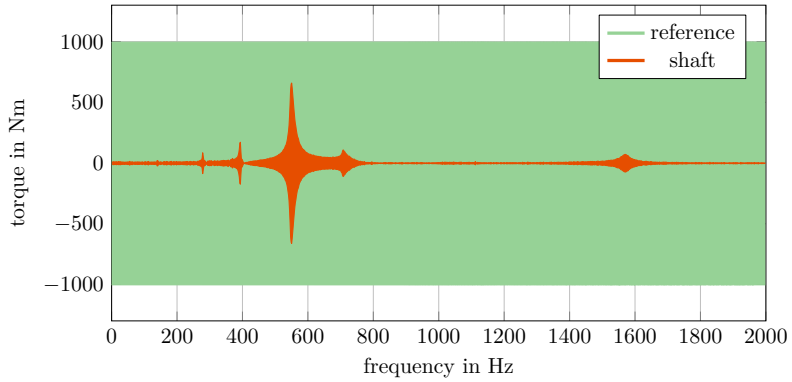

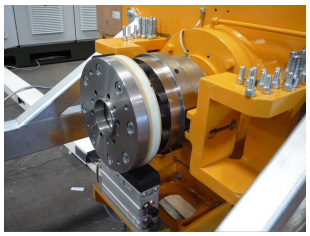

(a) Flange 1. Additional inertia: I_{f1}=0.14kgm^2.

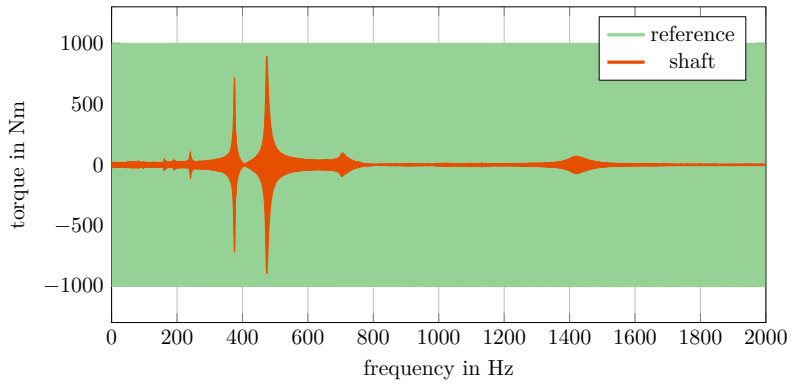

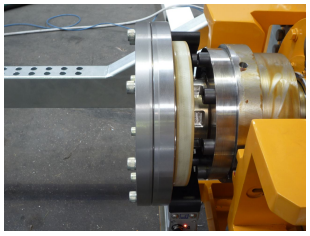

(b) Flange 2. Additional inertia: I_{f2}=0.14kgm^2.

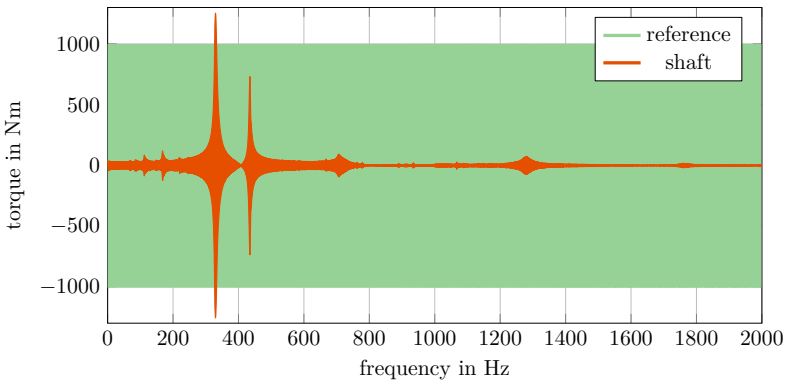

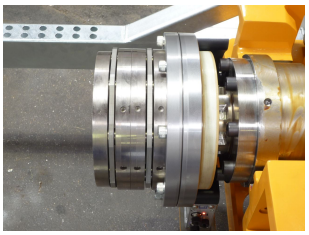

(c) Disk-pack coupling. Additional inertia: I_{mc}=0.28kgm^2.

Figure 2.11: Chirp experiments on the heavy-duty test bed for identification and validation purposes, next to the corresponding setup.

The objective of the modelling problem is to find a mathematical description of the setup, that is not only capable of reproducing the measured data for a given form of the drive line, but *also* physically meaningful, allowing to perform any real-life hardware-modification

also in the simulation model. This means that in case that the real drive line is altered, e.g., by adding inertia at the end of the line, that it must be possible to derive a new model for the altered setup simply by adding the same amount of inertia to the corresponding spot in the simulation model! It will be shown later that especially this requirement complicates the problem significantly.

Figure 2.11 shows that the setup exhibits at least four significant resonance frequencies (some of the peaks are not an individual resonances, like the one at 275Hz in Fig. 2.11(a); it lies at the half of the main resonance and is in fact caused by nonlinear actuator behaviour, i.e. that the produced airgap torque is not perfectly sinusoidal). To avoid confusion with angular speeds that are denoted by ω, frequencies in radians will in this work be denoted by ν, and frequencies in Hz by the common variable f. An intuitive way to model such a system, which is also proposed in literature [36], is to connect a sufficient number of inertias in series, at least five in this case, such that all of these resonances can be reproduced. Fig. 2.12 shows this model: the inertias $I_1, \ldots, I_5$ are connected by linear rotatory spring and damper elements, whose stiffness and damping coefficients along with the values of the inertias constitute the model's parameters. As the model structure along these lines can be found easily, the problem reduces to finding the right parameters.

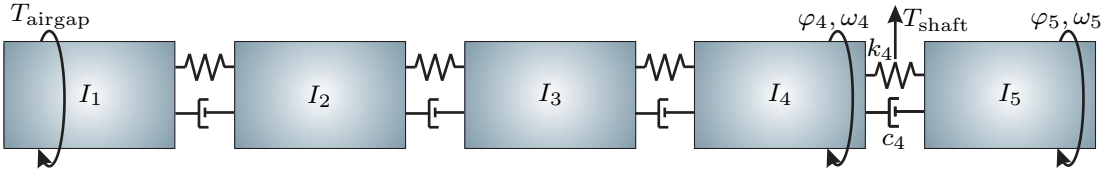

Figure 2.12: Chain of five inertias to model the heavy-duty test bed.

However, before this topic is treated, some mathematics regarding the representation of a system like the one shown in Fig. 2.12 is discussed. The following assumptions are made at this point to clarify the analysis:

1. Only the mechanical part of the system is investigated.
2. The considered system input is the airgap torque T_{airgap}, which can be calculated from measured machine currents according to the fundamental wave model for induction machines [37].
3. The considered output is the measured shaft torque T_{shaft}.
4. All system components, i.e. rotatory springs, dampers and lumped inertias, are considered linear.
5. The drive line is assumed to be free on both ends [38].

2.2.1 Model types

The state representation of a dynamical system is not unique, and different state coordinates may be interchanged by appropriate state transformations. The present case, however, is particularly ambiguous, as different model-types with different model orders may be employed to describe one and the same drive line. In the following, some of the possible approaches are presented by the means of the two-mass oscillator shown in Fig. 2.13. Therein, k, c, I_1, I_2, φ_1, φ_2, ω_1, ω_2 denote stiffness, damping, rotary inertias, angles and

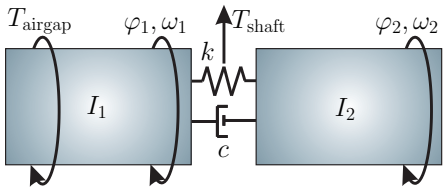

Figure 2.13: Two-mass oscillator.

angular velocities, respectively. All model-types described in the following are applicable to inertia chains of any length. A frequently seen mathematical description is obtained by using absolute signals only, i.e.

$$\begin{gathered}
\boldsymbol{x}_a := \left[\varphi_1, \omega_1, \varphi_2, \omega_2\right]^T, \\
\frac{\mathrm{d}}{\mathrm{d}t}\boldsymbol{x}_a = \underbrace{\begin{pmatrix} 0 & 1 & 0 & 0 \\ -\frac{k}{I_1} & -\frac{c}{I_1} & \frac{k}{I_1} & \frac{c}{I_1} \\ 0 & 0 & 0 & 1 \\ \frac{k}{I_2} & \frac{c}{I_2} & -\frac{k}{I_2} & -\frac{c}{I_2} \end{pmatrix}}_{=:\boldsymbol{A}_a} \boldsymbol{x}_a + \begin{bmatrix} 0 \\ \frac{1}{I_1} \\ 0 \\ 0 \end{bmatrix} T_{\text{airgap}}, \\
T_{\text{shaft}} = \begin{bmatrix} k & c & -k & -c \end{bmatrix} \boldsymbol{x}_a.
\end{gathered} \tag{2.8}$$

Also differential signals are used often, which yields

$$\begin{gathered}
\boldsymbol{x}_d := [\varphi_1 - \varphi_2, \omega_1 - \omega_2]^T =: [\Delta\varphi, \Delta\omega]^T, \\
\frac{\mathrm{d}}{\mathrm{d}t}\boldsymbol{x}_d = \underbrace{\begin{pmatrix} 0 & 1 \\ -k(\frac{1}{I_1} + \frac{1}{I_2}) & -c(\frac{1}{I_1} + \frac{1}{I_2}) \end{pmatrix}}_{=:\boldsymbol{A}_d} \boldsymbol{x}_d + \begin{bmatrix} 0 \\ \frac{1}{I_1} \end{bmatrix} T_{\text{airgap}}, \\
T_{\text{shaft}} = \begin{bmatrix} k & c \end{bmatrix} \boldsymbol{x}_d.
\end{gathered} \tag{2.9}$$

Model (2.9) requires two state variables less than model (2.8). However, every advantage comes at a cost, and so the lower model order is accompanied by the loss of information about absolute positions and velocities. A compromise that is employed by several authors, see e.g. [39], is the use of both absolute and differential signals, i.e.

$$\begin{gathered}\boldsymbol{x}_m \coloneqq [\varphi_1 - \varphi_2, \omega_1, \omega_2]^T, \\ \frac{\mathrm{d}}{\mathrm{d}t}\boldsymbol{x}_m = \underbrace{\begin{pmatrix} 0 & 1 & -1 \\ -k\frac{1}{I_1} & -c\frac{1}{I_1} & c\frac{1}{I_1} \\ k\frac{1}{I_2} & c\frac{1}{I_2} & -c\frac{1}{I_2} \end{pmatrix}}_{=:\boldsymbol{A}_m} \boldsymbol{x}_m + \begin{bmatrix} 0 \\ 0 \\ \frac{1}{I_1} \end{bmatrix} T_{\text{airgap}}, \\ T_{\text{shaft}} = \begin{bmatrix} k & c & -c \end{bmatrix} \boldsymbol{x}_m.\end{gathered} \tag{2.10}$$

Another approach, that is especially common in mechanical engineering, see e.g. [40–42], is the use of angles only. This leads to a second order differential equation, i.e.

$$\begin{gathered}\boldsymbol{x}_\varphi \coloneqq [\varphi_1, \varphi_2]^T, \\ \frac{\mathrm{d}^2}{\mathrm{d}t^2}\boldsymbol{x}_\varphi = \underbrace{\begin{pmatrix} -k\frac{1}{I_1} & k\frac{1}{I_1} \\ k\frac{1}{I_2} & -k\frac{1}{I_2} \end{pmatrix}}_{=:\boldsymbol{K}_\varphi} \boldsymbol{x}_\varphi + \underbrace{\begin{pmatrix} -c\frac{1}{I_1} & c\frac{1}{I_1} \\ c\frac{1}{I_2} & -c\frac{1}{I_2} \end{pmatrix}}_{=:\boldsymbol{C}_\varphi} \frac{\mathrm{d}}{\mathrm{d}t}\boldsymbol{x}_\varphi + \begin{bmatrix} \frac{1}{I_1} \\ 0 \end{bmatrix} T_{\text{airgap}}, \\ T_{\text{shaft}} = \begin{bmatrix} k & -k \end{bmatrix} \boldsymbol{x}_\varphi + \begin{bmatrix} c & -c \end{bmatrix} \frac{\mathrm{d}}{\mathrm{d}t}\boldsymbol{x}_\varphi,\end{gathered} \tag{2.11}$$

with the so-called stiffness and damping matrices $\boldsymbol{K}_\varphi$ and $\boldsymbol{C}_\varphi$. In that sense, the most compact description of a chain of inertias is achieved by applying the idea of differential signals to the second order system (2.11). For the two-mass oscillator, the result is a scalar equation:

$$\begin{gathered}x_\Delta \coloneqq \varphi_1 - \varphi_2, \\ \frac{\mathrm{d}^2}{\mathrm{d}t^2}x_\Delta = \underbrace{-k\left(\frac{1}{I_1} + \frac{1}{I_2}\right)}_{=:K_\Delta} x_\Delta \underbrace{-c\left(\frac{1}{I_1} + \frac{1}{I_2}\right)}_{=:C_\Delta} \frac{d}{dt}x_\Delta + \frac{1}{I_1}T_{\text{airgap}}, \\ T_{\text{shaft}} = kx_\Delta + c\frac{\mathrm{d}}{\mathrm{d}t}x_\Delta.\end{gathered} \tag{2.12}$$

In this work, all approaches are used at one point or the other, depending on the context and the needs of the given problem.

2.2.2 Practical resonance

In this work, resonance is interpreted as what is frequently termed *practical resonance*, which designates the frequencies that (locally) maximize a system's amplitude response [43, 44]. For the chirp experiments presented in Fig. 2.11, the local maxima are visible as the measured shaft torques' peaks. It is important to mention that for a multi-body system with damping, the practical resonance frequencies usually are highly similar, but not identical to the system's eigenfrequencies.

To clarify this distinction, the two-mass oscillator shown in Fig. 2.13 is considered again. On the one hand, the eigenvalues of matrix $\boldsymbol{A}_d$ according to (2.9) may be stated as

$$s_{d\{1,2\}} = -\frac{c}{2}\left(\frac{1}{I_1}+\frac{1}{I_2}\right) \pm \sqrt{\frac{c^2}{4}\left(\frac{1}{I_1}+\frac{1}{I_2}\right)^2 - k\left(\frac{1}{I_1}+\frac{1}{I_2}\right)}. \tag{2.13}$$

For the case that the discriminant's argument is negative, the system's eigenfrequency is given by the absolute value of the imaginary part of $s_{d\{1,2\}}$, i.e.

$$\nu_d = \sqrt{k\left(\frac{1}{I_1}+\frac{1}{I_2}\right) - \frac{c^2}{4}\left(\frac{1}{I_1}+\frac{1}{I_2}\right)^2}. \tag{2.14}$$

On the other hand, the transfer functions from T_{airgap} to any of the system's other signals share the same denominator, and may be represented in the general form of

$$G(s) = \frac{\mu(s)}{s^2 + c(\frac{1}{I_1}+\frac{1}{I_2})s + k(\frac{1}{I_1}+\frac{1}{I_2})}. \tag{2.15}$$

Therein, the numerator polynomial $\mu(s)$ differs from one output signal to the other; for $T_{\text{shaft}}(s)$, for example, it takes on the form of $\mu(s) = \frac{1}{I_1}(cs+k)$. Along these lines, the amplitude response may be expressed as

$$|G(j\nu)| = \frac{|\mu(j\nu)|}{\sqrt{(k(\frac{1}{I_1}+\frac{1}{I_2}) - \nu^2)^2 + c^2(\frac{1}{I_1}+\frac{1}{I_2})^2\nu^2}}, \tag{2.16}$$

whose denominator is minimized[3] for

$$\nu_{max} = \sqrt{k\left(\frac{1}{I_1}+\frac{1}{I_2}\right) - \frac{c^2}{2}\left(\frac{1}{I_1}+\frac{1}{I_2}\right)^2}. \tag{2.17}$$

Here, the squared damping coefficient is divided by 2, in contrast to (2.14). For output signals with a numerator polynomial of order zero, such as the differential angle $\Delta\varphi$ where

[3] For reasonable parameter settings, the second extremum $\nu_{max} = 0$ constitutes a maximum of the denominator polynomial, which is of no particular relevance for the present discussion.

$\mu(s) = \frac{1}{I_1}$, v_{max} in fact maximizes $|G(jv)|$, and so becomes the system's *practical resonance*. For other signals, such as T_{shaft}, also the numerator polynomial needs to be taken into account, which additionally modifies the outcome. One can see that already for the case of a two-mass oscillator, eigenfrequency and practical resonance are not equal.

For the drive lines considered in this work, however, the damping coefficients are small and by far exceeded by the systems' stiffness factors. Hence, eigenfrequencies and observed resonances are almost identical. It is for this reason that the following analysis focuses on assigning appropriate eigenvalues to the considered models in order to reproduce measured resonances in simulation, rather than manipulating the actual maxima of their amplitude responses, which usually constitutes an involved and complex task.

2.2.3 Eigenvalues

With regards to their eigenvalues, the modelling approaches presented in Sec. 2.2.1 show some appealing relations. To discuss those connections, a system of type (2.9), with state vector $\boldsymbol{x}_d$, dynamic matrix $\boldsymbol{A}_d$, and order n is considered first. Its eigenvalues are concatenated to the vector

$$\boldsymbol{s}_d = [s_{d,1}, s_{d,2}, \ldots, s_{d,n}]. \tag{2.18}$$

For the description presented in (2.8), which is based on absolute signals and uses the dynamic matrix $\boldsymbol{A}_a$ and the state vector $\boldsymbol{x}_a$, a transformation matrix in the form of

$$\boldsymbol{T} = \begin{pmatrix} \boldsymbol{I}_{2\times2} & \boldsymbol{0}_{2\times n} \\ \left(\begin{array}{c|c} \boldsymbol{I}_{n\times n} & \boldsymbol{0}_{n\times2} \end{array}\right) & -\left(\begin{array}{c|c} \boldsymbol{0}_{n\times2} & \boldsymbol{I}_{n\times n} \end{array}\right) \end{pmatrix}, \tag{2.19}$$

with appropriately dimensioned unity and zero matrices $\boldsymbol{I}$ and $\boldsymbol{0}$, can be used to transform the state vector $\boldsymbol{x}_a$ into

$$\boldsymbol{x}_{a,\text{new}} = \boldsymbol{T}\boldsymbol{x}_a = \begin{bmatrix} \varphi_1 \\ \omega_1 \\ \boldsymbol{x}_d \end{bmatrix}. \tag{2.20}$$

This modifies the dynamic matrix according to

$$\boldsymbol{T}\boldsymbol{A}_a\boldsymbol{T}^{-1} = \tilde{\boldsymbol{A}}_a = \begin{pmatrix} \begin{pmatrix} 0 & 1 \\ 0 & 0 \end{pmatrix} & \boldsymbol{M}_{2\times n} \\ \boldsymbol{0}_{n\times2} & \boldsymbol{A}_d \end{pmatrix}. \tag{2.21}$$

Therein, the upper right block $\boldsymbol{M}_{2\times n}$ does not have any effect on the eigenvalues of $\tilde{\boldsymbol{A}}_a$. Besides that, the eigenvalues of the upper left block are exclusively zero, which is also reflected in the characteristic equation of $\tilde{\boldsymbol{A}}_a$, i.e.

$$\det(s\boldsymbol{I}_{(n+2)\times(n+2)} - \tilde{\boldsymbol{A}}_a) = s^2 \cdot \det(s\boldsymbol{I}_{n\times n} - \boldsymbol{A}_d). \tag{2.22}$$

The solutions of (2.22) are of course also the eigenvalues of $\boldsymbol{A}_a$, as they are not modified by a similarity transformation. More precisely, the solutions of (2.22) are the eigenvalues of $\boldsymbol{A}_d$ extended by two zeros, i.e.

$$\boldsymbol{s}_a = [\boldsymbol{0}_{1\times 2}, \boldsymbol{s}_d]\,. \tag{2.23}$$

In the same fashion, one can show that the eigenvalues of a system of mixed absolute and differential variables as proposed in (2.10) are given by

$$\boldsymbol{s}_m = [0, \boldsymbol{s}_d]\,. \tag{2.24}$$

In both cases, the length of the additional zero vector is given by the number of state variables that exceed the order n. In a similar way, the structure of the set of eigenvalues can be analyzed for description (2.11) with the dynamic matrix $\boldsymbol{A}_\varphi$ and the state vector $\boldsymbol{x}_\varphi$, which uses absolute angles only. To that end, the system of absolute signals is transformed again, this time by the means of a row exchange matrix $\boldsymbol{P}$, such that

$$\boldsymbol{x}_{a,\text{new}} = \boldsymbol{P}\boldsymbol{x}_a = \left[\varphi_1\ \varphi_2\ \cdots\ \varphi_n \mid \omega_1\ \omega_2\ \cdots\ \omega_n\right]^T. \tag{2.25}$$

$\boldsymbol{P}$ can be represented as

$$\begin{aligned}\boldsymbol{P} = &\\ &\left(\begin{bmatrix}1\\ \boldsymbol{0}_{(N-1)\times 1}\end{bmatrix}\middle|\begin{bmatrix}\boldsymbol{0}_{(\frac{N}{2})\times 1}\\ 1\\ \boldsymbol{0}_{(\frac{N}{2}-1)\times 1}\end{bmatrix}\middle|\begin{bmatrix}\begin{bmatrix}0\\1\end{bmatrix}\\ \boldsymbol{0}_{(N-2)\times 1}\end{bmatrix}\middle|\begin{bmatrix}\boldsymbol{0}_{(\frac{N}{2}+1)\times 1}\\ 1\\ \boldsymbol{0}_{(\frac{N}{2}-2)\times 1}\end{bmatrix}\middle|\ \cdots\ \middle|\begin{bmatrix}\boldsymbol{0}_{(N-1)\times 1}\\ 1\end{bmatrix}\right)\\ &= \boldsymbol{P}^{-1},\end{aligned} \tag{2.26}$$

which is a so-called involutory matrix that is equal to its own inverse. It turns the dynamic matrix $\boldsymbol{A}_a$ into

$$\hat{\boldsymbol{A}}_a = \boldsymbol{P}\boldsymbol{A}_a\boldsymbol{P}^{-1} = \begin{pmatrix}\boldsymbol{0}_{\frac{N}{2}\times\frac{N}{2}} & \boldsymbol{I}_{\frac{N}{2}\times\frac{N}{2}}\\ \boldsymbol{K}_\varphi & \boldsymbol{C}_\varphi\end{pmatrix}, \tag{2.27}$$

where $N = n + 2$ stands for the order of $\boldsymbol{A}_a$. Given a description in the form of (2.11), the matrix $\hat{\boldsymbol{A}}_a$ can be built immediately with the matrices $\boldsymbol{K}_\varphi$ and $\boldsymbol{C}_\varphi$! Since (2.27) shows that $\hat{\boldsymbol{A}}_a$ and $\boldsymbol{A}_a$ are similar, one may build $\hat{\boldsymbol{A}}_a$ accordingly and compute directly the eigenvalues of $\boldsymbol{A}_a$. This dependency may be expressed by

$$\boldsymbol{s}_\varphi = \boldsymbol{s}_a = [\boldsymbol{0}_{1\times 2}, \boldsymbol{s}_d]\,. \tag{2.28}$$

Generally, finding the eigenvalues of a matrix means solving its characteristic equation. For the case of $\hat{\boldsymbol{A}}_a$, this results in

$$\begin{aligned}\det\begin{pmatrix}s\boldsymbol{I}_{\frac{N}{2}\times\frac{N}{2}} & -\boldsymbol{I}_{\frac{N}{2}\times\frac{N}{2}}\\ -\boldsymbol{K}_\varphi & s\boldsymbol{I}_{\frac{N}{2}\times\frac{N}{2}} - \boldsymbol{C}_\varphi\end{pmatrix} &= \det\left(s\boldsymbol{I}_{\frac{N}{2}\times\frac{N}{2}}\right)\det\left(s\boldsymbol{I}_{\frac{N}{2}\times\frac{N}{2}} - \boldsymbol{C}_\varphi - s^{-1}\boldsymbol{I}_{\frac{N}{2}\times\frac{N}{2}}\boldsymbol{K}_\varphi\right)\\ &= \det\left(s^2\boldsymbol{I}_{\frac{N}{2}\times\frac{N}{2}} - s\boldsymbol{C}_\varphi - \boldsymbol{K}_\varphi\right) = 0,\end{aligned} \tag{2.29}$$

where the argument of the det()-operation is the Laplace-transform of the original differential equation, which allows to gain another insight: As mentioned in Sec. 2.2.2, the damping coefficients are small compared to the stiffness parameters for the drive lines considered in this part of the thesis. Thus, neglecting the damping matrix often is a reasonable step to simplify the analysis. In the case of (2.29), this yields

$$\det\left(s_\varphi^2 \boldsymbol{I}_{\frac{N}{2}\times\frac{N}{2}} - \boldsymbol{K}_\varphi\right) = 0, \tag{2.30}$$

where the result is determined by the stiffness matrix $\boldsymbol{K}_\varphi$! As the actual eigenvalues s_K of $\boldsymbol{K}_\varphi$ are the solutions of

$$\det\left(s_K \boldsymbol{I}_{\frac{N}{2}\times\frac{N}{2}} - \boldsymbol{K}_\varphi\right) = 0, \tag{2.31}$$

one sees that s_K and s_φ are related via a simple square root operation. Along the same lines, a solution to the eigenvalue problem for model (2.12) can be found with the help of the matrix

$$\boldsymbol{A}_\Delta = \begin{pmatrix} \boldsymbol{0}_{(\frac{N}{2}-1)\times(\frac{N}{2}-1)} & \boldsymbol{I}_{(\frac{N}{2}-1)\times(\frac{N}{2}-1)} \\ \boldsymbol{K}_\Delta & \boldsymbol{C}_\Delta \end{pmatrix}, \tag{2.32}$$

which contains the reduced stiffness and damping matrices $\boldsymbol{K}_\Delta$ and $\boldsymbol{C}_\Delta$, respectively, and leads to

$$\boldsymbol{s}_\Delta = \boldsymbol{s}_d. \tag{2.33}$$

2.2.4 Eigenvectors

In addition to eigenvalues, also *eigenvectors* are critical for the analysis of oscillations. They determine the structure of a system's eigenmodes, and especially the eigenvector entries corresponding to angles allow an important insight: Their absolute values reveal the extent to which the related member takes part in the motion of a mode, and their

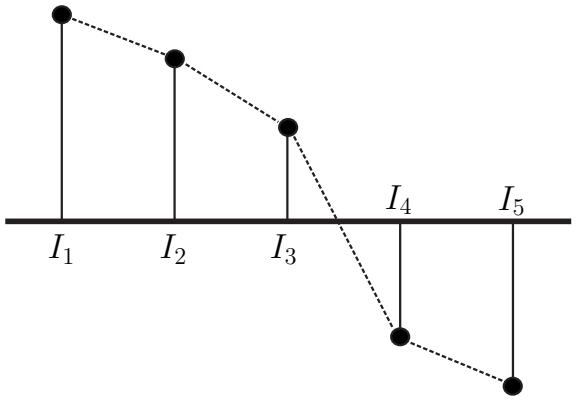

Figure 2.14: Possible mode shape for a five-mass oscillator.

signs allow to group the members into sections that move in phase. For systems whose states contain velocities, too, the corresponding eigenvector components are equal to the entries corresponding to angles multiplied with the respective eigenvalue [40, 45, 46]. An exemplary representation of an eigenmode by the means of the associated right-eigenvector is shown in Fig. 2.14.

In the case of the reduced stiffness matrix $\boldsymbol{K}_\Delta$, an interesting connection between left- and right-eigenvectors is found: For a given eigenvalue $s_{\Delta,i}$, the corresponding right-eigenvector $\boldsymbol{r}_i$ has to fulfil

$$\boldsymbol{K}_\Delta \boldsymbol{r}_i = s_{\Delta,i} \boldsymbol{r}_i. \tag{2.34}$$

Their counterparts, the left-eigenvectors $\boldsymbol{l}_i$ must solve the transposed version of (2.34), which follows as

$$\boldsymbol{l}_i^T \boldsymbol{K}_\Delta = \boldsymbol{l}_i^T s_{\Delta,i} \qquad \Rightarrow \qquad \boldsymbol{K}_\Delta^T \boldsymbol{l}_i = s_{\Delta,i} \boldsymbol{l}_i. \tag{2.35}$$

Taking a closer look at a general nth order reduced stiffness matrix, i.e.

$$\boldsymbol{K}_\Delta = \begin{pmatrix} -k_1(\frac{1}{I_1}+\frac{1}{I_2}) & k_2\frac{1}{I_2} & 0 & 0 & \cdots & 0 \\ k_1\frac{1}{I_2} & -k_2(\frac{1}{I_2}+\frac{1}{I_3}) & k_3\frac{1}{I_3} & 0 & \cdots & 0 \\ 0 & k_2\frac{1}{I_3} & -k_3(\frac{1}{I_3}+\frac{1}{I_4}) & k_4\frac{1}{I_4} & \cdots & 0 \\ \vdots & \cdots & & & \ddots & \vdots \\ 0 & 0 & 0 & & \cdots & -k_n(\frac{1}{I_n}+\frac{1}{I_{n+1}}) \end{pmatrix}, \tag{2.36}$$

one sees that transposing $\boldsymbol{K}_\Delta$ does not change much in the matrix; mainly because the entry in a row's *right* secondary diagonal only differs in its stiffness factor from the entry in the consecutive row's *left* secondary diagonal. Thus, to compute $\boldsymbol{K}_\Delta^T$, only these stiffness factors have to be interchanged. This can be achieved by the means of a similarity transformation that uses diagonal matrices only: Multiplying with

$$\boldsymbol{L} = \begin{pmatrix} 1 & 0 & \cdots & 0 \\ 0 & \frac{k_2}{k_1} & \cdots & 0 \\ \vdots & & \ddots & \vdots \\ 0 & 0 & \cdots & \frac{k_n}{k_1} \end{pmatrix} \tag{2.37}$$

from the left, and with its inverse

$$\boldsymbol{L}^{-1} = \begin{pmatrix} 1 & 0 & \cdots & 0 \\ 0 & \frac{k_1}{k_2} & \cdots & 0 \\ \vdots & & \ddots & \vdots \\ 0 & 0 & \cdots & \frac{k_1}{k_n} \end{pmatrix} =: \boldsymbol{R} \tag{2.38}$$

from the right, one obtains

$$\boldsymbol{L}\boldsymbol{K}_{\Delta}\boldsymbol{R} = \begin{pmatrix} -k_1(\frac{1}{I_1}+\frac{1}{I_2}) & k_1\frac{1}{I_2} & 0 & 0 & \cdots & 0 \\ k_2\frac{1}{I_2} & -k_2(\frac{1}{I_2}+\frac{1}{I_3}) & k_2\frac{1}{I_3} & 0 & \cdots & 0 \\ 0 & k_3\frac{1}{I_3} & -k_3(\frac{1}{I_3}+\frac{1}{I_4}) & k_3\frac{1}{I_4} & \cdots & 0 \\ \vdots & \cdots & & & \ddots & \vdots \\ 0 & 0 & 0 & & \cdots & -k_n(\frac{1}{I_n}+\frac{1}{I_{n+1}}) \end{pmatrix} = \boldsymbol{K}_{\Delta}^T. \tag{2.39}$$

For the connection between left- and right-eigenvectors, this leads to

$$\boldsymbol{K}_{\Delta}^T\boldsymbol{l}_i = \boldsymbol{L}\boldsymbol{K}_{\Delta}\boldsymbol{R}\boldsymbol{l}_i = s_{\Delta,i}\boldsymbol{l}_i, \tag{2.40}$$

which, after multiplying with $\boldsymbol{L}^{-1}$ from the left, yields

$$\boldsymbol{K}_{\Delta}\boldsymbol{R}\boldsymbol{l}_i = s_{\Delta,i}\boldsymbol{L}^{-1}\boldsymbol{l}_i. \tag{2.41}$$

Since $\boldsymbol{L}^{-1} = \boldsymbol{R}$, one obtains

$$\boldsymbol{K}_{\Delta}\boldsymbol{R}\boldsymbol{l}_i = s_{\Delta,i}\boldsymbol{R}\boldsymbol{l}_i, \tag{2.42}$$

and arrives at the insight that $\boldsymbol{R}\boldsymbol{l}_i$ solves the right-eigenvector-equation for $s_{\Delta,i}$. This result may be interpreted as a new set of eigenvectors

$$\tilde{\boldsymbol{r}}_i = \boldsymbol{R}\boldsymbol{l}_i, \tag{2.43}$$

which, as $\boldsymbol{R}$ is a simple diagonal matrix, demonstrates that a set of new right-eigenvectors can be produced by scaling the components of a given set of left-eigenvectors with fractions that consist of the stiffness factors of the model only! The idea can also be reversed, in order to introduce a new set of left-eigenvectors by using an initial set of right-eigenvectors, i.e.

$$\tilde{\boldsymbol{l}}_i = \boldsymbol{L}\boldsymbol{r}_i. \tag{2.44}$$

One possible application of these connections is to express the inverse of a matrix of eigenvectors. Denoting the matrix of right-eigenvectors[4] by $\boldsymbol{V}_r$, i.e.

$$\boldsymbol{V}_r = \left(\begin{array}{c|c|c|c} \boldsymbol{r}_1 & \boldsymbol{r}_2 & \cdots & \boldsymbol{r}_n \end{array} \right), \tag{2.45}$$

one may introduce a matrix of new left-eigenvectors as

$$\boldsymbol{V}_{\tilde{l}} = \left(\begin{array}{c|c|c|c} \tilde{\boldsymbol{l}}_1 & \tilde{\boldsymbol{l}}_2 & \cdots & \tilde{\boldsymbol{l}}_n \end{array} \right) = \boldsymbol{L}\boldsymbol{V}_r. \tag{2.46}$$

Since left- and right-eigenvectors of a matrix with distinct eigenvalues are orthogonal to each other, it follows that

$$\boldsymbol{V}_{\tilde{l}}^T\boldsymbol{V}_r = \boldsymbol{V}_r^T\boldsymbol{L}^T\boldsymbol{V}_r = \boldsymbol{V}_r^T\boldsymbol{L}\boldsymbol{V}_r = \boldsymbol{\Gamma}, \tag{2.47}$$

[4] Analogue ideas can of course be developed for a matrix of left-eigenvectors.

where the diagonal matrix

$$\boldsymbol{\Gamma} = \begin{pmatrix} \gamma_1 & 0 & \cdots & 0 \\ 0 & \gamma_2 & \cdots & 0 \\ \vdots & \cdots & \ddots & \vdots \\ 0 & \cdots & 0 & \gamma_n \end{pmatrix} \tag{2.48}$$

accounts for the fact that the considered vectors do not necessarily have to have length one, and that the matrix $\boldsymbol{L}$ in general does not conserve the length of a vector. Since (2.47) is a quadratic form, the entries $\gamma_1, \gamma_2, \ldots \gamma_n$ are non-negative. Rearranging (2.47), the inverse of $\boldsymbol{V}_r$ may thus be expressed as

$$\boldsymbol{V}_r^{-1} = \boldsymbol{\Gamma}^{-1} \boldsymbol{V}_r^T \boldsymbol{L}. \tag{2.49}$$

2.2.5 Eigenvalue derivatives

The results achieved in the preceding sections are now combined to discuss another important aspect, the derivatives of the considered models' eigenvalues. The upcoming considerations are partly based on ideas published in [47, 48], and start with the right-eigenvector equation for the reduced stiffness model in matrix form, i.e.

$$\boldsymbol{K}_\Delta \boldsymbol{V}_r = \boldsymbol{V}_r \boldsymbol{\Lambda}. \tag{2.50}$$

Therein, $\boldsymbol{V}_r$ as in (2.45) contains the right-eigenvectors as column vectors, and $\boldsymbol{\Lambda}$ is a diagonal matrix that comprises the eigenvalues of $\boldsymbol{K}_\Delta$. Assuming that the matrices depend on a scalar parameter p, i.e. $\boldsymbol{K}_\Delta(p)$, $\boldsymbol{V}_r(p)$ and $\boldsymbol{\Lambda}(p)$, and abbreviating the derivative $\frac{\mathrm{d}}{\mathrm{d}p}$ with a dash, the derivative of (2.50) with respect to p may be stated as

$$\boldsymbol{K}_\Delta' \boldsymbol{V}_r + \boldsymbol{K}_\Delta \boldsymbol{V}_r' = \boldsymbol{V}_r' \boldsymbol{\Lambda} + \boldsymbol{V}_r \boldsymbol{\Lambda}'. \tag{2.51}$$

Equation (2.51) can be rearranged to

$$\boldsymbol{K}_\Delta' \boldsymbol{V}_r - \boldsymbol{V}_r \boldsymbol{\Lambda}' = -\boldsymbol{K}_\Delta \boldsymbol{V}_r' + \boldsymbol{V}_r' \boldsymbol{\Lambda}, \tag{2.52}$$

where a left-multiplication with $\boldsymbol{V}_r^{-1}$ yields

$$\boldsymbol{V}_r^{-1} \boldsymbol{K}_\Delta' \boldsymbol{V}_r - \underbrace{\boldsymbol{V}_r^{-1} \boldsymbol{V}_r}_{=\boldsymbol{I}} \boldsymbol{\Lambda}' = -\boldsymbol{V}_r^{-1} \boldsymbol{K}_\Delta \boldsymbol{V}_r' + \boldsymbol{V}_r^{-1} \boldsymbol{V}_r' \boldsymbol{\Lambda}. \tag{2.53}$$

At this point, some linear algebra is employed for further simplification: Reduced stiffness-matrices like $\boldsymbol{K}_\Delta$ are non-defective for any reasonable parameter setting. Thus, their eigenvectors are linear independent, and span the whole $\mathbb{R}^n$ space. This allows to find a basis matrix $\boldsymbol{C}$ that linearly combines the right-eigenvectors in $\boldsymbol{V}_r$ such that they describe the derivative $\frac{\mathrm{d}}{\mathrm{d}p} \boldsymbol{V}_r = \boldsymbol{V}_r'$, i.e.

$$\boldsymbol{V}_r' = \boldsymbol{V}_r \boldsymbol{C} \quad \Rightarrow \quad \boldsymbol{C} = \boldsymbol{V}_r^{-1} \boldsymbol{V}_r' = \boldsymbol{V}_r^{-1} \boldsymbol{V}_r'. \tag{2.54}$$

Combining (2.53) and (2.54), one obtains

$$\boldsymbol{V}_r^{-1}\boldsymbol{K}_\Delta'\boldsymbol{V}_r - \boldsymbol{\Lambda}' = -\underbrace{\boldsymbol{V}_r^{-1}\underbrace{\boldsymbol{K}_\Delta\boldsymbol{V}_r}_{=\boldsymbol{V}_r\boldsymbol{\Lambda}}}_{=\boldsymbol{\Lambda}}\boldsymbol{C} + \underbrace{\boldsymbol{V}_r^{-1}\boldsymbol{V}_r}_{=\boldsymbol{I}}\boldsymbol{C}\boldsymbol{\Lambda}, \tag{2.55}$$

which leads to

$$\boldsymbol{\Lambda}' = \boldsymbol{V}_r^{-1}\boldsymbol{K}_\Delta'\boldsymbol{V}_r + \boldsymbol{\Lambda}\boldsymbol{C} - \boldsymbol{C}\boldsymbol{\Lambda}. \tag{2.56}$$

Therein, the main diagonal of $\boldsymbol{\Lambda}\boldsymbol{C} - \boldsymbol{C}\boldsymbol{\Lambda}$ is identically zero, which significantly simplifies the analysis, since the main diagonal of $\boldsymbol{\Lambda}'$ alone represents the sought eigenvalue derivatives. An important case in that regard are situations where the last inertia I_{n+1} is modified, as they describe the changeover from one device-under-test to another. In that sense, the reduced stiffness matrix $\boldsymbol{K}_\Delta$ is derived with respect to I_{n+1}, which yields

$$\frac{\mathrm{d}}{\mathrm{d}I_{n+1}}\boldsymbol{K}_\Delta = \begin{pmatrix} 0 & \cdots & 0 \\ \vdots & \ddots & 0 \\ 0 & \cdots & k_n\frac{1}{I_{n+1}^2} \end{pmatrix} = \boldsymbol{K}_\Delta'. \tag{2.57}$$

Inserting (2.57) into (2.56) and using expression (2.49) for $\boldsymbol{V}_r^{-1}$ gives

$$\boldsymbol{\Lambda}' = \boldsymbol{\Gamma}^{-1}\boldsymbol{V}_r^T\boldsymbol{L}\begin{pmatrix} 0 & \cdots & 0 \\ \vdots & \ddots & 0 \\ 0 & \cdots & k_n\frac{1}{I_{n+1}^2} \end{pmatrix}\boldsymbol{V}_r. \tag{2.58}$$

Reducing (2.58) to its main diagonal finally results in

$$\boldsymbol{\lambda}' = \frac{k_n^2}{k_1 I_{n+1}^2}\boldsymbol{\Gamma}^{-1}\begin{pmatrix} r_{1,n}^2 \\ \vdots \\ r_{n,n}^2 \end{pmatrix}, \tag{2.59}$$

where $\boldsymbol{\lambda}'$ represents the vector of eigenvalue derivatives, and $r_{i,n}$ stands for the nth entry of each of the right-eigenvectors. As all $r_{i,n}$ have to be non-zero[5], and since (2.59) holds for any positive I_{n+1}, one arrives at the following insight: If the last member in a chain of inertias is altered, then all the eigenvalues, and with them *all* the resonances, change. Moreover, as the eigenvalues of $\boldsymbol{K}_\Delta$ are negative, they move towards zero for a growing inertia I_{n+1}, which decreases their absolute values, and with that the associated eigenfrequencies.

[5]The opposite case would describe a situation where the last differential angle $\Delta\varphi_N$ is at standstill, while the remaining differential angles perform an oscillation. Since a combination of $\Delta\varphi_{N-1} \neq 0$ and $\Delta\varphi_N = 0$ results in a net torque acting on I_N and thus on φ_N, this is physically not possible.

2.2.6 Analytical solutions

This section discusses the question of analytical feasibility of the parametrization problem, which is *how* and *if* the parameters of a chain of inertias can be determined analytically from the knowledge about its practical resonances. It turns out that useful analytical solutions are achievable up until the class of three-mass oscillators.

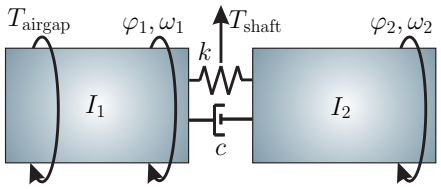

Figure 2.15: Two-mass oscillator.

Two-mass oscillator

The associated structure is once more the one shown in Fig. 2.15. To simplify the problem, the system's damping is neglected in a first step, in order to align the observed practical resonance with the system's eigenfrequency. By doing so, the connecting stiffness k can be obtained by rearranging either (2.14) or (2.17), which leads to

$$k = \frac{I_1 I_2}{I_1 + I_2} \nu_r^2, \tag{2.60}$$

given that the distribution of inertia between I_1 and I_2 and the practical resonance frequency ν_r are known a priori. If either I_1 or I_2 is not known from the beginning, but k is, then (2.60) may of course be solved for the missing inertia. What is still unknown is the damping parameter c. As discussed in Section 2.2.2, the damping parameters in the considered setups only marginally impact the locations of the observed resonances, and mainly affect the height of the peaks in the amplitude response. Thus, the values for the damping parameters are often determined in a separate, second step, either by numerical optimization [49] or by hand design, with the objective to adjust the form of the model's amplitude response.

Three-mass oscillator

The transition to a three-mass oscillator gravely increases the complexity of the problem. The corresponding structure is shown in Fig. 2.16, and allows to reproduce two resonance frequencies. If the system's damping is again neglected in a first step, two of the remaining parameters may be derived from two resonances $\nu_{r,1}$ and $\nu_{r,2}$. In case that the stiffnesses k_1

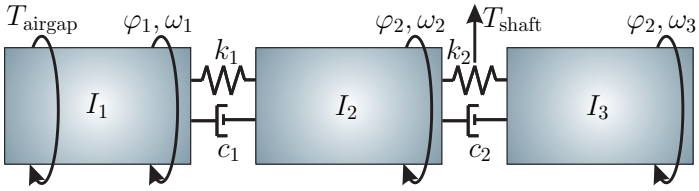

Figure 2.16: Three-mass oscillator.

and k_2 are unknown, one may proceed as follows: From the reduced stiffness matrix $\boldsymbol{K}_\Delta$, which in this case is given by

$$\boldsymbol{K}_\Delta = \begin{pmatrix} -k_1\left(\frac{1}{I_1}+\frac{1}{I_2}\right) & k_2\frac{1}{I_2} \\ k_1\frac{1}{I_2} & -k_2\left(\frac{1}{I_2}+\frac{1}{I_3}\right) \end{pmatrix}, \tag{2.61}$$

one may compute the characteristic polynomial

$$\begin{aligned} \det\left(s^2\boldsymbol{I}_{2\times2} - \boldsymbol{K}_\Delta\right) = s^4 + \left(k_1\left(\frac{1}{I_1}+\frac{1}{I_2}\right) + k_2\left(\frac{1}{I_2}+\frac{1}{I_3}\right)\right)s^2 \\ + k_1k_2\left(\frac{1}{I_1}\frac{1}{I_2} + \frac{1}{I_1}\frac{1}{I_3} + \frac{1}{I_2}\frac{1}{I_3}\right). \end{aligned} \tag{2.62}$$

To reproduce the two resonances mentioned earlier, the imaginary parts of the roots of (2.62) must coincide with $\nu_{r,1}$ and $\nu_{r,2}$. This demand can be formulated as

$$\det\left(s^2\boldsymbol{I}_{2\times2} - \boldsymbol{K}_\Delta\right) \stackrel{!}{=} (s^2+\nu_{r,1}^2)(s^2+\nu_{r,2}^2) = s^4 + (\nu_{r,1}^2+\nu_{r,2}^2)s^2 + \nu_{r,1}^2\nu_{r,2}^2, \tag{2.63}$$

from which the coefficients of s^2 and s^0 can be compared with those of (2.62). This step leads to

$$\begin{aligned} \text{I}: \quad \nu_{r,1}^2+\nu_{r,2}^2 &\stackrel{!}{=} k_1\left(\frac{1}{I_1}+\frac{1}{I_2}\right) + k_2\left(\frac{1}{I_2}+\frac{1}{I_3}\right) \\ \text{II}: \quad \nu_{r,1}^2\nu_{r,2}^2 &\stackrel{!}{=} k_1k_2\left(\frac{1}{I_1}\frac{1}{I_2} + \frac{1}{I_1}\frac{1}{I_3} + \frac{1}{I_2}\frac{1}{I_3}\right), \end{aligned} \tag{2.64}$$

a system of nonlinear equations, out of which k_1 and k_2 can be obtained. Unfortunately, (2.64) does not possess a unique solution. On the one hand, the tuple

$$\begin{aligned} k_1 &= \frac{1}{2\left(\frac{1}{I_1}+\frac{1}{I_2}\right)}\left(\nu_{r,1}^2+\nu_{r,2}^2 + \sqrt{\left(\nu_{r,1}^2+\nu_{r,2}^2\right)^2 - 4\nu_{r,1}^2\nu_{r,2}^2\frac{\left(\frac{1}{I_1}+\frac{1}{I_2}\right)\left(\frac{1}{I_2}+\frac{1}{I_3}\right)}{\frac{1}{I_1}\frac{1}{I_2}+\frac{1}{I_1}\frac{1}{I_3}+\frac{1}{I_2}\frac{1}{I_3}}}\right) \\ k_2 &= \frac{1}{2\left(\frac{1}{I_2}+\frac{1}{I_3}\right)}\left(\nu_{r,1}^2+\nu_{r,2}^2 - \sqrt{\left(\nu_{r,1}^2+\nu_{r,2}^2\right)^2 - 4\nu_{r,1}^2\nu_{r,2}^2\frac{\left(\frac{1}{I_1}+\frac{1}{I_2}\right)\left(\frac{1}{I_2}+\frac{1}{I_3}\right)}{\frac{1}{I_1}\frac{1}{I_2}+\frac{1}{I_1}\frac{1}{I_3}+\frac{1}{I_2}\frac{1}{I_3}}}\right) \end{aligned} \tag{2.65}$$

fulfils (2.64), but on the other hand also

$$k_1^* = \frac{1}{2\left(\frac{1}{I_1}+\frac{1}{I_2}\right)}\left(v_{r,1}^2 + v_{r,2}^2 - \sqrt{\left(v_{r,1}^2 + v_{r,2}^2\right)^2 - 4v_{r,1}^2 v_{r,2}^2 \frac{\left(\frac{1}{I_1}+\frac{1}{I_2}\right)\left(\frac{1}{I_2}+\frac{1}{I_3}\right)}{\frac{1}{I_1}\frac{1}{I_2}+\frac{1}{I_1}\frac{1}{I_3}+\frac{1}{I_2}\frac{1}{I_3}}}\right)$$
$$k_2^* = \frac{1}{2\left(\frac{1}{I_2}+\frac{1}{I_3}\right)}\left(v_{r,1}^2 + v_{r,2}^2 + \sqrt{\left(v_{r,1}^2 + v_{r,2}^2\right)^2 - 4v_{r,1}^2 v_{r,2}^2 \frac{\left(\frac{1}{I_1}+\frac{1}{I_2}\right)\left(\frac{1}{I_2}+\frac{1}{I_3}\right)}{\frac{1}{I_1}\frac{1}{I_2}+\frac{1}{I_1}\frac{1}{I_3}+\frac{1}{I_2}\frac{1}{I_3}}}\right), \tag{2.66}$$

where the signs in front of the square-root terms are reversed, qualifies as a solution. This property can be explained intuitively by performing the transition of $I_2 \to \infty$. In this case, the first tuple converges towards

$$k_1 = v_{r,1}^2 I_1 \qquad \text{and} \qquad k_2 = v_{r,2}^2 I_3, \tag{2.67}$$

while the second one turns into

$$k_1^* = v_{r,2}^2 I_1 \qquad \text{and} \qquad k_2^* = v_{r,1}^2 I_3. \tag{2.68}$$

The system then consists of two one-mass oscillators, whose spring is on the other side connected to the infinitely large inertia I_2. If it is not known which resonance belongs to which one-mass oscillator, a second solution can always be produced by exchanging the assignment of $v_{r,1}$ and $v_{r,2}$ to the one-mass oscillators belonging to I_1 and I_3, respectively. One can see that the complexity of the results increases rapidly with the number of involved inertias, and that on top of that, the results become more and more ambivalent. Thus, from the class of four-mass-oscillators onwards, methods of numerical optimization are usually employed to support the process of finding a model's parameters.

2.2.7 Numerical optimization

In order to satisfyingly reproduce the behaviour of the considered heavy-duty test bed's drive line, a simulation model needs to reflect at least the four resonance frequencies that are visible in the plots of Fig. 2.11. Additionally, it *must* be possible to alter the model exactly

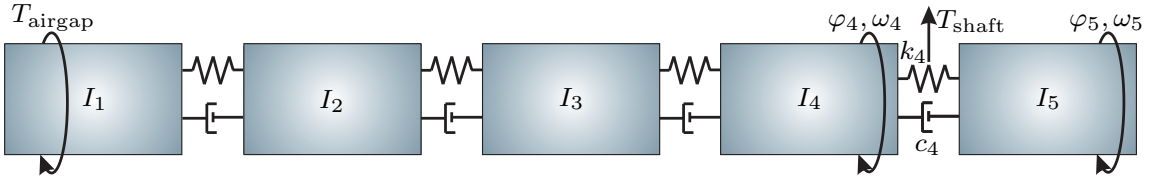

Figure 2.17: Five-mass oscillator.

like the real drive line, in this case inertia is added to the last member of the chain, and still preserve the model's capability of reproducing accurately the corresponding measured data. The four resonances require at least five rotational inertias, which in the simplest case leads to the five-mass oscillator shown in Fig. 2.17. Since the parameters of such a structure can no longer be found analytically, and moreover are not unique, they are determined by the means of numerical optimization.

In order to produce physically meaningful results, the elements of the model are inspired by certain parts of the real drive line: The first inertia is thought of as a representative of the induction machine rotor, the inertias I_2 and I_3 are interpreted as the sections neighbouring the connecting hub between the rotor and the torque measuring flange, and the two members of the latter are represented by I_4 and I_5. Consequently, the simulated equivalent of the measured shaft torque is the torque exchanged between I_4 and I_5, which leads to $T_{\text{shaft}} = k_4(\varphi_4 - \varphi_5) + c_4(\omega_4 - \omega_5)$, and the induction machine's air gap torque is once more denoted by T_{airgap}. In total, values for $I_1, \ldots, I_5$, and the stiffness and damping coefficients of the shafts, i.e. $k_1, \ldots, k_4$ and $c_1, \ldots, c_4$, have to be found. When looking to determine the parameters, data sheets or design drawings are often only of limited help, as especially the spring and damper elements do not have discrete physical counterparts in the actual setup. Eventually, a combination of two optimization problems was employed to find the parameters. The *first* one may be written out as

$$\begin{array}{lll} \underset{\boldsymbol{k},\mathcal{I}}{\text{minimize}} & \mathcal{J} = \boldsymbol{e}_\nu^T \boldsymbol{Q} \boldsymbol{e}_\nu & \\ \text{subject to} & I_{i,\min} \leq I_i \leq I_{i,\max}, & i = 1, \ldots, 5, \\ \text{and} & k_{i,\min} \leq k_i \leq k_{i,\max}, & i = 1, \ldots, 4, \end{array} \tag{2.69}$$

and aims at finding the right inertia and stiffness values to fix the location of the resonances, while the *second* one adjusts the damping parameters in order to shape the resulting amplitude response. The vectors $\mathcal{I} = \left[I_1, I_2, I_3, I_4, I_5\right]$ and $\boldsymbol{k} = \left[k_1, k_2, k_3, k_4\right]$ subsume the inertias and stiffnesses of the model. The cost function $\mathcal{J}$ is a quadratic form produced by the vector of frequency errors

$$\boldsymbol{e}_\nu = \begin{bmatrix} \nu_{r,1} - \tilde{\nu}_{r,1} \\ \nu_{r,2} - \tilde{\nu}_{r,2} \\ \nu_{r,3} - \tilde{\nu}_{r,3} \\ \nu_{r,4} - \tilde{\nu}_{r,4} \end{bmatrix} \tag{2.70}$$

and a diagonal weighting matrix $\boldsymbol{Q}$ with exclusively positive entries, which allows emphasize certain resonances. In (2.70), $\nu_{r,i}$ denotes the measured practical resonance frequencies, while $\tilde{\nu}_{r,i}$ stands for their counterparts predicted by the model. The inequality constraints $I_{i,\min} \leq I_i \leq I_{i,\max}$ and $k_{i,\min} \leq k_i \leq k_{i,\max}$ restrict each variable to at least the set of positive real numbers $\mathbb{R}^+$ – or to a subset of it, if any additional information about a parameter is available. This is, for instance, the case for inertia I_1. The latter is known to be close to $24\,\text{kgm}^2$, which led to choose $I_{1,\min} = 22.5$ and $I_{1,\max} = 25.5$, as it is known from experience that data sheet values for machine inertias frequently vary in the range of

±5%. The connection between $\mathcal{I}$, $\boldsymbol{k}$ and $\mathcal{J}$ is given by the characterstic eigenvalue equation of the used model, as laid out in Section 2.2.2, where it is shown that eigenvalues and resonances are identical for cases with negligible or very small damping, which is the case here. Unfortunately, these equations are highly nonlinear, which leads to optimization problems that are particularly hard to solve and puts a lot of weight also on the settings of the employed numerical algorithm. Eventually, MATLAB's *fmincon* algorithm turned out to perform reasonably well in the given setting.

The *second* optimization problem deals with finding the right damping parameters. The main idea in this regard is to adjust c_1, c_2, c_3 and c_4 such that the amplitude response of the model at the considered resonance frequencies coincides with that of the real system. Formally, this approach can be written out almost as before, i.e.

$$\begin{aligned} &\underset{\boldsymbol{c}}{\text{minimize}} && \mathcal{V} = \boldsymbol{e}_A^T \boldsymbol{R} \boldsymbol{e}_A \\ &\text{subject to} && c_{i,\min} \leq c_i \leq c_{i,\max}, \quad i = 1, \ldots, 4. \end{aligned} \tag{2.71}$$

Similar to (2.69), the cost function $\mathcal{V}$ is given by a quadratic form, with the diagonal matrix $\boldsymbol{R}$ to prioritize certain resonances. The variable $\boldsymbol{e}_A$ again corresponds to the error between model and measurement, in this case with regards to the amplitude response at the practical resonances $\nu_{r,i}$. The measured values are derived directly from the chirp experiments, and, using $G(j\nu)$ to represent the frequency response of the drive line, will in the following be denoted by $|G(j\nu_{r,i})|$. Introducing $|\tilde{G}(j\nu_{r,i})|$ for the results produced by the model[6], one arrives at

$$\boldsymbol{e}_A = \begin{bmatrix} |G(j\nu_{r,1})| - |\tilde{G}(j\nu_{r,1})| \\ \vdots \\ |G(j\nu_{r,4})| - |\tilde{G}(j\nu_{r,4})| \end{bmatrix}. \tag{2.72}$$

In consistency with the first optimization problem, MATLAB's *fmincon* algorithm was employed for the second one, too. The resulting parameter values and the settings for the algorithm are listed in Appendix A.1.

Eventually, the measurements presented in Fig. 2.11 were repeated in simulation. Of the three measurements, the information provided by the first one was used for the optimization process, while the other two experiments were considered for validation. To that end, the last inertia I_5 was increased stepwise, by adding the inertia values of the additionally mounted components[7]. In every simulation, the measured airgap torque was fed into the model, leading to the results shown in Figs. 2.18(a), 2.18(b) and 2.18(c).

[6] $\tilde{G}(j\nu_{r,i})$ can be computed with ease using MATLAB's *control-system-toolbox*.

[7] The incremental inertia values are known precisely from design drawings.

2.2.8 Results: chain of lumped inertias

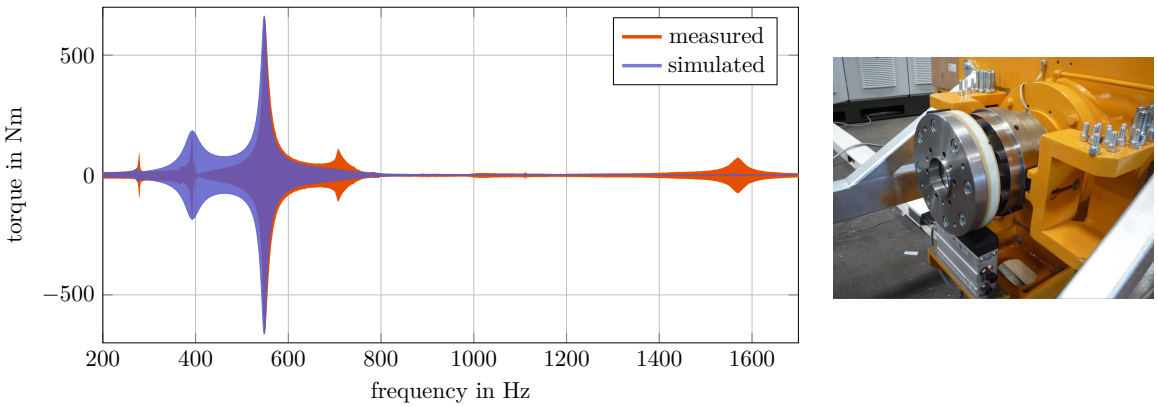

(a) Flange 1, additional inertia: I_{f1}=0.13kgm^2, which is included in $I_{5,1} = 0.14 kgm^2$, a result from optimization.

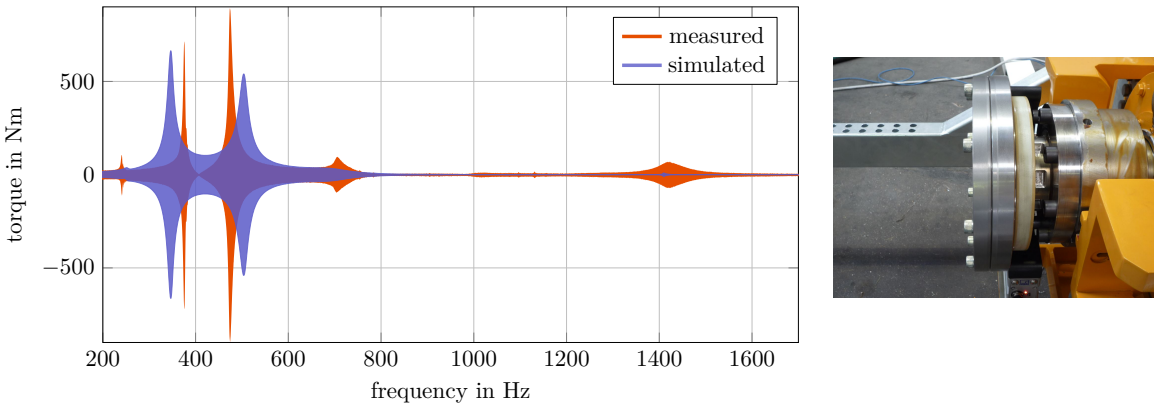

(b) Flange 2, additional inertia: I_{f2}=0.13kgm^2, thus $I_{5,2} = I_{5,1} + I_{f2}$ = 0.27kgm^2.

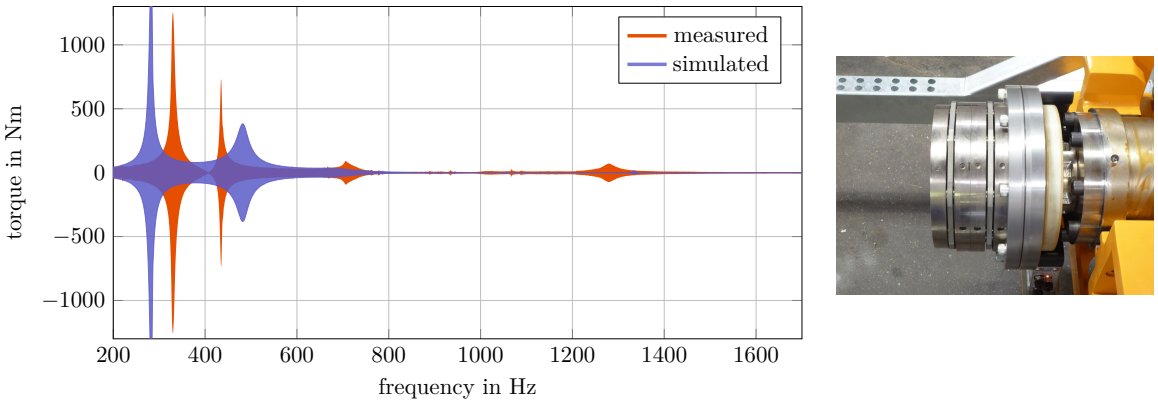

(c) Disc-pack coupling, additional inertia: I_{dp}=0.24kgm^2, thus $I_{5,3} = I_{5,2} + I_{dp}$ = 0.51kgm^2.

Figure 2.18: Chirp experiments on the heavy-duty test bed for identification and validation purposes, in comparison with simulation results obtained with a straight five-mass oscillator.

The presented results demand further discussion, in several aspects. Undeniably, the model fails to capture the dynamics of the drive line, which shows that parametrizing the five-mass oscillator shown in Fig. 2.17 clearly is *not* the final step towards solving the considered modelling problem.

A first difficulty arises for the first setup shown in Fig. 2.11(a) where finding a setting for the damping coefficients that allows to reproduce the highest resonance $\nu_{r,4}$ at $2\pi 1560\,\frac{\mathrm{rad}}{s}$ turns out to be practically not feasible. This resonance is comprised in the proposed model, but either the damping parameters are chosen such that $\nu_{r,4}$ can be seen clearly, which leads to resonance peaks for $\nu_{r,1}$ and $\nu_{r,2}$ that are much too high, or they are selected in the way it is done here, where the peaks belonging to $\nu_{r,1}$ and $\nu_{r,2}$ are represented properly, but that of $\nu_{r,4}$ vanishes almost entirely. Moreover, the real system possesses a significant transfer zero between the first two resonances, which is not represented by the proposed model at all. Especially the next chapter will show that this particular zero is of paramount importance for the derivation of a better model. Lastly, and this is probably the most striking flaw of the straight five-mass oscillator, the model fails dramatically when it comes to predicting the evolution of the system's dynamic properties in case of a hardware modification. Here, the inertia that is added to the end of the drive line is added to I_5 in the model, with a devastating outcome. The frequency-wise location of the resonances is predicted entirely falsely, and also the hull curves in general do not have much in common with the actual measurements.

Literature that is directly applicable to this problem is scarce: books on modelling flexible shafts (usually as part of drive trains), such as [36], use the approach described above, i.e. the chain-of-inertias model, and none of the several other publications that consider the modelling of shaft oscillations, like [50–52], encounter or consider the phenomena described above. All in all, one can conclude that the simple model of Fig. 2.17 is not suitable for describing the dynamical behaviour of the setup, and that a further investigation is needed.

2.2.9 Transfer zero

The results presented previously expose several severe drawbacks of the "naive" chain of inertias. Hence, the question of finding a suitable model structure is revisited. The starting point is the transfer zero located between the first two resonances, which is not contained in any of the simulations, and thus motivates a more thorough investigation in this direction. The first question that is dealt with at this point is whether a "naive" chain-of-inertia-model is capable of creating transfer zeros *at all*. To that end, $G(s)$ is again introduced to denote the transfer function of a given multi-body system from $T_{\text{airgap}}(s)$ to $T_{\text{shaft}}(s)$, and the following line of arguments is set up to structure the discussion:

1. A zero s_z of $G(s)$ blocks the transfer of an input signal with the complex frequency s_z, i.e., signals of the type $T_{\text{airgap}}(t) = e^{s_z t}$ [53].
2. The discussed systems' parameters are exclusively real-valued, thus they can solely form out real or complex-conjugate zeros [54].
3. In order to block a sinusoidal input $T_{\text{airgap}}(t) = A\cos(\nu_u t) = \frac{A}{2}\left(e^{j\nu_u t} + e^{-j\nu_u t}\right)$, $G(s)$ therefore must possess a complex-conjugate pair of zeros with imaginary parts $\pm j\nu_u$.
4. For linear systems, it is known that in case they are differentially flat, the transfer function from input to flat output does not possess *any* zeros [55, 56].

Reversing the last statement, one could argue that if it was possible to show that the "naive" chain-of-inertia-models were flat, and that the outputs considered so far were in fact the flat outputs, that these models would *in principle* not be able to create any transfer zeros. Picking up on this assessment, it is at first examined whether the considered systems are flat. As flatness in the linear case is equivalent to controllability [55, 57], this can be achieved by checking whether the models are controllable. For that purpose, a four-mass oscillator is considered first; on the one hand, because a chain of four inertias is complex enough to contain all the dynamical features that are decisive for the discussion, and on the other because it is still simple enough to keep the arguments compact and clear. Since the transfer characteristics from airgap torque to shaft torque does not change if the state variables are changed, it is sufficient to analyse just one of the models proposed in Section 2.2.1. Taking, for instance, the model comprising differential speeds and differential angles according to (2.9), one obtains

$$\frac{\mathrm{d}}{\mathrm{d}t}\boldsymbol{x}_d = \boldsymbol{A}_d\boldsymbol{x}_d + \boldsymbol{b}_d T_{\text{airgap}}, \qquad T_{\text{shaft}} = \boldsymbol{c}_d^T\boldsymbol{x}_d, \tag{2.73}$$

with

$$\begin{aligned} \boldsymbol{x}_d^T &= \begin{bmatrix} \Delta\varphi_1 & \Delta\omega_1 & \Delta\varphi_2 & \Delta\omega_2 & \Delta\varphi_3 & \Delta\omega_3 \end{bmatrix}, \\ \boldsymbol{b}_d^T &= \begin{bmatrix} 0 & \frac{1}{I_1} & 0 & 0 & 0 & 0 \end{bmatrix}, \\ \boldsymbol{c}_d^T &= \begin{bmatrix} 0 & 0 & 0 & 0 & k_3 & c_3 \end{bmatrix}, \end{aligned} \tag{2.74}$$

and

$$\boldsymbol{A}_d = \begin{pmatrix} 0 & 1 & 0 & 0 & 0 & 0 \\ -k_1(\frac{1}{I_1}+\frac{1}{I_2}) & -c_1(\frac{1}{I_1}+\frac{1}{I_2}) & k_2\frac{1}{I_2} & c_2\frac{1}{I_2} & 0 & 0 \\ 0 & 0 & 0 & 1 & 0 & 0 \\ k_1\frac{1}{I_2} & c_1\frac{1}{I_2} & -k_2(\frac{1}{I_2}+\frac{1}{I_3}) & -c_2(\frac{1}{I_2}+\frac{1}{I_3}) & k_3\frac{1}{I_3} & c_3\frac{1}{I_3} \\ 0 & 0 & 0 & 0 & 0 & 1 \\ 0 & 0 & k_2\frac{1}{I_3} & c_2\frac{1}{I_3} & -k_3(\frac{1}{I_3}+\frac{1}{I_4}) & -c_3(\frac{1}{I_3}+\frac{1}{I_4}) \end{pmatrix} \tag{2.75}$$

as a mathematical description. To simplify the analysis, the model's damping is again neglected at first, which reduces the dynamic matrix to

$$\tilde{\boldsymbol{A}}_d = \begin{pmatrix} 0 & 1 & 0 & 0 & 0 & 0 \\ a_1 & 0 & a_2 & 0 & 0 & 0 \\ 0 & 0 & 0 & 1 & 0 & 0 \\ a_3 & 0 & a_4 & 0 & a_5 & 0 \\ 0 & 0 & 0 & 0 & 0 & 1 \\ 0 & 0 & a_6 & 0 & a_7 & 0 \end{pmatrix}. \tag{2.76}$$

Therein, the abbreviations a_i represent the terms related to the model's stiffnesses, in order to allow for a clearer view on the system's structural properties. To see whether (2.73) without damping is controllable, one can compute Kalman's controllability matrix

$$\boldsymbol{S}_u = \begin{pmatrix} \boldsymbol{b} & \tilde{\boldsymbol{A}}_d\boldsymbol{b} & \tilde{\boldsymbol{A}}_d^2\boldsymbol{b} & \tilde{\boldsymbol{A}}_d^3\boldsymbol{b} & \tilde{\boldsymbol{A}}_d^4\boldsymbol{b} & \tilde{\boldsymbol{A}}_d^5\boldsymbol{b} \end{pmatrix}, \tag{2.77}$$

which in the present case results in

$$\boldsymbol{S}_u = \frac{1}{I_1}\begin{pmatrix} 0 & 1 & 0 & a_1 & 0 & a_1^2 + a_2a_3 \\ 1 & 0 & a_1 & 0 & a_1^2 + a_2a_3 & 0 \\ 0 & 0 & 0 & a_3 & 0 & a_1a_3 + a_3a_4 \\ 0 & 0 & a_3 & 0 & a_1a_3 + a_3a_4 & 0 \\ 0 & 0 & 0 & 0 & 0 & a_3a_6 \\ 0 & 0 & 0 & 0 & a_3a_6 & 0 \end{pmatrix}. \tag{2.78}$$

Since the non-zero elements of $\boldsymbol{S}_u$ are structured such that no row or column can be expressed as a linear-combination of the others, the matrix is regular, showing that system (2.73) without damping is controllable and therefore flat. To analyse whether T_{shaft} corresponds to the system's flat output, one may proceed as suggested in [55], where it is shown that the output vector $\boldsymbol{c}_d^T$ of a flat output must fulfil

$$\boldsymbol{c}_d^T\boldsymbol{S}_u \stackrel{!}{=} \begin{bmatrix} 0 & 0 & 0 & 0 & 0 & \kappa \neq 0 \end{bmatrix} \tag{2.79}$$

with $\kappa \in \mathbb{R}$, which corresponds to the output having a relative degree equal to the system order. For the present case, this leads to

$$\begin{aligned} \boldsymbol{c}_d^T \boldsymbol{S}_u &= \\ &= \begin{bmatrix} 0 & 0 & 0 & 0 & k_3 & 0 \end{bmatrix} \frac{1}{I_1} \begin{pmatrix} 0 & 1 & 0 & a_1 & 0 & a_1^2 + a_2 a_3 \\ 1 & 0 & a_1 & 0 & a_1^2 + a_2 a_3 & 0 \\ 0 & 0 & 0 & a_3 & 0 & a_1 a_3 + a_3 a_4 \\ 0 & 0 & a_3 & 0 & a_1 a_3 + a_3 a_4 & 0 \\ 0 & 0 & 0 & 0 & 0 & a_3 a_6 \\ 0 & 0 & 0 & 0 & a_3 a_6 & 0 \end{pmatrix} \\ &= \begin{bmatrix} 0 & 0 & 0 & 0 & 0 & \frac{k_3}{I_1} a_3 a_6 \end{bmatrix} \quad = \quad \begin{bmatrix} 0 & 0 & 0 & 0 & 0 & \frac{k_1 k_2 k_3}{I_1 I_2 I_3} \end{bmatrix}, \end{aligned} \tag{2.80}$$

which obviously fulfils (2.79). One may thus conclude that an undamped chain of inertias, where the airgap torque acts on the first inertia, and where the torque transmitted between the last and the second-last inertia is interpreted as the measured shaft torque, is a differentially flat system, whose output is flat, too. Such a structure is *not* capable of creating any zeros at all.

Graphical investigation

This insight can be derived in other ways, too. One alternative approach is presented in the following, employing a graphical investigation of the considered four-mass oscillator. The again undamped version of the latter is depicted in Fig. 2.19.

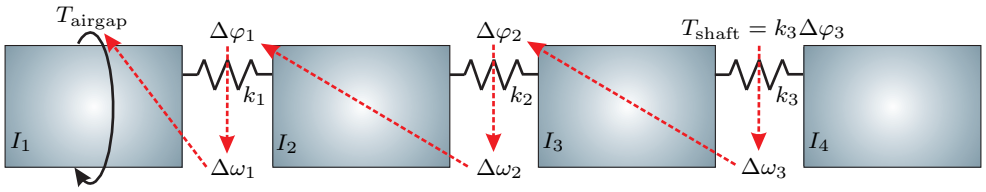

Figure 2.19: Four-mass oscillator: differential path from output to input.

Therein, the red arrows symbolize the derivations that need to be performed to get from T_{shaft} to T_{airgap}. Starting with T_{shaft}, the first step is trivial:

$$\frac{d}{dt} T_{\text{shaft}} = k_3 \frac{d}{dt} \Delta\varphi_3 = k_3 \Delta\omega_3. \tag{2.81}$$

The next step is more involved, and results in

$$\frac{d}{dt}(k_3 \Delta\omega_3) = k_3 \left(-(\frac{1}{I_3} + \frac{1}{I_4}) k_3 \Delta\varphi_3 + \frac{1}{I_3} k_2 \Delta\varphi_2 \right). \tag{2.82}$$

Therein, the term comprising $\Delta\varphi_3$ topologically coincides with the starting point of the procedure. Hence, the next step towards the model's input is to derive the expression $k_2 k_3 \frac{1}{I_3}\Delta\varphi_2$, which is again trivial and results in $k_2 k_3 \frac{1}{I_3}\Delta\omega_2$. Repeating these steps, one finds that it takes *six* iterations to arrive at an expression that contains T_{airgap}. Thus, the relative degree of T_{shaft} for the given model is six, which equals the model's order, and thus implies that this particular output is in fact the differentially flat one! For a linear SISO-system like the one present, this also means that the excess of poles is equivalent to the model order. Therefore, the numerator of the model's transfer function can only be a polynomial of order *zero*, which intuitively explains that such a system cannot contain any transfer zeros.

Graphical investigation with damping

The proposed graphical analysis is particularly helpful when one aims to include the priorly neglected damping. To that end, Fig. 2.20 again depicts the considered four-mass oscillator and the differential path from output to input, now with a damper element that is assumed non-zero. Obviously, each damper that is included decreases the number of derivations that are needed to get from T_{shaft} to T_{airgap} by one.

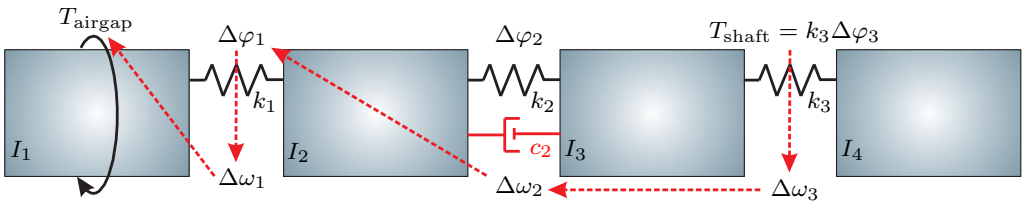

Figure 2.20: Four-mass oscillator with damping: differential path from output to input.

This modification decreases the pole excess, raises the degree of the numerator polynomial of the transfer function, and eventually introduces a zero into the system's transfer characteristics. To learn more about the actual value of this zero due to damping, the four-mass oscillator is represented once more in Fig. 2.21, this time by the means of the transfer functions of its components:

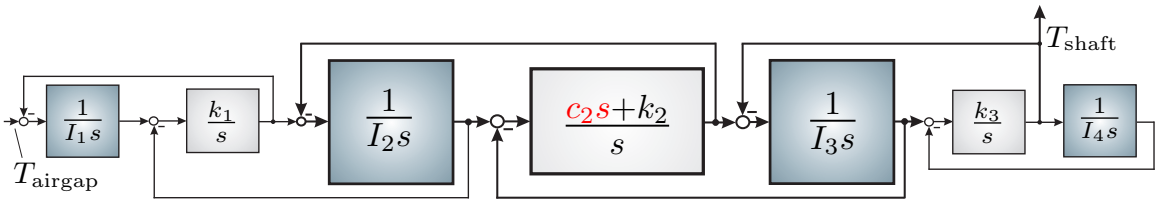

Figure 2.21: Four-mass oscillator in terms of transfer functions.

One can see that for $c_2 \neq 0$, the induced zero results as $s = -\frac{k_2}{c_2}$, as for this value the connection between T_{shaft} and T_{airgap} breaks apart at the second shaft between I_2 and I_3. The

insight that a zero due to damping must be real-valued can also be explained mathematically: As mentioned in the beginning of this section, all model parameters are real-valued, hence the zeros and poles of the transfer function can only be real-valued, too, or complex-conjugate pairs. Since one additional zero alone cannot create a whole complex-conjugate pair, it must real. To get back to the question of oscillation-blocking, this means that zeros due to damping do not solve the task of blocking a periodic input signal.

Structural modification

The preceding considerations suggest that a structural modification of the chain-of-inertia models is needed, in order to realize a complex-conjugate pair of transfer zeros that is capable of blocking an oscillation. One approach to do so is to change the location of the

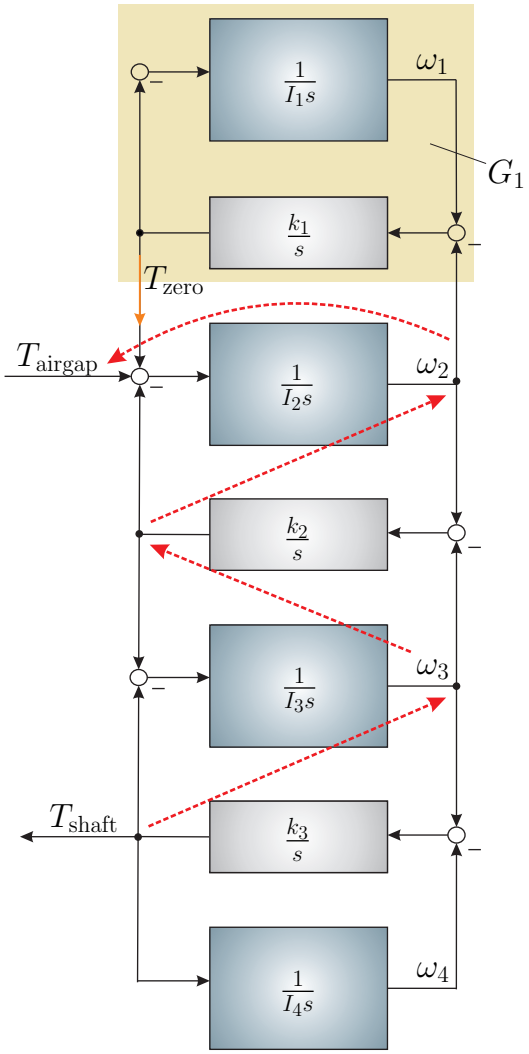

Figure 2.22: Four-mass oscillator: modified input with counter-oscillating subsystem.

input, i.e., to alter the inertia that is affected by T_{airgap}. Figure 2.22 depicts the outcome of one such modification for the undamped four-mass oscillator. Changing the point of entry as in Fig. 2.22 reduces the number of steps in the differential path from T_{shaft} to T_{airgap} by two, which induces *two* zeros into the system's transfer function. To learn more about the properties of these zeros, the transfer function from T_{shaft} to T_{airgap} for the undamped case is analysed, in a very general form at first, without any assumptions regarding the zeros:

$$G(s) := \frac{T_{\text{shaft}}(s)}{T_{\text{airgap}}(s)} = V\frac{(s-\beta_1)(s-\beta_2)}{\prod_{k=1}^{6}(s-\alpha_i)}. \tag{2.83}$$

Therein, the poles are denoted by α_i, $\beta_{1,2}$ stands for the two new zeros that are again either real or complex-conjugate, and V designates the scaling factor that results from factoring the numerator and denominator polynomials. For the moment, it shall be assumed that the acting airgap torque comprises both modes belonging to $\beta_{1,2}$, and may thus be expressed as

$$T_{\text{airgap}}(t) = T_1 e^{\beta_1 t} + T_2 e^{\beta_2 t}. \tag{2.84}$$

In any case, the weights $T_{1,2}$ have to be chosen such that imaginary values are prevented. Transforming $T_{\text{airgap}}(t)$ into the Laplace-domain, one sees that $T_{\text{shaft}}(s)$ evolves as

$$\begin{aligned} T_{\text{shaft}}(s) = G(s)T_{\text{airgap}}(s) &= V\frac{(s-\beta_1)(s-\beta_2)}{\prod_{k=1}^{6}(s-\alpha_i)}\left(\frac{T_1}{s-\beta_1}+\frac{T_2}{s-\beta_2}\right) \\ &= V\frac{T_1(s-\beta_2)+T_2(s-\beta_1)}{\prod_{k=1}^{6}(s-\alpha_i)}, \end{aligned} \tag{2.85}$$

where β_1 and β_2 are not among the poles. Thus, the exponentials $e^{\beta_1 t}$ and $e^{\beta_2 t}$ are not part of the output in *steady-state*, i.e. for $t \to \infty$, which has manifold consequences for the other signals in the system:

- If $e^{\beta_1 t}$ and $e^{\beta_2 t}$ are not contained in T_{shaft}, they cannot be contained in ω_4 either, as the latter is just an integral over T_{shaft}.
- If the exponentials are not contained in ω_4, they also can't be part of ω_3; in this case they would act on the third shaft and consequently be represented in T_{shaft}, which would contradict the former statement.
- Extending this line of arguments, one quickly reaches the conclusion that also ω_2 must be free from $e^{\beta_1 t}$ and $e^{\beta_2 t}$ in steady-state.

The last of the points above is a delicate finding: Regarding the system's motion related to the exponentials, this means that I_2 must come to rest as $t \to \infty$, no matter how large the corresponding modal components of T_{airgap} are! To make this possible, the torque T_{zero}, which is produced by the first shaft with stiffness k_1, must compensate $T_1 e^{\beta_1 t}$ and $T_2 e^{\beta_2 t}$. As argued above, however, the corresponding components of ω_2 go to zero during the

transition to steady-state, which leaves only one option for the compensation to work: The amplification of $e^{\beta_1 t}$ and $e^{\beta_2 t}$ through the boxed subsystem G_1 must grow, until it reaches infinity in steady-state. This, however, is only possible if β_1 and β_2 coincide with the *poles* of $G_1(s) := {}^{T_{\text{zero}}(s)}/_{\omega_2(s)}$! Since $G_1(s)$ is in the present case given by

$$G_1(s) = \frac{-k_1 s}{s^2 + \frac{k}{I_1}}, \tag{2.86}$$

the zeros induced by shifting the input from I_1 to I_2 result as

$$\beta_{1,2} = \pm j\sqrt{\frac{k_1}{I_1}} = \pm j\nu_z. \tag{2.87}$$

The absolute values of $\beta_{1,2}$ can also be regarded as the resonance frequency[8] of a two-mass oscillator comprising I_1, k_1 and I_2, where the latter in steady-state is at rest and thus acts as an infinitely large inertia. It is for this reason that these zeros are often referred to as *anti-resonances* [41]. One may resume that the existence of a sub-structure, which is capable of resonating against at least one inertia in the path from input to output, is an imperative prerequisite for blocking a sinusoidal input signal. This result itself is not new, and can also be found in [41, 58]; accompanied by different explanations, however. Moreover, to the best of the author's knowledge, a connection of these considerations with test bed drive lines comprising an induction machine is not yet found in literature. Furthermore, the insight is of great practical use, as including a zero into the parametrization process allows to create another equation for one more unknown.

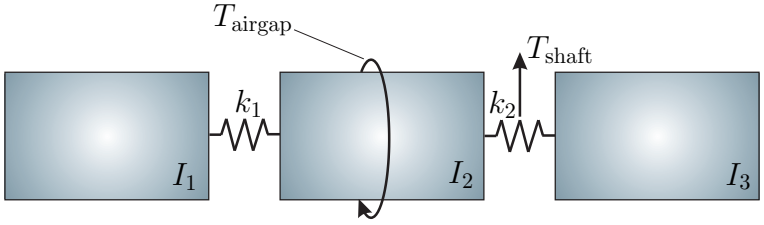

Figure 2.23: Undamped three-mass oscillator with shifted input.

Zero-equation

For the class of three-mass oscillators, shifting the input results in the structure shown in Figure 2.23, and allows to analyse an important case: Frequently, the sum $I_m = I_1 + I_2$ and the third inertia I_3 are given, while the stiffnesses $k_{1,2}$ and the distribution of inertia between I_1 and I_2 are sought; for instance, when the dynamometer is modelled by I_1 and I_2, and I_3 represents the device-under-test, whose inertia is specified in a data sheet. If the frequency

[8] In the undamped case, eigenmode-frequency and practical resonance are identical, cf. Section 2.2.2.

of the transfer zero ν_z and the resonances $\nu_{r1,2}$ are known, e.g., from a chirp experiment, one may proceed as discussed in Section 2.2.6, where the two possible analytical solutions for the conventional three-mass oscillator are developed. Again, the resonance frequencies may be used to construct a desired characteristic polynomial, i.e.

$$\det\left(s^2\boldsymbol{I}_{2\times2} - \boldsymbol{K}_\Delta\right) \stackrel{!}{=} (s^2 + \nu_{r,1}^2)(s^2 + \nu_{r,2}^2) = s^4 + (\nu_{r,1}^2 + \nu_{r,2}^2)s^2 + \nu_{r,1}^2\nu_{r,2}^2, \tag{2.88}$$

which allows to derive a set of equations from comparing the coefficients of s^2 and s^0. This time, the additional relations

$$I_1 \stackrel{!}{=} \frac{k_1}{\nu_z^2} \qquad \text{and} \qquad I_1 + I_2 \stackrel{!}{=} I_m \tag{2.89}$$

must be incorporated, which modifies the evolving system of equations to

$$\begin{aligned} \text{I}: \quad \nu_{r,1}^2 + \nu_{r,2}^2 &\stackrel{!}{=} k_1\left(\frac{1}{\frac{k_1}{\nu_z^2}} + \frac{1}{I_m - \frac{k_1}{\nu_z^2}}\right) + k_2\left(\frac{1}{I_m - \frac{k_1}{\nu_z^2}} + \frac{1}{I_3}\right) \\ \text{II}: \quad \nu_{r,1}^2\nu_{r,2}^2 &\stackrel{!}{=} k_1k_2\left(\frac{1}{\frac{k_1}{\nu_z^2}}\frac{1}{I_m - \frac{k_1}{\nu_z^2}} + \frac{1}{\frac{k_1}{\nu_z^2}}\frac{1}{I_3} + \frac{1}{I_m - \frac{k_1}{\nu_z^2}}\frac{1}{I_3}\right). \end{aligned} \tag{2.90}$$

Again, as (2.63), also (2.90) is capable of producing more than *one* solution. An important extension of the concept is to separate the acting airgap torque, and to connect it to both I_1 and I_2. This step results in the system presented in Fig. 2.24, and may, e.g., be motivated as a subdivision of the rotor of an electrical machine, where the whole body is touched by the produced airgap torque.

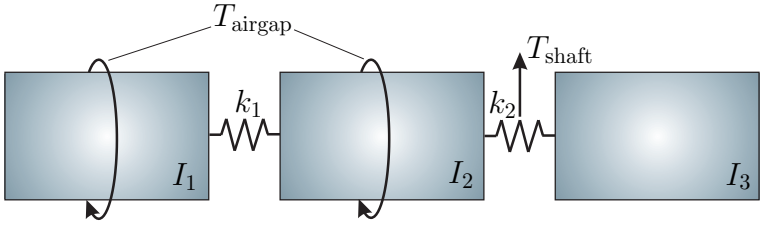

Figure 2.24: Three-mass oscillator with shifted input.

If T_{airgap} is distributed in proportion to I_1 and I_2, i.e.

$$T_{\text{airgap1}} = \underbrace{\frac{I_1}{I_1 + I_2}}_{=:\kappa_1} T_{\text{airgap}} \qquad \text{and} \qquad T_{\text{airgap2}} = \underbrace{\frac{I_2}{I_1 + I_2}}_{=:\kappa_2} T_{\text{airgap}}, \tag{2.91}$$

which is the physically most reasonable distribution, the induced zero results as the resonance frequency of the two-mass-oscillator that is affected by the input, i.e.

$$\nu_z = \sqrt{k_1(\frac{1}{I_1} + \frac{1}{I_2})}. \tag{2.92}$$

It must be noted, though, that ν_z can be positioned arbitrarily between 0 and ∞, simply by changing the weights κ_1 and κ_2. The result in this general case may be expressed as

$$\nu_z = \sqrt{\frac{k_1}{I_1}\left(\frac{\kappa_1}{\kappa_2} + 1\right)}, \tag{2.93}$$

where the question of whether a certain combination of values for κ_1 and κ_2 is physically meaningful has to be treated with some care. Of course, also (2.91) and (2.93) may be employed for parametrization purposes, which can be particularly useful when a simple simulation model is needed quickly. However, as the focus of this work is on reaching a high level of accuracy, no simulation results achieved with the models shown in Figs. 2.23 and 2.24 are discussed at this point.

2.2.10 Alternative structures

The understanding that certain structural modifications have the potential to significantly improve the considered models' quality led to an entirely different way of thinking, and to several exotic, almost to say bizarre, topologies that have been investigated in the course of this work. One of the first of these "alternative" structures is shown in Fig. 2.25. Here, and also in the other topology presented later on, the sizes of the blocks aim to insinuate the amount of represented inertia. As laid out by the results shown in Fig. 2.18, the "naive" five-mass oscillator, among other shortcomings, does not allow to sufficiently excite the highest resonance at 1560Hz in Fig. 2.18(a), which partly has to do with the huge inertia that needs to be overcome on the way from airgap to measuring shaft. Thus, a first idea was to shorten this path, by connecting the airgap torque also to inertias that are closer to the measuring flange. This measure can be interpreted as a splitting of the induction machine rotor into sub-inertias that are affected by T_{airgap}.

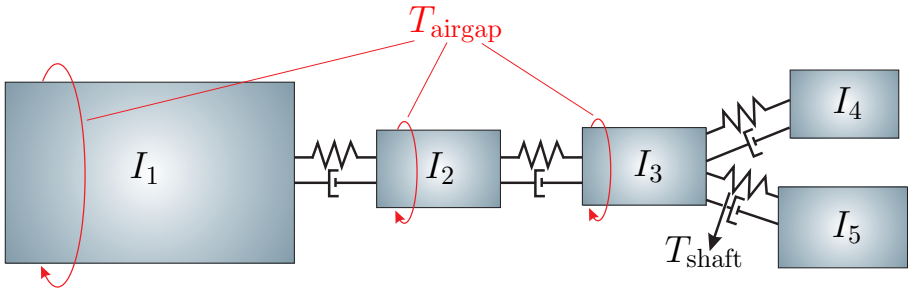

Figure 2.25: Alternative structures, one parallel inertia.

Additionally, the last inertia of the drive line is split into two inertias, which is in part inspired by the structure of the measuring flange shown next to Tab. 2.2: The outer ring with holes and the inner body of the measuring flange are interpreted as I_4 and I_5, respectively. A convenient side effect of this measure is that I_4 creates a counter-oscillating substructure that introduces another transfer zero. As with the straight, conventional chains of inertias discussed earlier, I_5 is interpreted as the last member of the drive line that whose inertia is raised by the inertia of the added flanges. Consequently, the measured shaft torque is compared to the torque that is transmitted through the shaft connected to I_5.

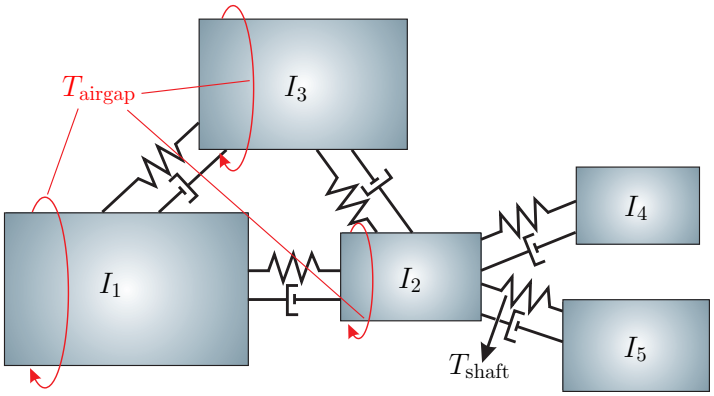

Figure 2.26: Alternative structures, two parallel inertias.

Unfortunately, the structure laid out in Fig. 2.25 did not lead to satisfactory results. Most importantly, also this model suffered from a lack of accuracy with regards to adapting to changes of the real drive line. Therefore, the remainder of this section focuses on another result of these rather creative attempts, which is shown in Fig. 2.26. One idea behind the topology shown in Fig. 2.26 was to further shorten the main path between T_{airgap} and T_{shaft}, that now comprises the inertias I_1, I_2 and I_5 only. Additionally, much effort was put in subdividing the big induction machine rotor. Particularly for the considered heavy-duty test bed, it began to appear more and more likely that certain parts of the massive rotor would form out some kind of individual dynamical behaviour, and eventually cause the transfer zero *and* the great number of resonance frequencies that are visible in the chirp experiments. In that sense, one may interpret the inertias I_1, I_2 and I_3 as a new take on the massive inertia that is introduced by the induction machine. As indicated in Fig. 2.26, the airgap torque acts on I_1, I_2 and I_3, and was scaled in proportion to their values. Structure 2.26 was used extensively in the course of this work. The parameters of the structure were again determined by the means of two combined optimization problems. The only difference to the straight chain of inertias was that the first of the two problems, whose purpose is to find the values for stiffnesses and inertias, was extended by the desired transfer zero. The latter was described as the resonance of the inertias that are touched by T_{airgap}, as explained for the three-mass oscillator in Sec. 2.2.9, and led to the results listed in Appendix A.2. Of the many simulations that were performed with this setup, again the three experiments that were already used to validate the straight chain of inertias are presented in Figs. 2.27.

2.2.11 Results: Alternative structures

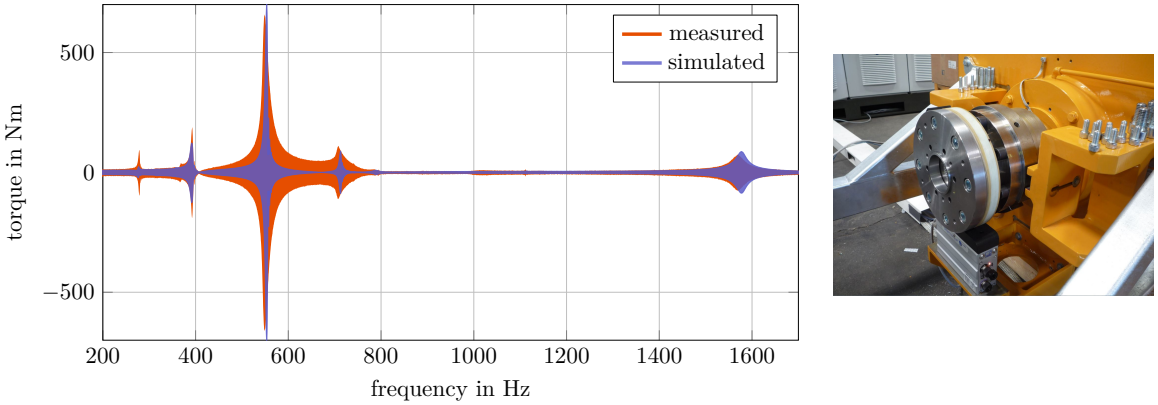

(a) Flange 1, additional inertia: I_{f1}=0.13kgm^2, which is included in $I_{5,1} = 0.20kgm^2$, a result from optimization.

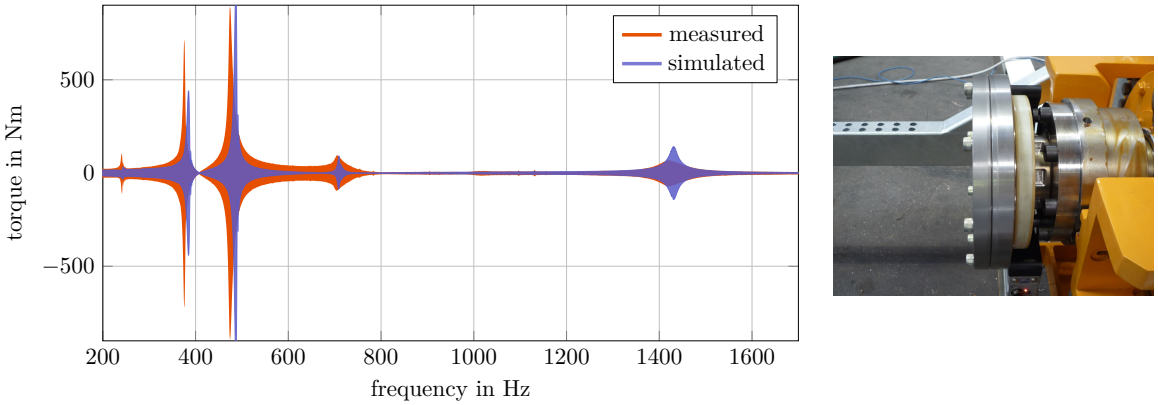

(b) Flange 2, additional inertia: I_{f2}=0.13kgm^2, thus $I_{5,2} = I_{5,1} + I_{f2}$ = 0.33kgm^2.

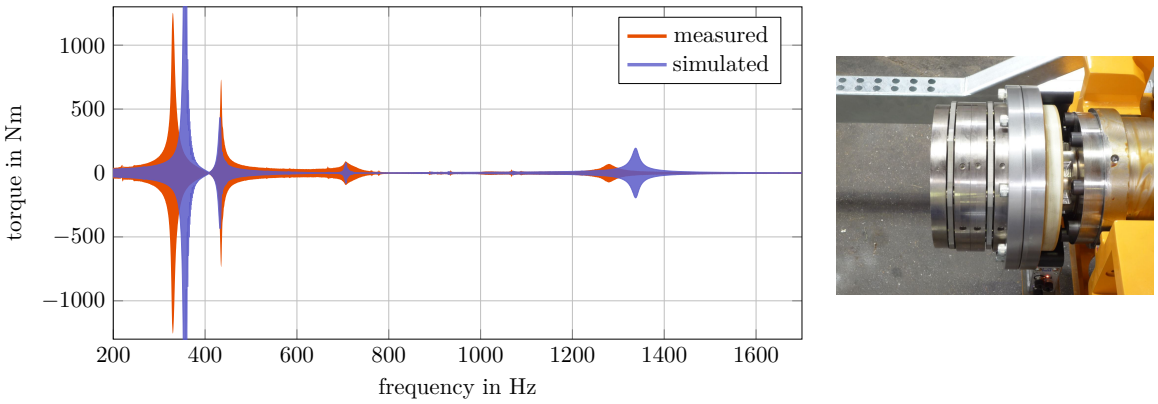

(c) Disc-pack coupling, additional inertia: I_{dp}=0.24kgm^2, thus $I_{5,3} = I_{5,2} + I_{dp}$ = 0.57kgm^2.

Figure 2.27: Chirp experiments on the heavy-duty test bed compared to simulation results obtained with the alternative structure comprising three parallel inertias.

The results are surprisingly positive. In contrast to the formerly discussed “naive” chain-of-inertia models, one may resume that the model complies with almost every requirement that was formulated so far: The resonances are met accurately, their evolution is reflected precisely, especially between the first and the second setup, the height of the resonance peaks coincides with the measurements, and also the transfer zero is clearly comprised in the model. The only noticeable deviation is found in the last experiment shown in Fig. 2.27(c); but compared to the attempt with the naive chain of inertias, also this result must be regarded as a significant improvement.

However, in spite of its convincing performance, the unorthodox “alternative” model is not entirely satisfying. Although it is well imaginable that parts of the huge machine rotor move relatively to each other, the proposed structure remains somewhat dubious. It is, for instance, not possible to deduce the proposed topology from the design drawings of the machine. Moreover, the adaptation of the concept to another dynamometer is not transparent, which limits the structure to the considered case. Lastly, there is no obvious physical interpretation of the circle of inertias that constitutes the inner life of the rotor. In essence, the proposed structure is an empirical finding, with all the drawbacks that come with this class of models. Additionally, a detailed analysis of the constructive properties of the measuring flange, which was conducted after the first successful simulation studies were performed, showed that the seemingly two parts of it are connected so stiffly that the theory of two secondary measuring flange inertias could not be motivated physically.

Nevertheless, one substantial, general finding may be condensed from the previous considerations, i.e., that the induction machine rotor needs to be split into several smaller inertias, in order to find a satisfying simulation model.

The next steps are based on this idea. In the following chapter, it is investigated how big inertias like that of the considered induction machine can be subdivided in a physically interpretable way, such that the demanded dynamical requirements are met.

2.3 Soft rotor

The preceding sections made clear that the "naive" chain of lumped inertias needs to be modified structurally, in order to obtain a satisfying simulation model for the considered drive line. More precisely, it turned out that it is imperative to change the representation of the involved induction machine rotor, allowing this large member of the drive line to form out a dynamical behaviour within itself. With regards to current literature, only few contributions deal with this problem, see [59], for instance, and most of the publications use a comparably small number of again lumped inertias, which leads to drawbacks similar to the ones discussed earlier on. Most prominently, the question of physical interpretability remains unsolved: In the case of a small and finite number of discrete inertias, the search for concrete physical counterparts usually requires much effort, and is most frequently not rewarded with success. Therefore, the modelling problem is approached entirely differently in this section: The massive rotor of the dynamometer is regarded as a system of infinitely many, infinitely small inertias, which shifts the analysis into the area of *distributed-parameter systems.*

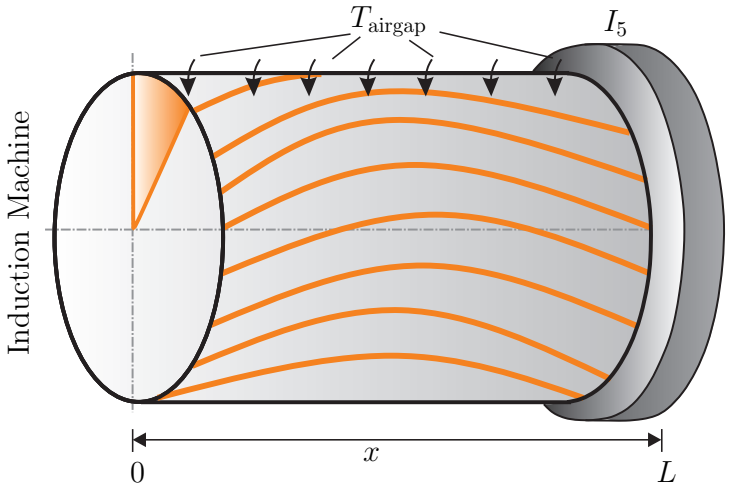

Figure 2.28: Soft rotor.

2.3.1 Analytical analysis

To analyse the effect of this methodological transition, the following section develops an analytical description of the resonance frequencies for the structure shown in Fig. 2.28, which represents just one topology that may be derived with the new modelling approach. Therein, the inertia of the induction machine is distributed continuously in axial direction, and a lumped inertia I_5 is pinned to the very right end of the body. As the setup is symmetric to rotation, only the axial dimension of the problem is considered further, with the spatial variable x denoting the position between left ("0") and right end ("L"). The airgap torque

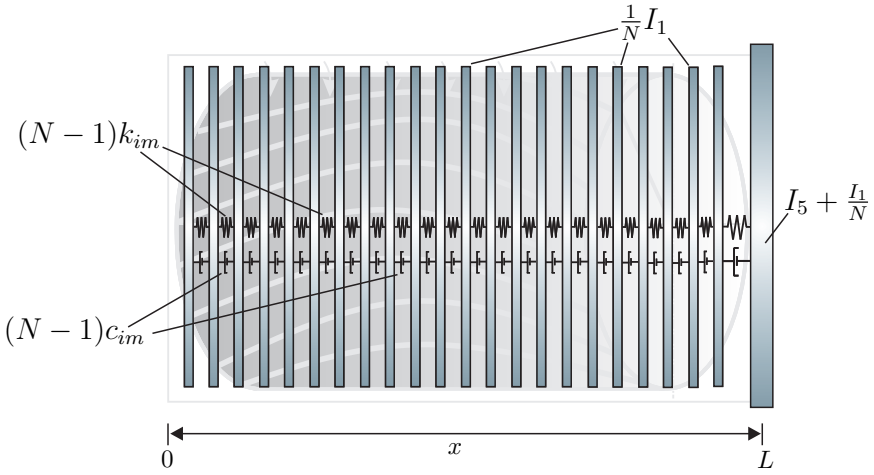

Figure 2.29: Soft rotor, division into N lumped inertias.

produced by the electrical machine is assumed to be equally distributed from $x = 0$ to $x = L$. To derive a mathematical description of the system, the rotor is at first divided into a finite number of N sub-inertias, as shown in Fig. 2.29. Therein, I_1 denotes the whole induction machine inertia, and k_{im} and c_{im} stand for the total stiffness and the total damping of the rotor, respectively, which map the total twisting angle and the total angular differential speed between front- and backside onto the torque that acts inside the body. Introducing N partial inertias leads to $(N-1)$ partial connection shafts, whose parameters are given by k_{im} and c_{im} scaled by (N-1) [27]. The absolute angular position of the ith discrete inertia is described by φ_i, for which Newton's second law of motion may be applied. Neglecting the system's damping for the beginning, this step results in

$$\frac{\partial^2 \varphi_i}{\partial t^2} = \frac{N}{I_1}\Big(k_{im}(N-1)\Big(\varphi_{i-1} - \varphi_i\Big) - k_{im}(N-1)\Big(\varphi_i - \varphi_{i+1}\Big)\Big), \tag{2.94}$$

which can be rearranged to

$$\frac{\partial^2 \varphi_i}{\partial t^2} = N(N-1)\frac{k_{im}}{I_1}\Big(\Big(\varphi_{i-1} - \varphi_i\Big) - \Big(\varphi_i - \varphi_{i+1}\Big)\Big). \tag{2.95}$$

To get back to the distributed rotor, the transition of $N \longrightarrow \infty$ is performed, which is accompanied by two important consequences: On the one hand, $N \approx N - 1$ for $N \longrightarrow \infty$, and on the other, $\Delta x = \frac{L}{N} \longrightarrow 0$. These relations may be used to modify (2.95) to

$$\frac{\partial^2 \varphi_i}{\partial t^2} = \left(\frac{L}{\Delta x}\right)^2 \frac{k_{im}}{I_1}\Big(\Big(\varphi_{i-1} - \varphi_i\Big) - \Big(\varphi_i - \varphi_{i+1}\Big)\Big) = L^2 \frac{k_{im}}{I_1} \frac{\frac{\varphi_{i-1}-\varphi_i}{\Delta x} - \frac{\varphi_i - \varphi_{i+1}}{\Delta x}}{\Delta x}, \tag{2.96}$$

which, as $\Delta x \longrightarrow 0$, yields the well-known wave equation

$$\frac{\partial^2 \varphi(x,t)}{\partial t^2} = L^2 \frac{k_{im}}{I_1} \frac{\partial^2 \varphi(x,t)}{\partial x^2}. \tag{2.97}$$

A common method to solve (2.97) is to use an ansatz of the form $\varphi(x,t) = f(t)y(x)$, as suggested in [60]. This separates the two variables and yields

$$\frac{\ddot{f}(t)}{f(t)} = L^2 \frac{k_{im}}{I_1} \frac{y''(x)}{y(x)}, \tag{2.98}$$

where the dots and the apostrophes denote the time- and spatial derivatives, respectively. As the left side of (2.98) does not depend on x, and since the right side does not depend on t, both of them need to be constant. This leads to

$$\frac{\partial^2 f(t)}{\partial t^2} = -\nu^2 f(t) \qquad \text{and} \qquad \frac{\partial^2 y(x)}{\partial x^2} = -q^2 y(x), \tag{2.99}$$

where the constant ν takes on the role of the time frequency, while the spatial frequency is denoted by

$$q = \nu \sqrt{\frac{I_1}{k_{im} L^2}}. \tag{2.100}$$

As explained in [60], the solutions to these differential equations are given by

$$f(t) = f_0 \cos(\nu t + \phi) \qquad \text{and} \qquad y(x) = A \sin(qx) + B \cos(qx), \tag{2.101}$$

where the phase variable ϕ may be set to zero without any loss of generality. Usually, the constant f_0 is found by comparing $\varphi(t)$ to initial conditions. However, as the scope of this work is not on finding specific solutions, but on general structural properties with regards to the models' resonances, only $y(x)$ is considered further.

$x = 0$:

The left end is investigated first. In the given case of a free body, the starting point in the derivation of the differential equation at this end takes on the form

$$\frac{\partial^2 \varphi_1}{\partial t^2} = L^2 \frac{k_{im}}{I_1} \frac{1}{\Delta x^2} (\varphi_1 - \varphi_2). \tag{2.102}$$

For $N \to \infty$, one arrives at

$$\frac{\partial^2 \varphi_1}{\partial t^2} = L^2 \frac{k_{im}}{I_1} \left(\lim_{\Delta x \to 0} \frac{1}{\Delta x} \right) \left(\lim_{\Delta x \to 0} \frac{1}{\Delta x} (\varphi_1 - \varphi_2) \right) = L^2 \frac{k_{im}}{I_1} \left(\lim_{\Delta x \to 0} \frac{1}{\Delta x} \right) \frac{\partial \varphi_1}{\partial x}. \tag{2.103}$$

To make sure that $\frac{\partial^2 \varphi_1}{\partial t^2}$ does not go to infinity as $\Delta x \to 0$, the first derivative of $\varphi(x,t)$ with respect to x must be zero here. Thus,

$$\left. \frac{dy(x)}{dx} \right|_{x=0} = \left. \frac{d}{dx} \big(A \sin(qx) + B \cos(qx) \big) \right|_{x=0} = \left. \big(Aq \cos(qx) - Bq \sin(qx) \big) \right|_{x=0} \stackrel{!}{=} 0, \tag{2.104}$$

which demands $A \stackrel{!}{=} 0$, and hence reduces the spatial component of $\varphi(x,t)$ to

$$y(x) = B \cos(qx). \tag{2.105}$$

$x = L$:

The right hand side of the rotor is more involved, essentially because the additional, pinned inertia I_5 must be taken into account here. Starting again with the spatially descretized version of Newtons's second law, one obtains

$$\frac{\partial^2 \varphi_N}{\partial t^2} = L \frac{k_{im}}{I_5} \frac{1}{\Delta x} (\varphi_{N-1} - \varphi_N). \tag{2.106}$$

Therein, the fact that $I_5 + \frac{I_1}{N} \approx I_5$ is exploited, which does *not* change throughout the continuity transformation, and thus reduces the number of involved differentials Δx to just one. Performing the transition of $\Delta x \to 0$ leads to

$$\left.\frac{\partial^2 \varphi}{\partial t^2}\right|_{x=L} = -L \frac{k_{im}}{I_5} \left.\frac{\partial \varphi}{\partial x}\right|_{x=L} \tag{2.107}$$

in this case. Inserting (2.105) into (2.107), and reducing the analysis again to just the spatial component $y(x)$, modifies the expression to

$$-\nu^2 y(L) = -L \frac{k_{im}}{I_5} y'(L), \tag{2.108}$$

which, with the help of (2.105), (2.108), may be rearranged further to

$$-\nu^2 \cos(qL) = L \frac{k_{im}}{I_5} q \sin(qL). \tag{2.109}$$

Employing $\nu = q\sqrt{\frac{k_{im}L^2}{I_1}}$ allows to eliminate ν and yields

$$-q^2 \frac{k_{im} L^2}{I_1} \cos(qL) = L \frac{k_{im}}{I_5} q \sin(qL), \tag{2.110}$$

which, after canceling $k_{im}L$ on both sides, results in the *spatial* eigenfrequency equation

$$-qL \operatorname{cotan}(qL) = \frac{I_1}{I_5}. \tag{2.111}$$

Equation (2.111) possesses an infinite number of solutions, where each solution describes a spatial eigenfrequency q_r of the system. Each eigenfrequency q_r in turn is connected to a *time* resonance frequency ν_r via relation (2.100). Graphically, the solutions of (2.111) may be interpreted as the intersection points between the constant right side and the trigonometric left side of the equation, which is represented qualitatively in Fig. 2.30. To recap this section and to evaluate the transition to distributed-parameter systems for the modelling of test bed drive lines, the following statements are made at this point:

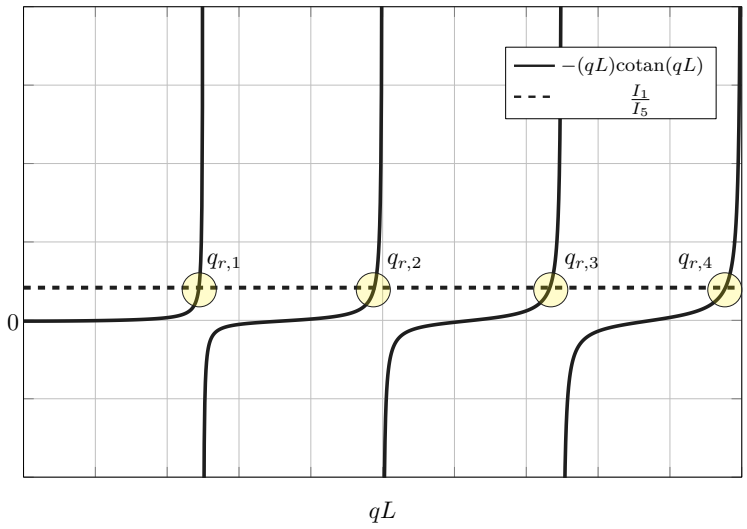

Figure 2.30: Qualitative representation of the transcendental, spatial eigenfrequency equation.

- Already for the simple setup shown in Fig. 2.28, the "soft" rotor introduces an infinite number of resonance frequencies. This ensures that no matter how many resonances a chirp experiment comprises, a soft-rotor model will be capable of reproducing a sufficient number of resonances.
- Although the number of available resonances goes to infinity, the number of parameters that are necessary to describe them is reduced drastically: For the setup presented in Fig. 2.28, only the inertias I_1 and I_5 and the stiffness k_{im} are needed to determine the system's resonances.
- As for the three-mass systems discussed in Section 2.2.9, the transfer zeros of the system are determined by the resonances of the counter-oscillating substructure. A soft-rotor model comprises infinitely many anti-resonances and thus introduces an infinite number of transfer zeros.
- Moreover, with the whole distributed body being affected by the airgap torque, the length of the shortest path between input to output is reduced significantly, which simplifies the task of exciting high resonances like the one at 1560Hz in Fig. 2.18(a).

2.3.2 Simulation study

Also the soft rotor approach was used to simulate the discussed heavy-duty drive line. To make this possible, *three* additional steps had to be taken: *Firstly*, the structure shown in Fig. 2.28 had to be extended by two external inertias. This step was necessary in order to account for the part of the drive line outside of the induction machine, of which especially the two members of the torque measuring flange were important. The outcome is the

"hybrid" mechanical system consisting of *distributed* and *lumped* components depicted in Fig. 2.31, with addiotional inertias I_4 and I_5 and no pinned element at one of the ends of the rotor. A practical, and rather heuristical extension of the formalism to describe the resonances of a distributed model aiming at the structure shown in Fig. 2.31 is discussed in Appendix B. Additionally, the depicted system allows to create a clear counterpart of the measured shaft torque; again, the torque transmitted by k_4 and c_4 from I_4 to I_5 was used to compare simulation and measurement.

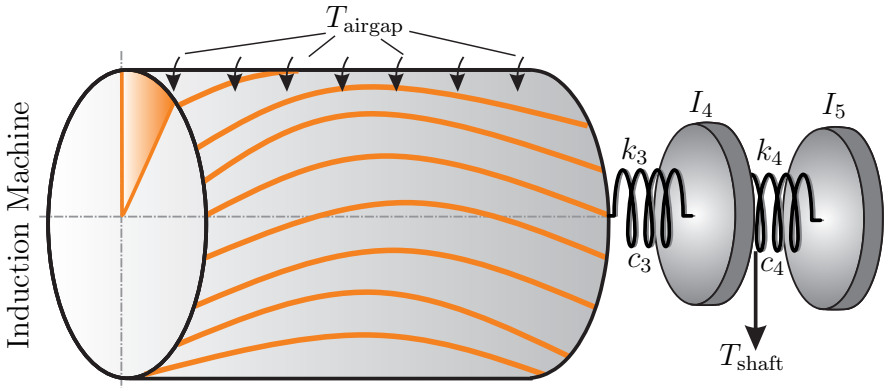

Figure 2.31: Soft rotor with external two-mass oscillator.

Secondly, in order to implement the discussed model on the chosen simulation platform, the soft rotor had to be discretized spatially again, which causes a deviation from the desired distributed-parameter character of the model. However, the number of sub-inertias was chosen comparably large, for the present case 100 same-sized sub-inertias were used, in order to conserve the properties of the distributed model well, while trying to keep the numerical complexity low. Besides the drawback of losing the full distributed-parameter character of the simulation model, the usage of a finite-dimensional model also brings an advantage: It allows to employ the same methods of numerical optimization to find the model's parameters, which have already been used for the previous models.

Thirdly, the acting airgap torque was not connected to the *entire* soft body: The very right and the very left end, meaning the outer five inertias on each side, were assumed not to be touched by T_{airgap}, in order to account for the parts of the rotor that do not carry any electrical conductors, and lay above the bearings of the machine, for example.

As for the alternative topologies discussed in Sec. 2.2.10, a combination of two optimization problems was used to find the model's parameters. The details of the procedure, where again also the desired transfer zeros were included in the problem statement and the resulting parameters are given in Appendix A.3. As mentioned above, the parametrization effort compared to the prior modelling attempts is reduced, also in case of an again spatially discretized soft rotor, mainly because all inertias and all connecting shafts inside the rotor receive the same values. Once more, the experiments that are also considered for the other modelling approaches were repeated in simulation, now using the soft-rotor approach. The results are shown in Figs. 2.32.

2.3.3 Results: Soft rotor

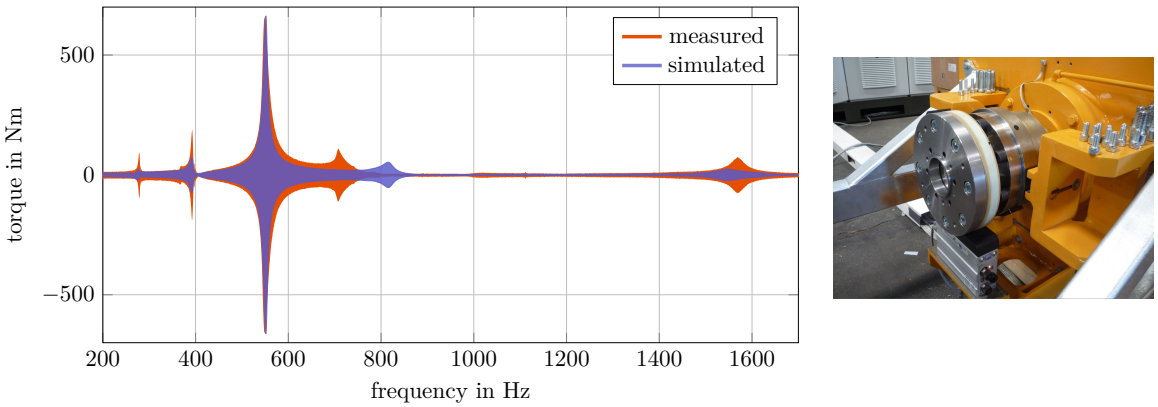

(a) Flange 1, additional inertia: I_{f1}=0.13kgm^2, which is included in $I_{5,1} = 0.16 kgm^2$, a result from optimization.

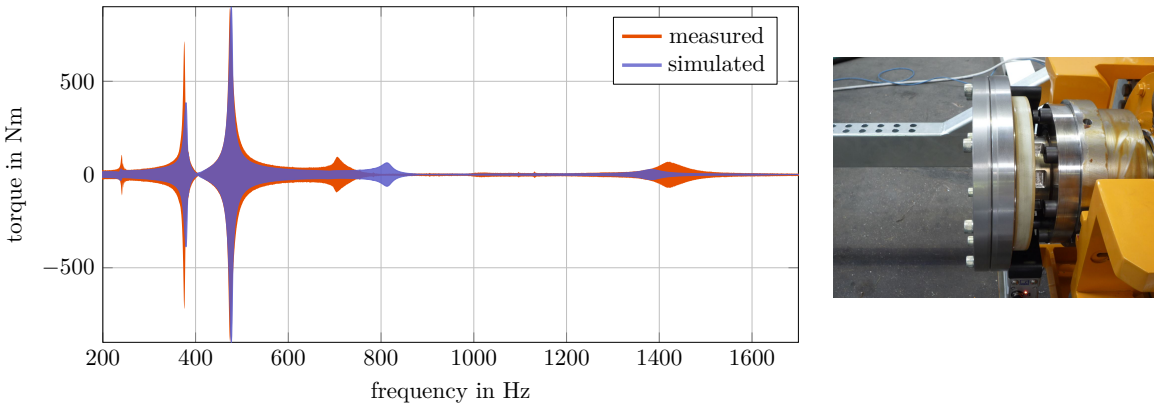

(b) Flange 2, additional inertia: I_{f2}=0.13kgm^2, thus $I_{5,2} = I_{5,1} + I_{f2}$ = 0.29kgm^2.

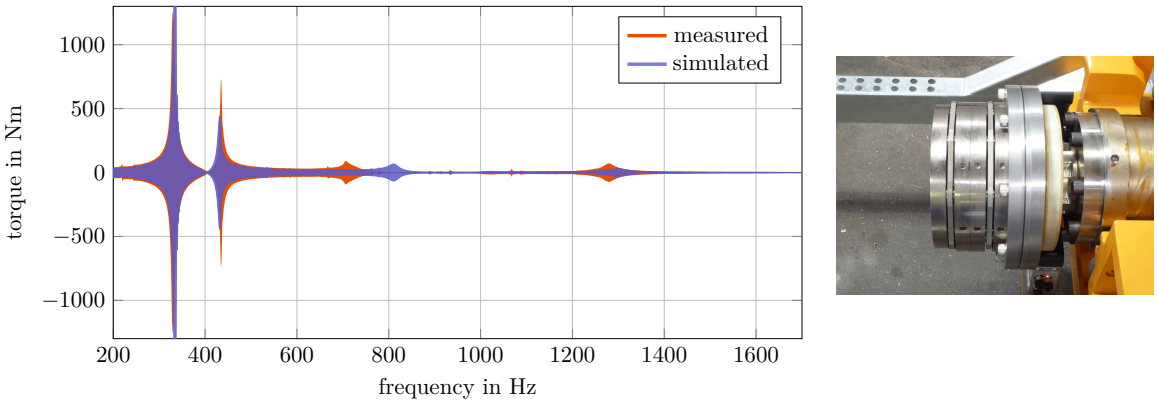

(c) Disc-pack coupling, additional inertia: I_{dp}=0.24kgm^2, thus $I_{5,3} = I_{5,2} + I_{dp}$ = 0.53kgm^2.

Figure 2.32: Chirp experiments on the heavy-duty test bed compared to simulation results obtained with the soft-rotor approach. The soft rotor was divided into 100 partial inertias, and the airgap torque again did not act on the outer five inertias on each end of the body.

2.3.4 Results: Soft rotor, R2R test bed

As mentioned in the very beginning of this chapter, the heavy-duty test bed was shipped to the customer in the midst of the project. From that point on, the R2R test bed introduced in Sec. 2.1.2 served as a new platform for experiments. The idea behind the trials, however, did not change: Concentrated inertia was added to the end of the drive line, while consecutive chirp experiments were performed. The relevant section of the R2R test bed, four specifically designed test flanges, and the considered drive line with and without test flange are shown in Figs. 2.33(a)-2.33(d). Three selected measurements are shown in Figs. 2.34, accompanied by simulation results that were again achieved with the soft rotor model.

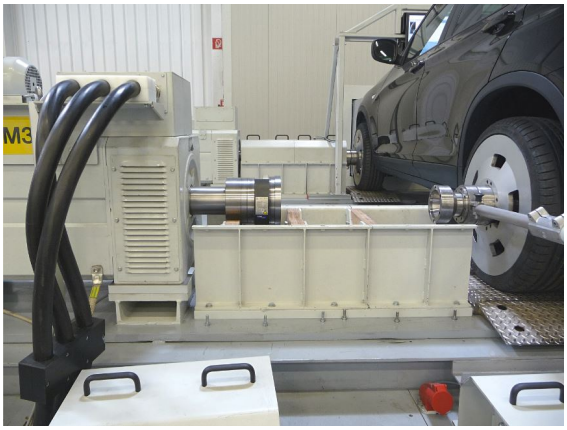

(a) R2R test bed with dismantled shaft.

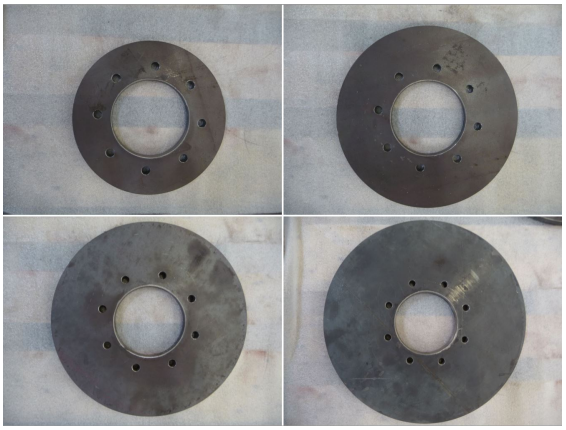

(b) Test flanges.

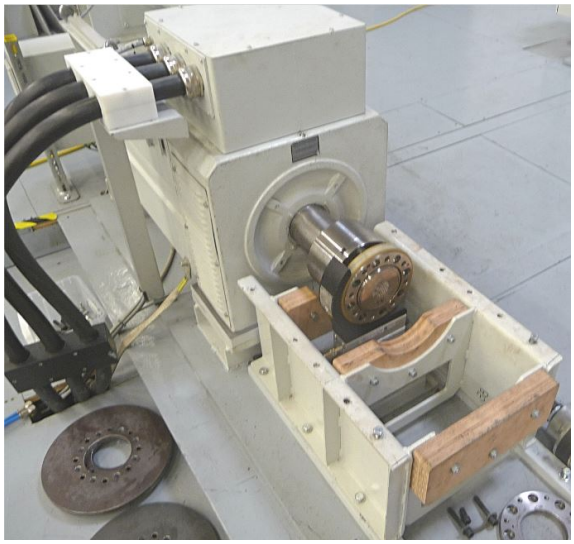

(c) Power train without test flange.

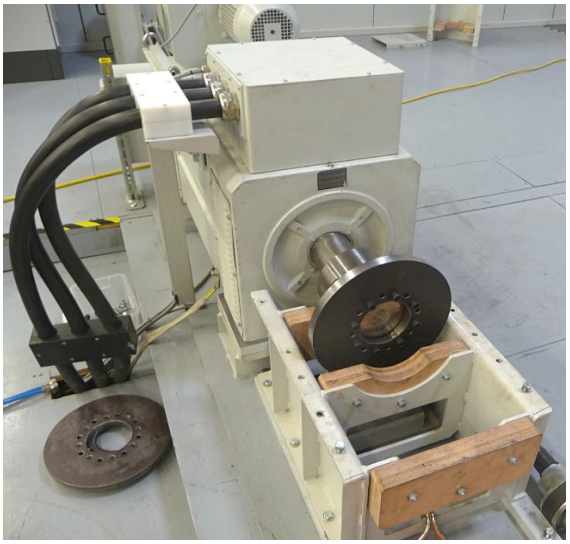

(d) Power train with test flange.

Figure 2.33: Drive line modelling, experimental setup on R2R test bed.

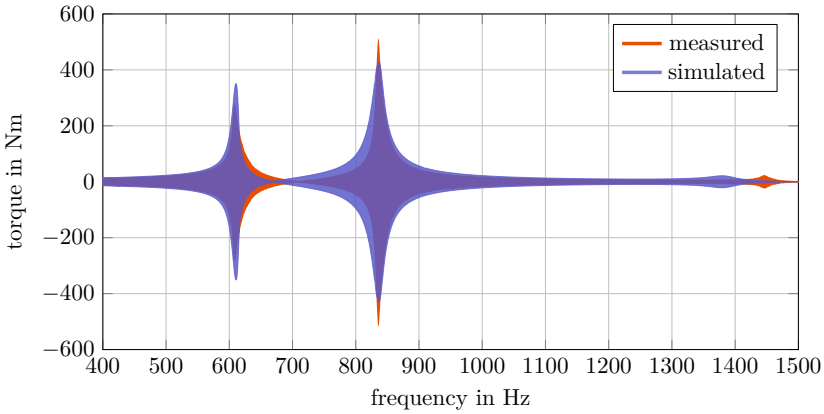

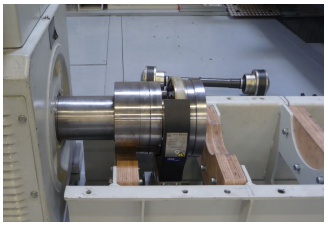

(a) Setup 1, no additional flange. Secondary inertia of measuring flange: $I_{5,1}$ = 0.08kgm^2.

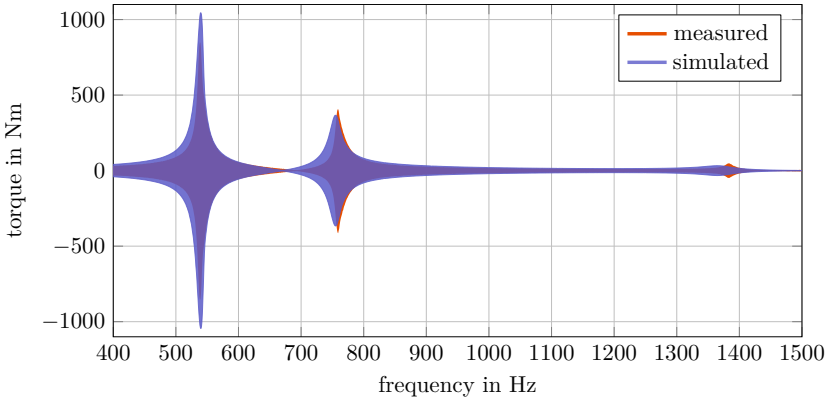

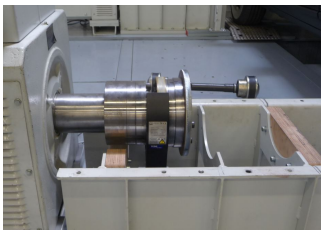

(b) Setup 2, additional inertia: I_{f1}=0.09kgm^2, thus $I_{5,2} = I_{5,1} + I_{f1}$ = 0.17kgm^2.

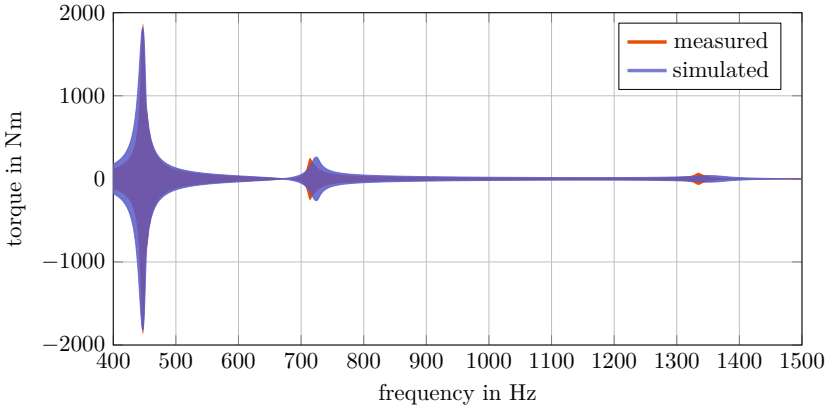

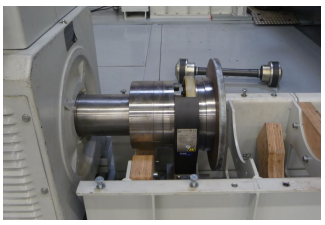

(c) Setup 3, additional inertia: I_{f2}=0.23kgm^2, thus $I_{5,3} = I_{5,1} + I_{f2}$ = 0.31kgm^2.

Figure 2.34: Chirp experiments on the R2R test bed and simulation results obtained with the soft-rotor model. The soft rotor was divided into 70 partial inertias, and the airgap torque again did not act on the first four inertias on the left, and the last three inertias on the right end of the soft body.

The experiments on both the R2R and the heavy-duty test bed show one thing clearly: Large machine rotors *must* be represented as distributed structures. Conceptually, the trials on the two platforms were almost equivalent, with only one minor difference. On the R2R test bed, the flanges were not stacked, in the sense that one flange would be mounted on the back of the other. The idea was to make absolutely sure that no unintended dynamics would be added to the system; hence, only one flange was present at a time, and after completing the experiments with it, it was taken off and replaced by the next one. To model this setup, the soft rotor was distributed into 70 partial inertias, and it was found that good results could be achieved if the first four inertias on the left, and the last three inertias on the right were not touched by the induced airgap torque. The used parameters are again listed in Appendix A.3. Besides that, the chirp experiments were exactly the same as before, and made clear that the proposed soft structure allows to create a physically interpretable model, that excels in various aspects. In response to the alternative structure discussed in Sec. 2.2.10, one must note that also the soft-rotor model is capable of reproducing the resonances accurately, that it reflects their evolution in accordance with the measurements, and that it also comprises the desired transfer zeros. In contrast to the alternative approach, however, the soft-rotor structure is not accompanied by any physical shortcomings, that would raise doubts about the model itself and consequently also about the achieved results. Nevertheless, some deviations may be found in Figs. 2.32 and 2.34; but especially in comparison to the attempt employing the naive chain of inertias, the presented results may be regarded as a significant improvement. Furthermore, it must be noted that even though the mathematical complexity of the soft-rotor model increases through the introduction of a partial differential equation, the number of parameters is reduced, mainly because only one stiffness, damping and inertia value are needed to represent the induction machine! In that light, the already very satisfying simulation results shown in Figs. 2.32 and 2.34 must be valued even higher.

2.4 Conclusion

To summarize, one may state that the use of partial differential equations is key for obtaining suitable mathematical models of the mechanical side of big electrical machines. The proposed model may be used for simulations and analysis of any kind, not just for control-oriented purposes. An aspect that bears the potential of further improvement is the selection of identification experiments. Although the considered chirp experiments allow to quickly create a precise view on the dynamical properties that are of importance from a control engineering point of view, it may very well be that other experiments could also be suitable for the purpose of parametrization. Possible candidates in that regard are speed ramps, to give an example. An extension of the proposed model, where again speed ramps might be beneficial for identification, could involve nonlinear friction terms, to reproduce also the measured angular velocity with high accuracy. These questions are in the scope of ongoing research.

Chapter 3

Backlash and Gear Play

Frequently, the dynamical behaviour of test bed drive lines is influenced strongly by components that mechanically connect the priorly discussed rotary inertias. Clutches, couplings, transmissions, and also gearboxes are just some examples thereof. Two of these elements and some novel ideas with regards to their modelling are discussed in the following: hydrodynamic couplings and components containing backlash. The present chapter starts with an analysis of the latter, an outstandingly important topic in mechanical systems from gear trains to aerospace applications. Parts of the presented content can also be found in [61], in a to some degree modified version.

When present, backlash often turns out to be among the critical attributes of the affected system, which motivated some authors to characterize backlash as *the most important nonlinearity in modern drive systems* [62, 63]. Altogether, a great number of papers dealing with backlash have been published, while most recently a shift towards the application of state-of-the-art observers in combination with advanced nonlinear methods, such as sliding-mode or flatness-based control, with the aim of compensating the nonlinearity can be recognized [64–67]. Despite the fact that there has been a lot of interest in systems comprising backlash, contributions that tackle its mathematical modelling are rare. One of the most prominent references in that regard is [62], where several approaches that map the states of the two sides of the backlash gap onto the transmitted torque are presented. While they are perfectly sound for the setting assumed by the authors, certain assumptions may not be valid in other applications. Most importantly, there may be contact in the sense of *viscous friction* in phases where there is *no classical backlash contact*. This drawback is also present in other contributions that focus on the modelling of backlash, see e.g. [68–70]. In that sense, the following section addresses this highly relevant limitation by extending existing backlash models to take these friction effects into account.

Also in this research, extensive experiments played a crucial role. In Section 3.1, the test bed used for that purpose is presented, and the main ideas for the modelling of its drive line are discussed. The test bed was equipped with a shaft that comprises a specifically designed backlash spot, with known geometry and material properties. This allows for

a rigorous assessment of any simulation model. Section 3.2 reviews the backlash models given in literature, which is followed by a comparison of measured data from two selected experiments with simulation results to highlight the shortcomings of these models. Section 3.3 outlines the novel approach, which essentially includes viscous damping into phases that are free from classical backlash contact. In Section 3.4, a comparison with the same experimental data shows that simulation results obtained with the new model agree much better with the considered measurements.

3.1 Test bed

The previously mentioned experiments were conducted on the test bed depicted in Fig. 3.1. This particular test stand[1] serves a purely scientific purpose, which explains the relatively long drive line and the high number of sensors and other components. These are a) induction machine 2 (IM_2), b) torque transducers, c) bearing blocks, d) flywheel, e) incremental encoder, f) elastic coupling, g) IM_1. The induction machines are of type Lenze MCA14L16, whose rated parameters are listed in Table C.3 in Appendix C. The elastic coupling f) was replaced by a shaft that comprises a pre-designed backlash-spot. The latter is shown in Fig. 3.3, while its constructive characteristics are listed in Table C.2, also in Appendix C.

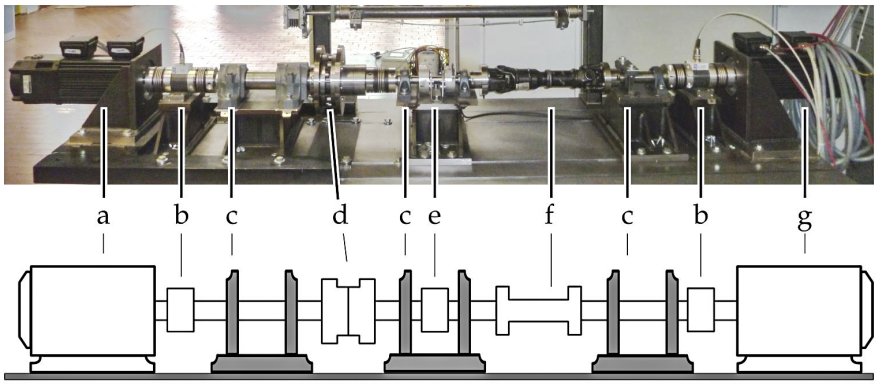

Figure 3.1: Mechanical setup of the test bed. Picture taken from [31].

In order to objectively assess the various backlash models and to draw the correct conclusions from simulations, sufficiently accurate models of the other system components are required. These components are the neighbouring drive line sections and the induction machines, whose models are briefly discussed in the following. For the model derivation, IM_1 and IM_2 are represented by fundamental wave models [37, 72]. The controllers for current, angular velocity and magnetic flux that are used in simulation were exactly the

[1] Details for the test bed can be found in [31, 71].

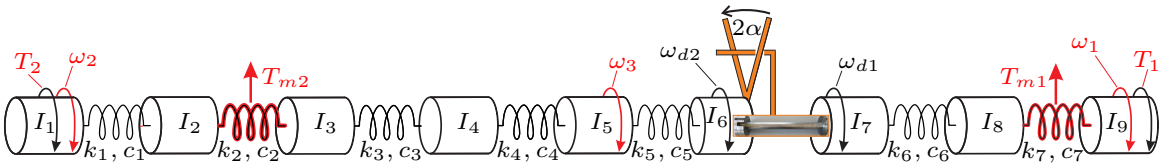

Figure 3.2: Structure of the drive line simulation model.

same as those active on the test bed. The drive line itself is modelled as a series of lumped inertias connected via torsional springs with damping. In contrast to the big induction machine inertias discussed in Chapter 2, the inertias in this case are so small that they are interpreted as lumped elements only, leading to the mechanical model that is shown in Fig. 3.2. The line is driven by the air gap torques T_1 and T_2. The induction machine[2] IM_2, the left torque transducer, the two parts of the flywheel, the incremental encoder and the front end of the backlash shaft are represented by I_1, I_2, I_3, I_4, I_5 and I_6, respectively. The back end of the backlash shaft, the other torque transducer and IM_1 are denoted by I_7, I_8 and I_9, respectively. All inertias are connected by torsional springs with stiffness k_i and damping c_i. The variables available as measurements are highlighted in red in Fig. 3.2. Besides the airgap torques T_1 and T_2, these are the torques transmitted via k_2 and k_7, and the angular speeds of the induction machines and the flywheel. They are denoted by T_{m1} and T_{m2}, and ω_1, ω_2 and ω_3, respectively.

Precisely determining the model parameters is of great importance. Fig. 3.4 shows a small excerpt of the numerous experiments that were carried out for model identification and

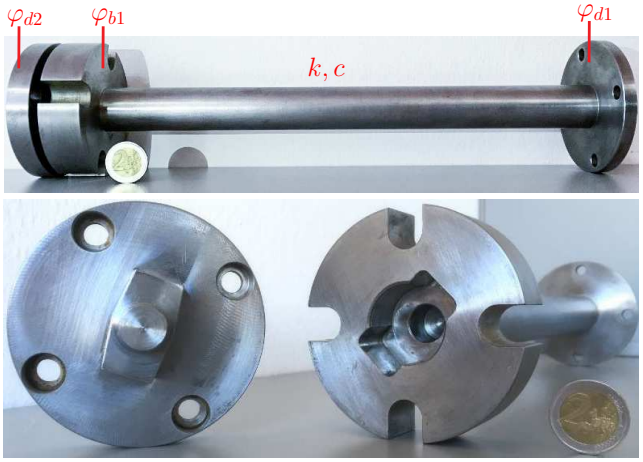

Figure 3.3: Shaft with pre-designed backlash; on top as mounted in the drive line, at the bottom the disassembled components.

[2]Particularly the rotary inertias of the induction machine rotors are so small that it is not necessary to use the soft-rotor approach. Specifically, $I_{\mathrm{Lenze}} = 0.0019\mathrm{kgm}^2$ and $k_{\mathrm{Lenze}} \approx 1\frac{\mathrm{MNm}}{\mathrm{rad}}$, where already a separation into only a three-mass-oscillator leads to a lowest additionally introduced resonance frequency of 6417 Hz, which is far above the frequency range of interest.

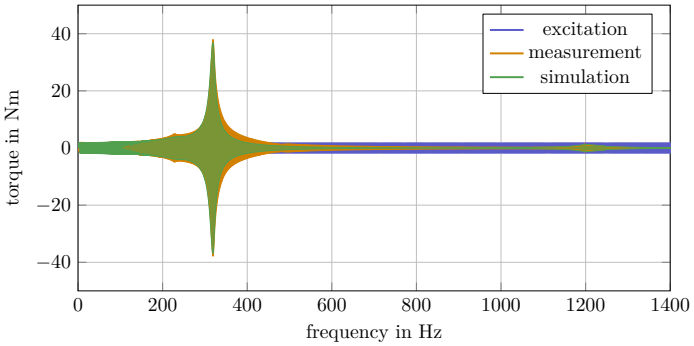

Figure 3.4: Chirp experiment to identify the parameters of the drive line section left of the backlash. Excitation is a chirped air gap torque T_2, the torque T_{m2} is measured.

validation purposes. Here, the backlash shaft is taken out of the drive line and a chirped airgap torque T_2 with amplitude $\hat{T}_2 = 2\,\mathrm{Nm}$ and a frequency that is increased from 0 Hz to 1400 Hz is applied. The model parameters are the outcome of combined analytical and numerical computations, similar to the procedures discussed in Chapter 2. The resulting values are shown in Table C.3 in Appendix C.

As indicated in Fig. 3.3, the angles of the inertias neighbouring the backlash are φ_{d1} and φ_{d2}. The angle of the driving axis at the backlash spot is denoted by φ_{b1}, while α stands for half the backlash gap. In most of the following considerations, the differences $\varphi_d = \varphi_{d1} - \varphi_{d2}$ and $\varphi_b = \varphi_{b1} - \varphi_{d2}$ will be used, with the corresponding velocities being denoted as ω_d and ω_b. Stiffness and damping of the backlash shaft are represented by k and c, and the transmitted backlash torque is abbreviated as T.

3.2 Backlash models

As most published approaches are closely related to [62], only models from this contribution are reviewed here. Therein, only the differential angle φ_d is used - and not φ_b. This restriction is due to practical considerations: In most use cases, the positions of the members connected to the backlash shaft are known, but not the positions right next to the backlash spot itself. However, it is assumed that the driven member is located immediately behind the backlash. Hence, φ_{d2} equals the front side backlash position. These assumptions are fulfilled in many practical setups, including the one shown in Fig. 3.3, where the incremental encoder e) provides information about φ_{d2}.

3.2.1 Dead-zone model

The most simple and thus probably most widely used model is the so-called dead-zone model. It can be stated as

$$T = \begin{cases} k(\varphi_d - \alpha) + c\omega_d & \varphi_d > \alpha \\ 0 & |\varphi_d| \leq \alpha \\ k(\varphi_d + \alpha) + c\omega_d & \varphi_d < -\alpha. \end{cases} \tag{3.1}$$

A significant drawback of this approach is that it might predict unphysical pull forces. In the case of $\varphi_d > \alpha$, for instance, the transmitted torque $T = k(\varphi_d - \alpha) + c\omega_d$ becomes negative for $\omega_d < -\frac{k}{c}(\varphi_d - \alpha)$.

3.2.2 Revised dead-zone model

To fix this error, the condition for whether torque is transmitted or not can be extended by the term $\frac{c}{k}\omega_d$:

$$T = \begin{cases} k(\varphi_d - \alpha) + c\omega_d & \varphi_d + \frac{c}{k}\omega_d > \alpha \\ 0 & |\varphi_d + \frac{c}{k}\omega_d| \leq \alpha \\ k(\varphi_d + \alpha) + c\omega_d & \varphi_d + \frac{c}{k}\omega_d < -\alpha. \end{cases} \tag{3.2}$$

3.2.3 Phase-plane model

However, the actual physical reality is that in order to transmit torque, the inequality $|\varphi_b| > \alpha$ must hold, which is analysed in great detail in [62]. To check this condition without using φ_b, the latter must be estimated by the means of φ_d and ω_d. As described in [62], this idea can be used to motivate activation areas in the (φ_d, ω_d)-plane, leading to

$$T = \begin{cases} k(\varphi_d - \alpha) + c\omega_d & (\varphi_d, \omega_d) \in A^+ \\ 0 & (\varphi_d, \omega_d) \in A_0 \\ k(\varphi_d + \alpha) + c\omega_d & (\varphi_d, \omega_d) \in A^-. \end{cases} \tag{3.3}$$

The areas A^+, A^- and A_0 combine a mapping of (φ_d, ω_d) onto the corresponding angle φ_b followed by a check of whether $|\varphi_b| > \alpha$ is fulfilled. For the given setup, Fig. 3.5 shows

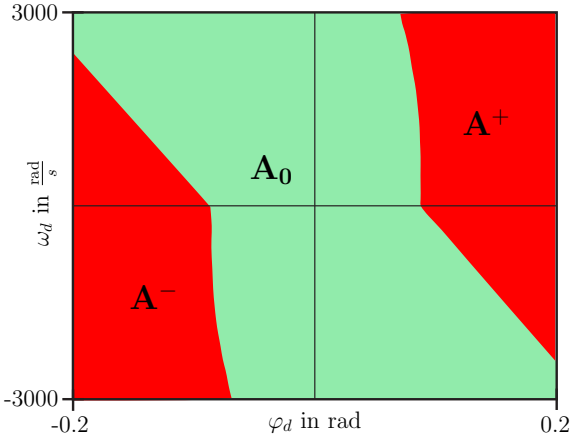

Figure 3.5: Phase plane plot for the phase plane model.

these areas, which are computed according to the description provided in [62]:

$$
\begin{aligned}
A^+ &= \left\{ (\varphi_d, \omega_d) : \left\{ \begin{array}{l} \varphi_d + (\frac{c}{k}\omega_d) e^{-\frac{k}{c}\frac{\varphi_d+\alpha}{\omega_d}-1} \geq \alpha, \ \omega_d > 0 \\ k(\varphi_d - \alpha) + c\omega_d \geq 0, \quad \forall \omega_d \end{array} \right. \right\} \\
A^- &= \left\{ (\varphi_d, \omega_d) : \left\{ \begin{array}{l} \varphi_d + (\frac{c}{k}\omega_d) e^{-\frac{k}{c}\frac{\varphi_d+\alpha}{\omega_d}-1} \leq -\alpha, \ \omega_d < 0 \\ k(\varphi_d + \alpha) + c\omega_d \leq 0, \quad \forall \omega_d \end{array} \right. \right\} \\
A_0 &= \{(\varphi_d, \omega_d)\} \setminus (A^+ \cup A^-).
\end{aligned}
\tag{3.4}
$$

3.2.4 Validation

Numerous experiments were conducted on the test bed, and repeated in simulation with the same boundary conditions. The chosen simulation platform was MATLAB&SIMULINK®. The drive line and the backlash models were implemented as continuous time systems, while the controllers for the induction machines were computed at a sampling rate of 10kHz, as on the test bed. In the following, measurements and simulation results are compared for two exemplary experiments. In both of them, IM_2 acts in speed control mode with ω_3 as the controlled variable, while IM_1 is used to set T_1. In the *first* experiment, which is depicted in Fig. 3.6, the set point for IM_2 is $\omega_3^* = 0 \frac{\text{rad}}{\text{s}}$, while T_1 performs a jump from -1 to +1 Nm.

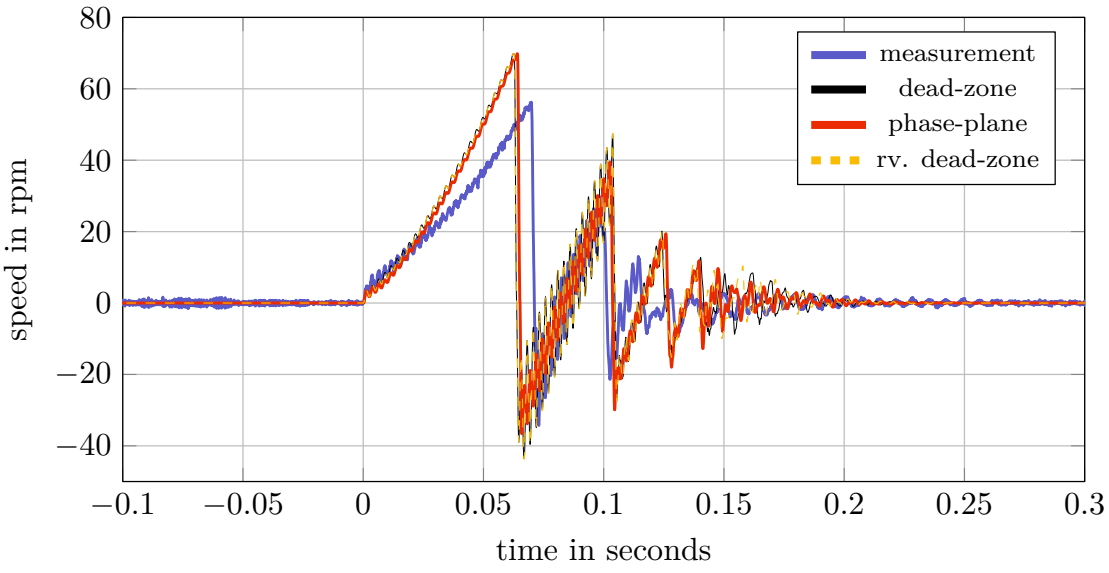

Figure 3.6: Simulation results and simulations of ω_1 for experiment I.

For the *second* experiment, $\omega_3^* = 20.94\,\frac{\text{rad}}{\text{s}}$ is used as a set point, while T_1 jumps from -3 to +3 Nm. The simulated angular speeds of IM_1 are presented in Fig. 3.7.

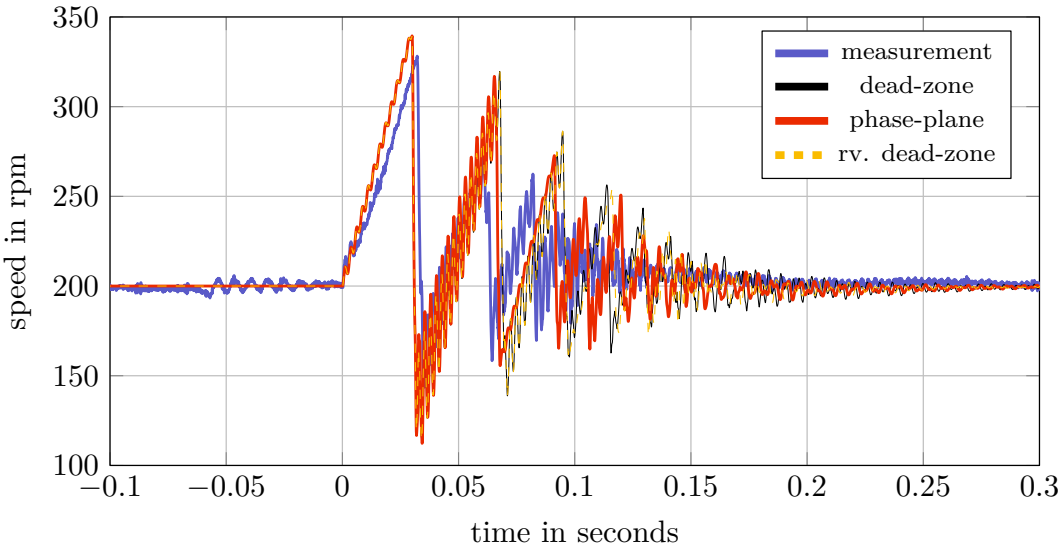

Figure 3.7: Simulation results and simulations of ω_1 for experiment II.

For the given setup, $\frac{k}{c} \approx 3 \cdot 10^4$, which causes the three models to be highly similar. This fact is also expressed in Figs. 3.6 and 3.7, where especially between the *dead-zone* and the *revised dead-zone model* almost no deviation is visible. One can see clearly that for all three backlash models the simulation gravely fails to reproduce the measurements.

3.3 Backlash models with damping

A significant drawback of the discussed models is that they do not incorporate damping between the primary and secondary part when there is no backlash contact in classical sense, i.e., when $|\varphi_b| < \alpha$. However, such a damping may still occur due to friction phenomena. The two parts of the backlash might touch, even when their side faces are not in contact. This is especially true for the considered setup, where the front of the plug rubs against the back wall of the cave in the primal part. A common practical example that may be described by this characteristic are universal joints. In this section, possible extensions for all three models are proposed that take damping in the contact-less phase into account. The additional damping is denoted by c_f.

3.3.1 Dead-zone and revised dead-zone model

With the *dead-zone* model, adding the damping is straightforward. The associated torque is applied in the case that $|\varphi_d| \leq \alpha$, replacing the zero torque term. This yields

$$T = \begin{cases} k(\varphi_d - \alpha) + c\omega_d & \varphi_d > \alpha \\ c_f\omega_d & |\varphi_d| \leq \alpha \\ k(\varphi_d + \alpha) + c\omega_d & \varphi_d < -\alpha. \end{cases} \tag{3.5}$$

Still, the *dead-zone model* remains an unphysical description that suffers from potential pull forces if $c \neq 0$. For the *revised dead-zone model*, the extension has to be carried out in the same fashion. In that case, however, if and how the activation conditions should be modified is not entirely clear.

3.3.2 Damped phase-plane model

The only model that allows to integrate the additional damping in a methodically correct way is the *phase-plane model*. As in [62], φ_b is estimated in order to check whether $|\varphi_b| < \alpha$ or $|\varphi_b| = \alpha$ is fulfilled. The initial values at the beginning of a contact-less period are denoted by φ_{b0}, ω_{b0}, φ_{d0} and ω_{d0}, and the following assumptions are made:

1. The additional damping torque is given by $T_d = c_f\omega_b$.
2. The shaft is inertia-free, meaning that the torque on both of its sides is equal.
3. In case of initial left contact, $\varphi_{b0} = -\alpha$; in case of right contact, $\varphi_{b0} = \alpha$, and in both cases $\omega_{b0} = 0$.
4. During the contact-less periods, ω_d is assumed constant, which implies $\omega_d = \omega_{d0}$.[a]

[a] Due to external torques and the introduced damping, ω_d may change during the contact-less periods. As these are typically very short, only small deviations from ω_{d0} are to be expected, which are thus neglected, cf. [62].

Throughout the interval without backlash contact

$$T = k(\varphi_d - \varphi_b) + c(\omega_d - \omega_b) = c_f\omega_b, \tag{3.6}$$

which differs from [62], where $T = 0$. Using the fact $\frac{\mathrm{d}}{\mathrm{d}t}\varphi = \omega$, (3.6) may be rearranged to obtain a differential equation for the angle φ_b, i.e.

$$\frac{\mathrm{d}}{\mathrm{d}t}\varphi_b = -\frac{k}{c + c_f}\varphi_b + \frac{k}{c + c_f}\varphi_d + \frac{c}{c + c_f}\omega_d. \tag{3.7}$$

A consequence of assumption *4* is that $\frac{c}{c+c_f}\omega_d$ stays constant during the contact-free interval, and moreover,

$$\varphi_d = \varphi_{d0} + \omega_{d0} t, \tag{3.8}$$

which allows (3.7) to be solved analytically! To that end, the equation is turned into

$$\frac{\mathrm{d}}{\mathrm{d}t}\varphi_b = -p\varphi_b + q + rt, \tag{3.9}$$

where the abbreviations $p = \frac{k}{c+c_f}$, $q = \frac{k}{c+c_f}\varphi_{d0} + \frac{c}{c+c_f}\omega_{d0}$ and $r = \frac{k}{c+c_f}\omega_{d0}$ are used. Its solution can be found by variation of constants, and turns out as

$$\varphi_b = \underbrace{\frac{-r+pq}{p^2} + \frac{r}{p}t}_{\theta_{bp}} + C \cdot e^{-pt}. \tag{3.10}$$

Here, the integration constant C has to be chosen such that the initial conditions are matched. Note that φ_{bp} represents the particular solution of (3.9), which is caused by the damping term $c_f\omega_b$, and thus comprises the main difference to the model proposed in [62]! Depending on whether contact was lost on the right or the left side, $\varphi_{b0} = \mp\alpha$, and thus

$$C = \mp\alpha + \frac{r-pq}{p^2}. \tag{3.11}$$

In order to make φ_d and ω_d the only independent variables in the mapping, the time t is expressed in terms of the two variables. Therefore, (3.8), (3.6) evaluated for the initial values, and the fact that $\varphi_{b0} = \mp\alpha$ and $\omega_{b0} = 0$ are combined. In the case of initial left contact, this leads to

$$t = \frac{\varphi_d + \alpha}{\omega_d} + \frac{c}{k}. \tag{3.12}$$

To obtain, e.g., A^+, the conditions $\varphi_b > \alpha$ for $\omega_b > 0$, and $T > 0$ for $\omega_b \leq 0$ have to be combined. Exploiting symmetry for right contact and resubstituting p, q, r and (3.12) into the new expression for φ_b in (3.10), the new activation areas can be formulated as

$$\begin{aligned}
A^+ &= \{(\varphi_d, \omega_d) : \\
&\left\{\begin{array}{ll} \varphi_d - \frac{c_f}{k}\omega_d + \frac{c+c_f}{k}\omega_d e^{-\frac{k}{c+c_f}\left(\frac{\varphi_d+\alpha}{\omega_d}+\frac{c}{k}\right)} \geq \alpha, & \omega_d > 0 \\ k(\varphi_d - \alpha) + c\omega_d \geq 0, & \forall \omega_d \end{array}\right\} \\
A^- &= \{(\varphi_d, \omega_d) : \\
&\left\{\begin{array}{ll} \varphi_d - \frac{c_f}{k}\omega_d + \frac{c+c_f}{k}\omega_d e^{-\frac{k}{c+c_f}\left(\frac{\varphi_d-\alpha}{\omega_d}+\frac{c}{k}\right)} \leq -\alpha, & \omega_d < 0 \\ k(\varphi_d - \alpha) + c\omega_d \leq 0, & \forall \omega_d \end{array}\right\} \\
A_0 &= \{(\varphi_d, \omega_d)\} \setminus (A^+ \cup A^-).
\end{aligned} \tag{3.13}$$

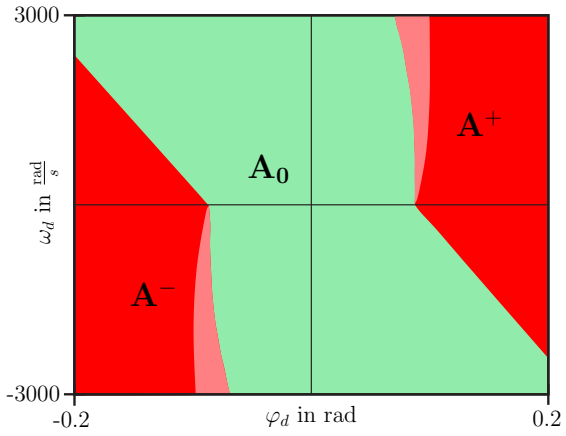

Figure 3.8: Phase plane plot for the damped model; difference to the undamped version in rose.

A graphical representation of the new activation areas is shown in Fig. 3.8, alongside the difference to the original version. Note that the old and the new areas converge for $c_f \to 0$. An important asset of this approach is that it allows to include an estimate of ω_b, which is indispensable for accurately calculating the additional damping torque. Depending on whether contact was lost on the left or the right side,

$$\omega_b = \omega_d - \varphi_b \cdot e^{-(\frac{k}{c+c_f})(\frac{\varphi_d \mp \alpha}{\omega_d} + \frac{c}{k})}, \tag{3.14}$$

which eventually leads to the *damped phase-plane model*:

$$T = \begin{cases} k(\varphi_d - \alpha) + c\omega_d & (\varphi_d, \omega_d) \in A^+ \\ c_f(\omega_d - \varphi_b e^{-\frac{k}{c+c_f}(\frac{\varphi_d + \alpha}{\omega_d} + \frac{c}{k})}) & (\varphi_d, \omega_d) \in A_0 \ \wedge \ \omega_d \geq 0 \\ c_f(\omega_d - \varphi_b e^{-\frac{k}{c+c_f}(\frac{\varphi_d - \alpha}{\omega_d} + \frac{c}{k})}) & (\varphi_d, \omega_d) \in A_0 \ \wedge \ \omega_d < 0 \\ k(\varphi_d + \alpha) + c\omega_d & (\varphi_d, \omega_d) \in A^-. \end{cases} \tag{3.15}$$

3.4 Experimental results

To assess the new approach, simulation results are again compared to measurements from the experiments discussed earlier. As before, $\frac{k}{c}$ is large, which leads to only small deviations between the different models. For the sake of clarity, only the *damped phase-plane model* and the original *phase-plane model* are graphed in Figs. 3.9 and 3.10. For the results obtained with the new approach, a significant improvement of the simulation results is visible. Especially the speed of IM_1, ω_1, is predicted much more accurately. Besides ω_1, the torques T_{m1} and T_{m2} are shown, which are matched more closely, too.

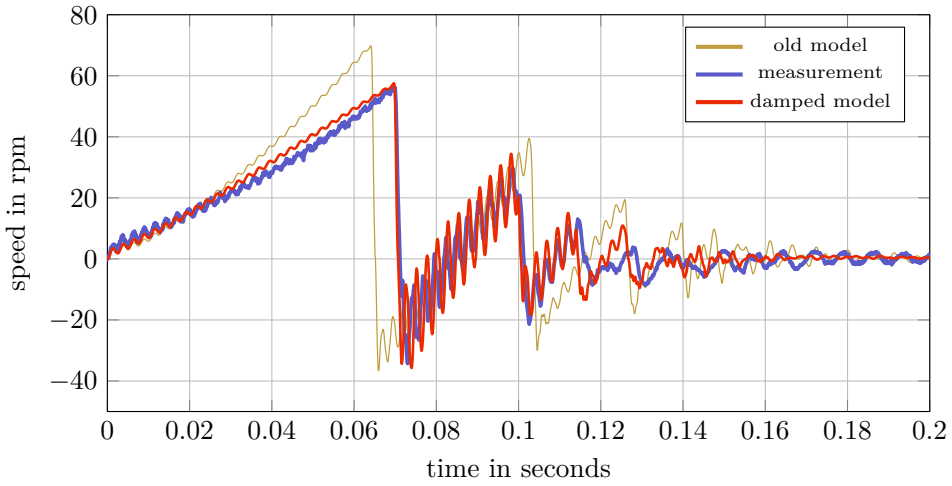

(a) Angular speed ω_1.

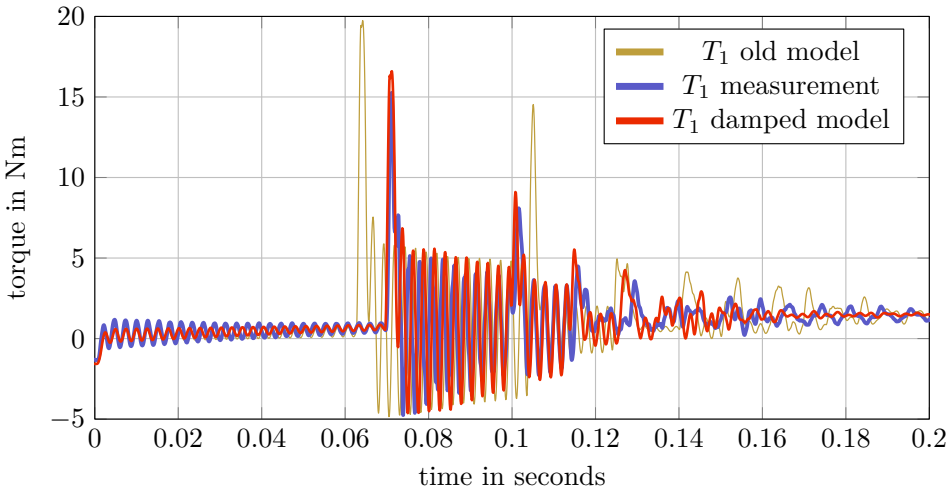

(b) Torque T_1.

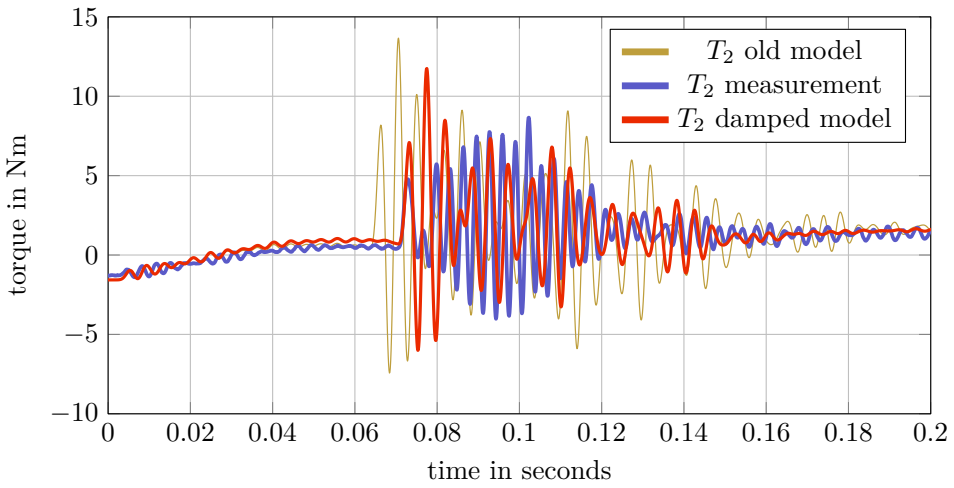

(c) Torque T_2.

Figure 3.9: Measurements and simulation results for experiment I, using the damped and the undamped phase-plane model.

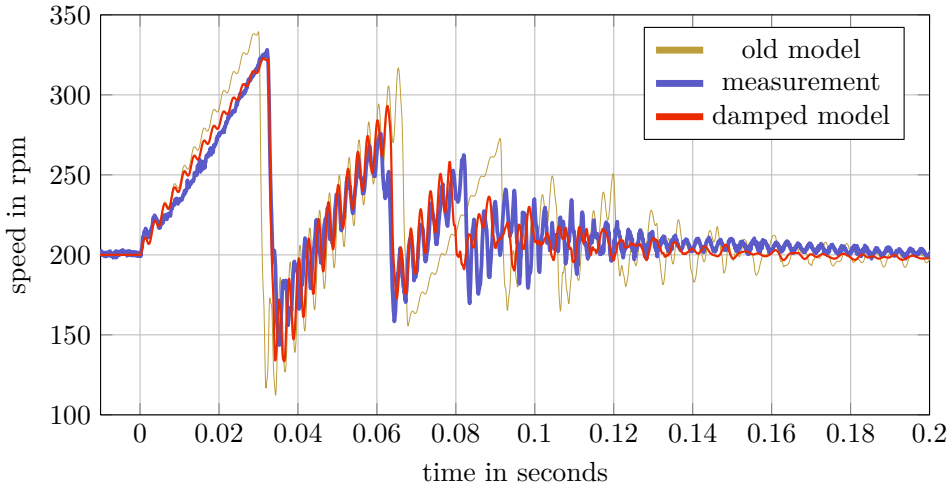

(a) Angular speed ω_1.

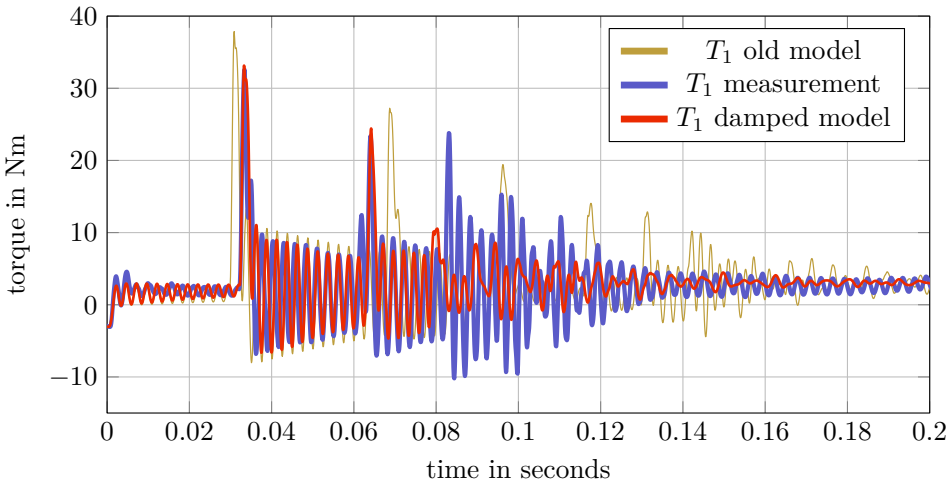

(b) Torque T_1.

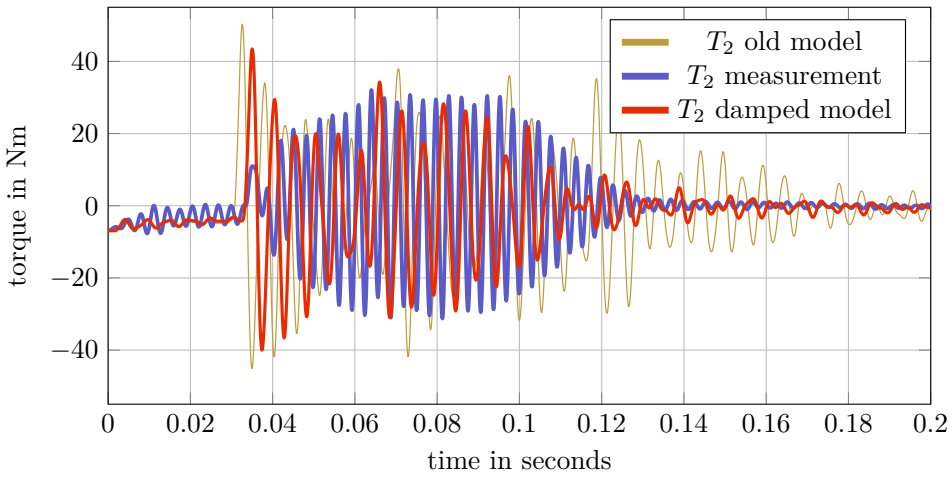

(c) Torque T_2.

Figure 3.10: Measurements and simulation results for experiment II, using the damped and the undamped phase-plane model.

3.5 Conclusion

The main result of the preceding chapter is the *damped phase-plane model*, an extension of the backlash models introduced in [62]. In essence, the new model integrates damping that is present in phases without classical backlash contact into the well established *phase-plane model*. Extensive experiments were conducted on a highly dynamic research test bed. A comparison between measurements and simulation results shows that the additional damping significantly contributes to improving the quality of the given simulation model. The proposed extension only marginally increases the original models' complexity, which makes especially the *damped phase-plane model* an attractive tool for simulation studies. However, some deviations between simulation and measurement, as in the case of T_{m1} in experiment I, cannot be denied, which indicates that there still is room for improvement. Nonetheless, Figs. 3.9 and 3.10 clearly suggest that adding damping in the contact-free periods has the potential to significantly improve the models proposed in [62].

Chapter 4

Hydrodynamic Couplings

As laid out in the introduction to Chapter I, undesired torsional oscillations can be a significant limiting factor for a system's performance, in automotive testing as well as in other technical areas. An important trend in this regard is the ever increasing power density of today's diesel and gas engines, which aggravates occurring torque pulses and boosts the demand for strategies to overcome vibration related problems. Frequently, these strategies include the incorporation of a *hydrodynamic coupling* with desirable damping characteristics into the drive line. However, no mathematical model of a hydrodynamic coupling that is suitable for both controller design *and* transient simulations has been published so far, despite the fact that model based control is omnipresent in modern drive systems. A description in the form of a so-called *Kelvin-Voigt*[1] model is proposed in [74], which is the simplest and most widely used model for a hydrodynamic coupling. Unfortunately, this approach is valid only in a single operating point. In [75, 76], the issue is treated in a rather complex fashion, using the bond graph method; and even more involved techniques are employed in [77–80], such as neural nets and linear sectional models. While these contributions invest a great deal of effort to model the coupling, obvious drawbacks are the lack of physical insight or a high model complexity. The following chapter aims to fill the gap between the simple Kelvin-Voigt model and the more sophisticated strategies, and derives a linear and time invariant model that accurately describes the coupling's transmission characteristics. Additionally, the model is physically meaningful, has a simple structure, and is thus ideally suited for controller design.

In the following, Section 4.1 discusses the working principles of hydraulic couplings, followed by Section 4.2, where a case study shows some of the shortcomings of the Kelvin-Voigt model. Section 4.3 presents the new modelling approach, and Section 4.4 evaluates the proposed model in time and frequency domain. In a slightly modified version, the contents and ideas of the following sections are also contained in [81].

[1] Interpreting a visco-elastic object as *Kelvin-Voigt material* [73] assumes the object to behave like a conventional shaft connection, as used throughout Chapters 2 and 3. This means that the difference in position and speed between its two ends is mapped onto the transmitted torque by the means of a stiffness and damping factor, i.e., $T = k\Delta\varphi + c\Delta\omega$.

Figure 4.1: Structure of the considered coupling, taken from [82].

4.1 The hydrodynamic coupling

As described in [82], a hydrodynamic coupling can be characterized *as a torsionally elastic, high damping steel spring coupling* that typically is a significant aid to *dampen torsional vibrations and to move natural frequencies out of the operating range*. The internal structure, as illustrated in Fig. 4.1 and Fig. 4.2, consists of two main elements: *spring packs* and *intermediate pieces*. The spring packs are clamped at the outer member and fitted into groves on the inner member. Together they form numerous chambers that are filled with oil. In case of a relative movement between the inner and the outer member, a part of the oil is pushed through the gaps underneath the intermediate pieces, and so dampens the movement. An accurate dynamic model thus has to take the oil and its impact on the transmitted torque into account. Unfortunately, data sheets in general do not provide information in that regard. Instead, specifications of the stationary transfer characteristics are usually given, i.e., the mapping from differential angular speed between the inner and outer member $\Delta\omega(t) = \omega_I(t) - \omega_{II}(t)$ onto the coupling torque $T(t)$ in steady state [82]. To that end many suppliers introduce a so called *dynamic stiffness* $c(\nu)$ and a *dynamic damping* $d(\nu)$. Both parameters depend on the excitation frequency ν and relate $\Delta\omega(t)$ and the torsional angle $\Delta\varphi(t)$ with $T(t)$ as if the coupling was a conventional shaft, i.e.

$$T(t) = k(\nu) \cdot \Delta\varphi(t) + c(\nu) \cdot \Delta\omega(t). \tag{4.1}$$

Fig. 4.3 shows the corresponding curves for k and c as a function of ν. They are taken from the datasheet [82, p. 42] for the specific coupling number *41/10/125U* (without pressurized oil supply) considered here. Note that relation (4.1) is only valid for *stationary* sinusoidal signals with a constant frequency ν; it is therefore inadequate for modelling or simulating the coupling's *transient* behaviour.

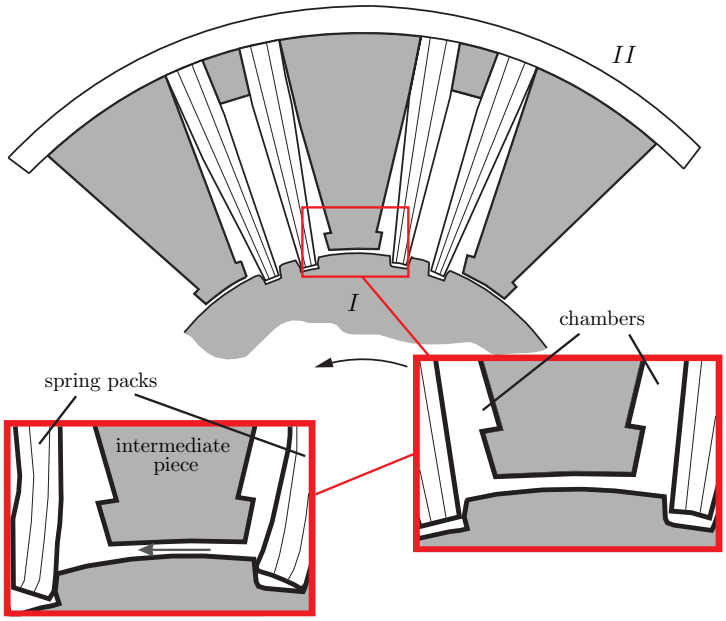

Figure 4.2: Inner structure of the coupling. I and II denote the inner and the outer member, respectively. The left frame present the zoomed section under load.

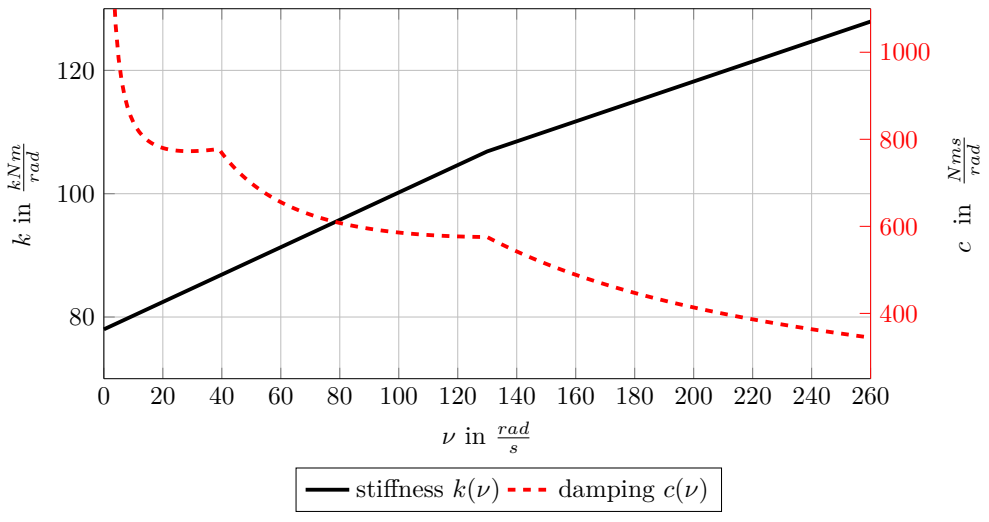

Figure 4.3: Data sheet curves of the considered coupling.

4.2 Case study

Test beds for internal combustion engines are an important area of application for hydrodynamic couplings. Overcoming harmful torque pulses during transient tests while preserving the agility of the powertrain demands just the right amount of damping. Since speed and torque control can constitute challenging tasks in this context, a sufficiently accurate model of the given setup for simulation and design purposes is often needed.

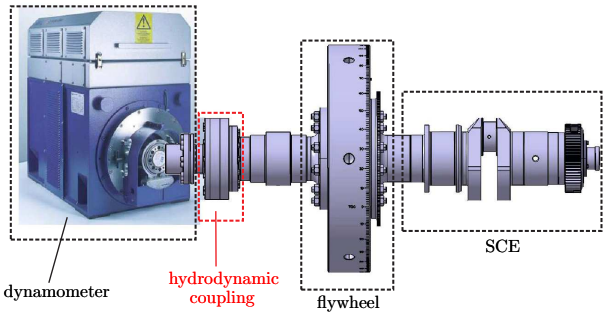

Figure 4.4: SCE test bed, mechanical structure.

The mechanical structure of the considered test bed[2] is depicted in Fig. 4.4. The device under test is a single-cylinder 4-stroke combustion engine (SCE) that is part of a 20 cylinder gas generator with 9.5MW electrical power. To reduce cost and complexity, the remaining 19 cylinders are simulated and connected to the SCE via a hardware-in-the-loop (HiL) platform, see [83]. The powertrain consists of four essential subsystems: the SCE, the flywheel, the dynamometer and the hydrodynamic coupling described previously. The structure of the derived model is shown in Fig. 4.5. The dynamometer is modelled by the soft rotor approach, implemented as a 100-mass oscillator as discussed in Sec. 2.3, with overall inertia I_1, stiffness k_1 and damping c_1. The SCE is interpreted as a two mass oscillator, with inertias I_5 and I_6. The flywheel[3], the inner, and the outer member of the hydrodynamic coupling are represented by the lumped inertias I_3, I_4 and I_5, respectively. All inertias except for the inner and outer member of the coupling are connected by torsional springs with stiffness and damping factors k_i and c_i, respectively. The setup's parameters are listed in Tab. 4.1. The powertrain is driven by the dyno torque T_c and the SCE torque T_g. The torque transmitted via k_2 and the angular dyno speed are measured and denoted as T and ω_d, respectively. The modelling of the mechanical setup is straightforward, with exception of the hydrodynamic coupling. For the coupling model, the curves from Fig. 4.3 cannot be used directly, as relation (4.1) is valid only for stationary excitation with sinusoidal signals.

[2]The same test bed is also considered in Part III of this work, where its pneumatic subsystems and a hardware-in-the-loop system are investigated.

[3]The flywheel's inertia with 585kgm^2 is exceptionally large, which is mainly due to a large diameter, i.e. $d = 1150mm$, and the used structural steel *St-52*. The axial expansion, however, is comparably small, i.e. $l = 100mm$, thus the flywheel is interpreted as just one single inertia, despite its large value.

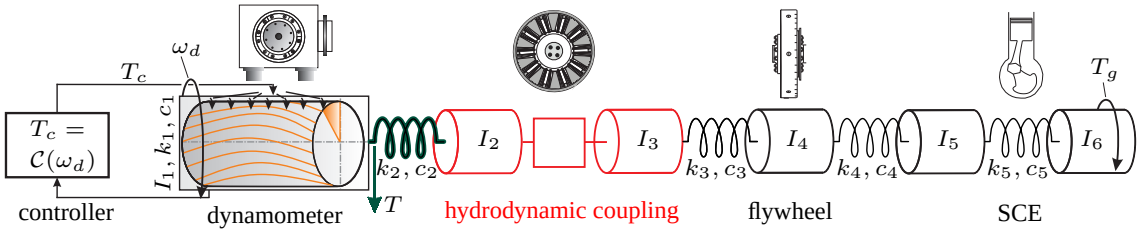

Figure 4.5: SCE Testbed, simulation model

In highly dynamic test bed scenarios this typically is not the case. As mentioned earlier, a model that *is* used widely for hydrodynamic couplings is the so called Kelvin-Voigt model. Its mathematical description in the form of a transfer function reads as

$$G(s) = \frac{T(s)}{\Delta\omega(s)} = k_{KV}\frac{1}{s} + c_{KV}. \tag{4.2}$$

The constants k_{KV} and c_{KV} are picked according to the procedure recommended by Geislinger in [84, pp. 22–24]: First, an approximate value of the natural frequency ν_0 of the coupling operating in the mechanical setup shown in Fig. 4.5 is computed. For this purpose, the coupling is replaced by a spring without damping and with the static stiffness of the coupling, i.e. with stiffness $k(\nu = 0)$ from Fig. 4.3. A state-space model of the resulting mechanical setup is then derived; note that the controller is not included in this model, as it is typically designed after a complete drive train model is available. All mode shapes of this model are computed and scaled such that all have the same absolute sum of angle differences between inertias. The frequency ν_0 is taken as the frequency of the oscillatory mode whose modeshape exhibits the largest difference between the angles of inertias I_3 and I_4. The constant parameters of the coupling's Kelvin-Voigt model are then selected as $k_{KV} = k(\nu_0)$ and $c_{KV} = c(\nu_0)$ using Fig. 4.3. For the present setup, the values $\nu_0 = 73.3\frac{\text{rad}}{\text{s}}$, $k_{KV} = 0.094\frac{\text{MNm}}{\text{rad}}$ and $c_{KV} = 618\frac{\text{Nms}}{\text{rad}}$ are obtained. The model parametrised in this way is applied to simulate the starting procedure of the test bed, a speed ramp from 0 to 1000rpm.

parameter	unit	value	param.	unit	value	param.	unit	value
I_1	kgm^2	14.4	I_2	kgm^2	0.13	I_3	kgm^2	3.15
I_4	kgm^2	585.0	I_5	kgm^2	11.2	I_6	kgm^2	1.5
k_1	MNm/rad	8.0	k_2	MNm/rad	32.6	k_3	MNm/rad	4.1
k_4	MNm/rad	35.0	k_5	MNm/rad	24.1			
c_1	Nms/rad	10	c_2	Nms/rad	10	c_3	Nms/rad	1
c_4	Nms/rad	20	c_5	Nms/rad	17			

Table 4.1: Parameters of the drive train model.

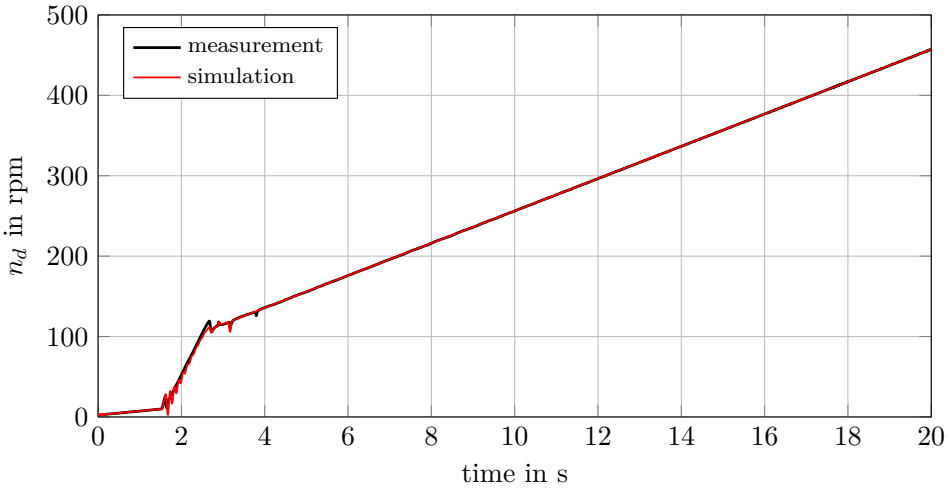

(a) Angular velocity $n_d = \omega_d \frac{30}{\pi}$.

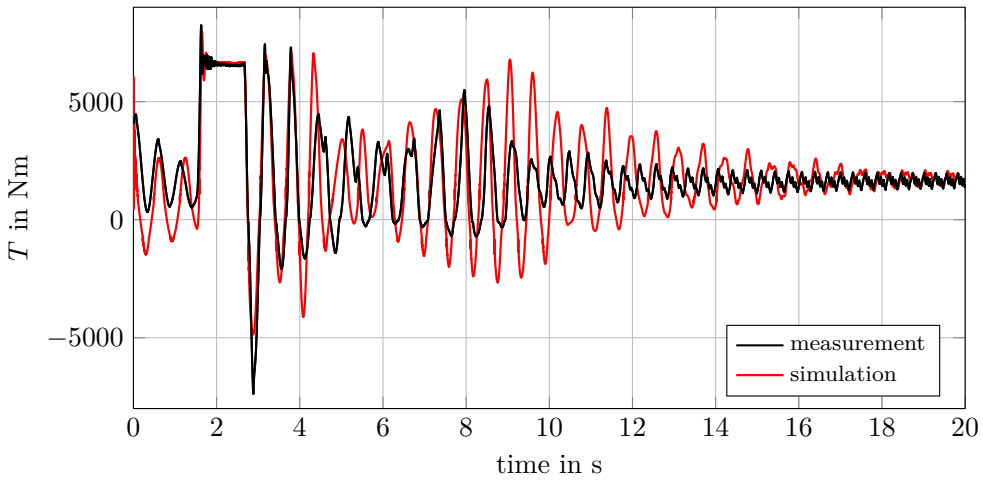

(b) torque T.

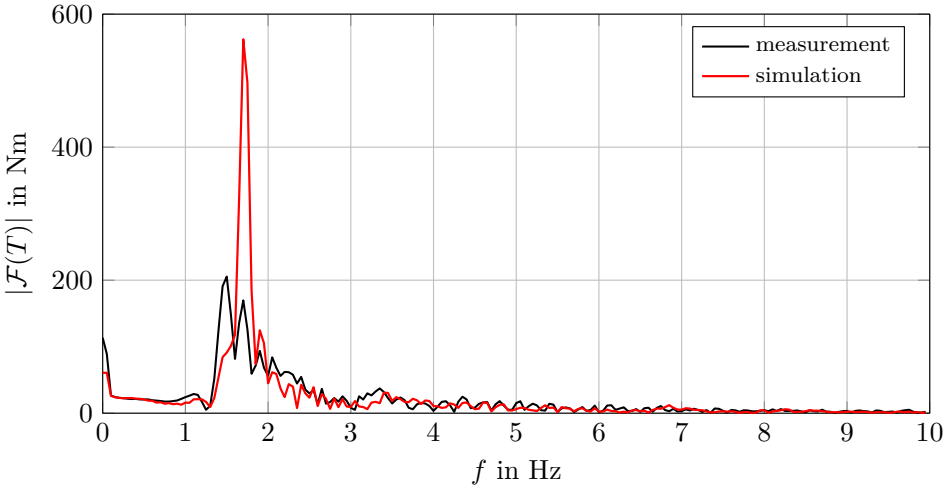

(c) spectral magnitude $|\mathcal{F}(T)|$ of T.

Figure 4.6: Measurement vs. simulation of the test bed start up applying the Kelvin-Voigt model.

Figure 4.6 compares the results to actual test bed measurements. While the simulation reproduces the measured dyno speed with only small deviations, a significant mismatch between measured and simulated torque is visible. This motivates the following derivation of a more accurate, yet still simple model.

4.3 Modelling

This section discusses the derivation of a new model for a hydrodynamic coupling. To that end, Fig. 4.7 provides a detailed sketch of the latter. As the repeating segments are symmetric to rotation, it is sufficient to analyse just one of them and to multiply the corresponding torque by their number.

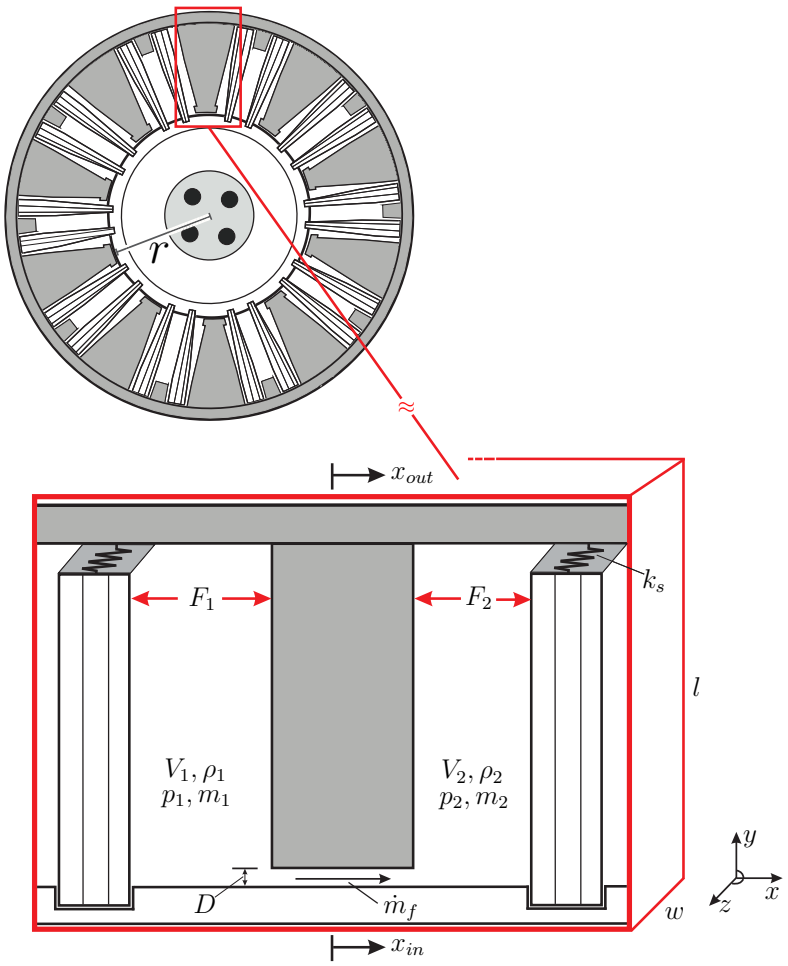

Figure 4.7: The repeating segment of the coupling.

In order to keep the model simple, the spring packs and the intermediate piece inside the considered segment are straightened. V_1 and V_2 denote the volumes of the chambers in the considered segment. The corresponding pressures, densities, masses and forces are denoted by $p_{1,2}$, $\rho_{1,2}$, $m_{1,2}$ and $F_{1,2}$, respectively. The massflow that is exchanged between the chambers is denoted by $\dot{m}_f$. The geometrical quantities x_{in}, x_{out}, D, r, l and w designate the position of the inner and the outer member, the height of the connecting gap, the inner radius and the length and the width of the segment, respectively. The pressure drop between the two chambers is denoted by $\Delta p \coloneqq p_1 - p_2$. The spring packs are assumed to be infinitely stiff, while their actual stiffness k_s and the occurring twist are shifted into a fictitious lumped spring underneath the outer member. In the derivation of the model, the oil movement is taken into account explicitly: First, a relation between the pressure drop inside a segment and its contribution to the coupling torque is derived. Next, the dynamical behaviour of the pressure drop is expressed mathematically. Finally, the resulting differential equation and the torque equation are combined to a second order linear and time-invariant state-space model.

4.3.1 Hydraulic torque

For the hydraulic torque T_c, which is contributed by a single segment, the differential $\mathrm{d}T_c = \Delta p \cdot w \cdot \mathrm{d}y \cdot (r_i + y)$ has to be integrated along the length l. Multiplying T_c with the number of symmetric segments N gives the overall hydraulic torque T_H, i.e.

$$\begin{aligned} T_H = NT_c &= N \int_r^{r+l} \mathrm{d}T_c \\ &= Nw \left(\frac{l^2}{2} + 2lr \right) \Delta p. \end{aligned} \tag{4.3}$$

Introducing $k_p \coloneqq Nw(\frac{l^2}{2} + 2lr)$ yields

$$T_H = k_p \cdot \Delta p. \tag{4.4}$$

4.3.2 Oil dynamics

Wave propagation phenomena are neglected as all occurring wavelengths are large compared to the coupling's dimensions. Additionally, by assuming a constant oil temperature, the set of fundamental equations for the oil is reduced to the continuity equation of mass. It states that the rate of change of the oil mass m is equal to the massflow $\dot{m}_f$ underneath the intermediate piece times the respective sign, i.e.

$$\frac{\mathrm{d}}{\mathrm{d}t} m = \mp \dot{m}_f. \tag{4.5}$$

To simplify notation the indices are dropped. The minus and plus sign indicate the left and right chamber, respectively. To connect (4.5) with Δp, the mass m is expressed in terms of density ρ and chamber volume V

$$\frac{\mathrm{d}m}{\mathrm{d}t} = \frac{\mathrm{d}}{\mathrm{d}t}(\rho V) = V\frac{\mathrm{d}\rho}{\mathrm{d}t} + \rho\frac{\mathrm{d}V}{\mathrm{d}t} = \mp\dot{m}_f. \tag{4.6}$$

A division by V leads to

$$\frac{\mathrm{d}}{\mathrm{d}t}\rho = \mp\frac{1}{V}\dot{m}_f - \rho\frac{\frac{\mathrm{d}}{\mathrm{d}t}V}{V}. \tag{4.7}$$

Commonly, see e.g. [85] or [86], the relation between density ρ and pressure p in the case of isothermal processes is approximated by

$$\rho = \rho_0 + \frac{\rho_0}{\beta}(p - p_0), \tag{4.8}$$

where the constant parameters β, ρ_0 and p_0 are the bulk modulus, the initial density and the initial pressure, respectively. The time derivative of (4.8)

$$\frac{\mathrm{d}}{\mathrm{d}t}\rho = \frac{\rho_0}{\beta}\frac{\mathrm{d}}{\mathrm{d}t}p \tag{4.9}$$

together with (4.7) yields

$$\frac{\mathrm{d}}{\mathrm{d}t}p = \mp\frac{\beta}{V\rho_0}\dot{m}_f - \beta\frac{\rho}{\rho_0}\frac{\frac{\mathrm{d}}{\mathrm{d}t}V}{V}. \tag{4.10}$$

As hydraulic oil is almost incompressible, the corresponding bulk modulus is very high. For a hydraulic coupling $\beta \approx 3.5 \cdot 10^4 bar$ and $(p - p_0) < 10 bar$ will hold, suggesting the approximation

$$\frac{\rho}{\rho_0} = 1 + \frac{1}{\beta}(p - p_0) \approx 1. \tag{4.11}$$

Equations (4.10) and (4.11) can now be combined to a differential equation for the pressure drop

$$\begin{aligned}\frac{\mathrm{d}}{\mathrm{d}t}\Delta p \;=\; & -\beta\left(\frac{1}{V_1} + \frac{1}{V_2}\right)\frac{1}{\rho_0}\dot{m}_f \\ & -\beta\left(\frac{\frac{d}{dt}V_1}{V_1} - \frac{\frac{d}{dt}V_2}{V_2}\right).\end{aligned} \tag{4.12}$$

4.3.3 Volumetric flow

For the majority of hydrodynamic couplings, the Reynolds number *Re* typically is bounded by[4]

$$Re \leq 400. \tag{4.13}$$

As this upper bound is far from the critical value 2000, the massflow $\dot{m}_f$ will be laminar. According to [87], it can thus be expressed by means of the Hagen-Poiseuille law, i.e.

$$\dot{m}_f = \rho_0 Q = \rho_0 \kappa_{\mathrm{HP}} \Delta p \tag{4.14}$$

where Q is the volumetric flow rate and κ_{HP} is a constant that depends on the geometry of the pipe and the viscosity of the oil. Combining Eqs. (4.14) and (4.12) gives

$$\frac{\mathrm{d}}{\mathrm{d}t}\Delta p = -\beta\left(\frac{1}{V_1}+\frac{1}{V_2}\right)\kappa_{HP}\Delta p - \beta\left(\frac{\frac{\mathrm{d}}{\mathrm{d}t}V_1}{V_1} - \frac{\frac{\mathrm{d}}{\mathrm{d}t}V_2}{V_2}\right). \tag{4.15}$$

4.3.4 Chamber volume

The chamber volumes in the stretched segment in Fig. 4.7 can be expressed as

$$V = V_0 \mp A\Delta x \tag{4.16}$$

where V_0, $A = w \cdot l$ and $\Delta x = x_{in} - x_{out}$ denote the initial volume, the area of the sideface and the difference between inner and outer position, respectively. As $\Delta x \ll \frac{V_0}{A}$ holds in the entire operating range,

$$\frac{1}{V_1}+\frac{1}{V_2} = \frac{2V_0}{V_0^2 - A^2\Delta x^2} \approx \frac{2}{V_0}. \tag{4.17}$$

The time derivative of Δx can be approximated by the means of $\Delta\omega$, i.e. $\frac{d}{dt}\Delta x \approx (r + \frac{l}{2})\Delta\omega$. Furthermore, exploiting the symmetry of the segment, i.e.

$$\frac{\mathrm{d}}{\mathrm{d}t}V_1 = -A\left(r+\frac{l}{2}\right)\Delta\omega = -\frac{\mathrm{d}}{\mathrm{d}t}V_2, \tag{4.18}$$

and introducing the constants $\kappa_p := \beta\frac{2}{V_0}k_{\mathrm{HP}}$ and $\kappa_\omega := \beta\frac{2}{V_0}A(r+\frac{l}{2})$, leads to

$$\frac{\mathrm{d}}{\mathrm{d}t}\Delta p = -\kappa_p\Delta p + \kappa_\omega\Delta\omega. \tag{4.19}$$

[4]The gap underneath the intermediate piece forms a fully filled rectangular duct with the hydraulic diameter $D_H = \frac{2Dw}{w+D}$. Generally $D \approx 0.001m$ and $D \ll w$, yielding $D_H \approx 2D = 0.002m$. For the flow velocity $v \leq 10\frac{m}{s}$ and the viscosity of the oil $\sigma \approx 50 \cdot 10^{-6}\frac{m^2}{s}$ will hold. Thus, $Re = \frac{vD_H}{\sigma} \leq 400$.

4.3.5 State space model

The overall model can now be expressed as a linear time invariant ("LTI") state space model with states Δp and $\Delta\theta$. For the output equation, the torsional torque contributed by the lumped spring k_s is added to (4.4), which finally results in

$$\frac{\mathrm{d}}{\mathrm{d}t}\begin{bmatrix}\Delta\varphi\\ \Delta p\end{bmatrix} = \begin{bmatrix}0 & 0\\ 0 & -\kappa_p\end{bmatrix}\begin{bmatrix}\Delta\varphi\\ \Delta p\end{bmatrix} + \begin{bmatrix}1\\ \kappa_\omega\end{bmatrix}\Delta\omega, \qquad T = k_s\Delta\varphi + k_p\Delta p. \tag{4.20}$$

4.4 Results

To asses the quality of the obtained model, it is evaluated in terms of its frequency characteristics and validated using the experiment presented in Section 4.2. Its parameters are calculated from the coupling's geometry and the viscosity of the oil, see Tab. 4.2.

k_s	k_p	κ_p	κ_ω
0.078 $^{\mathrm{MNm}}/_{\mathrm{rad}}$	0.07 m^3	190 $^{1}/_{\mathrm{s}}$	2.2 $^{\mathrm{MPa}}/_{\mathrm{rad}}$

Table 4.2: Parameters of the proposed model.

4.4.1 Frequency characteristics

Evaluating the transfer function of system (4.20) for $s = j\nu$ yields the frequency response of the model. Splitting the result into its real and imaginary part leads to analytical expressions for both $k(\nu)$ and $c(\nu)$,

$$G(j\nu) = \frac{T(j\nu)}{\Delta\omega(j\nu)} = \underbrace{\frac{\kappa_\omega k_p \kappa_p}{\nu^2 + \kappa_p^2}}_{c(\nu)} + \frac{1}{j\nu}\Bigg[\underbrace{k_s + \frac{\kappa_\omega k_p \nu^2}{\nu^2 + \kappa_p^2}}_{k(\nu)}\Bigg]. \tag{4.21}$$

Fig. 4.8 compares the corresponding curves to the ones given in the data sheet and to those of the Kelvin-Voigt model. It becomes apparent that the new model matches the specifications more accurately. Nonetheless, deviations from the specified stiffness and damping occur at high and low frequencies, respectively. It is, however, questionable whether the infinitely large damping for $\nu = 0$ given in the data sheet is physically meaningful. Such a damping behaviour is commonly associated with the modelling of Coulomb friction, see e.g. [88]. For the considered coupling this type of friction is negligibly small, as almost all friction is caused by the viscous oil movement. Apart from these very low frequencies, the proposed model describes the specified damping highly accurately. Given that the coupling is the main source of damping in the drive train, this is one of its main assets.

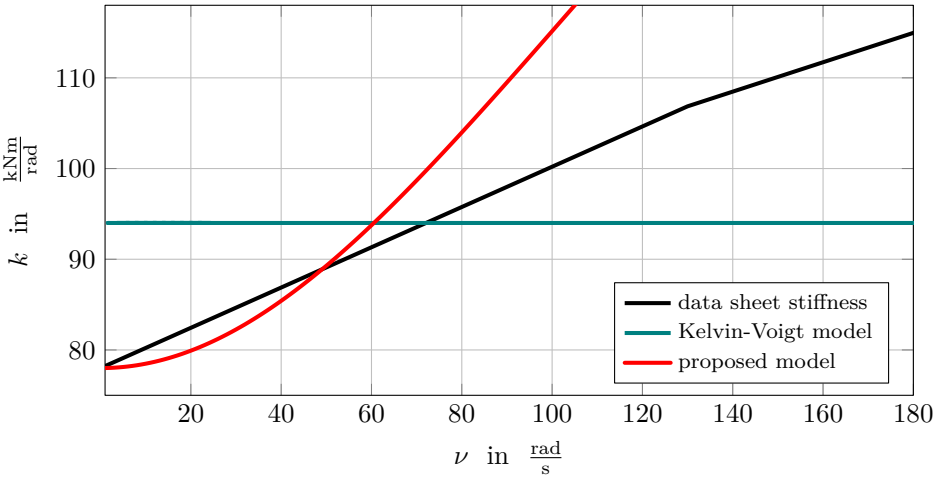

(a) stiffness k

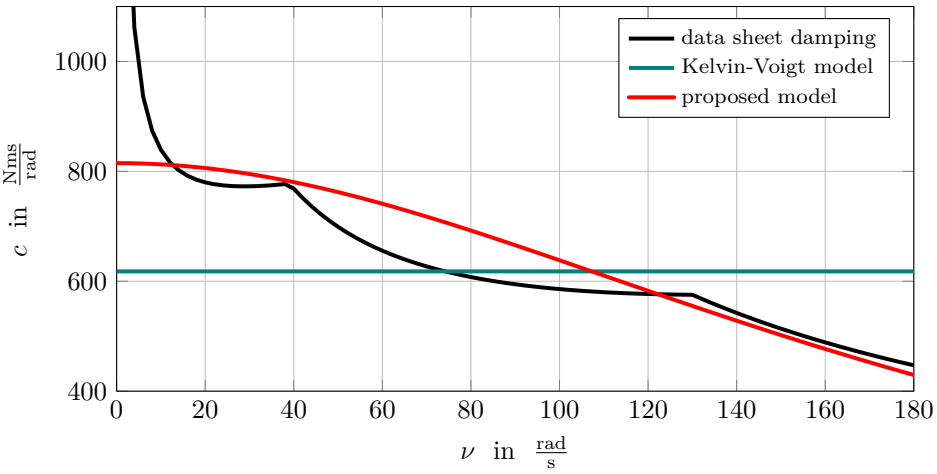

(b) damping c

Figure 4.8: Data sheet vs. frequency characteristics of the models.

4.4.2 Experimental validation

The results of a simulation of the testbed startup discussed in Section 4.2 with the proposed as well as with the Kelvin-Voigt model are visualized in Fig. 4.9. One can see that the proposed model clearly improves the quality of the simulation. The Fourier analysis depicted in Fig. 4.10 shows that both frequency and magnitude of the torque oscillations are reflected more accurately. These oscillations mainly stem from the first torsional resonance of the interconnection of the mechanical setup and the speed controller. Note that due to the influence of the controller this electro-mechanical resonance frequency is significantly lower than that of the mechanical resonance considered for choosing the parameters of the Kelvin-Voigt model. *For the considered experiment* one could thus improve the results

obtained with the Kelvin-Voigt model by choosing its parameters differently; this would essentially make the parameters of the model depend on the controller's parameters and structure, however, preventing the use of the Kelvin-Voigt model for controller design. Additionally, the model quality would deteriorate *for other experiments* in which different frequencies are excited (e.g. when the SCE is at idle speed). The proposed model avoids these problems by reflecting a key feature of a hydrodynamic coupling: the adaptation of its transfer characteristics to the given excitation frequencies shown above.

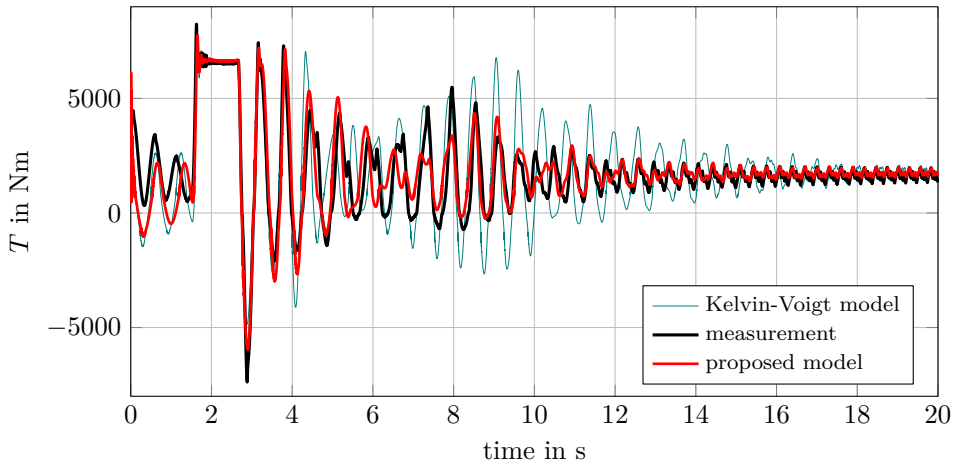

Figure 4.9: Comparison of measured and simulated torque T during the test bed start up.

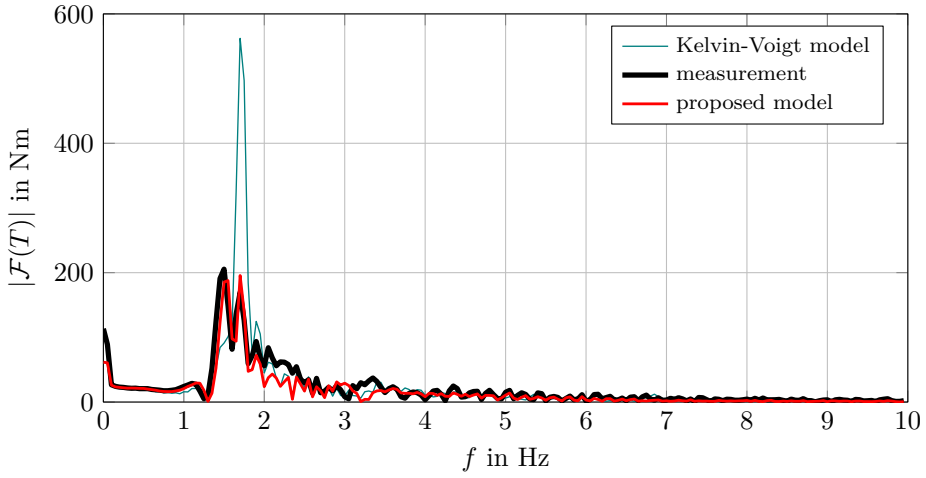

Figure 4.10: Comparison of measured and simulated torque FFT during the test bed start up.

4.5 Conclusion

The preceding section presents a new modelling approach for a hydrodynamic coupling, in which the behaviour of the oil is taken into account explicitly. In an experimental validation the resulting model is shown to be much more accurate than the widely used Kelvin-Voigt model. While more detailed and involved approaches may provide even better simulation results, the remarkable trade-off between simplicity and accuracy of the proposed model makes it attractive when it comes to controller design. Furthermore, the fact that all the involved parameters can be computed directly from data-sheet specifications without the need for additional optimization completes a package that can be a useful tool for controller design.

Part II

Control of Mechanical Components

Chapter 5

Adaptive Resonance Suppression

The following chapter deals with the control problem that originally laid the foundation for this thesis: *The suppression of torque oscillations in automotive test bed drive lines*. To that end, Section 5.1 at first discusses the phenomenon of torque oscillations, aiming at a concise and clear description of their root causes. Based on this stocktaking, Section 5.2 introduces an extension of the control loop presented in Fig. 5.1, in order to overcome undesired torque oscillations like the one depicted. Subsequently, Section 5.3 reviews several approaches that are found in current literature and address the question of how the proposed structure should be operated. The benefits and drawbacks of the published methods are highlighted, and it will be shown that the existing attempts suffer from several shortcomings in the given setting. Hence, Sections 5.4 and 5.5 outline a new concept, whose capability to successfully mitigate undesired oscillations was proven in a series of experiments on the R2R test bed that is also considered in Part I of this work. Section 5.6 presents some of the obtained results.

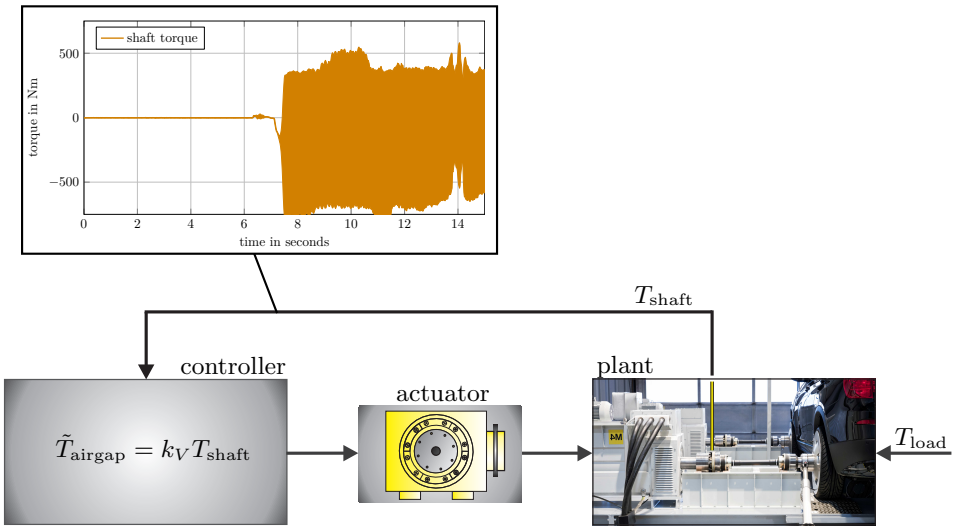

Figure 5.1: Undesired torque oscillation and reduced control loop considered for analysis.

5.1 Torque oscillations

To discuss the issue of torque oscillations with regards to the test beds considered in this chapter, the controller depicted in Fig. 5.1 is reduced to the direct path that feeds through the measured shaft torque, i.e., $\tilde{T}_{\text{airgap}} = k_V T_{\text{shaft}}$. This simplification corresponds to the situation described in [89], and is more than just a methodological short-cut: As discussed in the introduction to Part I, the gain k_V needs to adhere to several critical inequalities, such as (2.6), in order to ensure BIBO-stability, and also from a practical point of view, the path comprising k_V often turns out to be the decisive part of the controller.

Regarding the matter of torque oscillations, it is well known that the combination of an open-loop gain above 0dB and a phase-shift of $-180°$ at the same frequency can lead to growing oscillations[1], and stressing again the practical point of view, experience shows that the resonances of the plant often are the main reason for these conditions to be met simultaneously. To discuss those connections in more detail, Figs. 5.2 and 5.3 present several exemplary magnitude and phase responses, which were obtained by simulations using the soft-rotor model of the R2R test bed from Section 2.3.4.

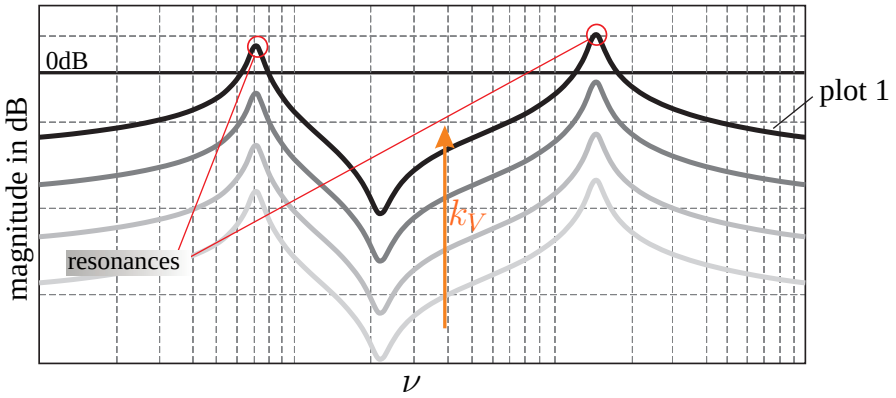

Figure 5.2: Open loop magnitude responses of the system shown in Fig. 5.1, for different gains k_V.

A trivial but important insight that may be deduced from the magnitude responses shown in Fig. 5.2 is that they are shifted up and down the y-axis for different values of k_V. If k_V becomes large, the 0dB line may be crossed – firstly in the area of the resonances of the plant. To analyse also the aspect of phase responses, Fig. 5.3 presents three plots, where a series of marks is assigned to each of the graphs in order to represent the sequence of poles ("×") and zeros ("∘") that is contained in the transfer function of the associated system.

[1] Finding rigorous conditions for feedback oscillations can be a complicated task [90–93]. Hence, only this application-oriented argument is given here. However, if the open loop $L(s)$ is BIBO-stable, has positive gain and $|L(j\nu)| \to 0$ as $\nu \to \infty$, if there exist frequencies ν_i where $|L(j\nu_i)| > 1$ and $\angle L(j\nu_i) = \pi$, and if $\frac{\mathrm{d}}{\mathrm{d}\nu}\angle L(j\nu) < 0 \;\forall\; \nu_i$, i.e., that the derivative of the phase with respect to ν is negative at every ν_i, the closed loop in fact is not BIBO-stable. This seems to be always the case for the considered drive lines if they fulfil both the >0dB and the $-180°$ condition at at least one frequency. [41] offers an instructive discussion of these topics, and also analyses the derivative $\frac{\mathrm{d}}{\mathrm{d}\nu}\angle L(j\nu)$ at the intersection points with the negative real axis.

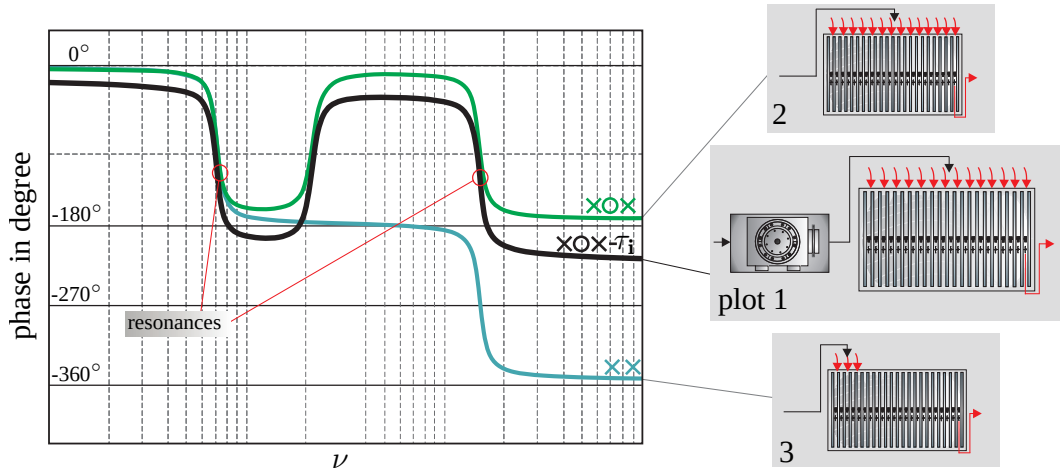

Figure 5.3: Typical open loop phase responses.

In Fig. 5.3, plot number 1 corresponds to plot number 1 in Fig. 5.2, and incorporates the dynamics of the actuator by representing it with a first-order lag-element. Plot 2 displays the phase response of *only* the mechanical system behind plot 1, hence neglecting the influence of the actuator. To obtain plot 3, again only the mechanical part of the open loop was simulated; this time, however, the acting airgap torque was connected to only the first left quarter of the rotor model, which modifies the path from input to output such that the transfer zero is shifted out of the range between the first and the second resonance.

The plots demonstrate that conjugate-complex pole pairs asymptotically subtract 180° from the resulting phase response, while conjugate-complex zeros add 180°. Since these values are obtained only for $\nu \to \infty$, one may draw the conclusion that a mechanical system, where each resonance is followed by a zero[2] *by itself* can never reach a phase shift of -180° for a finite frequency. Things are different for plot 3. Here the two resonances do *not* encapsulate a transfer zero, which allows the phase to cross the -180° line, due to the mechanical system alone. The practically relevant case is depicted by plot 1 of Fig. 5.3, however, where the effect of the actuator, which is present in any real application, is included. This graph allows to deduce the following observations, and lays the ground for the following steps:

- Frequencies in the area of the first resonance are capable of fulfilling the oscillation conditions of an open-loop-gain above 0dB and a phase-shift of $-180°$ only if additional actuator dynamics is present.
- Large values of k_V can lead to the crossing of the 0dB line in the open-loop magnitude response, which may result in undesired oscillations.
- If an actuator is present, all the resonances of the plant bear the potential of creating a torque oscillation – in case k_V is chosen large enough.

[2]Input and output of such systems are often termed *collocated*. An example thereof is a lumped structure, where the input acts on the member whose speed or position is also the system's output [41].

5.2 Notch filters

The previous section laid out that high-gain settings for k_V can cause undesired oscillations, particularly in combination with parasitic actuator dynamics. To achieve fast dynamics in the presence of disturbances, however, high gains are often needed, which calls for an extension of the control system displayed in Fig. 5.1. To elaborate the details of this extension, one may recall that the resonance frequencies are the first frequencies to cross the 0dB line for large values of k_V. For this reason, an often seen remedy against undesired oscillations is the introduction of *notch filters* into the system, in order to compensate for the magnitude increase caused by the resonances. This measure is also chosen in this work.

Out of the many options to describe a notch filter mathematically, the z-transfer function

$$H(z) := \frac{y(z)}{u(z)} = K\frac{1 - 2\cos(\nu_0)z^{-1} + z^{-2}}{1 - 2r\cos(\nu_0)z^{-1} + r^2 z^{-2}} \tag{5.1}$$

is used in this thesis. Therein, $\nu_0 \in [0, \pi]$ denotes the discrete time notch frequency, which may be derived from a continuous time frequency ν_{cont} and the discretization time T_d via $\nu_0 = \nu_{cont} T_d$. Furthermore, r stands for the pole radius that shapes the width of the ampli-

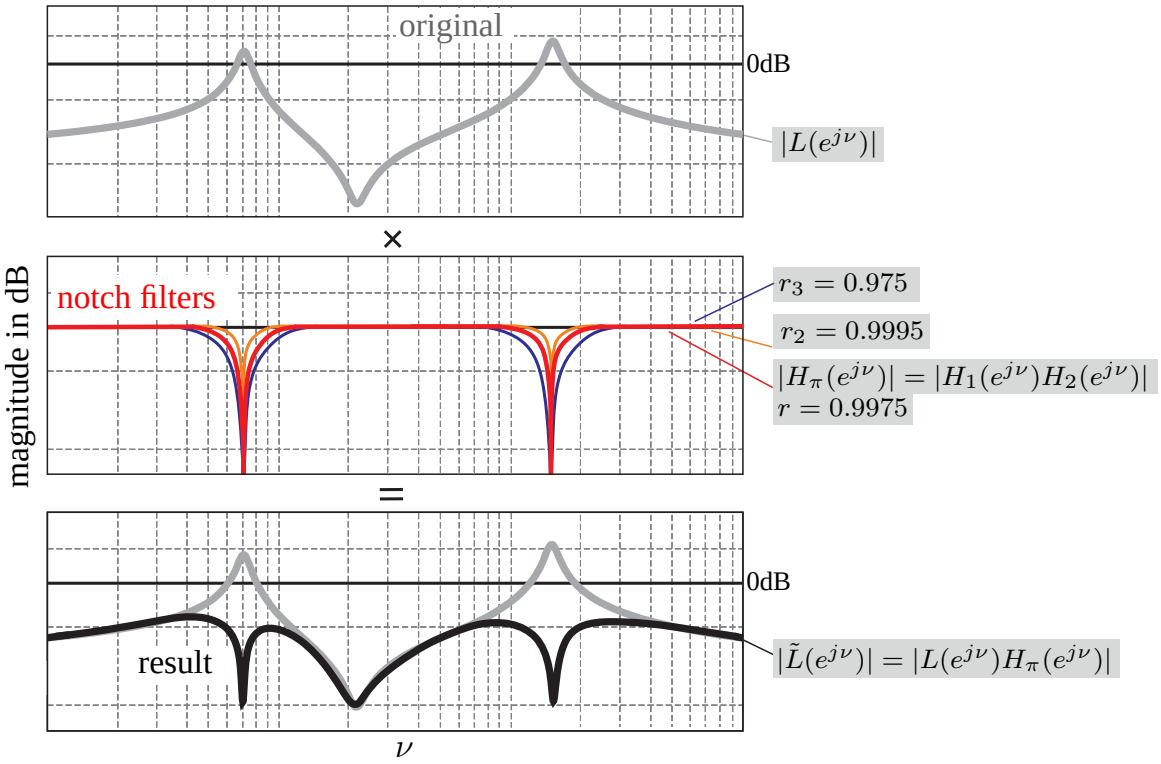

Figure 5.4: Effect of two notch filters (in red), denoted by $H_\pi(z) = H_1(z)H_2(z)$, on the discretized open loop from Fig. 5.1, which is denoted by $L(z)$ and contains the induction machine and its rotor. Two alternative filter versions with pole radii r_2 and r_3 are shown, too.

tude notch, and K is a scaling factor to adjust the filter gain to 0 dB at $\nu = 0\,\frac{\text{rad}}{\text{s}}$. A discussion of this particular representation is provided in Appendix D. Clearly, one notch filter can suppress only one resonance; hence n notch filters with appropriate notch frequencies $\nu_{0,1}, \nu_{0,2}, \ldots, \nu_{0,n}$ must be put in series to suppress n resonances, yielding $H_\pi(z) = H_1(z)H_2(z)\ldots H_n(z)$. The desired filter-effect is depicted in Fig. 5.4, where the discretized open loop from Fig. 5.1, which is denoted by $L(z)$ and contains the induction machine and its rotor, is multiplied with two filters $H_1(z)$ and $H_2(z)$. The magnitude response now is far from the 0 dB line throughout the considered frequency range, and previously problematic frequencies do not pose a problem any more. Unfortunately, this modification of the magnitude response is accompanied by an additional phase shift, as shown in Fig. 5.5. As any additional phase shift may severely deteriorate the dynamical properties of the control loop, it is usually desired to keep r close to 1, knowing that a bigger pole radius decreases the width of the amplitude notch and thus reduces the robustness of the system.

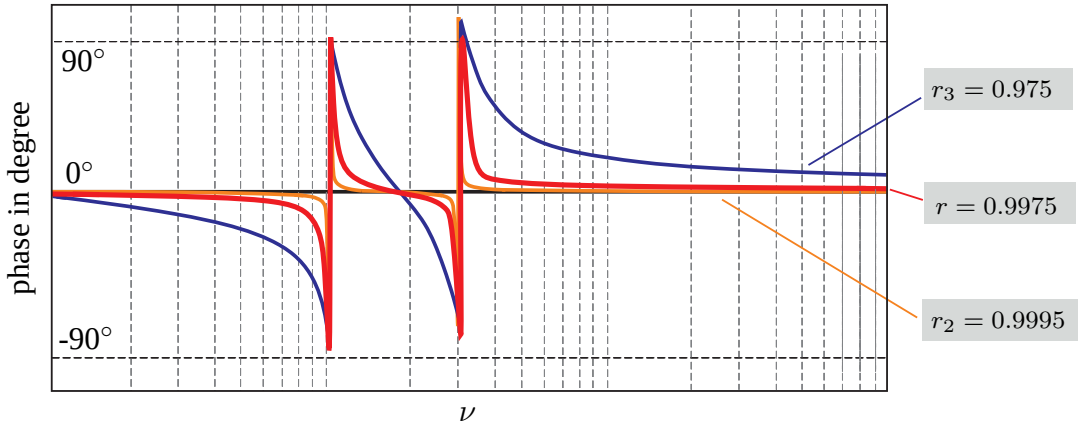

Figure 5.5: Phase response of three pairs of notch filters with different pole radii r_i.

The parametrization of the notch filters necessitates precise knowledge about the plant's resonances. Detecting them a priori, e.g., by the means of chirp experiments during the commissioning of a test bed may often not be feasible due to organisational constraints, however. Moreover, the resonances may vary over time, due to wear, temperature influx, or simply a change of the device-under-test. Thus, implementing the filters as adaptive systems, which are capable of finding the notch frequencies on their own *and* of reacting to potential changes of the plant, is highly desirable. The outcome of this consideration is presented exemplarily in Fig. 5.6, where two *adaptive* notch filters are comprised in the torque feedback path.

In the following, the question of how the adaptation should be performed is discussed, starting with an overview of approaches that are found in literature. The main ideas of the present section are summarized below, extended by two clarifying restrictions in order to prepare the next steps:

- Properly parametrized notch filters are a well-suited tool to avoid undesired torque oscillations in test bed drive lines.
- Using an adaptive scheme to find the notch frequencies $\nu_{0,i}$ provides a series of practical advantages.
- The number of notch filters is fixed[a] a priori, and must in any case be higher than the number of relevant resonances, which requires some insight into the system's dynamics.
- The pole radii of the involved filters are not considered for adaptation, and set to the constant[b] value of $r = 0.995$.

[a] Adapting also the number of filters would gravely complicate the implementation of the scheme, and is thus not pursued further.

[b] The main obstacle in this regard is again an increased implementation complexity. Appendix E presents a possible strategy in this direction, which is yet to be evaluated on the test bed.

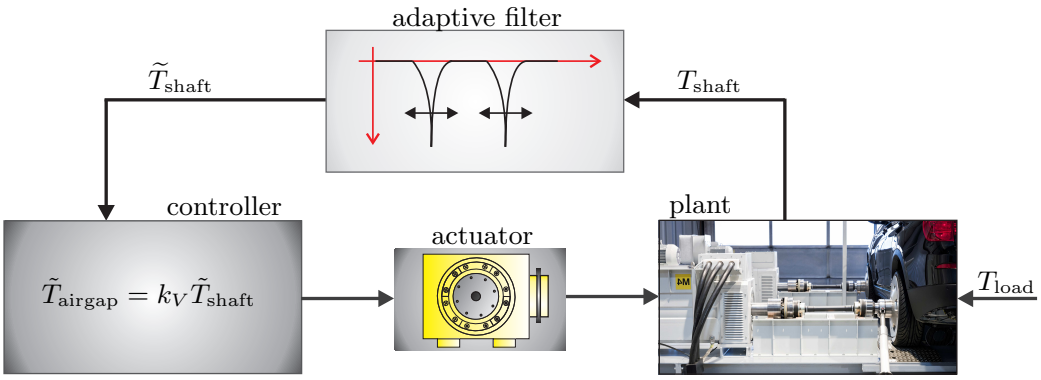

Figure 5.6: Control loop with adaptive notch filter in the torque feedback path. $\tilde{T}_{\text{shaft}}$ denotes the filtered shaft torque.

5.3 Classical adaptive notch filters

This section attempts to give an overview of ideas from the area of adaptive control, which have been applied to the problems of frequency estimation and oscillation suppression. Current literature provides a great number of contributions that deal with adapting the notch frequencies of a series of notch filters, whereof especially [94–116] were considered in this work.

A central and particularly frequently cited contribution is [101], where a stripped down version of the transfer function proposed in (5.1) is considered, i.e.

$$\tilde{H}_{\nu_0}(z) := \frac{y(z)}{u(z)} = \frac{1}{2}\left[1 - \frac{e^{j\nu_0} z^{-1} - r}{1 - r e^{j\nu_0} z^{-1}}\right], \tag{5.2}$$

which is capable of suppressing a single complex mode[3] with frequency ν_0. The problem that [101] deals with is the suppression of an input of the form

$$u(n) = Ae^{j(\nu n+\phi)}, \tag{5.3}$$

whose frequency ν is unknown. In order to find ν, the update law

$$\nu_0(n+1) = \nu_0(n) + \mu \cdot \mathrm{Im}[y(n)u^*(n)] \tag{5.4}$$

is suggested, where $u^*(n)$ stands for the complex-conjugate of $u(n)$, the step size μ modifies the speed of the algorithm, and $\mathrm{Im}[y(n)u^*(n)]$ denotes the imaginary part of the scalar product of filter-input and filter-output. One reason to term this section "Classical adaptive notch filters" and to start it particularly with algorithm (5.4) is the right hand side of (5.4): In steady-state,

$$\nu_0(n+1) = \nu_0(n), \qquad \text{and thus} \qquad \mathrm{Im}[y(n)u^*(n)] = 0 \tag{5.5}$$

hold, which implies that the complex signals $u(n)$ and $y(n)$ are orthogonal to each other. Achieving orthogonality between input and output, however, is one of the fundamental concepts in adaptive filtering, see [120, 121], and is at the core of one of the most prominent adaptive algorithms: the Wiener-Hopf filter! Maybe in part for this reason, [101] inspired *many* subsequent publications that also focus on adaptive notch filtering. In [122], for instance, a method to transfer the update rule (5.4) into continuous time is proposed, which results in

$$\dot{\nu}_0 = -\mu \cdot y(u - r\nu_0\dot{y}), \tag{5.6}$$

and allows to apply methods of continuous nonlinear control for analysis, as in [100], where the Krasovskii-LaSalle principle is employed. In (5.6), μ and r are again design parameters, and u and y as before stand for the input and output of the filter, respectively. Various modifications of (5.6) have been published, such as [95], where the, with regards to its convergence properties, improved version

$$\dot{\nu}_0 = -\mu \cdot (|\nu_0 y| - \sqrt{uy}) \tag{5.7}$$

is employed to find a frequency estimate that is subsequently passed on to a notch filter. Generally, many of the published adaptive notch-filtering algorithms rely on assigning a dynamical behaviour to the adapted frequency ν_0 that builds on the product of filter-input and filter-output. The latter is frequently scaled or additionally fed through some static function. An in this regard particularly interesting concept is the one presented in [103], which connects this strategy with two additional aspects: On the one hand, the algorithm uses almost the same filter as explained earlier, i.e.

$$\hat{H}(z) := \frac{y(z)}{u(z)} = \frac{1 - 2\cos(\nu_0)z^{-1} + z^{-2}}{1 - 2rcos(\nu_0)z^{-1} + r^2z^{-2}}, \tag{5.8}$$

[3] Transfer functions with complex-valued coefficients are broadly used in, e.g., signal processing [117, 118], but to some degree also in control engineering [119]. In the present case, the filter $\tilde{H}_{\nu_0}(z)$ would have to be multiplied with a version for the negative frequency $-\nu_0$, i.e. $\tilde{H}_{-\nu_0}(z)$, in order to block a real-valued signal, which reveals an interesting connection to $H(z)$ from (5.1), as $\tilde{H}_{\nu_0}(z)\tilde{H}_{-\nu_0}(z) = \frac{(1+r)^2}{4K}H(z)$.

which equals (5.1) except for the scaling factor K. On the other hand, the algorithm aims to minimize[4] the cost function $\mathcal{J}(n) = \frac{1}{2}y^2(n)$, which may be interpreted as the instantaneous filter output power. To achieve this goal, the output is expressed in time domain, i.e.

$$y(n) = u(n) - 2\cos(\nu_0)u(n-1) + u(n-2) + 2rcos(\nu_0)y(n-1) - r^2y(n-2), \tag{5.9}$$

from which the gradient

$$\begin{aligned}\frac{\mathrm{d}}{\mathrm{d}\nu_0}\mathcal{J}(n) &= y(n)\frac{\mathrm{d}}{\mathrm{d}\nu_0}y(n)\\ &= y(n)\Bigg(2\sin(\nu_0)u(n-1) - 2r\sin(\nu_0)y(n-1)\\ &\qquad + 2rcos(\nu_0)\frac{\mathrm{d}}{\mathrm{d}\nu_0}y(n-1) - r^2\frac{\mathrm{d}}{\mathrm{d}\nu_0}y(n-2)\Bigg)\end{aligned} \tag{5.10}$$

can be computed. Together with the abbreviation

$$\beta(n) \coloneqq \frac{\mathrm{d}}{\mathrm{d}\nu_0}y(n), \tag{5.11}$$

this leads to the update law

$$\nu_0(n+1) = \nu_0(n) - 2\mu y(n)\beta(n), \tag{5.12}$$

which minimizes the instantaneous output power $\mathcal{J}(n)$. Update rules of this kind are often referred to as least-mean-squares or "LMS"-algorithms. If $u(n)$ contains one significant oscillation with frequency ν, the notch frequency will – given the algorithm is stable, for details in this regard see [103] – converge to the latter, as suppressing the main frequency component of the input leads to the most significant reduction in output power. As suggested in [103], a cascaded higher order version of (5.8) can simply be obtained by stacking several filters in series. Since algorithm (5.12) incorporates the same basic idea as many other algorithms, employs the z-transfer function that is also considered in this work, and may easily be extended to suppress more than one resonance, particularly this approach was employed for a series of simulation studies.

5.3.1 Simulation study

As an adequate representative of the discussed algorithms, the scheme proposed in [103] was employed exhaustively for simulations. The used plant model is a replica of the setup presented in Fig. 2.2, extended by a cascade of two adaptive notch filters in the torque feedback path, like Fig. 5.6. The filters were put in series, i.e. $H_\pi(z) = \hat{H}_1(z)\hat{H}_2(z)$, and their

[4] An instructive explanation that optimality and orthogonality as in (5.5) are very frequently two sides of the same coin can be found in [120].

notch frequencies $\nu_{0,1}$ and $\nu_{0,2}$ were adapted according to (5.12). As mentioned earlier, the number of relevant resonances must be estimated in advance, to prepare a sufficient number of filters. As the soft rotor model for the R2R test bed described in 2.3.4, which was treated exhaustively in Part I of this work, was used to represent the plant in simulation, it was known that especially the first two resonances would be relevant. The electrical part of the induction machine was simulated by a fundamental wave model, governed by the full field-oriented-control scheme that is also used on the test bed. The parameters used in simulation were exactly those that are also active in reality. Of the parameters that are crucial for the present discussion, the torque-feedback gain was set to $k_V = 9.7$, and the notch frequencies were initialized at $\nu_{0,1}(0) = \nu_{0,2}(0) = 2\pi 1500 T_d$, which is far out of the relevant frequency range. Besides that, both pole radii were set to $r = 0.995$, and $\mu = 5 \cdot 10^{-10}$ was used as a step size. The experiment selected for discussion comprised the following scenario: The gain k_V is parametrized such that the first two resonances without counter-measure create a growing oscillation. This happens right after the test is started, where the notch frequencies are still equal to their initial values. During that time, the load torque is set to zero, i.e. $T_{\text{load}} = 0\,\text{Nm}$. After a second, the latter is changed to $T_{\text{load}} = 65 - 400\sin(2\pi 225 t) + 300\sin(2\pi 450 t)\,\text{Nm}$, a combination of a small DC-component and two harmonics, which roughly describes a torque profile that might also be produced by a combustion engine. The resulting torques and notch frequencies are presented in Figs. 5.7 and 5.8, respectively.

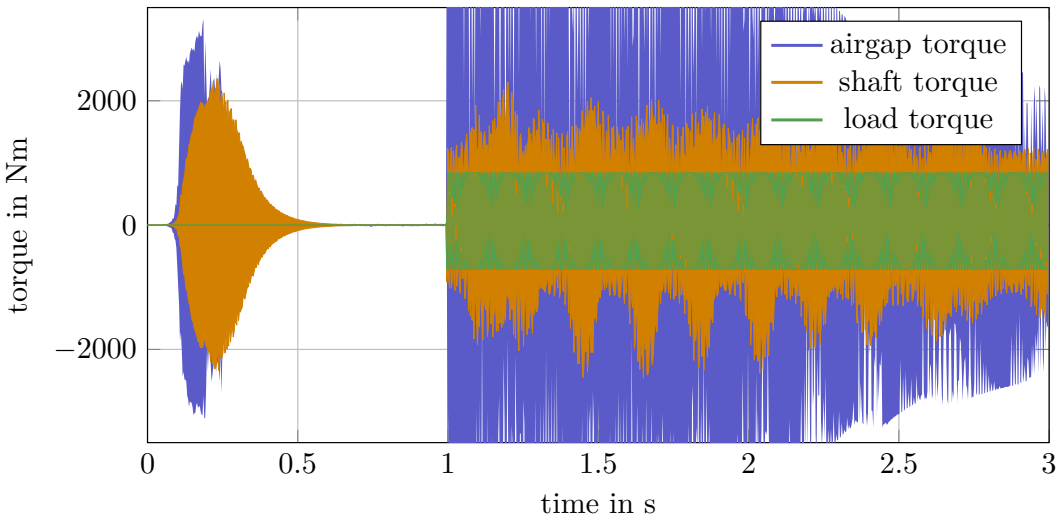

Figure 5.7: Simulated shaft, airgap and load torque obtained by applying the adaptive notch filter proposed in [103] to the simulation model of the R2R test bed.

One can see that the algorithm at first does its job properly, by finding and suppressing the correct resonances of the plant. However, as soon as the undesired oscillations have vanished and the external load torque starts to act, the dynamical behaviour of the notch

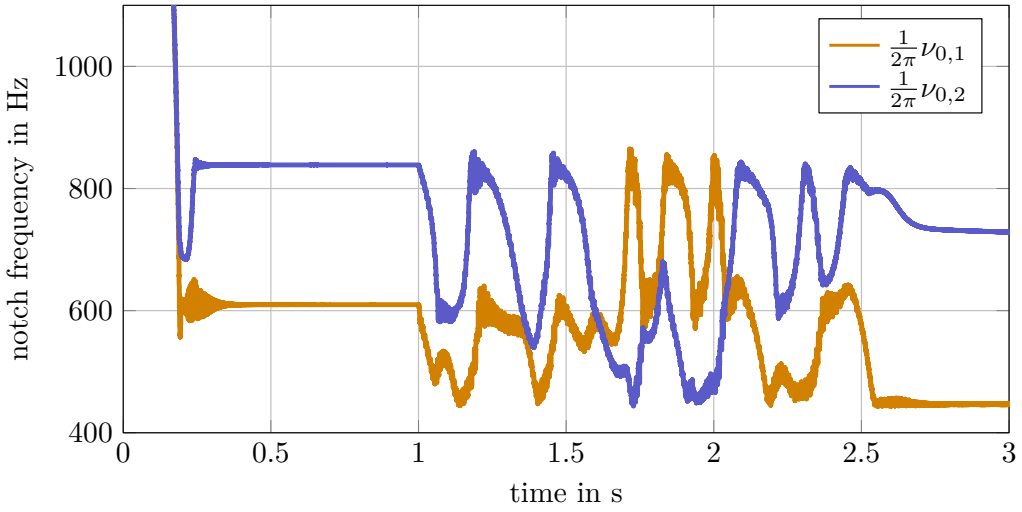

Figure 5.8: Notch frequencies $\nu_{0,1}$ and $\nu_{0,2}$, scaled by $\frac{1}{2\pi}$ to allow for a representation in Hz.

frequencies becomes "confused" and chaotic. Such situations are not unlikely, as e.g. the prompt start up of the device-under-test may result in similar load torques. Generally, an adaptive filter should be *immune* to external disturbances, which points to a significant drawback of the algorithms discussed so far: As soon as the initially intended job is done, there is no incentive for the filter to stay where it has settled. Moreover, if a frequency does not carry energy any more, an algorithm of type (5.8) might just look for the next frequency to further minimize $\mathcal{J}(n)$, which carries the potential for unpredictable limit cycles: If the filter leaves an originally correctly suppressed frequency, the latter might create a growing oscillation again, which may lead to a cycle of suppressing and un-suppressing. To solve this dilemma, a possible strategy for the setup presented in Fig. 5.6 is to make sure that the adaptive algorithm solely reacts to oscillations that are linked to resonances of the closed control loop. Unfortunately, none of the discussed attempts addresses this problem, and moreover, the discussed approaches also do not provide a basis that would allow an investigation of the origin of the frequency components that make up T_{shaft}. To put the arguments in a nutshell, one may state that

- The established approaches work well in an *undisturbed* environment.
- In the presence of external disturbances, the filter *must* assess the origin of a given oscillation, in order to decide whether it should react or not.
- The attempts found in current literature do not address this problem.

The second point of the summary motivates the modified block diagram presented in Fig. 5.9, where frequency estimation and filter parametrization are separated, to allow for

an intermediate check on the root cause of the oscillation. In the following, the questions of frequency estimation and filter activation are discussed consecutively in detail.

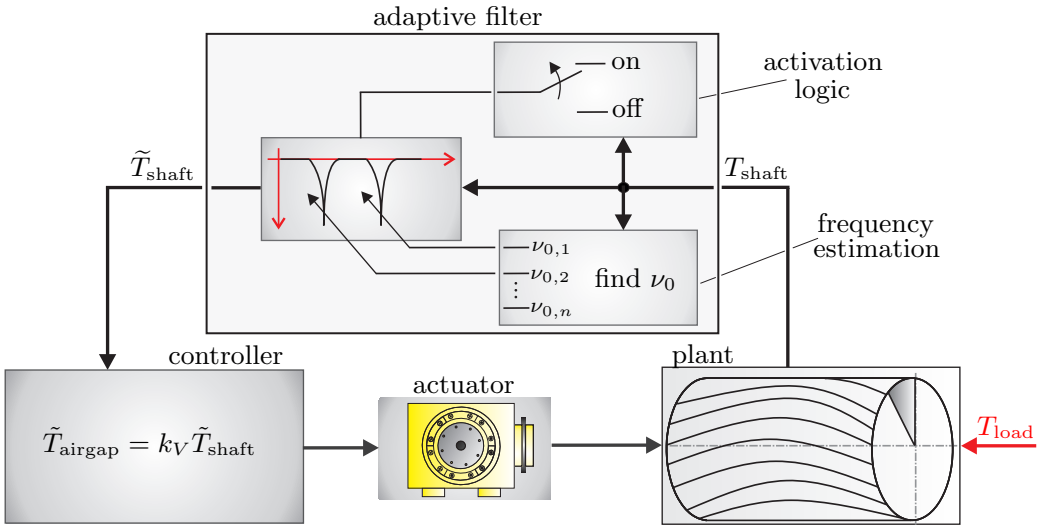

Figure 5.9: Block diagram of the test bed control scheme with an adaptive filter comprising notch filter, frequency estimator and activation logic.

5.4 Frequency estimation

This section discusses possible stand-alone approaches to find an unknown oscillation frequency, which is the first problem that needs to be solved in order to implement the scheme presented in Fig. 5.9.

5.4.1 Filter-based estimation

Several contributions analyse the outputs of one or more linear filters, in order to find an unknown frequency. One particularly often seen idea [108, 109] builds on a pair of band-pass filters, as suggested by Fig. 5.10. Therein, W_l and W_h represent a lower and a higher band-pass filter, respectively, and ν_1, ν_2, $\nu_0 = \sqrt{\nu_1 \nu_2}$, and ν_{real} stand for the lower and higher band-pass frequencies, the geometrical centre frequency between the two, and the actual frequency of the investigated signal, respectively. As pointed out in [108], if $\nu_{real} = \nu_0$, the magnitudes of the outputs of W_l and W_h and thus the corresponding filter output powers are equal. However, if $\nu_{real} > \nu_0$, which is the case for Fig. 5.10, the output of W_h carries more energy than that of W_l. Obviously, the opposite is true for $\nu_{real} < \nu_0$, which motivates the update scheme

$$\nu_0(n+1) = \nu_0(n) + \Delta_\nu \phi(n), \tag{5.13}$$

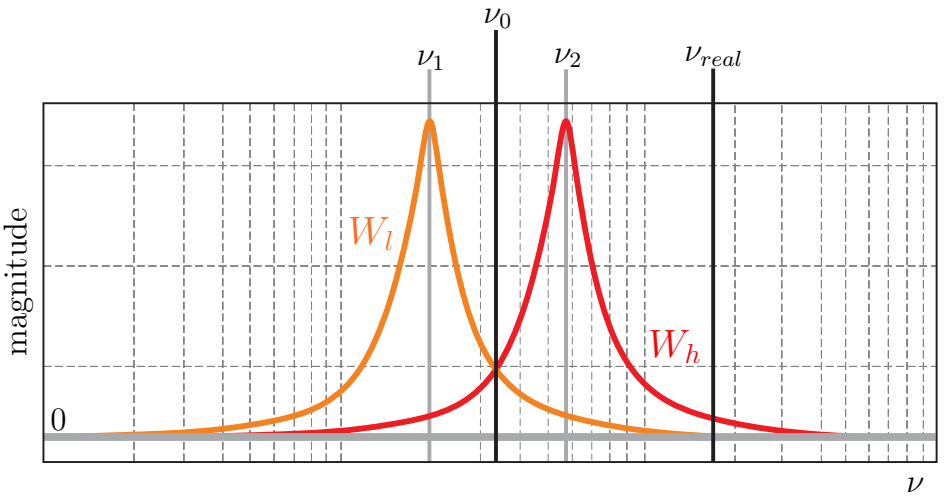

Figure 5.10: Magnitude responses of two band-pass filters used for frequency tracking.

in order to drive ν_0 towards ν_{real}. Therein, the weight $\phi(n)$ reflects the idea described above, and specifies the direction of the modification. One possibility to compute $\phi(n)$ is to utilize the sums of squared outputs to resemble the filters' output powers, i.e.

$$\phi(n) = \begin{cases} 1, & \text{if} \quad \sum_{k=0}^{M} y_h^2(n-k) - \sum_{k=0}^{M} y_l^2(n-k) > 0 \\ -1, & \text{if} \quad \sum_{k=0}^{M} y_h^2(n-k) - \sum_{k=0}^{M} y_l^2(n-k) < 0, \end{cases} \tag{5.14}$$

where the output $y_l(n)$ and $y_h(n)$ of W_l and W_h, respectively, are squared and summed up over the last M samples. Besides that, the frequency increment Δ_ν must be chosen such that a compromise between frequency resolution and convergence speed is found. A significant advantage of this approach is its low computational cost. However, it also suffers from several drawbacks: On the one hand, for frequencies that are far from the centre frequency, the outputs of the two filters become more and more alike, which makes it hard to tell a difference between $y_l(n)$ and $y_h(n)$. It is for this reason that e.g. [109] requires a reasonably precise initial estimate about the location of the subsequently identified resonances. For the cases of the considered test bed drive lines, this is usually not possible. On the other hand, this scheme provides just a frequency estimate, and no additional information that could be used for a decision on whether an oscillation is caused by resonance or not. Unfortunately, also other estimation methods that are based on the analysis of filter outputs, like [107, 110], suffer from certain shortcomings, be it again a lack of additionally provided information, high computational complexity that can cause problems with regards to real-time, or certain conservative boundary conditions, such as the demand for the plant to be in steady-state, that contradict the environment of the setups considered in this work.

5.4.2 Fourier-based estimation

From the considerations laid out earlier, one may deduce that a satisfying frequency estimation scheme must provide sufficient additional information, to allow for an educated check on the root causes of a given oscillation. Two in this regard highly interesting aspects are the magnitude that is associated with an identified frequency, and the spectral content of the remaining part of the considered signal. Both of these attributes may be obtained by methods of what one could call *Fourier-based signal analysis*, such as the discrete Fourier transform (DFT). These methods, however, have a bad reputation especially when execution in real-time is demanded; mainly because of the excessive computational requirements[5] that are often associated with them [95]. In spite of this perception, several publications show that it is frequently possible to create a modified version of a selected Fourier technique, which is specifically tailored to the needs of a given problem in order to avoid potentially problematic computational aspects [123–125]. The following section attempts to transfer this idea to the problem of resonance suppression in test bed drive lines, and outlines a DFT-strategy that is capable of providing precise frequency estimates, delivers additional information to enable a decision on whether an oscillation stems from resonance or external load, and may still be executed in real-time.

The first step in this process is to significantly reduce the number of bins in the frequency domain, which are needed to compute the frequency of a shaft torque oscillation. To that end, one may recall the definition of the DFT, which is usually expressed as

$$X_k = \sum_{n=0}^{N-1} x(n) e^{-j\frac{2\pi k n}{N}}, \tag{5.15}$$

a complex-valued, discrete function of the frequency index k [126]. Therein, $x(n)$ is the time-domain signal that is transformed, X_k denotes the kth spectral component, and N stands for the number of data points that is contained in the analysed interval. It is well known that a complex oscillation $x(n) = \eta_x e^{j2\pi f_x T_d n}$, where η_x stands for the signal's amplitude and T_d denotes the sampling time, leads to just one entry at a single bin in the frequency domain, if its frequency[6] f_x is an integer multiple of the frequency increment $\Delta f = \frac{1}{NT_d}$ [127, 128]. This is usually not the case, and the actual signal frequency will be located between two bins in the discrete spectrum, as depicted in Fig. 5.11. With regards to the result of the DFT, this leads to

$$X_k = \sum_{n=0}^{N-1} \eta_x e^{j2\pi f_x T_d n} e^{-j\frac{2\pi k n}{N}} = \eta_x e^{j\pi\frac{N-1}{N}\Delta k} \frac{\sin(\pi\Delta k)}{\sin(\frac{\pi}{N}\Delta k)}, \quad \text{where} \quad \Delta k = f_x N T_d - k. \tag{5.16}$$

[5] The test beds considered in this work are operated at a sampling rate of $T_d = 100\mu s$. As the frequency resolution of a classical DFT is given by the fraction $\frac{1}{NT_d}$, where N denotes the number of processed data points, this means that in order to achieve a frequency resolution of just 1 Hz, at least 10000 samples need to be processed at every time step!

[6] In this section, frequencies will be denoted by f in Hz, instead of the priorly used ν in $\frac{\text{rad}}{s}$, plainly because it is more common in the context of Fourier-methods.

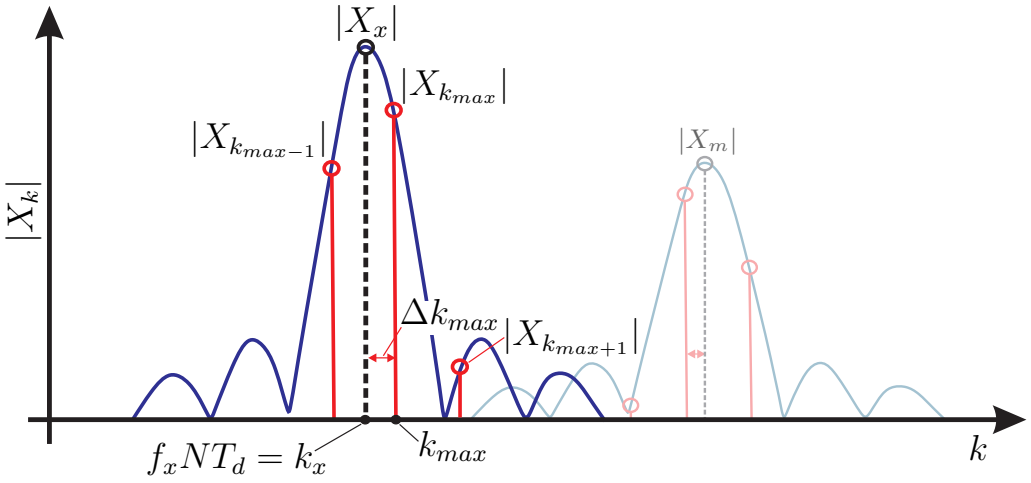

Figure 5.11: Spectral magnitude representation of a single complex oscillation. The main lobe's maximum $|X_x| = \eta_x N$ is emphasized by the dashed black line at index k_x.

As suggested by [129–131], the signal's actual frequency can be reconstructed if the index error Δk is known for just one single index, by evaluating

$$f_x = \frac{k_x}{NT_d} = \frac{k + \Delta k}{NT_d}. \tag{5.17}$$

For the sake of simplicity, the analysis in many papers focuses on the index with the biggest magnitude entry and thus the smallest index error, as shown in Fig. 5.11. Introducing k_{max} for this index, one finds that $|\Delta k_{max}| = |f_x NT_d - k_{max}| \leq \frac{1}{2}$, as otherwise a different bin would be closer to $f_x NT_d$. Moreover, as k is an integer, the error entries for the left and right neighbours of k_{max} are $\Delta k_{max\pm1} = \Delta k_{max} \mp 1$. The idea now is to take a look at the absolute values of the spectral components in the area of k_{max}, and to investigate the fraction

$$\begin{aligned} &\frac{|X_{k_{max+1}}| - |X_{k_{max-1}}|}{|X_{k_{max}}|} = \\ &= \frac{\frac{|\sin\left(\pi(\Delta k_{max}-1)\right)|}{|\sin\left(\frac{\pi}{N}(\Delta k_{max}-1)\right)|} - \frac{|\sin\left(\pi(\Delta k_{max}+1)\right)|}{|\sin\left(\frac{\pi}{N}(\Delta k_{max}+1)\right)|}}{\frac{|\sin\left(\pi\Delta k_{max}\right)|}{|\sin\left(\frac{\pi}{N}\Delta k_{max}\right)|}} = \frac{\frac{|\sin\left(\cancel{\pi\Delta k_{max}-\pi}\right)|}{|\sin\left(\frac{\pi}{N}(\Delta k_{max}-1)\right)|} + \frac{|\sin\left(\cancel{\pi\Delta k_{max}+\pi}\right)|}{|\sin\left(\frac{\pi}{N}(\Delta k_{max}+1)\right)|}}{\frac{|\sin\left(\cancel{\pi\Delta k_{max}}\right)|}{|\sin\left(\frac{\pi}{N}\Delta k_{max}\right)|}} \end{aligned} \tag{5.18}$$

Given that $\frac{\pi}{N}$ typically is small, the approximation $\sin(\frac{\pi}{N}\Delta k_{max}) \approx \frac{\pi}{N}\Delta k_{max}$ and thus

$$\frac{|X_{k_{max+1}}| - |X_{k_{max-1}}|}{|X_{k_{max}}|} \approx \frac{\frac{1}{|\frac{\pi}{N}(\Delta k_{max}-1)|} - \frac{1}{|\frac{\pi}{N}(\Delta k_{max}+1)|}}{\frac{1}{|\frac{\pi}{N}\Delta k_{max}|}} = \frac{\frac{1}{1-\Delta k_{max}} - \frac{1}{1+\Delta k_{max}}}{\frac{1}{|\Delta k_{max}|}} \tag{5.19}$$

will hold, which may be rearranged to

$$\frac{|X_{k_{max+1}}| - |X_{k_{max-1}}|}{|X_{k_{max}}|} \approx \frac{|\Delta k_{max}|(\cancel{1} + \Delta k_{max} - \cancel{1} + \Delta k_{max})}{(1 - \Delta k_{max})(1 + \Delta k_{max})} = \frac{2\Delta k_{max}|\Delta k_{max}|}{1 - \Delta k_{max}^2}. \tag{5.20}$$

Since $|\Delta k_{max}| = \Delta k_{max}\mathrm{sgn}(\Delta k_{max})$, (5.20) may be solved for Δk_{max}^2, which gives

$$\Delta k_{max}^2 \approx \frac{|X_{k_{max+1}}| - |X_{k_{max-1}}|}{2\mathrm{sgn}(\Delta k_{max})|X_{k_{max}}| + |X_{k_{max+1}}| - |X_{k_{max-1}}|}. \tag{5.21}$$

The right hand side of (5.21) is always positive, hence computing its square root is always possible. To get hold of Δk_{max}, one may employ the fact that if f_x is located between k_{max} and k_{max+1}, then $\Delta k_{max} > 0$ and $|X_{k_{max+1}}| > |X_{k_{max-1}}|$, but if it lies between k_{max-1} and k_{max}, then $\Delta k_{max} < 0$ and $|X_{k_{max+1}}| < |X_{k_{max-1}}|$. Therefore $\mathrm{sgn}(\Delta k_{max}) = \mathrm{sgn}(|X_{k_{max+1}}| - |X_{k_{max-1}}|)$, which eventually yields

$$\Delta k_{max} \approx \sqrt{\frac{|X_{k_{max+1}}| - |X_{k_{max-1}}|}{2\mathrm{sgn}(|X_{k_{max+1}}| - |X_{k_{max-1}}|)|X_{k_{max}}| + |X_{k_{max+1}}| - |X_{k_{max-1}}|}} \cdot \mathrm{sgn}(|X_{k_{max+1}}| - |X_{k_{max-1}}|). \tag{5.22}$$

Similar procedures are frequently called “interpolated DFT” [129–131] and are particularly useful for improving frequency estimations that are based on a given DFT-spectrum. The actual benefit of this concept in the context of adaptive notch filtering is that it allows to drastically reduce the number of spectral elements that need to be computed, in order to find the frequency of a given oscillation!

Nonetheless, one important extension of the presented formalism is necessary, in order to allow for a successful application in real operation: the use of *windowed* signals. The latter refers to the outcome of a point-wise multiplication of the signal of interest with a so-called *window sequence*, as proposed by Von Hann, Kaiser or Blackman [126, 127, 132]. As already presented in Fig. 5.11, the transformation of a pure oscillation, which is often

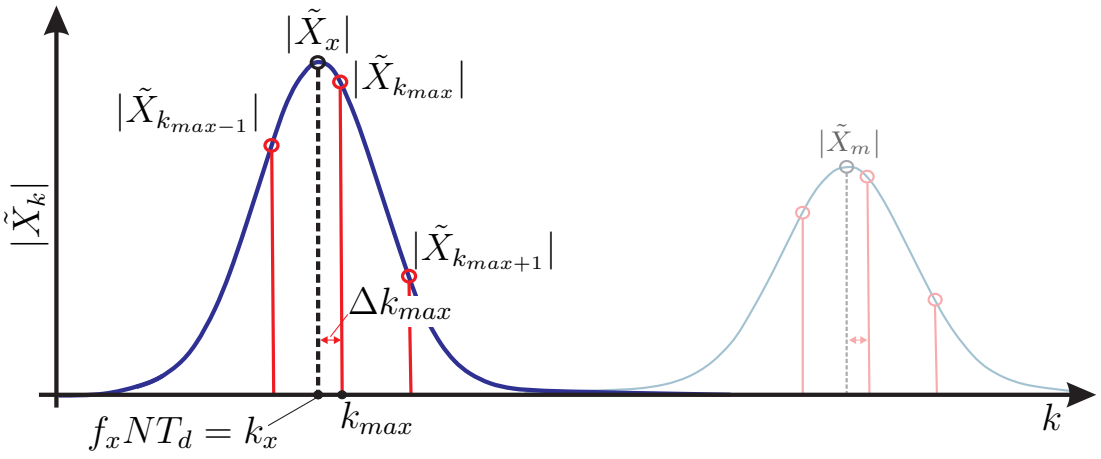

Figure 5.12: Spectral magnitude representation of a single complex oscillation, after multiplication with a Blackman-window (thus the use of $\tilde{X}_k$, instead of the prior X_k). The maximum of the lobe is now given by $|\tilde{X}_x| = 0.42\eta_x N$.

termed *rectangularly windowed*, leads to entries at all bins in the frequency domain, if the signal frequency is not a multiple of the frequency increment. In the present context, this so-called *leakage* effect is a serious threat to the discussed DFT interpolation, as already a single real-valued sinusoid according to Euler's identity introduces two components into the spectrum – which without counter-measure interfere and disturb the concept. Besides that, also other frequency components that actually are far away may impact the spectral components that are used for computation, as insinuated by the grey component X_m in Fig. 5.11. Thus, to avoid this interference, all signals are at first multiplied with a Blackman window, before the transformation into the frequency domain is carried out. This particular window may be expressed as

$$w(n) = 0.42 - 0.5\cos(\frac{2\pi n}{N}) + 0.08\cos(\frac{4\pi n}{N}), \quad \text{for} \quad n = 0, \ldots, N-1, \tag{5.23}$$

and leads to the windowed version

$$\tilde{x}(n) = x(n)w(n) \tag{5.24}$$

of an N-element excerpt of the signal $x(n)$. The spectral components that are obtained by the means of $\tilde{x}(n)$ are furthermore denoted by $\tilde{X}_k$. In the frequency domain, this modifies the situation depicted in Fig. 5.11 to that shown in Fig. 5.12, with the desired effect: Frequency components that are sufficiently far apart do not interfere any more! Clearly, this modification affects the formalism behind the DFT-interpolation, and the equations have to be adapted. To that end, the exact same fraction of spectral entries as in (5.18), i.e.

$$\frac{|\tilde{X}_{k_{max+1}}| - |\tilde{X}_{k_{max-1}}|}{|\tilde{X}_{k_{max}}|} =: b(\Delta k_{max}), \tag{5.25}$$

is considered again, which is a monotonic function in Δk_{max} also in the case of Blackman-windowed signals, and may thus be inverted to find Δk_{max}. Remarkably, the inverse $b^{-1}(\cdot)$ is almost linear in the area of interest: The exact inverse and the approximation

$$\hat{b}^{-1}\left(\frac{|\tilde{X}_{k_{max+1}}| - |\tilde{X}_{k_{max-1}}|}{|\tilde{X}_{k_{max}}|}\right) := 0.75\frac{|\tilde{X}_{k_{max+1}}| - |\tilde{X}_{k_{max-1}}|}{|\tilde{X}_{k,max}|} \tag{5.26}$$

deviate only minimally for the relevant interval of $|\Delta k_{max}| < 0.5$, as shown in Fig. 5.13, which suggests

$$\Delta k_{max} \approx 0.75\frac{|\tilde{X}_{k_{max+1}}| - |\tilde{X}_{k_{max-1}}|}{|\tilde{X}_{k,max}|} \tag{5.27}$$

to find the sought index error in the case of Blackman-windowed signals! Furthermore, it is also possible to trace back the actual amplitude of a considered spectral component. For the case of a Blackman window, the lobe that is centred around the signal frequency f_x, where all the magnitude entries lie on, may be approximated almost perfectly by the "normal distribution"-like expression

$$|\tilde{X}(\Delta k)| \approx |\tilde{X}_x| e^{\ln(\frac{0.25}{0.42})\Delta k^2}, \tag{5.28}$$

with $|\tilde{X}_x|$ denoting the lobe's maximum. If the index error Δk_{max} and the absolute value of the corresponding spectral entry $|\tilde{X}_{k_{max}}|$ are known, $|\tilde{X}_x|$ may be found by rearranging (5.28) to

$$|\tilde{X}_x| \approx |\tilde{X}_{k_{max}}| e^{-\ln(\frac{0.25}{0.42})\Delta k_{max}^2}, \tag{5.29}$$

which also allows to compute the signal's amplitude, since $\eta_x = \frac{1}{0.42N}|\tilde{X}_x|$.

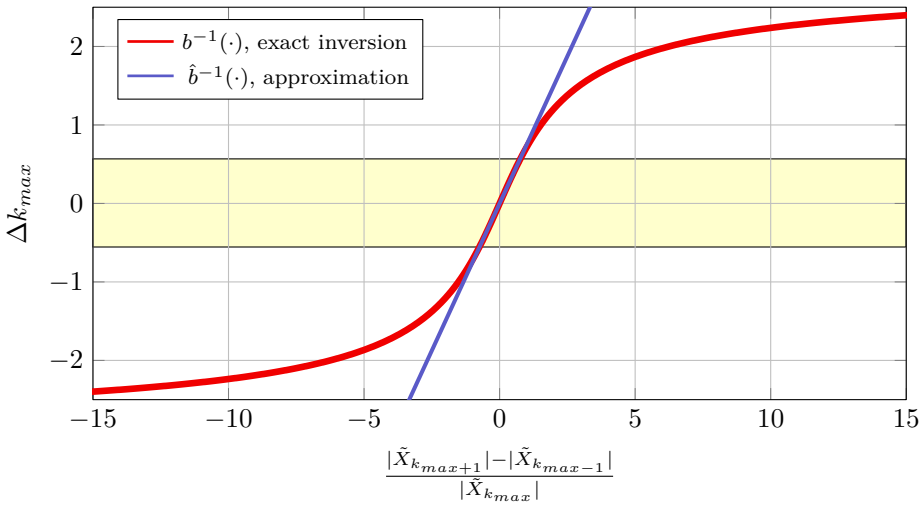

Figure 5.13: New approach to find the index error Δk for Blackman-windowed signals. In the relevant area ($|\Delta k| < 0.5$, yellow section) approximation and exact inversion are almost identical. The parts of the plot where $|\Delta k| > 0.5$ are added for explanatory reasons only - for these values the maximum $|\tilde{X}_{k_{max}}|$ would occur at a different bin.

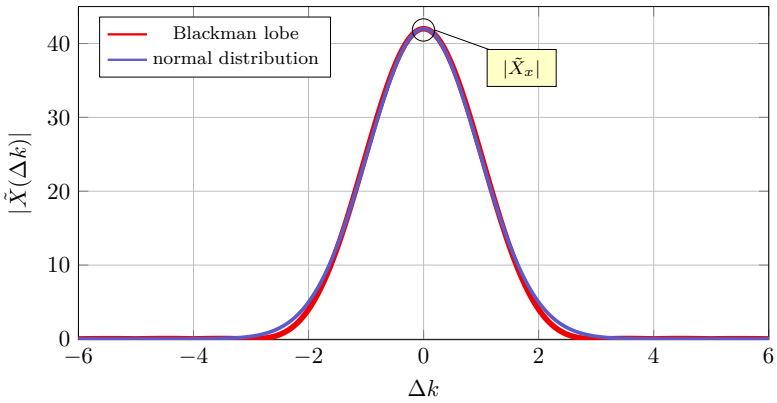

Figure 5.14: Approximation of the Blackman-main lobe of a complex exponential ($N = 100$, $\eta_x = 1$) by the means of a normal distribution. If the absolute value of just one entry along the lobe is known together with the corresponding index error, $|\tilde{X}_x|$, which corresponds to the value for $\Delta k = 0$, can be reconstructed.

Lastly, the spectral components that enter the DFT-interpolation must be made available. Among the tools that may be employed for this purpose, especially *Goertzel*'s algorithm turned out to work stably and reliably in the given setting. The equations of the algorithm to repeatedly compute a spectral component $\tilde{X}_k$ may be expressed in the following form:

$$y(n) = \begin{cases} \tilde{x}(n), & \text{if} \quad n \equiv 1 \bmod N \\ 2\cos(2\pi k N) y(n-1) + \tilde{x}(n), & \text{if} \quad n \equiv 2 \bmod N \\ 2\cos(2\pi k N) y(n-1) - y(n-2) + \tilde{x}(n), & \text{else.} \end{cases} \tag{5.30}$$

$$\tilde{X}_k(n) = \begin{cases} y(n) - e^{j2\pi \frac{k}{N}} y(n-1), & \text{if} \quad n \equiv 0 \bmod N \\ \tilde{X}_k(n-1), & \text{else.} \end{cases}$$

Therein, the components $\tilde{X}_k$ are updated every N steps, and the filter part corresponding to $y(n)$ is periodically reset after that. All signals are initialized with zeros, i.e. $y(n) = \tilde{X}_k(n) = 0$ $\forall n \leq 0$. Clearly, several aspects, such as the number of selected frequency bins, their location, and the number of used signal samples, depend on the concrete use case. For the case of the R2R test bed, these topics are discussed in Section 5.6. To summarize and lay the ground for the next steps, one may state that

- The number of frequency bins needed to find an unknown oscillation frequency may be reduced drastically by using the proposed DFT-interpolation method.
- To find the bins that eventually enter the DFT-interpolation, the algorithm proposed by Goertzel is used.
- The output of the algorithm are N_g spectral components $\tilde{X}_1, \tilde{X}_2, \ldots, \tilde{X}_{N_g}$ of the shaft torque T_{shaft}, accompanied with the estimated maximum amplitude[a] η_x and the corresponding maximum frequency f_x. The spectral elements are updated every N time steps.
- The presented DFT-formalism assumes that the DFT-entries used for computation enclose just one spectral component of the analysed signal. What can be done if that is not the case is discussed in the upcoming section.

[a] This point requires some care: Until now, only single complex exponentials were considered, such as $x(n) = \eta_x e^{j2\pi f_x T_d n}$, where the maximum of the Blackman-lobe and the signal's magnitude are related via $\eta_x = \frac{1}{0.42N}|\tilde{X}_x|$. A real-valued oscillation, such as $x_r(n) = \eta_x \cos(2\pi f_x T_d n) = \frac{\eta_x}{2}\left(e^{j2\pi f_x T_d n} + e^{-j2\pi f_x T_d n}\right)$ introduces *two* complex exponentials with half the cosine's amplitude, however, where typically the first one enters the interpolation scheme. Therefore, the result of the DFT-interpolation $|\tilde{X}_x|$ must be scaled by $\frac{2}{0.42N}$.

5.5 Adaptation logic

This section employs the DFT-interpolation method presented previously, and outlines a series of ideas to distinguish between resonance and external excitation as the sources of torque oscillations. Generally, torque oscillations in test bed drive lines can be put in two categories, as suggested graphically by the figures below: *Firstly*, Fig. 5.15 presents a situation where the oscillation conditions discussed in Sec. 5.1 are fulfilled, which leads to a growing oscillation. The latter eventually stalls at a value that depends on the various limitations that are present in the control loop, e.g., for torque, currents and voltages [27, 133]. In this case, a notch filter to suppress the oscillation is highly desired.

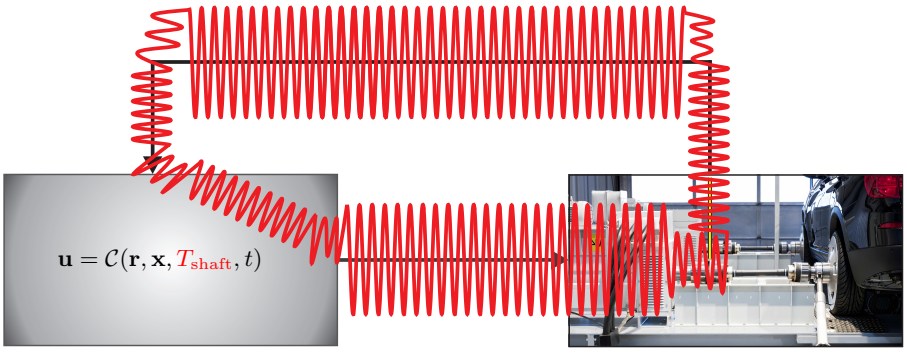

Figure 5.15: Torque oscillation due to "unstable" resonance.

Secondly, Fig. 5.16 depicts an oscillation that stems from the device-under-test, and is not linked to the controller a priori. In these situations, the involvement of a notch filter must be avoided, and, which is almost equally important, the adaptation algorithm should not be confused as in Fig. 5.8.

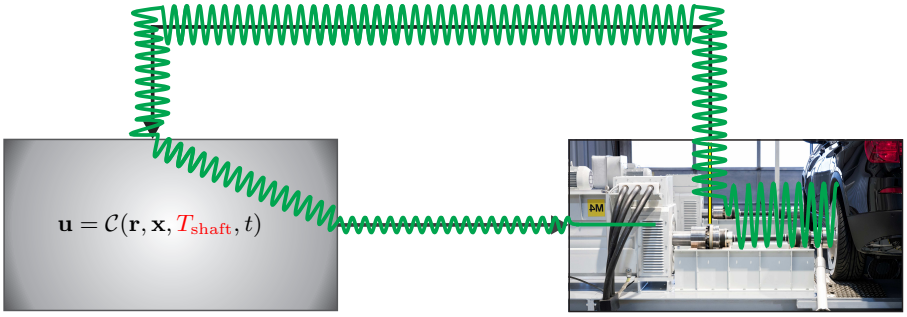

Figure 5.16: Torque oscillation in case of external excitation.

With this classification, the remainder of this section discusses how the spectral components $\tilde{X}_1, \tilde{X}_2, \ldots, \tilde{X}_{N_g}$ of T_{shaft} can be used to perform various checks with regards to their origin, to allow for an educated decision on whether a notch filter should be adapted or not.

5.5.1 Condition 1: Magnitude threshold

A first and obvious step is to make sure that small and insignificant oscillations do not disturb the suppression algorithm. To that end, it is reasonable to require the magnitude that is associated with a potential notch frequency to exceed a certain threshold. Introducing T_{min} for the latter, one may represent this idea by the inequality

$$\eta_x = \frac{2}{0.42N}|\tilde{X}_x| \overset{!}{>} T_{min}. \tag{5.31}$$

The scaling factor 2 accounts for the fact that the measured signals can only be real-valued.

5.5.2 Condition 2: Low- and high-frequency components

For the considered systems, the open loop phase shift for frequencies close to 0Hz (e.g. f<10Hz) typically is close to 0°, and in any case far from -180°. This is mainly because in most cases the phase is turned towards -180° for the first time by the lowest resonance, which normally lies well above 100Hz. Consequently, oscillations with frequencies close to 0Hz usually are *not* caused by resonance, and therefore should *not* be blocked. Moreover, putting a notch frequency close to 0Hz can also be dangerous, as this essentially opens up the control loop in an area that is absolutely crucial for the functionality of the system. Hence, it is reasonable to require also the frequencies to surpass a pre-set minimum. In the case of a dominating low-frequency component, the lowest spectral component $|\tilde{X}_1|$ carries the largest magnitude. Additionally, the formalism (5.27) requires one element to the left and to the right of the maximum to work, which is why

$$|\tilde{X}_{k_{max}}| \overset{!}{>} \max(|\tilde{X}_1|, |\tilde{X}_{N_g}|) \tag{5.32}$$

qualifies as a second condition. The idea can be formulated more conservatively by

$$|\tilde{X}_{k_{max}}| \overset{!}{>} \max(|\tilde{X}_1|, \ldots, |\tilde{X}_p|, |\tilde{X}_{N_g-q}|, \ldots, |\tilde{X}_{N_g}|), \quad p, q \in \mathbb{N}, \tag{5.33}$$

which may be interpreted as the introduction of a lower and an upper bound for the notch frequencies, such that

$$f_{min} \overset{!}{<} f_x \overset{!}{<} f_{max}. \tag{5.34}$$

5.5.3 Condition 3: Separate spectral components

The interpolation formalism discussed in Section 5.4.2 assumes that the DFT-bins, which are used to find η_x and f_x, encapsulate just one spectral component of T_{shaft}. However, no matter how many DFT-bins the interpolation scheme comprises and how high the resulting frequency resolution eventually is, the theoretical possibility that two or potentially even

more spectral entries lie between two bins cannot be ruled out per se. Fortunately, it may be checked whether this is the case or not: Using approximation (5.28) to describe the main lobe in case of a blackman-windowed sequence, one can see that

$$\frac{|X(\Delta k_{max})|}{|X(\Delta k_{max\pm1})|} \approx \frac{e^{\ln(\frac{0.25}{0.42})\Delta k_{max}^2}}{e^{\ln(\frac{0.25}{0.42})\Delta k_{max\pm1}^2}} = e^{\ln(\frac{0.25}{0.42})(\Delta k_{max}^2 - \Delta k_{max\pm1}^2)} \tag{5.35}$$

is fulfilled only if either the spectral proximity of the considered frequency bins k_{max} and $k_{max\pm1}$ is dominated by just one spectral element of T_{shaft}, or if all the given spectral components are arranged in a highly specific way with regards to their frequency and magnitude, such that the cumulative magnitude response again takes on exactly the form of the priorly discussed "normal distribution"-like Blackman-lobe. The second scenario, however, is so unlikely in practice that it is not taken into further consideration. Besides that, (5.35) extends the set of conditions for whether T_{shaft} stems from resonance or external excitation, by checking for equality between the right and the left side of (5.35) (in practice, a deviation of ±5% was allowed), as a resonance oscillation in this work is assumed to comprise just one single dominating frequency.

5.5.4 Condition 4: Steady-state

Besides the advantage of avoiding cumbersome commissioning trials, a strong argument for employing adaptive notch filters is their ability to react to changes of the plant. These changes usually do not occur abruptly while the system is in operation, meaning that also the frequencies of oscillations due to resonance normally do not perform sudden and stepwise changes. This consideration suggests to require a detected frequency to be in steady-state[7], before it is passed on to one of the available notch filters. Such a measure rules out a big class of load torque profiles that arise in transient test bed operation. Mathematically, the idea may be represented as

$$\sum_{i=0}^{N_s-1} |f_x\Big(n - iN\Big) - f_x\Big(n - (i+1)N\Big)| \overset{!}{<} \varepsilon, \tag{5.36}$$

with the discrete time variable n and the number N of samples processed in the Goertzel-algorithm. Therein, the sum accumulates the differences of N_s successive results of the DFT-interpolation scheme. The design parameter ε describes a limit that must not be exceeded, and additionally, it needs to be made sure that the samples of $f_x(n)$ stem from different results of the employed Goertzel-algorithm, whose outcome is updated only every N samples.

[7] This does not mean that the whole control system must be in steady-state, in contrast to, e.g., [110]!

5.5.5 Filter placement

It is assumed that a *finite* and *fixed* number of notch filters is available for adaptation. This number will be denoted by N_f, and as mentioned earlier, must be equal to or higher than the number of resonances that need to be suppressed. When a new oscillation that fulfils criteria (5.31), (5.33), (5.35) and (5.36) arrives, one of the N_f notch filters must be selected to accept its frequency. To clarify the discussion, the notch frequencies of the N_f filters are stored in a vector, i.e. $\boldsymbol{f} := \left[f_1, f_2, \ldots, f_{N_f}\right]$, and the highest amplitudes that have been observed at these frequencies are saved in $\boldsymbol{\eta} := \left[\eta_1, \eta_2, \ldots, \eta_{N_f}\right]$. It turns out to be reasonable to initialize $\boldsymbol{f}$ by frequencies far out of the crucial operating range, and to initially assign zeros to the magnitude vector $\boldsymbol{\eta}$. Additionally, the index i_f fulfilling $1 \leq i_f \leq N_f$ is introduced to pick out one specific filter, meaning η_{i_f} and f_{i_f}. Generally, the possible scenarios can be put in two categories:

Category 1: As long as unused filters are available, which means that there exist indices i_f such that $\eta_{i_f} = 0$, the filter corresponding to the lowest of these indices is chosen to accept the new frequency f_x.

Category 2: If all filters are already in use and a new oscillation occurs, its magnitude $\eta_x = \frac{2}{0.42N}|\tilde{X}_x|$ is compared to the elements stored in the vector $\boldsymbol{\eta}$. If the new magnitude surpasses or equals at least one entry of $\boldsymbol{\eta}$, the notch frequency of the filter corresponding to the smallest entry of $\boldsymbol{\eta}$ is exchanged with the new candidate. In case two or more entries of $\boldsymbol{\eta}$ are equal and thus come into question, the one corresponding to the smallest index is selected.

If the plant changes over time, the algorithm will sooner or later arrive at a scenario belonging to *Category 2*, as, according to the directive contained in *Category 1*, it will react to a modified resonance frequency by activating an unused filter - as long as these are available. Once all the available filters are in operation, another change of the plant will lead to a *Category 2*-situation. Clearly, if the plant is modified, e.g., by replacing the device-under-test by a successor with significantly different rotational inertia, the number of resonances that need to be suppressed still has to be lower than or equal to N_f. If that is the case, the only requirement for the algorithm to adapt to the resonances of the new setup is that the corresponding magnitudes rise to at least the levels of the entries in $\boldsymbol{\eta}$. To simplify such a transition, it is helpful to slightly decrease $\boldsymbol{\eta}$ over time in the phases where no adaptation takes place. This idea may be expressed mathematically in the form of

$$\eta_{i_f}(n+1) = \begin{cases} \max\left(\alpha\eta_{i_f}(n), \zeta T_{min}\right), & \text{if} \quad \eta_{i_f}(n) > 0 \\ 0, & \text{else.} \end{cases} \tag{5.37}$$

Therein, the design parameter α fulfils $\alpha \leq 1$, and determines the dynamics of X_{i_f} outside the overall adaptation process, while ζT_{min} defines a lower bound. To ensure that the

stored magnitudes do not drop under the threshold motivated in (5.31), $\zeta \geq 1$ must hold. Eventually, the ideas presented in Sections 5.5.1 to 5.5.5 are combined to complete the algorithm. Figure 5.17 presents the outcome by the means of a flow chart, where qualitative mathematical expressions are used mostly, in order to keep the diagram simple. Therein, the function $\psi(\Delta k_{max}) := e^{\ln(\frac{0.25}{0.42})(\Delta k_{max}^2 - \Delta k_{max\pm1}^2)}$ abbreviates the complex exponential from (5.35). Furthermore, the priorly introduced *Category 1* and *Category 2* are combined; ultimately, a new oscillation magnitude always surpasses at least one entry of $\boldsymbol{\eta}$ if an unused filter is still available, as the entries X_{i_f} are initialized with zeros. Moreover, minima and maxima are interpreted as extrema along the first dimension. It must be noted that this block only becomes active in case that the new magnitude fulfils $\eta_x \geq \min(\boldsymbol{\eta})$; otherwise, the vector of notch frequencies $\boldsymbol{f}$ and the vector of stored magnitudes $\boldsymbol{\eta}$ remain unchanged.

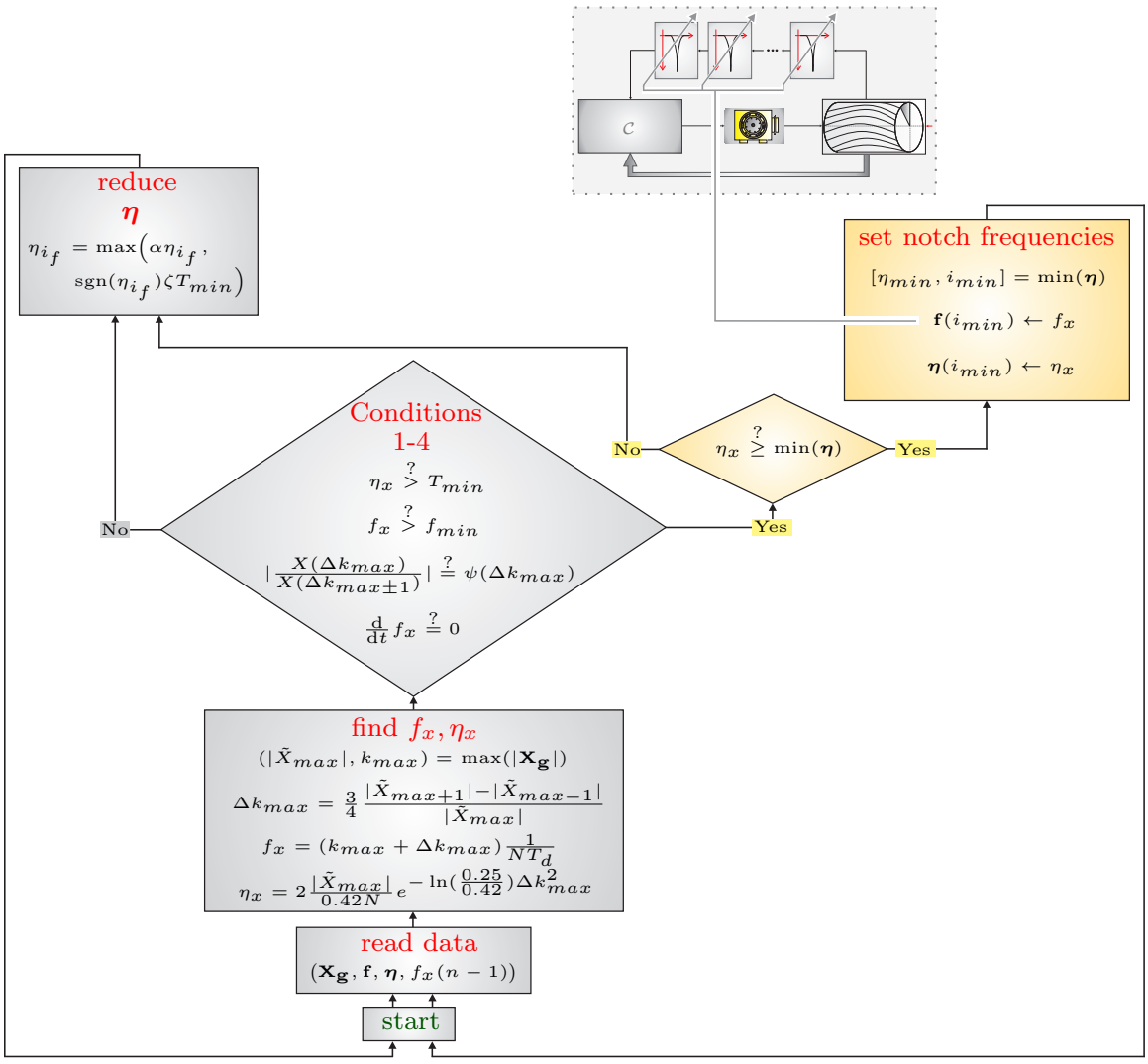

Figure 5.17: Representation of the algorithm as a flow-diagram.

Some aspects of the proposed algorithm demand further discussion. With regards to external excitations, it is not impossible that a sequence of T_{load} fulfils conditions (5.31), (5.33), (5.36) and (5.35), and surpasses at least one element of $\boldsymbol{\eta}$, while all filters are already active. However, the plants considered in this work may reasonably be interpreted as linear systems, which means that, in case of instability, the affected frequency components grow until one of the saturations in the control loop becomes active. Formulated differently, one may state that an oscillation due to instability takes what it can get in terms of available magnitude, which is usually not the case for oscillations caused by external excitations. This consideration highlights the fact that the proposed magnitude-comparison-strategy is another check that targets the origin of an observed torque oscillation.

Nonetheless, if *any* conceivable behaviour of T_{load} is allowed and if literally no restrictions are applied to its shape, frequency content, etc., it will always be possible to construct a profile of T_{load} for which the algorithm will *not* find the correct resonance frequencies. In the most extreme case, one could think of the following diabolic sequence of T_{load}, which consists of two parts: The first part would entirely compensate the effect of T_{airgap}, while the second part would enforce some other, totally arbitrary behaviour. Since only T_{airgap} and T_{shaft} are available as measurements, their inspection in such a case would give the impression of an entirely different dynamical system. Still, some additional ideas that extend the presented conditions are discussed in Appendix E, which might further refine the considered set of checks, but are still in the scope of ongoing research.

In contrast to this sinister assessment, the following section presents a series of highly positive and convincing results, which have been achieved in simulation and on the actual test bed. It will be shown that the proposed conditions are sufficiently conservative, sufficiently strict and sufficiently concise for all the cases that have been considered in the course of this work, that the *diabolic sequence* presented above is mostly a theoretical concept, and that satisfying results could be achieved consistently.

5.6 Results

To assess the quality of the proposed resonance suppression scheme, a significant number of experiments was carried out, in simulation and on the considered R2R test bed. As mentioned in the summary of Section 5.4.2, certain parameters need to be chosen with care. For the application in simulation and on the actual test bed, only two notch filters were employed; essentially because it was known that for the given induction machine and the involved drive line mostly just one, and only in some cases two resonances would create problematic oscillations. For both filters the pole radius was set to $r = 0.995$. Excerpts of T_{shaft} with a length of $N = 128$ data points were used as the input to the Goertzel-algorithm, which means that a frequency resolution of $\Delta f = 78.125\text{Hz}$ was achieved prior to the DFT-interpolation. A total number of $N_g = 24$ frequency bins were computed, which were distributed evenly, starting with X_1 at a frequency of $f_1 = 78.125\text{Hz}$, and ending at a maximum frequency of $f_{24} = 1875\text{Hz}$. The threshold variables that were introduced in the derivation of conditions (5.31) and (5.34) were chosen as $T_{min} = 20\text{Nm}$, $f_{min} = 156\text{Hz}$ and $f_{max} = 1797\text{Hz}$, and the number of differing Goertzel-results over which f_x was not allowed to change was set to $N_s = 10$, which describes a time interval with a length of 0.128 seconds. The corresponding threshold variable was set to $\varepsilon = 10\text{Hz}$, both notch frequencies were initialized at 1500Hz, and for the dynamics of $\boldsymbol{\eta}$, $\alpha = 1 - 10^{-9}$ and $\zeta = 1.1$ was selected.

5.6.1 Simulation

Figures 5.18, 5.19 and 5.20 present a repetition of the simulation study laid out in Figs. 5.7 and 5.8, which was used to assess the established, classical adaptive approaches. A clear improvement in the overall system's behaviour is visible; mainly because the adaptive suppression algorithm is not disturbed by T_{load} arriving at $t = 1s$ any longer.

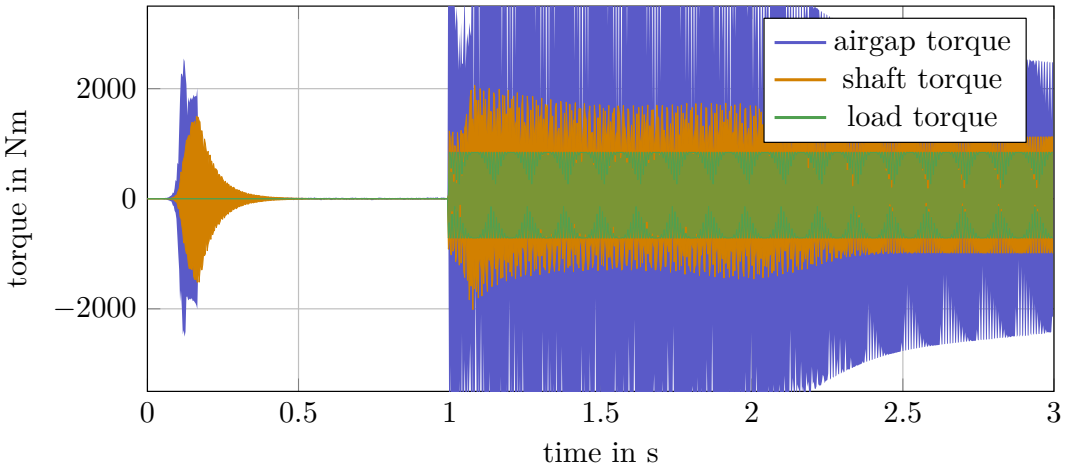

Figure 5.18: Simulated shaft, airgap and load torque.

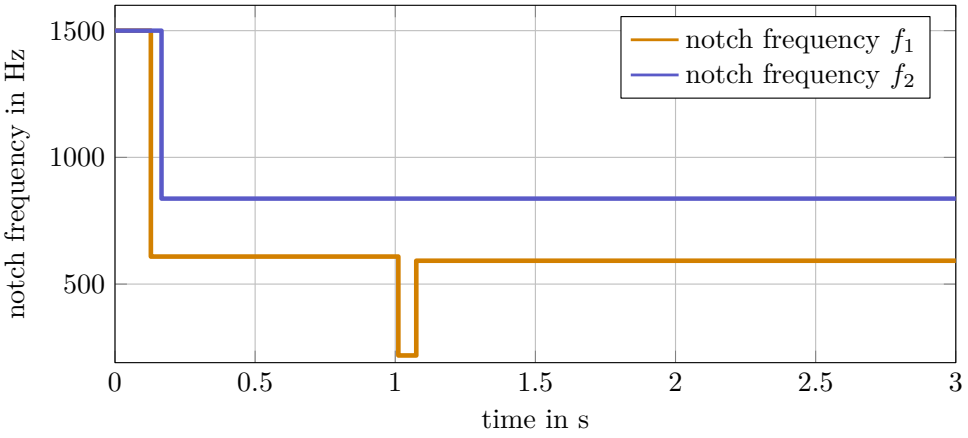

Figure 5.19: Notch frequencies f_1 and f_2.

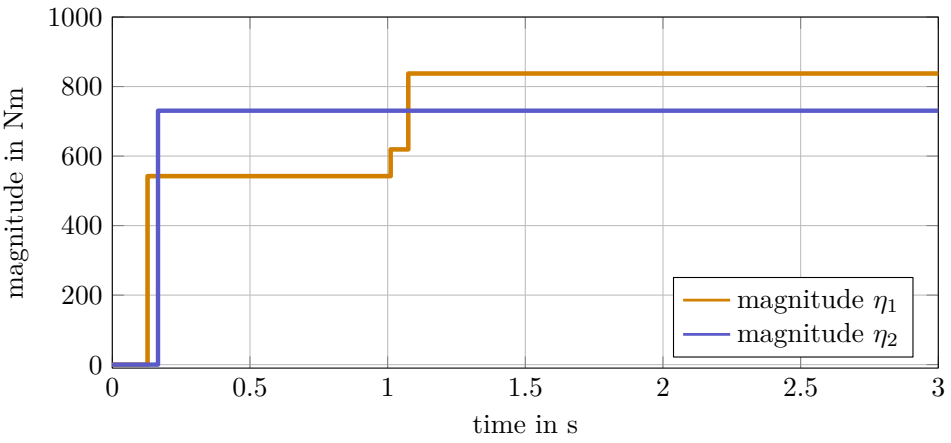

Figure 5.20: Oscillation magnitudes η_1 and η_2.

5.6.2 R2R Test Bed - Experiment I

Figures 5.21, 5.22 and 5.23 depict one of the first trials that were conducted on the R2R test bed. In this particular case, no vehicle, but the second test flanges discussed in Section 2.3.4 was connected to the considered drive line. At $t = 1s$, the feed through gain was changed from $k_V = 1$ to $k_V = 4.5$, which led to a temporary loss of stability. At $t = 1.5s$, the adaptive algorithm is activated, thereafter quickly finds the resonance frequencies, and suppresses them appropriately, which expectedly restores stability. As no device-under-test that would produce a disturbing load torque was present, the stored magnitudes do not change any further, and especially η_2 remains at a comparably low level.

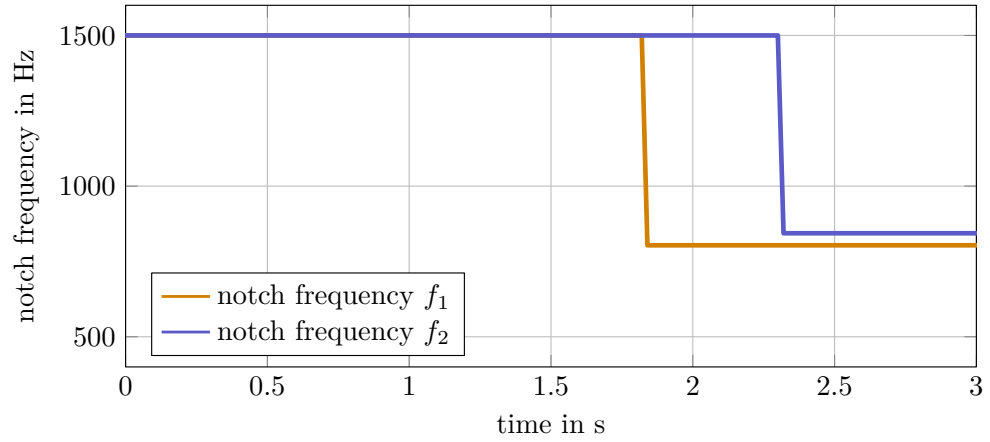

Figure 5.22: Notch frequencies f_1 and f_2.

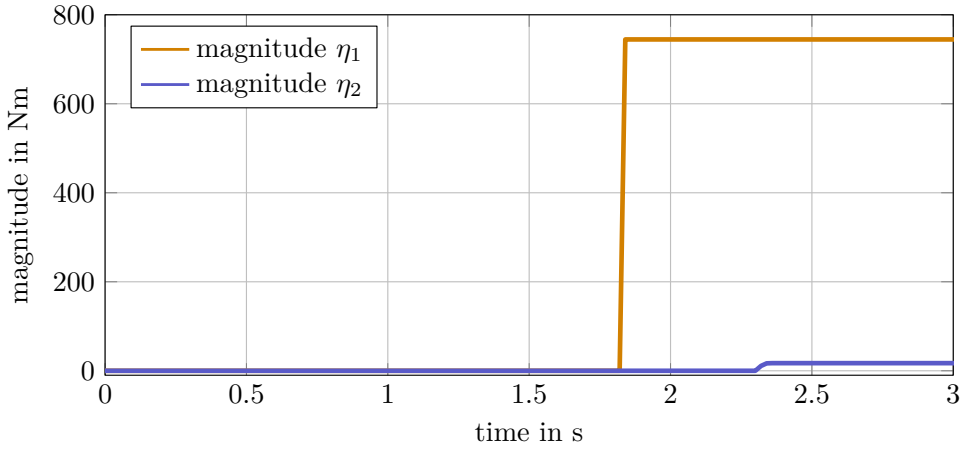

Figure 5.23: Oscillation magnitudes η_1 and η_2.

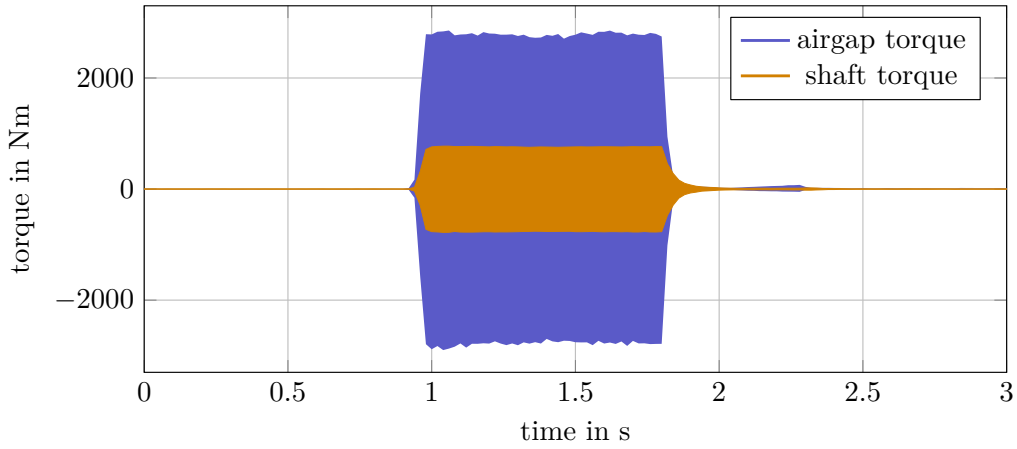

Figure 5.21: Measured shaft, airgap and load torque.

5.6.3 R2R Test Bed - Experiment II

This second experiment from the R2R test bed may be interpreted as the *supreme discipline* for the adaptive resonance suppression scheme. Throughout the experiment, where $k_V = 4.3$ was chosen, the test bed was in full operation, with a test bed operator sitting inside the car, performing a regular test run. One can see that the algorithm quickly and reliably finds the resonances of the system, and is not disturbed by the load torque that is produced by the device-under-test.

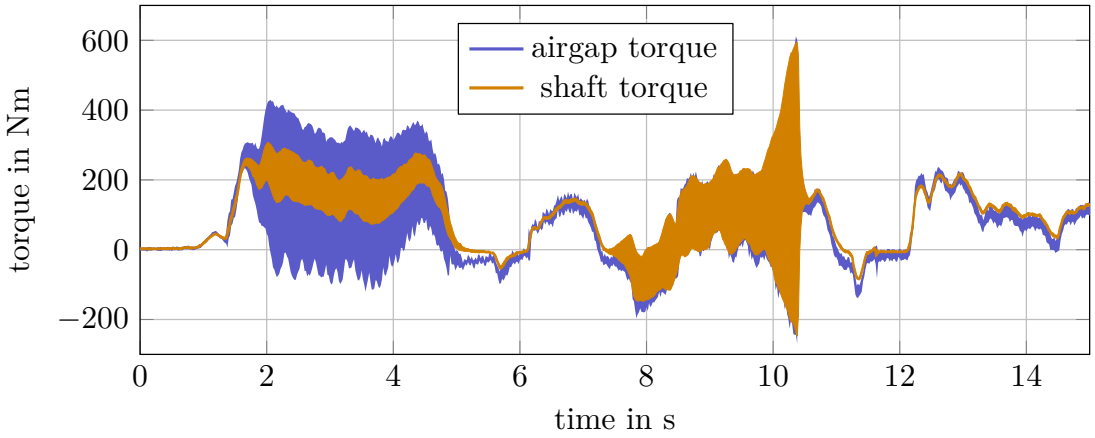

Figure 5.24: Measured shaft, airgap and load torque.

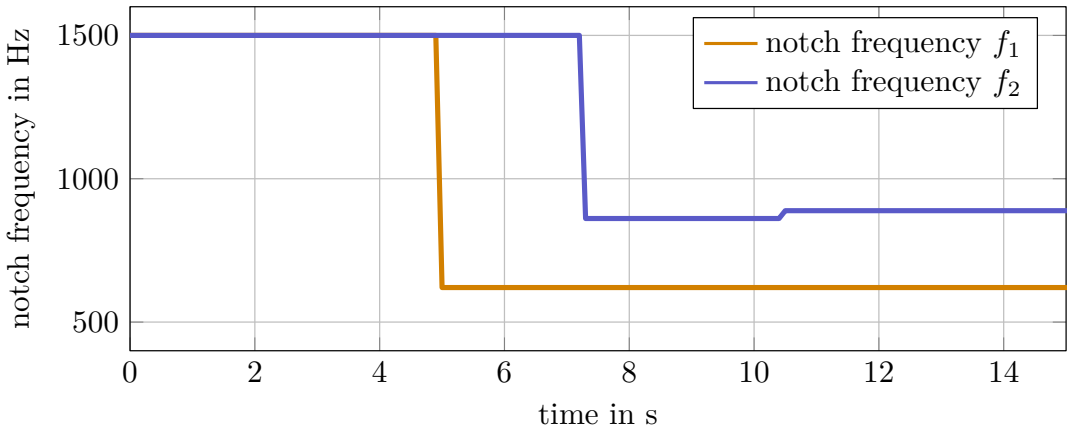

Figure 5.25: Notch frequencies f_1 and f_2.

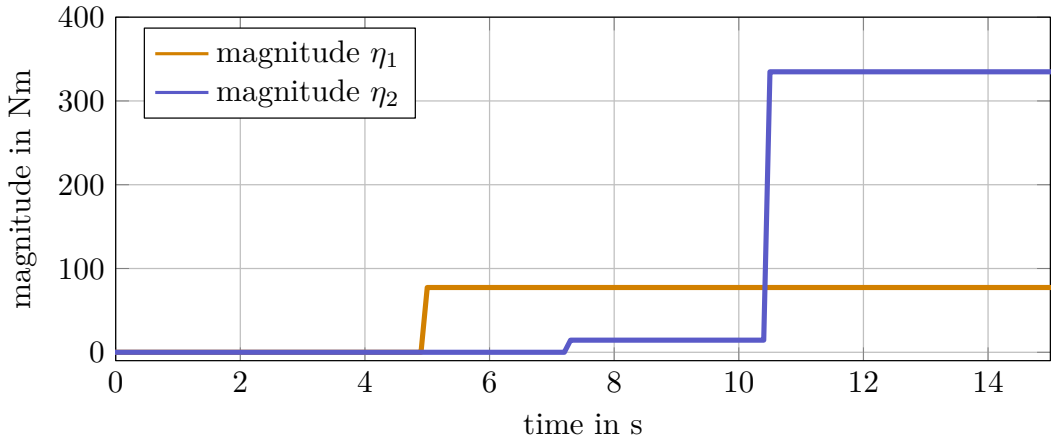

Figure 5.26: Oscillation magnitudes η_1 and η_2.

5.6.4 R2R Test Bed - Experiment III

The last experiment to be discussed in this section was conducted on the R2R test bed, too. It is presented in Figs. 5.27, 5.28 and 5.29, and stands for the nominal, in practice most likely case to happen. This time, the controller is parametrized such ($k_V = 2.1$) that only one resonance frequency is on the brink to instability, also causes a growing oscillation, and eventually is suppressed successfully. As the other resonance frequency, which had to be mitigated in the experiments presented previously, in this case is far from the stability boarder, the second notch filter did not have to be activated at all.

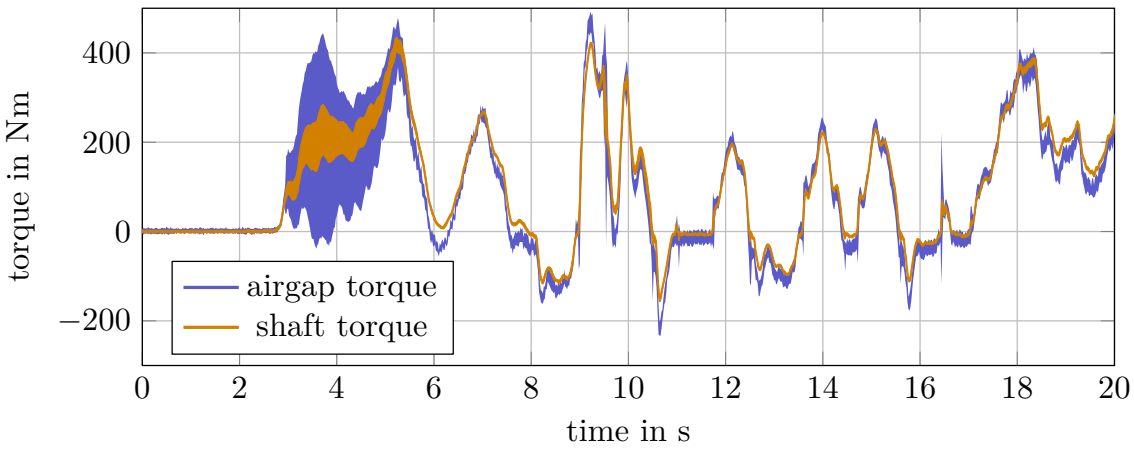

Figure 5.27: Measured shaft, airgap and load torque.

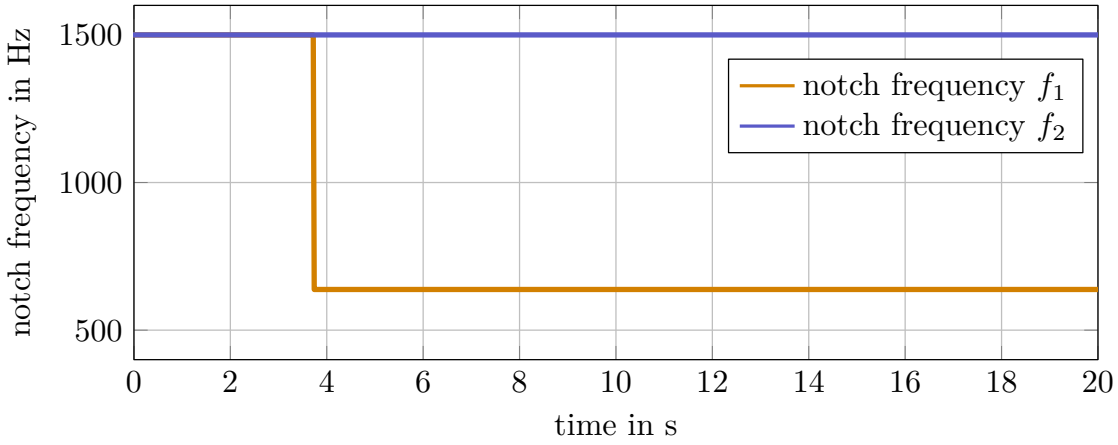

Figure 5.28: Notch frequencies f_1 and f_2.

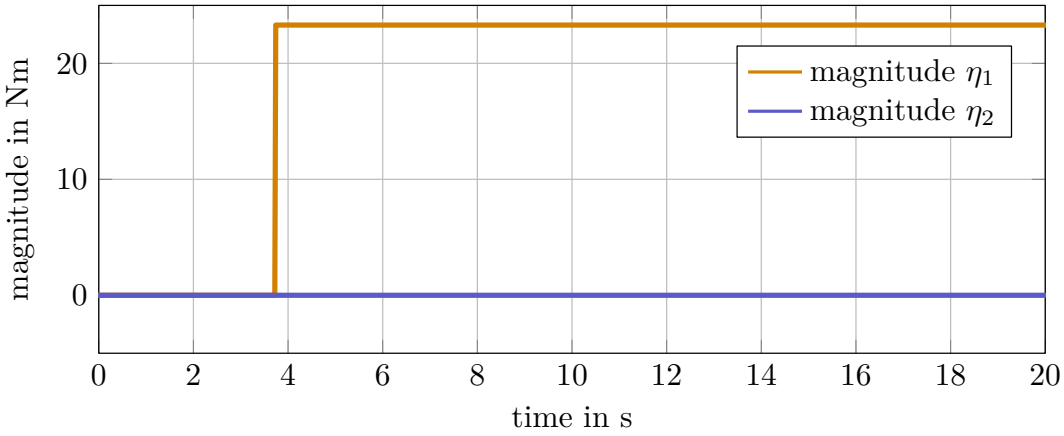

Figure 5.29: Oscillation magnitudes η_1 and η_2.

5.7 Conclusion

In the preceding section, a novel adaptive resonance-suppression-scheme is presented. The proposed concept builds on the application of the idea of DFT-interpolation to Blackman-windowed signals, and creates an accurate and robust scheme to identify previously unknown resonance frequencies. The method's capability to suppress undesired oscillations caused by resonances is proven in simulation and in measurement. The presented results were obtained mainly on the R2R test bed that is considered on numerous occasions throughout this work, yielding satisfying and consistently convincing results.

Part III

Control of Air and Gas Pressure

Chapter 6

Charge Air and Fuel Gas Pressure Control

The final part of the thesis discusses *two* aspects that play a crucial role in many modern testing systems, besides the control of mechanical quantities: the interaction of test bed hardware with real-time software, *and* the control of pressures of media that are supplied to the device under test. In that sense, the following chapter considers a test bed for the development of transient strategies for large multi-cylinder gas engines, using only a single cylinder in a hardware-in-the-loop setup. The contents and ideas of the following section are also contained in [134], in a slightly modified version.

The starting point for the following considerations is the current trend towards green energy, where particularly the transition to electricity from renewable sources plays an important role as one of the keys for capping global warming from anthropogenic carbon dioxide emissions. This shift places great demands on the electrical grid, however, as especially wind and solar power are subject to high volatility and may not always be available at the location where electrical power is needed [135–137]. Therefore, power sources that are able to react quickly and flexibly to peak loads or drops in renewable power generation are an indispensable part of the electrical grid of the future. Of the technologies that can be used for this kind of decentralized power generation, reciprocating combustion engines have the highest degree of flexibility [138], and among those, large bore gas engines stand out for high efficiency throughout all load conditions and a low environmental impact. However, the load acceptance of high-performance gas engines is subject to limits due to knocking combustion and misfire, and especially their ramping rates are lower than those of comparable diesel engines. To overcome those shortcomings, much effort is invested in the improvement of the transient operation of large gas engines. A crucial tool on the path to improvement are precise and efficient testing systems. A compact single-cylinder engine (SCE) test bed that replaces a large multi-cylinder engine (MCE) is an example thereof, which can be regarded as state-of-the-art for the development of steady-state combustion strategies. The transient case, however, turns out to be much more demanding;

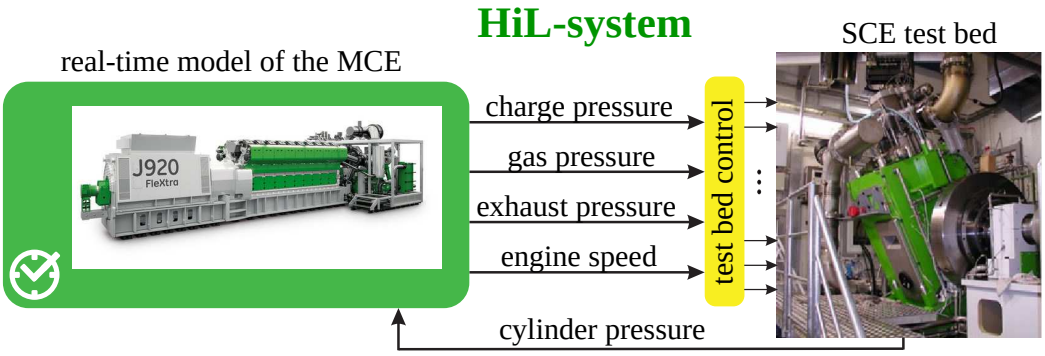

Figure 6.1: HiL-system for transient SCE operation.

in particular, enabling an SCE test bed to provide the transient MCE boundary conditions for the combustion process requires intense efforts [139, 140]. This challenging transient scenario is considered in the following: a hardware-in-the-loop (HiL) system is presented that permits the development of *transient* MCE combustion strategies on an SCE test bed. For that purpose, the system reproduces the behaviour of the full MCE using real-time models and highly dynamic controllers. As representatives of all the test bed controllers, simple yet effective controller designs for the charge air and fuel gas pressure are presented. These controllers in particular have to meet high standards in terms of speed and accuracy. In the course of experiments, it is shown that the proposed concepts fulfil the challenging demands of transient testing and significantly improve on the performance of existing controllers that are designed mainly for steady-state operation. Subsequently, Section 6.1 presents an approach to transfer the transient behaviour of an MCE to an SCE test bed, and Sections 6.2 and 6.3 discuss the control of the above-mentioned pressures. Section 6.4 presents experimental results to validate the proposed concepts.

6.1 HiL-system

Fig. 6.1 depicts the HiL-system comprising mainly a real-time model of the MCE and controllers to apply trajectories obtained from this model to the test bed. In this section, the most significant components are explained briefly.

6.1.1 Multi-cylinder engine

The engine considered for validation is a V20 spark ignited pre-chamber gas engine with two-stage turbocharging. After each stage, the charge air is cooled. The charge air pressure is controlled by a blow off valve. While the pre-chamber is scavenged with gas, the main combustion chamber is supplied by cylinder individual port injection, cf. [139, 141, 142].

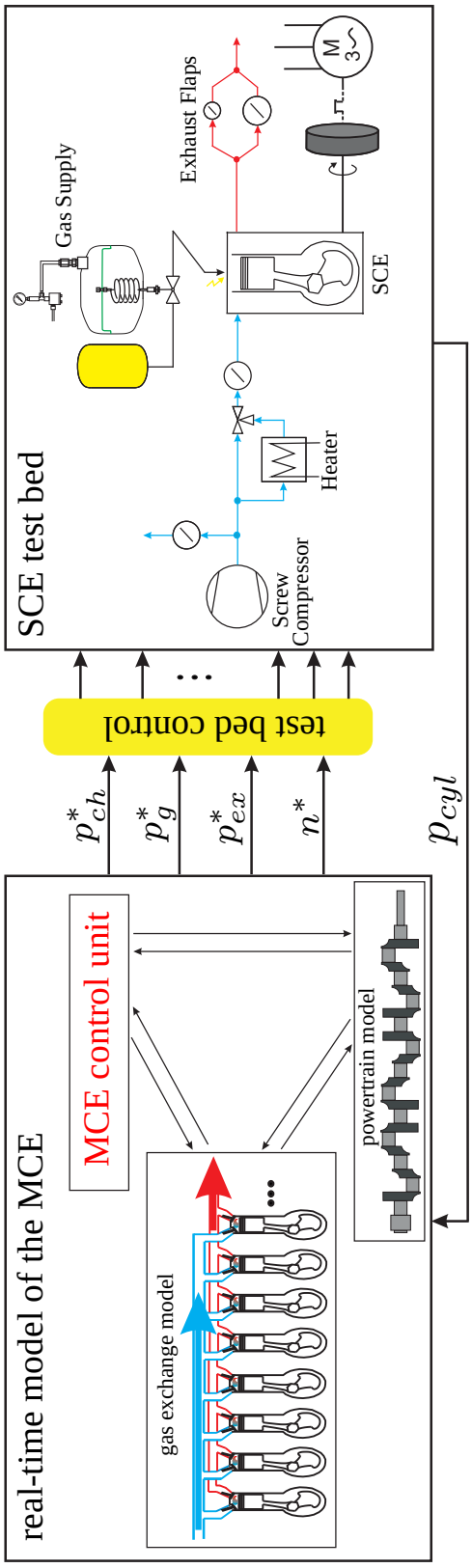

Figure 6.2: Detailed representation of the HiL-system. The real-time model provides references for charge-, gas-, back pressure and engine speed; the measured SCE cylinder pressure is fed back from the test bed.

6.1.2 Single-cylinder engine test bed

Fig. 6.2 presents the considered setup in more detail. The SCE as the essential part of the test bed is derived directly from the MCE. This means that piston, connecting rod, liner, cylinder head including pre-chamber, port injection gas valve as well as the valve lift curves of intake and exhaust valves are identical to the MCE. Hence, if the pressures at the intake and exhaust ports of the SCE are identical to those at the MCE, the same combustion behaviour can be assumed. Since the application of two-stage turbocharging to the SCE is a cumbersome task, the charge air is delivered by a screw compressor. The temperature of the compressed air is conditioned by an electric heater and a mixing valve. Charge air pressure and exhaust pressure are controlled by the means of two flaps each. To control the engine speed and suppress torsional vibrations, a flywheel and an induction machine are connected to the SCE. The fuel gas pressure is adjusted by the means of a pneumatic regulator [143].

6.1.3 Real-time model

The real-time model comprises models of the MCE gas exchange system, the MCE powertrain and a simplified replica of the MCE control unit (MCE-CU). The latter contains controllers for *knock*, *engine speed* and NO_x. The main HiL-model is a 0D model (i.e., a model without spatial dependency, see [144]) of one MCE cylinder bank comprising turbochargers, cylinders and piping. To simulate the turbochargers, the exhaust enthalpy flux has to be known. This quantity depends on the outflow over the exhaust valves which in turn depends on the cylinder pressures, whose dynamics thus have to be captured. For modelling the gas exchange phase, where either intake or exhaust valve are open, the differential equation

$$\begin{aligned}\frac{\mathrm{d}}{\mathrm{d}t}p_{\mathrm{cyl}} = \frac{\chi-1}{V_{\mathrm{cyl}}}\Bigg[&\frac{\vartheta_{\mathrm{cyl}}}{\chi-1}\sum_{j=1}^{2}R_j\frac{\mathrm{d}m_j}{\mathrm{d}t} - \vartheta_{cyl}\sum_{j=1}^{2}\frac{R_j}{\chi_j-1}\frac{\mathrm{d}m_j}{\mathrm{d}t}\\ &-\frac{\chi}{\chi-1}p_{\mathrm{cyl}}\frac{\mathrm{d}V_{\mathrm{cyl}}}{\mathrm{d}t} + \frac{\mathrm{d}Q_w}{\mathrm{d}t} + \frac{\mathrm{d}m_{in}}{\mathrm{d}t}h_{in} - \frac{\mathrm{d}m_{out}}{\mathrm{d}t}h_{out}\Bigg]\end{aligned} \tag{6.1}$$

is used, see [145, 146]. Corresponding to one cylinder, V_{cyl} denotes the displacement volume, p_{cyl} the pressure and ϑ_{cyl} the temperature inside the cylinder. The symbols R_j, m_j, χ_j are the specific gas constant, the mass inside the cylinder and the heat capacity ratio of either fresh air ($j = 1$) or exhaust gas ($j = 2$). The quantities $\frac{\mathrm{d}Q_w}{\mathrm{d}t}$, $\frac{\mathrm{d}m_{in}}{\mathrm{d}t}$, $\frac{\mathrm{d}m_{out}}{\mathrm{d}t}$ and h_{in}, h_{out} describe the wall heat flux, the in- and outgoing mass flows and the corresponding specific enthalpies, respectively; furthermore, χ describes the heat capacity ratio of the mixture. The presented approach does not include a model of the combustion process. Instead, pressure measurements obtained from the real combustion in the SCE are used to update the simulation: At the time of exhaust-valve-opening (EVO) of each cycle the SCE cylinder pressure is

measured; this value is then used to reinitialize the pressure simulated according to (6.1) in each cylinder at its respective EVO. This ensures that the increase of p_{cyl} due to combustion is considered correctly but assumes that all cylinders show the same combustion behaviour. Fig. 6.3 visualizes this approach by depicting the pressure reinitialization process exemplarily for one cylinder of the HiL real-time model. The angular speeds of turbocharger and powertrain[1] are calculated by means of a power balance. The acting torques are computed from the powers transmitted over the corresponding shafts. The angular speed ω of the crankshaft, for example, is obtained by integrating

$$\frac{\mathrm{d}}{\mathrm{d}t}\omega = \frac{1}{I}\Big[T_{\text{indicated}} - T_{\text{friction}} - T_{\text{consumer}}\Big]. \tag{6.2}$$

Therein I denotes the lumped inertia of the crank-shaft, and $T_{\text{indicated}}$, T_{friction}, and T_{consumer} indicate the torques associated with the indicated power, the friction, and the power demanded by the consumer, respectively.

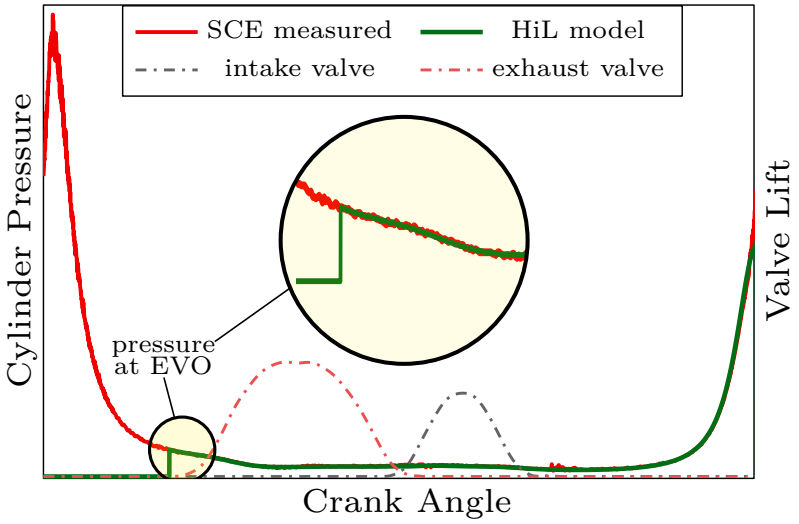

Figure 6.3: Imposing the cylinder pressure at EVO.

[1]Technically, a powertrain model is only needed when the MCE model is operated in *island mode*, i.e. independent from the grid. In *grid parallel mode*, the engine speed is determined by the grid; see [145] for details.

6.2 Charge air pressure

The objective of the air intake system shown in Fig. 6.4 is to control the charge air pressure p_{ch} and to track its reference p^*_{ch}. The constant air mass flow supplied by the compressor is distributed by the flaps f_1 and f_2, whose positions are considered as the control inputs. The supply pressure is measured downstream the screw compressor and labelled p_s. As p_s is a test bed specific variable, the MCE model does not provide a reference p^*_s. All pressures are absolute, with an ambient pressure of $p_{\text{amb}} \approx 1\text{bar}$.

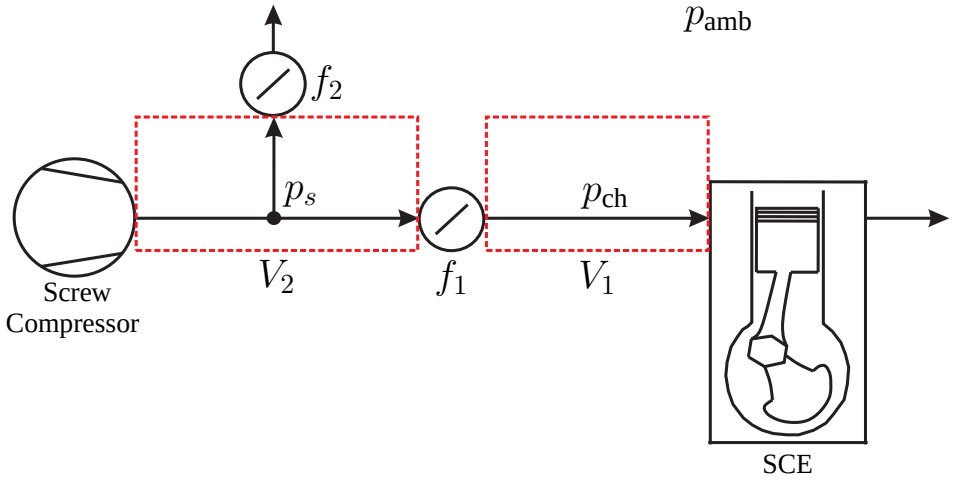

Figure 6.4: Air intake system of the considered SCE test bed.

6.2.1 Modelling

As indicated in Fig. 6.4, the piping system is subdivided into two segments with volumes V_1 and V_2. The thermodynamic states of the air are assumed the same throughout the volumes (lumped parameter approach, see [147]). The air temperature denoted by ϑ is controlled by a heater and is hence assumed to be constant. This leads to

$$\begin{aligned} \frac{\mathrm{d}}{\mathrm{d}t} p_{\text{ch}} &= \frac{R\vartheta}{V_1}(q_1 - q_e), \\ \frac{\mathrm{d}}{\mathrm{d}t} p_s &= \frac{R\vartheta}{V_2}(q_c - q_2 - q_1), \end{aligned} \tag{6.3}$$

where R denotes the specific gas constant of the air, q_1 and q_2 indicate the air mass flows passing f_1 and f_2, respectively, and q_e and q_c are the air consumed by the SCE and supplied by the compressor, respectively. The mass flows q_1 and q_2 are given by

$$\begin{aligned} q_1 &= A_1(u_1)\frac{p_s}{\sqrt{R\vartheta}}\Psi(\alpha_1), \quad \alpha_1 = \frac{p_s}{p_{\text{ch}}} \\ q_2 &= A_2(u_2)\frac{p_s}{\sqrt{R\vartheta}}\Psi(\alpha_2), \quad \alpha_2 = \frac{p_s}{p_{\text{amb}}}. \end{aligned} \tag{6.4}$$

Therein, A_1, A_2 are the effective flap areas, which are highly nonlinear functions of the corresponding positions u_1, u_2. The latter are bounded by $\underline{u}_1 \leq u_1 \leq \overline{u}_1$ and $\underline{u}_2 \leq u_2 \leq \overline{u}_2$ and are considered as the control inputs of the system. The function Ψ denotes the flow function. A reasonable approximation for it is given by [147]

$$\Psi(\xi) \approx \begin{cases} \sqrt{\frac{2}{\xi}(1-\frac{1}{\xi})}, & \text{if } \xi \leq 2 \\ \frac{1}{\sqrt{2}}, & \text{otherwise.} \end{cases} \tag{6.5}$$

Under normal operating conditions, the supply pressure p_s exceeds 2 bar. Furthermore, it will be ensured by proper design of the controllers that $p_s \leq 2p_{\text{ch}}$ holds. Hence, $\alpha_1 \leq 2$ and $\alpha_2 > 2$, which allows to write the model as

$$\begin{aligned} \frac{\mathrm{d}}{\mathrm{d}t}\begin{bmatrix} p_{\text{ch}} \\ p_s \end{bmatrix} = &\begin{bmatrix} \frac{R\vartheta}{V_1} & 0 \\ -\frac{R\vartheta}{V_2} & -\frac{R\vartheta}{V_2} \end{bmatrix} \begin{bmatrix} A_1(u_1)\sqrt{\frac{2}{R\vartheta}}\sqrt{p_{\text{ch}}(p_s - p_{\text{ch}})} \\ A_2(u_2)\frac{p_s}{\sqrt{2R\vartheta}} \end{bmatrix} \\ &+ \begin{bmatrix} \frac{R\vartheta}{V_1} & 0 \\ 0 & \frac{R\vartheta}{V_2} \end{bmatrix} \begin{bmatrix} -q_e \\ q_c \end{bmatrix}. \end{aligned} \tag{6.6}$$

6.2.2 Reference planning

While the gas exchange model provides a reference p_{ch}^* for p_{ch}, no reference p_s^* for the supply pressure p_s is given a priori. As mentioned before, p_s has to stay in the range $(p_{\text{ch}}, 2p_{\text{ch}})$ for the model in (6.6) to be valid. Additionally, p_s must not exceed an upper limit $\overline{p}_s$ to prevent a breakdown of the compressor. This leads to the constraint

$$p_{\text{ch}} < p_s < \min(2p_{\text{ch}}, \overline{p}_s). \tag{6.7}$$

The approach for determining p_s^* attempts to keep the position of f_1 equal to the arithmetic mean of its saturation interval, i.e. $\frac{1}{2}(\overline{u}_1 + \underline{u}_1) =: \mathcal{U}$, when the system is in steady state. The idea of this strategy is to maximize the actuator range available for disturbance rejection. In steady state

$$\frac{\mathrm{d}}{\mathrm{d}t}p_{\text{ch}} = \frac{\sqrt{2R\vartheta}}{V_1}A_1(u_1)\sqrt{p_{\text{ch}}(p_s - p_{\text{ch}})} - \frac{R\vartheta}{V_1}q_e = 0 \tag{6.8}$$

and consequently

$$A_1(u_1)\sqrt{p_{\text{ch}}(p_s - p_{\text{ch}})} = \sqrt{\frac{R\vartheta}{2}}q_e \tag{6.9}$$

will hold. If the engine is approximated as a volumetric pump, a typical formulation [147] for the mass flow q_e is

$$q_e = \rho_{\text{ch}}\lambda(p_m, n)\frac{V_d}{N_r}\frac{\omega_e}{2\pi}. \tag{6.10}$$

Here ρ_{ch} denotes the density of the air at the engine's intake, ω_e the angular velocity of the engine, p_m the mean effective pressure inside the cylinder, λ the volumetric efficiency, V_d the displaced volume and N_r the number of cylinder revolutions per combustion cycle. To simplify the next steps, λ is assumed to be constant. Combining (6.9) and (6.10) with $\rho_{\mathrm{ch}} = \frac{p_{\mathrm{ch}}}{R\vartheta}$ yields

$$A_1(u_1)\sqrt{p_{\mathrm{ch}}(p_s - p_{\mathrm{ch}})} = \frac{\lambda V_d \omega_e}{\sqrt{2R\vartheta}N_r 2\pi} p_{\mathrm{ch}}. \tag{6.11}$$

This equation can be rearranged as

$$p_s = (K+1)p_{\mathrm{ch}}, \tag{6.12}$$

where

$$K = \left(\frac{\lambda V_d \omega_e}{A_1(u_1)\sqrt{2R\vartheta}N_r 2\pi}\right)^2. \tag{6.13}$$

Consequently, one can ensure that f_1 settles at $\mathcal{U}$ in steady state by computing K from (6.13) with $u_1 = \mathcal{U}$ and using (6.12) to compute the reference p_s^*. Taking (6.7) into account, one finally obtains the calculation law

$$p_s^* = \min((1+K)p_{\mathrm{ch}}, \overline{p}_s). \tag{6.14}$$

The bound $p_s > p_{\mathrm{ch}}$ is automatically met since $K > 0$.

6.2.3 Decoupling

The effective flap areas $A_1(u_1), A_2(u_2)$ are monotonic functions of the flap positions u_1, u_2. Hence, corresponding inverse functions exist. Furthermore, the pressure drops over the flaps are always positive, which allows the exact compensation of the input nonlinearities:

$$u_1 = A_1^{-1}\left(\frac{\sqrt{R\vartheta}}{\sqrt{2p_{\mathrm{ch}}(p_s - p_{\mathrm{ch}})}} q_1\right), \quad u_2 = A_2^{-1}\left(\frac{\sqrt{2R\vartheta}}{p_s} q_2\right). \tag{6.15}$$

Transformation to the new pair of inputs

$$\begin{bmatrix} w_1 \\ w_2 \end{bmatrix} := \begin{bmatrix} 1 & 0 \\ -1 & -1 \end{bmatrix} \begin{bmatrix} q_1 \\ q_2 \end{bmatrix} \tag{6.16}$$

and introducing $\delta_1 = \frac{R\vartheta}{V_1} q_e$ and $\delta_2 = \frac{R\vartheta}{V_2} q_c$ leads to

$$\frac{\mathrm{d}}{\mathrm{d}t}\begin{bmatrix} p_{\mathrm{ch}} \\ p_s \end{bmatrix} = \begin{bmatrix} \frac{R\vartheta}{V_1} & 0 \\ 0 & \frac{R\vartheta}{V_2} \end{bmatrix} \begin{bmatrix} w_1 \\ w_2 \end{bmatrix} + \begin{bmatrix} \delta_1 \\ \delta_2 \end{bmatrix}. \tag{6.17}$$

6.2.4 Controller design

For each pressure a PI-controller with a feed-forward path conditioned in the sense of [148] is used. In the case of p_{ch} a possible representation of the controller is given by

$$\begin{aligned} \frac{\mathrm{d}}{\mathrm{d}t}x_I &= k_I(p^*_{\mathrm{ch}} - p_{\mathrm{ch}}) + \frac{k_I}{k_P + k_F}(w_1 - \hat{w}_1) \\ w_1 &= k_P(p^*_{\mathrm{ch}} - p_{\mathrm{ch}}) + k_F p^*_{\mathrm{ch}} + x_I, \end{aligned} \tag{6.18}$$

where x_I, k_I, k_P, k_F, $\hat{w}_1$ are the state of the integrator, the integrator and proportional gain, the feed forward gain and the saturated control input w_1, respectively. Due to the input nonlinearities, the saturation limits for w_1 and w_2 depend on p_{ch} and p_s. In the case of w_1, for example,

$$A_1(\underline{u}_1)\sqrt{\frac{2p_{\mathrm{ch}}(p_s - p_{\mathrm{ch}})}{R\vartheta}} \le w_1 \le A_1(\overline{u}_1)\sqrt{\frac{2p_{\mathrm{ch}}(p_s - p_{\mathrm{ch}})}{R\vartheta}}. \tag{6.19}$$

For the unsaturated controller the closed-loop reference transfer function for p_{ch} is

$$T(s) := \frac{p_{\mathrm{ch}}(s)}{p^*_{\mathrm{ch}}(s)} = \frac{(k_P + k_F)s + k_I}{\frac{V_1}{R\vartheta}s^2 + k_P s + k_I}. \tag{6.20}$$

Choosing

$$k_I = \frac{V_1}{R\vartheta}\nu_n^2, \quad k_P = 2\frac{V_1}{R\vartheta}\nu_n, \quad k_F = -\frac{V_1}{R\vartheta}\nu_n \tag{6.21}$$

turns $T(s)$ into the first order lag element

$$T(s) = \frac{\nu_n s + \nu_n^2}{s^2 + 2\nu_n s + \nu_n^2} = \frac{\nu_n}{s + \nu_n}. \tag{6.22}$$

This is done to avoid overshoots of the charge pressure, which in gas engines can have harmful consequences such as knocking combustion, but still react quickly to the demands of the HiL-system. For the undamped natural frequency of the resulting system, $\nu_n = 2\pi f_n$ with $f_n = \frac{1}{2}$ Hz turned out to be a good choice. For the pressure p_s an identically structured PI-controller with $f_n = \frac{1}{6}$ Hz is used.

6.3 Gas pressure

A sketch of the fuel gas system is shown in Fig. 6.5. The natural gas fuelling the SCE is supplied by a high pressure tank system, which, for the sake of simplicity, is indicated as a single reservoir that imposes a constant pressure of $p_{\mathrm{res}} = 10$ bar on the high pressure side of the valve v_g. The pressure to be controlled is measured upstream the port injection valve of the SCE and is denoted by p_g. For modelling purposes, the crucial piping segment indicated by V is interpreted as a lumped volume. To actuate the system, a current-to-pressure (I/P)

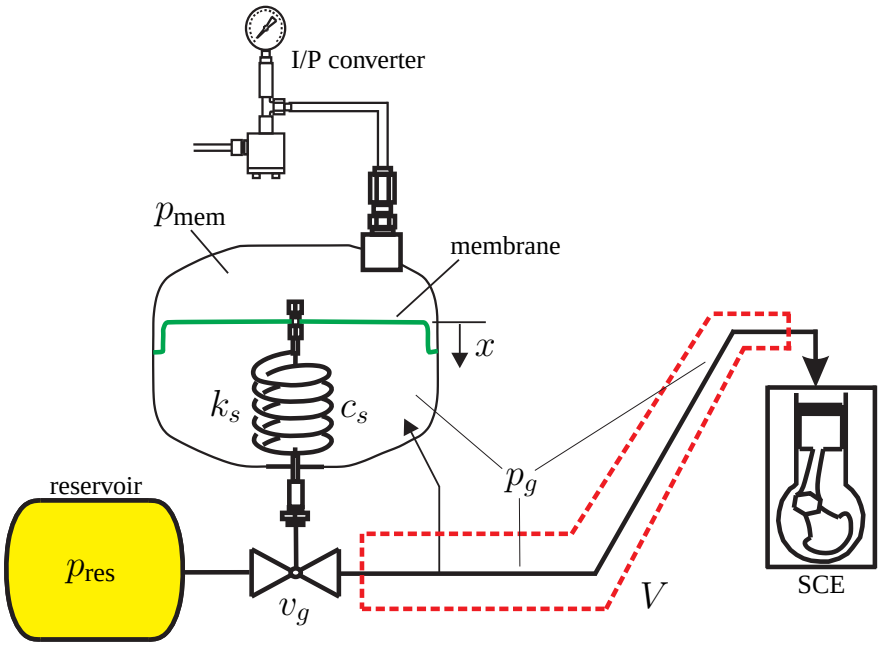

Figure 6.5: Gas supply piping on the SCE test bed.

converter turns the electrical actuation signal to an air pressure p_{mem}. That pressure is compared to p_g by means of a balancing membrane close to the pipe [143, 149]. In case of a difference, the membrane experiences a force that pushes or stretches a spring underneath. The spring acts on a rod that eventually opens or closes the valve v_g. As the I/P converter is by far faster than the membrane or the gas pressure p_g, the pressure p_{mem} is considered as the control input. The vertical position of the membrane is denoted by x. The quantities k_s, c_s and F_{s0} represent the stiffness, the damping and the pre-load force of the spring, respectively.

6.3.1 Modelling

With q_g and q_e denoting the gas flows passing v_g and entering the SCE, respectively, the pressure p_g is governed by the differential equation

$$\frac{\mathrm{d}}{\mathrm{d}t}p_g = \frac{R\vartheta}{V}(q_g - q_e). \tag{6.23}$$

The mass flow q_g is given by a relation similar to (6.4). As $p_{\text{res}} \approx 10\,\text{bar}$, the pressure drop over v_g is large enough for the second case in (6.5) to be valid throughout operation. This leads to

$$q_g = A_v(x)\frac{p_{\text{res}}}{\sqrt{2R\vartheta}}, \tag{6.24}$$

where $A_v(x)$ represents the effective opening area of v_g as a function of x. As the membrane performs small movements only, $A_v(x)$ may be linearised around $x = 0$, finally leading to the model

$$q_g \approx k_q x + d_q \tag{6.25}$$

with

$$k_q := \frac{p_{\text{res}}}{\sqrt{2R\vartheta}} \left.\frac{dA_v(x)}{dx}\right|_{x=0}, \qquad d_q := \frac{p_{\text{res}}}{\sqrt{2R\vartheta}} A_v|_{x=0}\,. \tag{6.26}$$

To capture the dynamics of the membrane, Newton's second law is applied. With m for the mass of the membrane one obtains

$$m\frac{\mathrm{d}^2}{\mathrm{d}t^2}x = F_p - F_s. \tag{6.27}$$

Therein F_s and F_p denote the forces resulting from the spring and the pressure difference on the two sides of the membrane, respectively. Introducing A for the membrane area, F_p and F_s can be expressed as

$$F_p = A(p_{\text{mem}} - p_g) \quad \text{and} \quad F_s = F_{s0} + k_s x + c_s \dot{x}. \tag{6.28}$$

Combining the last equations leads to a linear, third order state-space model:

$$\begin{aligned}\frac{\mathrm{d}}{\mathrm{d}t}\begin{bmatrix} x \\ \dot{x} \\ p_g \end{bmatrix} = &\begin{bmatrix} 0 & 1 & 0 \\ -\frac{k_s}{m} & -\frac{c_s}{m} & -\frac{A}{m} \\ k_q\frac{R\vartheta}{V} & 0 & 0 \end{bmatrix}\begin{bmatrix} x \\ \dot{x} \\ p_g \end{bmatrix} + \\ &\begin{bmatrix} 0 & 0 & 0 & 0 \\ \frac{A}{m} & -\frac{1}{m} & 0 & 0 \\ 0 & 0 & -\frac{R\vartheta}{V} & 1 \end{bmatrix}\begin{bmatrix} p_{\text{mem}} \\ F_{s0} \\ q_e \\ d_q \end{bmatrix}.\end{aligned} \tag{6.29}$$

The transfer function from p_{mem} to p_g follows as

$$P(s) = \frac{\frac{A}{m}k_q\frac{R\vartheta}{V}}{s^3 + \frac{c_s}{m}s^2 + \frac{k_s}{m}s + \frac{A}{m}k_q\frac{R\vartheta}{V}}, \tag{6.30}$$

which allows an interesting insight into the stability properties of the system. Applying the Routh-Hurwitz criterion, see e.g. [33, 34], to (6.30) yields

$$k_s > Ak_q\frac{R\vartheta}{V}\frac{m}{c_s} =: k_{s,\min}. \tag{6.31}$$

This means that for reasons of stability k_s has to exceed a certain minimum value depending on c_s and cannot be chosen arbitrarily! Another property of the system can be seen from the steady-state version of (6.29), namely

$$p_{g,\infty} = p_{\text{mem},\infty} - \frac{F_{s,0}}{A} - \frac{k_s}{A}\frac{q_e}{k_V}, \tag{6.32}$$

which implies that due to $F_{s,0}$ and q_e the two pressures can never match exactly.

6.3.2 Controller design

A PI-controller with the same structure as in Section 6.2.4 is used, which in the Laplace domain is given by

$$p_{\text{mem}}(s) = k_F p_g^*(s) + \frac{k_P s + k_P}{s}\left[p_g^*(s) - p_g(s)\right]. \tag{6.33}$$

Due to (6.32) the feed-forward gain is set to $k_F = 1$. Unfortunately, q_e is not known accurately enough to make further use of that relation for compensation purposes. Combined with (6.30) one obtains the closed-loop transfer-function

$$T(s) = \frac{p_g(s)}{p_g^*(s)} = \frac{(1+k_p)\frac{A}{m}k_q\frac{R\vartheta}{V}s + K_I\frac{A}{m}k_q\frac{R\vartheta}{V}}{s^4 + \frac{c_s}{m}s^3 + \frac{k_s}{m}s^2 + (1+k_p)\frac{A}{m}k_q\frac{R\vartheta}{V}s + k_i\frac{A}{m}k_q\frac{R\vartheta}{V}}, \tag{6.34}$$

where again the Routh-Hurwitz criterion is a useful tool to gain insight into the system. The denominator is a fourth order polynomial. In the general case, i.e.

$$v(s) = s^4 + a_3 s^3 + a_2 s^2 + a_1 s + a_0, \tag{6.35}$$

all coefficients have to be positive and the conditions

$$a_3 a_2 > a_1 \quad (a_3 a_2 - a_1)a_1 > a_3^2 a_0 \tag{6.36}$$

have to be fulfilled to ensure stability. Equation (6.36) can be applied to the denominator of (6.34), leading to

$$k_p < \frac{k_s}{k_{s,\min}} - 1, \qquad k_i < \frac{k_s - k_{s,\min}(1+k_p)}{c_s}(1+k_p). \tag{6.37}$$

The first inequality shows that high proportional gains have a destabilizing effect. Indeed, $k_p = 0$ turned out to be a good choice for the practical implementation. This narrows the interval for k_i to

$$k_i < \frac{k_s - k_{s,\min}}{c_s}, \tag{6.38}$$

but since $k_s - k_{s,\min} \gg c_s$, the integrator gain can be used reasonably. In practice,

$$k_i = \frac{9}{10}\frac{k_s - k_{s,\min}}{c_s}. \tag{6.39}$$

was selected.

6.4 Experimental results

The following section provides a comparison between the proposed controllers and their predecessors on the considered SCE test bed. The latter are PI-controllers that were designed mainly for steady-state tests, without any decoupling or feed-forward paths. The flap influencing the supply pressure in the charge air control setup is slowly varied whenever the charge air pressure controller is in saturation. Additionally, measurement data from the MCE is compared to results obtained with the presented HiL-system.

6.4.1 Charge air pressure

To validate the charge air and fuel gas pressure controllers, consecutive load ramps and drops were performed with both the original and the presented controller. Figs. 6.6, 6.7 and 6.8 depict measured charge air pressure, supply pressure and flap positions for a small excerpt of these experiments. Due to the security concept of the test bed the position of flap f_1 is bounded by $\underline{u}_1 = 0$ and $\overline{u}_1 = 50$. Hence, the desired steady state position is $\mathcal{U} = 25$. With the new controller, the supply pressure p_s behaves such that flap values close to $\mathcal{U}$ are attained in all steady state phases. Generally, one can see that the proposed controller is able to track the desired charge air trajectory more accurately with almost no overshoot.

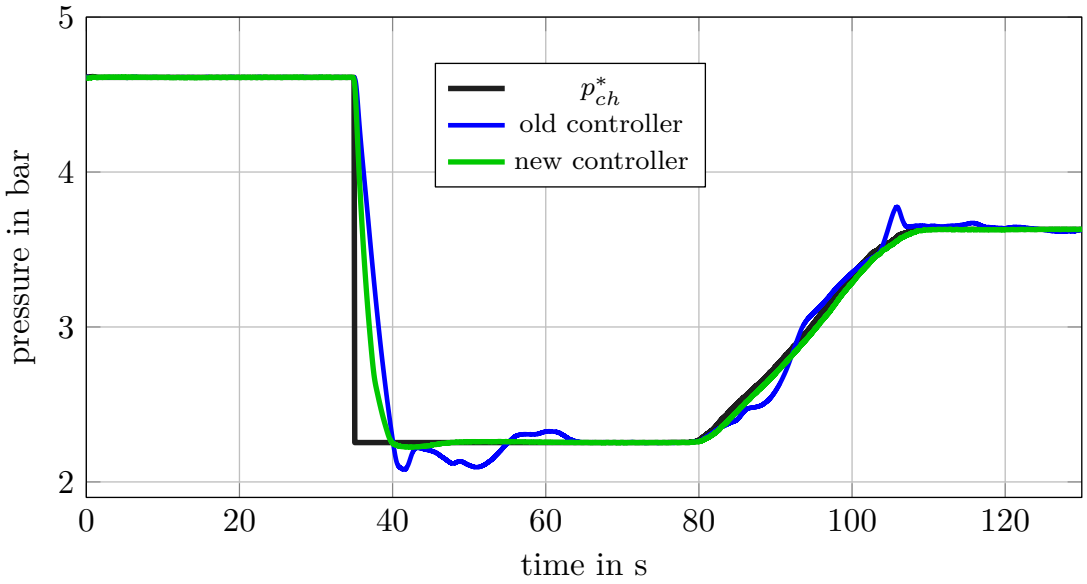

Figure 6.6: Charge pressure.

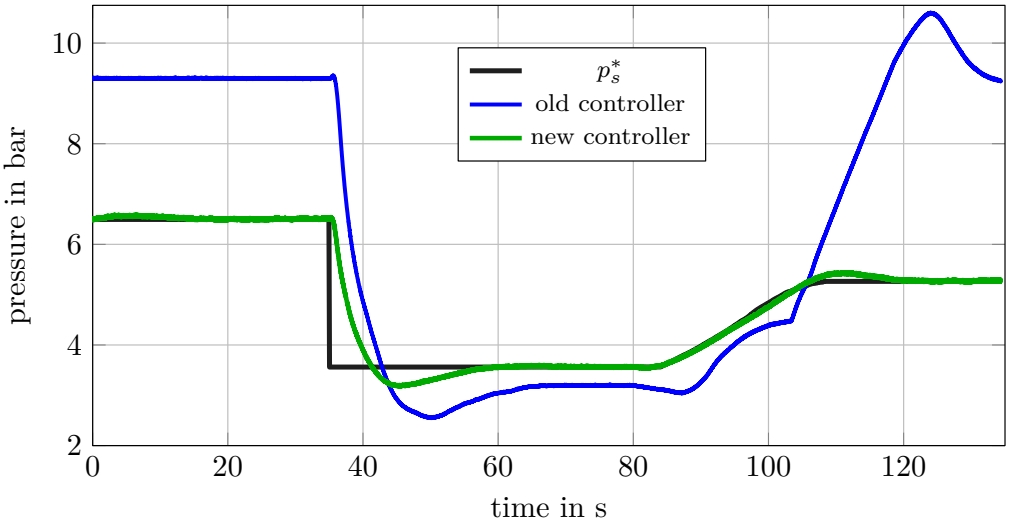

Figure 6.7: Supply pressure.

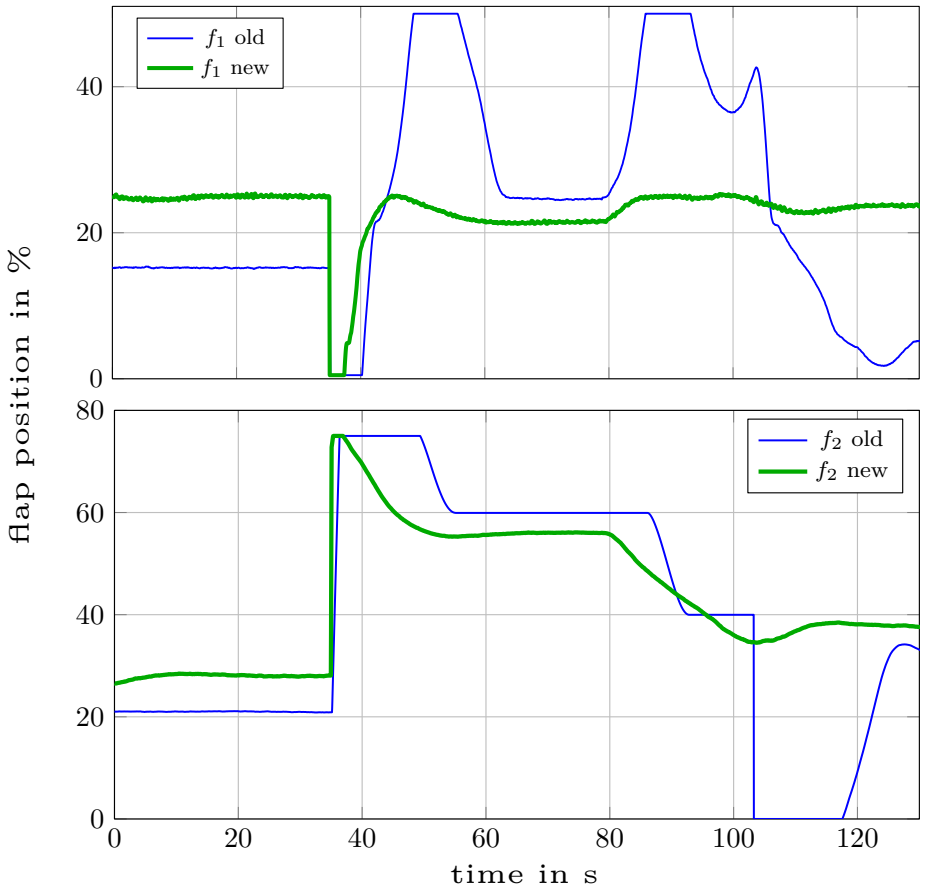

Figure 6.8: Flap positions of f_1 and f_2.

6.4.2 Gas pressure

Fig. 6.9 shows the fuel gas pressure during a load ramp. While the original controller exhibits a significant delay in tracking the reference, the new controller follows the trajectory with very small deviations. This is mainly due to the feed-forward path of the new controller, which anticipates the steady-state relation between p_{mem} and p_g.

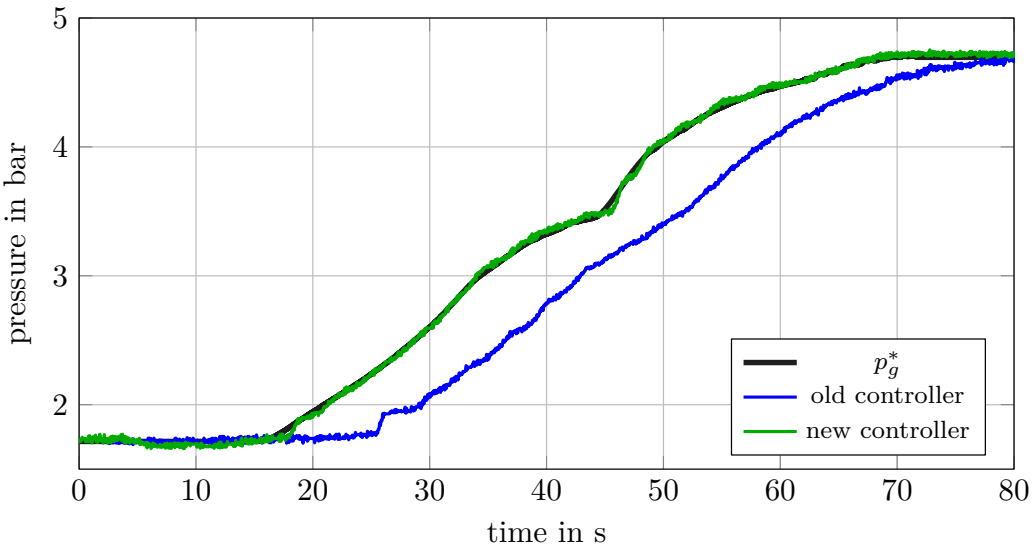

Figure 6.9: Gas pressure p_g.

6.4.3 HiL-system

Fig. 6.10 presents a sudden load step realized by connecting an additional electrical resistor to the MCE generator in parallel. In the HiL-system the temperature dependency of the load system is not modelled, which leads to a deviation from the MCE behavior in terms of the initial overshoot. Due to the imbalance of mechanical and electrical power the engine speed drops (Fig. 6.10 (b)). To recover the original engine speed, the corresponding control units reduce the generator voltage and hence the electrical power (Fig. 6.10 (a)).

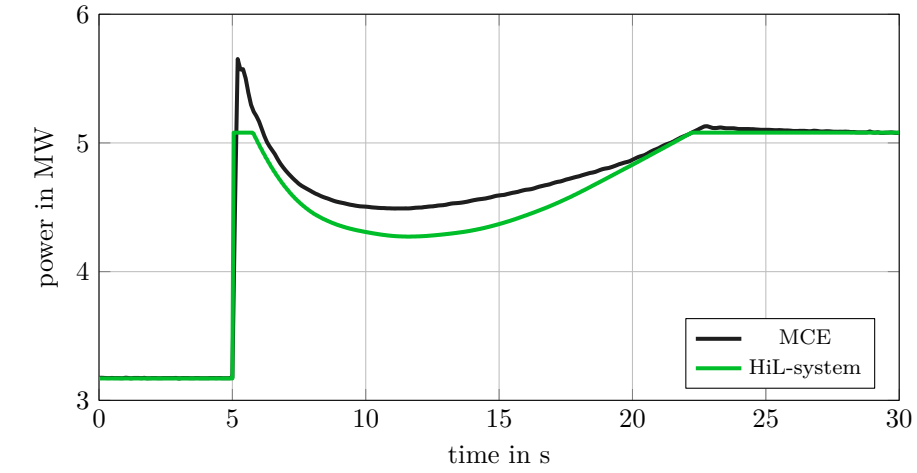

(a) electrical Power

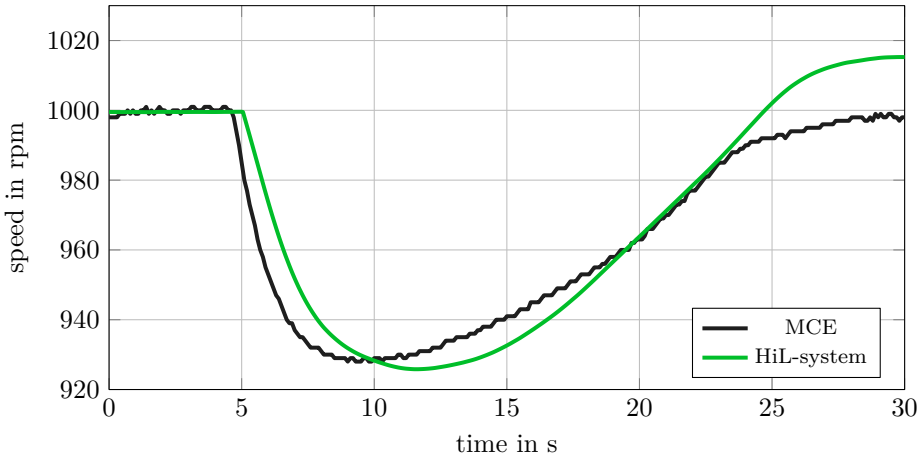

(b) engine speed

Figure 6.10: MCE measurement vs HiL-system.

6.5 Conclusion and outlook

This chapter demonstrates how the behaviour of two test bed controllers for media pressures can be improved significantly by simple but effective model based control techniques. The test bed and the discussed controllers are embedded in a methodology to transfer the transient behaviour of a large bore MCE to an SCE HiL-system. Physics-based real-time models are created that are able to provide the boundary conditions for combustion from an MCE during transient operation. It is shown that transient testing on large bore SCE test beds is a feasible task.

Appendix

Appendix A

Parameters of the Drive Line Models

A.1 Straight chain of inertias

Table A.1 summarizes the parameter values that were used to simulate the first setup of the heavy-duty test bed with only one additional flange, as displayed in e.g. Fig. 2.11(a). As explained in Figs. 2.18, $I_{5,1}$ stands for the first value that is assigned to the last inertia of the chain, which is incremented by the inertia values of the added flanges. One can see that the algorithm tends to assign values to the parameters that can only hardly be motivated physically, for instance, the first three inertias together by far exceed the induction machines inertia of 24kgm^2, and also the damping parameters are not physical: Particularly

model data		
parameter	unit	value
I_1	kgm^2	25.082
I_2	kgm^2	6.352
I_3	kgm^2	1.572
I_4	kgm^2	0.159
$I_{5,1}$	kgm^2	0.140
k_1	MNm·rad^{-1}	60.99
k_2	MNm·rad^{-1}	17.99
k_3	MNm·rad^{-1}	3.36
k_4	MNm·rad^{-1}	6.28
c_1	Nms·rad^{-1}	850.4
c_2	Nms·rad^{-1}	800.0
c_3	Nms·rad^{-1}	0.0
c_4	Nms·rad^{-1}	0.0

Table A.1: Parameters of the straight-chain-of-inertias model.

the first two damping parameters are critical to some extent, as they violate the assumption of low damping, which leads to deviations between practical resonance and eigenmode-frequency. These attributes can already be seen as signs of the wrong modelling approach. As mentioned in Sec. 2.2.7, MATLAB's *fmincon* algorithm was used to find the numerical values shown in Tab. A.1. The settings and the inequality bounds used for the algorithm in are listed in Tabs. A.2 and A.3, respectively.

	lower bound	unit	upper bound
I_1	22.5	kgm^2	25.5
I_2	0.01	kgm^2	10.0
I_3	0.01	kgm^2	10.0
I_4	0.01	kgm^2	10.0
I_5	0.01	kgm^2	10.0
k_1	0.1	$\mathrm{MNm{\cdot}rad}^{-1}$	100
k_2	0.1	$\mathrm{MNm{\cdot}rad}^{-1}$	100
k_3	0.1	$\mathrm{MNm{\cdot}rad}^{-1}$	100
k_4	0.1	$\mathrm{MNm{\cdot}rad}^{-1}$	100
c_1	0	$\mathrm{Nms{\cdot}rad}^{-1}$	1000
c_2	0	$\mathrm{Nms{\cdot}rad}^{-1}$	1000
c_3	0	$\mathrm{Nms{\cdot}rad}^{-1}$	1000
c_4	0	$\mathrm{Nms{\cdot}rad}^{-1}$	1000

Table A.2: Upper and lower bounds for the sought parameters used for optimization.

optimization settings	
parameter	value
TolFun	10^{-9}
TolCon	10^{-9}
MaxIter	10^6
MaxFunEvals	$4 \cdot 10^6$

Table A.3: Settings for the *fmincon* optimization algorithm.

A.2 Alternative chain of inertias

Table A.2 displays the values that were used to parametrize the finally used alternative structure of inertias, as shown in Fig. 2.26, where the damping and stiffness parameters are not mentioned in order to preserve a clear structure. In the following table, (k_{12}, c_{12}) denotes the connection between I_1 and I_2, (k_{13}, c_{13}) the one between I_1 and I_3, (k_{23}, c_{23}) the one between I_2 and I_3, (k_{24}, c_{24}) the one between I_2 and I_4, and lastly, (k_{25}, c_{25}) the one between I_2 and I_5.

model data		
parameter	unit	value
I_1	kgm^2	23.534
I_2	kgm^2	0.285
I_3	kgm^2	0.475
I_4	kgm^2	0.045
$I_{5,1}$	kgm^2	0.198
k_{12}	$\mathrm{MNm{\cdot}rad}^{-1}$	4.95
k_{13}	$\mathrm{MNm{\cdot}rad}^{-1}$	8.16
k_{23}	$\mathrm{MNm{\cdot}rad}^{-1}$	1.00
k_{24}	$\mathrm{MNm{\cdot}rad}^{-1}$	0.29
k_{25}	$\mathrm{MNm{\cdot}rad}^{-1}$	10.25
c_{12}	$\mathrm{Nms{\cdot}rad}^{-1}$	1.7
c_{13}	$\mathrm{Nms{\cdot}rad}^{-1}$	2.3
c_{23}	$\mathrm{Nms{\cdot}rad}^{-1}$	1.2
c_{24}	$\mathrm{Nms{\cdot}rad}^{-1}$	1.2
c_{25}	$\mathrm{Nms{\cdot}rad}^{-1}$	14.5

Table A.4: Parameters of the alternative structure comprising three parallel inertias.

The evolving parameter values are much closer to what one might intuitively assume. With regards to the optimization algorithm, the same settings as shown in Tab. A.3 were used again, and also the same bounds for inertias, stiffness and damping parameters were employed.

A.3 Soft-rotor model

Table A.5 displays the values that were used to parametrize the model for the heavy-duty test bed comprising the soft rotor, as shown in Fig. 2.31.

model data		
parameter	unit	value
I_1	kgm^2	25.308
I_4	kgm^2	0.235
$I_{5,1}$	kgm^2	0.159
k_{im}	$\mathrm{MNm{\cdot}rad}^{-1}$	16.5
k_3	$\mathrm{MNm{\cdot}rad}^{-1}$	5.1
k_4	$\mathrm{MNm{\cdot}rad}^{-1}$	7.99
c_{im}	$\mathrm{Nms{\cdot}rad}^{-1}$	85.6
c_3	$\mathrm{Nms{\cdot}rad}^{-1}$	18.2
c_4	$\mathrm{Nms{\cdot}rad}^{-1}$	23.0

Table A.5: Parameters of the soft-rotor-model used for the heavy-duty test bed.

To obtain the parameters listed above, a rough estimate for I_1 and k_{im} and the sum of I_4 and I_5 was obtained first by the means of the analytical approach explained in Sec. 2.3.1, by neglecting the external two-mass oscillator and assuming the external inertia to be pinned to the right end of the rotor. These results later on served as the basis for a numerical optimization, as for the lumped structures discussed previously. For the latter, the *fmincon* algorithm provided by MATLAB was used again. To that end, the bounds listed below were used, along with again the settings presented in Tab. A.3. As discussed earlier, the soft rotor was subdivided into 100 partial inertias.

	lower bound	unit	upper bound
I_1	22.5	kgm^2	25.5
I_4	0.01	kgm^2	10.0
I_5	0.01	kgm^2	10.0
k_{im}	0.1	$\mathrm{MNm{\cdot}rad}^{-1}$	100
k_3	0.1	$\mathrm{MNm{\cdot}rad}^{-1}$	100
k_4	0.1	$\mathrm{MNm{\cdot}rad}^{-1}$	100
c_{im}	0	$\mathrm{Nms{\cdot}rad}^{-1}$	1000
c_3	0	$\mathrm{Nms{\cdot}rad}^{-1}$	1000
c_4	0	$\mathrm{Nms{\cdot}rad}^{-1}$	1000

Table A.6: Upper and lower bounds for the sought parameters used for optimization.

model data		
parameter	unit	value
I_1	kgm^2	4.813
I_4	kgm^2	0.137
$I_{5,1}$	kgm^2	0.081
k_{im}	$\mathrm{MNm{\cdot}rad}^{-1}$	8.90
k_3	$\mathrm{MNm{\cdot}rad}^{-1}$	5.76
k_4	$\mathrm{MNm{\cdot}rad}^{-1}$	6.37
c_{im}	$\mathrm{Nms{\cdot}rad}^{-1}$	28.4
c_3	$\mathrm{Nms{\cdot}rad}^{-1}$	5.5
c_4	$\mathrm{Nms{\cdot}rad}^{-1}$	125.1

Table A.7: Parameters of the soft-rotor-model as used for the R2R test bed.

For the R2R test bed, the parameters listed in Tab. A.7 were used. To get hold of the parameters, the same procedure as for the heavy-duty test bed was used at this point, too, consisting of hand design and numerical optimization. For the latter, almost identical settings have been used, this time based on a division of the machine rotor into 70 partial inertias. The only differing aspect were the bounds for the induction machine inertia, which was, again based on data-sheet information, in this case restricted to $3 \leq I_1 \leq 5$.

Appendix B

A Special Mechanical Structure

To simulate the considered test bed drive lines, the distributed-parameter body for the induction machine rotor was extended by two lumped inertias, in order to represent, e.g., the two members of the measuring flange. For such a setup, the formalism to find the model's resonances presented in Sec. 2.3.1 cannot be used any more. This was not an issue, as the "soft" rotor had to be discretized in space again, to make it compatible with the chosen simulation platform. For this discretized version of the model, the priorly employed methods of numerical optimization could be applied again to find the parameters.

Out of pure curiosity, however, the question of whether there was a simple and practical way to include an external oscillator into the analysis of a distributed-parameter system was looked at also in the course of this work. This section presents some of the findings that were made in that regard. To begin with, Fig. B.1 depicts a distributed rotor at one of the discretized intermediate steps in the course of the continuity transformation. On its right end, the rotor is connected to spring k_4 and inertia I_5. The red box $\mathcal{O}$ ("oscillator") subsumes the external oscillator and the last inertia I_N of the rotor, while the left block $\mathcal{R}$ ("rotor") bundles the remainder of the rotor. Moreover, $\tilde{T}$ stands for the torque that is exchanged between the two parts, and damping is neglected throughout the analysis.

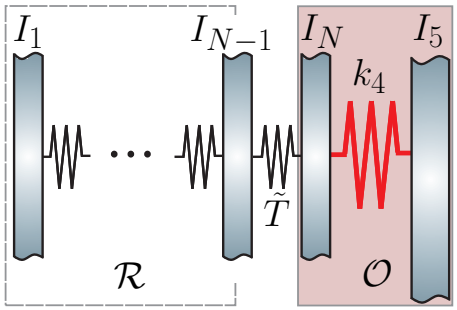

Figure B.1: Soft rotor: Including an external spring-mass system.

If O were just one lumped inertia, which would be the case if k_4 were infinitely stiff, the situation would be the same as in Sec. 2.3.1. For $k_4 < \infty$, however, O obviously behaves differently. It turns out, however, that a practical approximation for the behaviour of O can be obtained by interpreting this part of the system as a frequency-dependent lumped inertia, which also allows to use the same mathematical framework as in Sec. 2.3.1. The new quantity is denoted by $I_o(\nu)$, and a rather *qualitative* and *heuristic* reasoning is employed at this point, in order to obtain a mathematical description for it: In case the system is excited at the resonance of the external oscillator, which is given by

$$\tilde{\nu}_0 = \sqrt{\frac{k_4}{I_5}}, \tag{B.1}$$

I_5 will oscillate against I_N, such that the latter in steady-state comes to rest and acts towards $\mathcal{R}$ as if it were infinitely large. If, on the contrary, the excitation frequency coincides with the resonance

$$\tilde{\nu}_r = \sqrt{k_4(\frac{1}{I_1} + \frac{1}{I_5})} \tag{B.2}$$

of the two-mass-oscillator comprising I_1, k_4 and I_5, the movement at the right end of the chain will be large, giving the impression of a very small inertia. This motivates

$$I_0(\nu) = I_5 \frac{\nu - \tilde{\nu}_r}{\nu - \tilde{\nu}_0} \tag{B.3}$$

as a description of the frequency dependent inertia $I_0(\nu)$, which may be inserted into the eigenfrequency-equation (2.111) and leads to

$$-qL\,\mathrm{cotan}(qL) = \frac{I_1}{I_5}\frac{\nu - \tilde{\nu}_0}{\nu - \tilde{\nu}_r}. \tag{B.4}$$

The effect of this measure is shown in Fig. B.2, by the means of an academic example system:

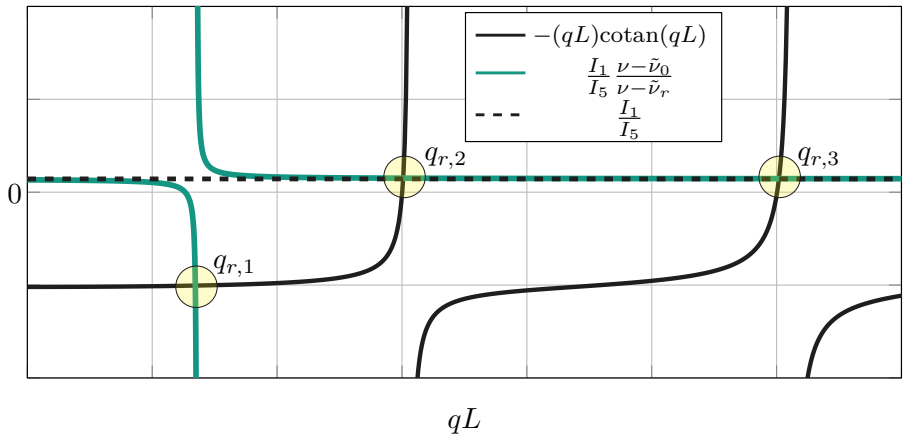

Figure B.2: Eigenfrequency equation with frequency-dependent inertia.

parameter	unit	value
I_1	kgm^2	20
k_{im}	$\mathrm{MNm{\cdot}rad}^{-1}$	30
I_5	kgm^2	0.35
k_4	$\mathrm{MNm{\cdot}rad}^{-1}$	1

Table B.1: Example system for the frequency-dependent lumped inertia approach.

The parameters used to obtain Fig. B.2 are listed in Tab. B.1. One can see that the first resonance frequency $q_{r,1}$, which is predicted by the extended version of the eigenfrequency equation, is not contained in the classical version with the constant $\frac{I_1}{I_5}$ on the right hand side. Using the values listed above, the predicted value of the corresponding time frequency results as $\nu_{r_1} = 2\pi 269.1 \frac{rad}{s}$, and corresponds almost perfectly to the result obtained by the means of a numerical computation based on 1000 partial inertias, which suggests $\nu_{r_1} = 2\pi 269.7 \frac{rad}{s}$. The proposed method apparently works well for this case; it must be pointed out, however, that (B.4) is by no means an exact formula for the resonances produced by the structure shown in Fig. B.1. However, if one keeps in mind that the result of this section is a rather rough and empirical finding, it may be a valuable tool, for instance, when a quick estimate about the resonance frequencies of a hybrid lumped-distributed mechanical structure such as Fig. B.1 or Fig. 2.31 is needed.

Appendix C

Parameters of the Backlash Test Bed

Lenze MCA14L16		
rated parameter	unit	value
power	kW	2.1
speed	rpm	1635
torque	Nm	12
current	A	4.8
voltage	V	390
no. of pole pairs	–	2

Table C.1: Nominal parameters of the induction machines.

backlash-shaft		
backlash gap	degrees	11
length	mm	300
diameter	mm	30
stiffness	kNm· rad^{-1}	15
damping	Nms· rad^{-1}	0.5
direct damping c_f	Nms· rad^{-1}	0.1

Table C.2: Shaft properties.

model data		
parameter	unit	value
I_1	kgm^2	$2.6 \cdot 10^{-3}$
I_2	kgm^2	$0.5 \cdot 10^{-3}$
I_3	kgm^2	$28.3 \cdot 10^{-3}$
I_4	kgm^2	$15.5 \cdot 10^{-3}$
I_5	kgm^2	$2.8 \cdot 10^{-3}$
I_6	kgm^2	$6.0 \cdot 10^{-3}$
I_7	kgm^2	$2.6 \cdot 10^{-3}$
I_8	kgm^2	$0.6 \cdot 10^{-3}$
I_9	kgm^2	$2.6 \cdot 10^{-3}$
k_1	$\mathrm{kNm{\cdot}rad}^{-1}$	14.6
k_2	$\mathrm{kNm{\cdot}rad}^{-1}$	18.1
k_3	$\mathrm{kNm{\cdot}rad}^{-1}$	26.9
k_4	$\mathrm{kNm{\cdot}rad}^{-1}$	17.6
k_5	$\mathrm{kNm{\cdot}rad}^{-1}$	10.4
k_6	$\mathrm{kNm{\cdot}rad}^{-1}$	11.3
k_7	$\mathrm{kNm{\cdot}rad}^{-1}$	34.5
c_1	$\mathrm{Nms{\cdot}rad}^{-1}$	0.07
c_2	$\mathrm{Nms{\cdot}rad}^{-1}$	0.01
c_3	$\mathrm{Nms{\cdot}rad}^{-1}$	2.0
c_4	$\mathrm{Nms{\cdot}rad}^{-1}$	0.01
c_5	$\mathrm{Nms{\cdot}rad}^{-1}$	0.1
c_6	$\mathrm{Nms{\cdot}rad}^{-1}$	0.01
c_7	$\mathrm{Nms{\cdot}rad}^{-1}$	0.15

Table C.3: Parameters of the drive line model of the test bed used for backlash experiments.

Appendix D

Notch Filter Properties

In this work, the considered notch filters are described by

$$H(z) := \frac{y(z)}{u(z)} = K\frac{1 - 2\cos(v_0)z^{-1} + z^{-2}}{1 - 2rcos(v_0)z^{-1} + r^2z^{-2}} =: K\frac{m(z)}{n(z)}, \tag{D.1}$$

a z-transfer function with the numerator and denominator polynomials $m(z)$ and $n(z)$, respectively, the discrete notch frequency v_0, which can be derived from a continuous time frequency via $v_0 = v_{cont}T_d$, and the so-called pole radius r, which is restricted to $0 < r \leq 1$. The scaling factor $K = \frac{1+r^2-2r\cos(v_0)}{2-2\cos(v_0)}$ adjusts the filter-gain at $v = 0$ the notch to 0dB. A typical pole-zero-diagram for this kind of filter is shown in Fig. D.1.

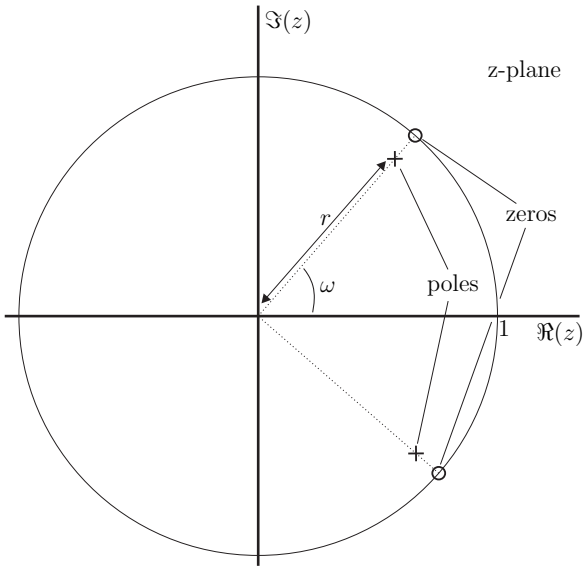

Figure D.1: Exemplary pole-zero diagram of the considered type of notch filters.

To understand the effect of the filter, one may take a look at its frequency response

$$H(e^{j\nu}) = K\frac{1 - 2\cos(\nu_0)e^{-j\nu} + e^{-j2\nu}}{1 - 2rcos(\nu_0)e^{-j\nu} + r^2e^{-j2\nu}} =: \frac{m(e^{j\nu})}{n(e^{j\nu})}. \tag{D.2}$$

One can see that for $r = 1$, numerator $m(e^{j\nu})$ and denominator $n(e^{j\nu})$ cancel out, which degenerates the filter to $H(e^{j\nu}) = K|_{r=1} = 1$. Extracting $e^{j\nu}$ in both $m(e^{j\nu})$ and $n(e^{j\nu})$, one obtains

$$\begin{aligned} H(e^{j\nu}) &= K\frac{\cancel{e^{-j\nu}}\left(e^{j\nu} - 2\cos(\nu_0) + e^{-j\nu}\right)}{\cancel{e^{-j\nu}}\left(e^{j\nu} - 2r\cos(\nu_0) + r^2e^{-j\nu}\right)} \\ &= K\frac{\cos(\nu) - \cos(\nu_0)}{r^2\cos(\nu) - r\cos(\nu_0) + \frac{1-r^2}{2}e^{j\nu}} =: K\frac{\tilde{m}(e^{j\nu})}{\tilde{n}(e^{j\nu})}, \end{aligned} \tag{D.3}$$

where the filtering effect can be seen nicely, as obviously

$$\tilde{m}(e^{j\nu_0}) = \cos(\nu_0) - \cos(\nu_0) = 0. \tag{D.4}$$

Taking a look at $\nu = 0$, the impact of the scaling factor K becomes clear:

$$\begin{aligned} H(e^{j0}) = K\frac{\tilde{m}(e^{j0})}{\tilde{n}(e^{j0})} &= \frac{1 + r^2 - 2r\cos(\nu_0)}{2 - 2\cos(\nu_0)}\frac{1 - \cos(\nu_0)}{r^2 - r\cos(\nu_0) + \frac{1-r^2}{2}} \\ = \quad \frac{\cancel{\frac{1+r^2}{2} - r\cos(\nu_0)}}{\cancel{1 - \cos(\nu_0)}}\frac{\cancel{1 - \cos(\nu_0)}}{\cancel{\frac{1+r^2}{2} - r\cos(\nu_0)}} \quad &= \quad 1. \end{aligned} \tag{D.5}$$

To assess the influence of $H(e^{j\nu})$ on frequencies besides ν_0, one may take a look at its amplitude response, which is given by

$$\begin{aligned} |H(e^{j\nu})| = \quad |K| \quad &\cdot \quad \frac{|\cos(\nu) - \cos(\nu_0)|}{|r^2\cos(\nu) - r\cos(\nu_0) + \frac{1-r^2}{2}e^{j\nu}|} \\ = \quad \frac{|\cos(\nu) - \cos(\nu_0)|}{|1 - \cos(\nu_0)|} \quad &\cdot \quad \frac{|\frac{1+r^2}{2} - r\cos(\nu_0)|}{|\frac{1+r^2}{2}\cos(\nu) - r\cos(\nu_0) + j\frac{1-r^2}{2}\sin(\nu)|}. \end{aligned} \tag{D.6}$$

As already pointed out by the plots presented in Figs. 5.4, a smaller pole radius r grows the notch of the filter, and thus decreases the magnitude of $H(e^{j\nu})$ for $\nu \approx \nu_0$. Frequencies $\nu \gg \nu_0$ have to be treated with care, however. If ν approaches the largest possible frequency, i.e. $\nu = \pi$, then $\cos(\nu) = -1$ and $\sin(\nu) = 0$. This turns (D.6) into

$$|H(e^{j\pi})| = \frac{|-1 - \cos(\nu_0)|}{|1 - \cos(\nu_0)|}\frac{|\frac{1+r^2}{2} - r\cos(\nu_0)|}{|-\frac{1+r^2}{2} - r\cos(\nu_0)|} = \frac{|1 + \cos(\nu_0)|}{|1 - \cos(\nu_0)|}\frac{|\frac{1+r^2}{2} - r\cos(\nu_0)|}{|\frac{1+r^2}{2} + r\cos(\nu_0)|}, \tag{D.7}$$

which can become exceptionally large, especially if both r *and* ν_0 are small! High gains at high frequencies lead to an unnecessary amplification of measurement noise, which can

severly deteriorate the performance of the control system. Hence, r should be larger than 0.95 in any case. To analyse the phase response of the filter, it suffices to investigate the denominator $\tilde{n}(e^{j\nu})$ of (D.3), as $\tilde{m}(e^{j\nu})$ and K are exclusively real-valued. One finds

$$\tilde{n}(e^{j\nu}) = \frac{1+r^2}{2}\cos(\nu) - r\cos(\nu_0) + j\frac{1-r^2}{2}\sin(\nu), \tag{D.8}$$

whose imaginary part grows for a decreasing r at *any* frequency, which increases the angle between real- and imaginary part, and ultimately raises the phase shift that is introduced by $H(z)$.

Appendix E

Resonance Identification

Equations (5.31), (5.33), (5.35) and (5.36) provide several reasonable conditions that undoubtedly need to be checked before a frequency is passed on to a notch filter. As discussed in Section 5.5.5, however, if T_{load} is not restricted by any means, it is theoretically possible to construct a *diabolic* sequence of T_{load}, that causes the proposed suppression algorithm to converge towards wrong frequencies, no matter how involved and sophisticated the prior scrutiny of T_{load} is.

Despite this unfortunate - even if rather theoretical - consideration, the question of further refining the set of checks to target the origin of a T_{shaft}-component is an ongoing issue of interest. Serving this purpose, the present section outlines an additional idea, which could be added to the list of checks that is put forward in Section 5.5. It must be noted, though, that the following concept has not yet been tested on a real test bed.

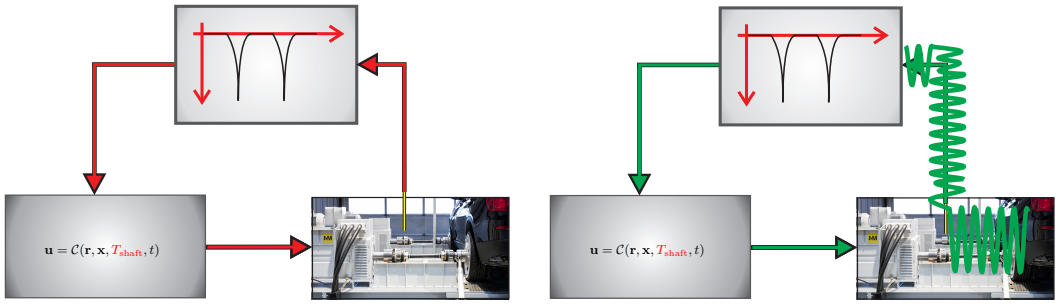

(a) Unstable resonance. (b) External excitation.

Figure E.1: Effect of active notch filter on the two oscillation scenarios.

At first, one may recall that an oscillation due to instability is an intrinsic procedure *inside* the control loop. This means that the properties and characteristics of the evolving oscillation depend on the structure and the parametrization of the loop. Most prominently, the open loop phase shift, whose value is strongly influenced by the actuator dynamics,

must be equal to -180°. On the contrary, an *external* influence is in essence *independent* from controller, actuator, or any other test bed component[1]. These situations are depicted in Figs. E.1, and suggest that the activation of an appropriate notch filter eliminates an oscillation due to resonance, while in the opposite case of external excitation, the oscillation does not disappear. Hence, a possible strategy to differentiate between the two scenarios is to pause the overall adaptation process, start an encapsulated *identification-process* that consists of positioning a notch filter at a found frequency, and inspect whether the considered spectral component of T_{shaft} indeed vanishes. Unfortunately, this approach requires a severe modification of the control loop in any case, *also* if it later on turns out that the notch filter should be deactivated again.

To avoid this drawback, a "softer" implementation of the proposed *identification-process* is derived in the following. The first step therefore is to interpret the activation of a notch filter as the process of gradually decreasing its pole radius r. As explained in Appendix D, the effect of the considered notch filters disappears for $r = 1$, while it is maximized for $r = 0$. This means that decreasing the pole radius grows the magnitude notch *and* increases the phase shift that is introduced. A direct consequence thereof is that the -180° condition can no longer be fulfilled at exactly the initially found frequency. Moreover, if r is decreased only marginally from 1, and if stability is not restored again for the given value of r, then the frequency of the observed oscillation will change – to the next spot where the -180° condition holds again! This insight may be used to outline a new strategy: Starting with a first frequency estimate that fulfils conditions (5.31), (5.33), (5.35) and (5.36), a notch filter with a pole radius very close to 1 is activated. It is then investigated whether the frequency of the given oscillation changes accordingly. If so, the pole radius is decreased further. Mathematically, these steps may be expressed as

$$r_i(n+1) = \min\Big(1, \max\big(r_i(n) - \gamma, r_{min}\big)\Big), \tag{E.1}$$

with the real-valued design parameter $\gamma \geq 0$, and are repeated as long as necessary to restore stability. A pleasant by-product of this approach is that it automatically provides an adaptation mechanism for the pole radius, too. Nevertheless, and as mentioned before, the implementation and testing of this strategy is still in the scope of ongoing research.

[1]Clearly, there usually is a certain dependency between the torque produced by the DUT and that produced by the test bed controller. However, the questions of *when*, *with which frequency*, and *with which magnitude* a torque oscillation from the DUT occurs are usually not touched by the controller.

Bibliography

[1] K. H. Pries and J. M. Quigley, *Testing complex and embedded systems*. CRC Press, 2018.

[2] L. M. Klyatis, *Accelerated reliability and durability testing technology*. John Wiley & Sons, 2012, vol. 70.

[3] S. Mourad and Y. Zorian, *Principles of testing electronic systems*. John Wiley & Sons, 2000.

[4] R. V. Percival, C. H. Schroeder, A. S. Miller and J. P. Leape, *Environmental regulation: Law, science, and policy*. Wolters Kluwer Law & Business, 2017.

[5] B. Blackwelder, K. Coleman, S. Colunga-Santoyo, J. S. Harrison and D. Wozniak, 'The volkswagen scandal', 2016.

[6] M. Contag, G. Li, A. Pawlowski, F. Domke, K. Levchenko, T. Holz and S. Savage, 'How they did it: An analysis of emission defeat devices in modern automobiles', in *2017 IEEE Symposium on Security and Privacy (SP)*, IEEE, 2017, pp. 231–250.

[7] W. Leal Filho and R. Kotter, *E-Mobility in Europe: Trends and good practice*. Springer, 2015.

[8] M. Hülsmann and D. Fornahl, *Evolutionary paths towards the mobility patterns of the future*. Springer, 2014.

[9] M. Maurer, J. C. Gerdes, B. Lenz, H. Winner *et al.*, 'Autonomous driving', *Berlin, Germany: Springer Berlin Heidelberg*, vol. 10, pp. 978–3, 2016.

[10] P. E. Ross, 'Robot, you can drive my car', *IEEE Spectrum*, vol. 51, no. 6, pp. 60–90, 2014.

[11] H. Maschmeyer, M. Kluin and C. Beidl, 'Real driving emissions — Ein Paradigmenwechsel in der Entwicklung', *MTZ-Motortechnische Zeitschrift*, vol. 76, no. 2, pp. 36–41, 2015, (in German).

[12] A. Tiwary and I. Williams, *Air pollution: measurement, modelling and mitigation*. CRC Press, 2018.

[13] A. Riedler, *Wissenschaftliche Automobil-Wertung: Berichte I-[X] des Laboratoriums für Kraftfahrzeuge an der Königlichen Technischen Hochschule zu Berlin*. R. Oldenbourg, 1912, vol. 6, (in German).

[14] B. Bond, *Vehicle demonstrating and testing device.* US Patent 1,155,126, 1915.

[15] K. Ogata and Y. Yang, *Modern control engineering*. Prentice-Hall, 2002, vol. 4.

[16] E. Ajav, B. Singh and T. Bhattacharya, 'Experimental study of some performance parameters of a constant speed stationary diesel engine using ethanol–diesel blends as fuel', *Biomass and Bioenergy*, vol. 17, no. 4, pp. 357–365, 1999.

[17] J. D. Bishop, M. E. Stettler, N Molden and A. M. Boies, 'Engine maps of fuel use and emissions from transient driving cycles', *Applied energy*, vol. 183, pp. 202–217, 2016.

[18] E. Silvas, K. Hereijgers, H. Peng, T. Hofman and M. Steinbuch, 'Synthesis of realistic driving cycles with high accuracy and computational speed, including slope information', *IEEE Transactions on Vehicular Technology*, vol. 65, no. 6, pp. 4118–4128, 2016.

[19] S. Klein, R. Savelsberg, F. Xia *et al.*, 'Engine in the loop: Closed loop test bench control with real-time simulation', *SAE International journal of commercial vehicles*, vol. 10, no. 2017-01-0219, pp. 95–105, 2017.

[20] T. Jung, M. Kötter, J. Schaub *et al.*, 'Engine-in-the-loop: A method for efficient calibration and virtual testing of advanced diesel powertrains', in *Simulation und Test 2018*, Springer, 2019, pp. 209–224.

[21] C. Gühmann, J. Riese and K. Von Rüden, *Simulation and Testing for Vehicle Technology"*. Springer, 2016.

[22] A. Michailidis, U. Spieth, T. Ringler, B. Hedenetz and S. Kowalewski, 'Test front loading in early stages of automotive software development based on autosar', in *2010 Design, Automation & Test in Europe Conference & Exhibition (DATE 2010)*, IEEE, 2010, pp. 435–440.

[23] United Nations, *Global Technical Regulation No. 4. Test procedure for compression-ignition (C.I.) engines and positive-ignition (P.I.) engines fuelled with natural gas (NG) or liquefied petroleum gas (LPG) with regard to the emission of pollutants (ECE/TRANS/180/Add.4)*, 2004.

[24] M Williams and R Minjares, 'A technical summary of euro 6/vi vehicle emission standards', *International Council for Clean Transportation (ICCT), Washington, DC, accessed July*, vol. 10, p. 2017, 2016.

[25] T. V. Johnson, 'Review of diesel emissions and control', *SAE International Journal of Fuels and Lubricants*, vol. 3, no. 1, pp. 16–29, 2010.

[26] M. Forstinger, R. Bauer, A. Hofer and W. Rossegger, 'Multivariable control of a test bed for differential gears', *Control engineering practice*, vol. 57, pp. 18–28, 2016.

[27] M. Forstinger, 'Modelling, simulation, and control of power train test beds', PhD thesis, Graz University of Technology, 2017.

[28] R. Bauer, F. Uphaus, A. Gebhardt, F. Kirschbaum, R. Jakobi and W. Rossegger, 'Agility simulation for driveability calibration on powertrain test beds', in *7th International Symposium on Development Methodology*, Wiesbaden, Germany, 2017.

[29] R. Bauer, 'New methodology for dynamic drive train testing', SAE Technical Paper, Tech. Rep., 2011.

[30] ——, 'Neues Regelkonzept für die dynamische Antriebsstrangprüfung', in *17. Steirisches Seminar über Regelungs-technik und Prozessautomatisierung*, 2011, p. 104.

[31] D. Muschick, 'Online parameter identification of induction machines', (in German), PhD thesis, Graz University of Technology, 2014.

[32] dSpace GmbH, *Ds1006 processor board*, Brochure, Accessed: 2019-06-13, 2018. [Online]. Available: https://www.dspace.com/shared/data/pdf/2018/dSPACE_DS1006_DS911_Catalog2018.pdf.

[33] M. Horn and N. Dourdoumas, *Regelungstechnik*. Pearson, 2010, (in German).

[34] W. S. Levine, *Control system fundamentals*. CRC Press, 1999.

[35] S. I. GmbH, *Application manual power semiconductors*, Accessed: 2019-06-13, 2018. [Online]. Available: https://www.semikron.com/dl/service-support/downloads/download/semikron-application-manual-power-semiconductors-english-en-2015.pdf.

[36] H. Dresig and F. Holzweißig, *Maschinendynamik*. Springer-Verlag, 2013.

[37] F. Blaschke, 'The principle of field orientation as applied to the new transvector closed-loop system for rotating-field machines', *Siemens review*, vol. 34, no. 3, pp. 217–220, 1972.

[38] S. S. Rao and F. F. Yap, *Mechanical vibrations*. Prentice hall Upper Saddle River, 2011, vol. 4.

[39] M. Wipfler, 'Control methods for torsional vibration damping at test benches', (in German), PhD thesis, Institute of Automation and Control, Graz University of Technology, 2018.

[40] D. Dinkler, *Einführung in die Strukturdynamik*. Springer, 2017, (in German).

[41] K. Janschek, *Systementwurf mechatronischer Systeme: Methoden–Modelle–Konzepte*. Springer-Verlag, 2009, (in German).

[42] J. Wittenburg, *Dynamics of multibody systems*. Springer Science & Business Media, 2007.

[43] G. Gustafson, *Pure and practical resonance in forced vibrations*, Accessed: 2019-06-13, 2008. [Online]. Available: http://www.math.utah.edu/\~gustafso/s2010/forcedVibrationsResonance2008.pdf.

[44] A. M. Mughal, *Real time modeling, simulation and control of dynamical systems*. Springer, 2016.

[45] S. Vöth, *Dynamik schwingungsfähiger Systeme: Von der Modellbildung bis zur Betriebsfestigkeitsrechnung mit MATLAB/SIMULINK®*. Springer-Verlag, 2007, (in German).

[46] M. R. Hatch, *Vibration simulation using MATLAB and ANSYS*. Chapman and Hall/CRC, 2000.

[47] N. Van Der Aa, H. Ter Morsche and R. Mattheij, 'Computation of eigenvalue and eigenvector derivatives for a general complex-valued eigensystem', *Electronic Journal of Linear Algebra*, vol. 16, no. 1, p. 26, 2007.

[48] T. Kato, *Perturbation theory for linear operators*. Springer Science & Business Media, 2013, vol. 132.

[49] R. Priesner, 'Impedance control of internal combustion engine test beds', PhD thesis, Faculty of Mechanical and Industrial Engineering, Vienna University of Technology, 2013.

[50] E. Rigaud and J. Sabot, 'Effect of elasticity of shafts, bearings, casing and couplings on the critical rotational speeds of a gearbox', *arXiv preprint physics/0701038*, 2007.

[51] J. T. Sawicki, X. Wu, G. Y. Baaklini and A. L. Gyekenyesi, 'Vibration-based crack diagnosis in rotating shafts during acceleration through resonance', in *Nondestructive Evaluation and Health Monitoring of Aerospace Materials and Composites II*, International Society for Optics and Photonics, vol. 5046, 2003, pp. 1–11.

[52] J. E. Penny and M. I. Friswell, 'The dynamics of cracked rotors', in *IMAC-XXV: A Conference & Exposition on Structural Dynamics, Orlando, FL, February*, 2007, pp. 19–22.

[53] F. Svaricek, 'Nulldynamik linearer und nichtlinearer Systeme: Definitionen, Eigenschaften und Anwendungen (zero dynamics of linear and nonlinear systems: Definitions, properties and applications)', *at-Automatisierungstechnik*, vol. 54, no. 7/2006, pp. 310–322, 2006, (in German).

[54] *Understanding poles and zeros*, Accessed: 2019-06-13. [Online]. Available: `http://web.mit.edu/2.14/www/Handouts/PoleZero.pdf`.

[55] M. Zeitz, 'Differenzielle Flachheit: Eine nützliche Methodik auch für lineare SISO-Systeme differential flatness: A useful method also for linear SISO systems', *at-Automatisierungstechnik Methoden und Anwendungen der Steuerungs-, Regelungs-und Informationstechnik*, vol. 58, no. 1, pp. 5–13, 2010, (in German).

[56] J. Adamy, *Nichtlineare Systeme und Regelungen*. Springer, 2018.

[57] R. Bauer, 'Modellbildung und modellbasierte Regelungsstrategien am Beispiel einer Biomasse-Feuerungsanlage', 2009, (in German).

[58] D. K. Miu, *Mechatronics: electromechanics and contromechanics*. Springer Science & Business Media, 2012.

[59] T. Haidinger, 'Modellierung und Regelung eines elektrischen Rotationsaktuators', (in German), PhD thesis, Graz University of Technology, 2010.

[60] W. von der Linden, *Lecture notes in analytical mechanics*, (in German), 2007.

[61] K. Kranawetter, R. Seeber, R. Bauer and M. Horn, 'A new backlash and gear play model with friction', in *2019 IEEE International Conference on Mechatronics (ICM)*, IEEE, vol. 1, 2019, pp. 346–351.

[62] M. Nordin, J. Galic and P.-O. Gutman, 'New models for backlash and gear play', *International journal of adaptive control and signal processing*, vol. 11, no. 1, pp. 49–63, 1997.

[63] M. Nordin and P.-O. Gutman, 'Controlling mechanical systems with backlash - a survey', *Automatica*, vol. 38, no. 10, pp. 1633–1649, 2002.

[64] D. Papageorgiou, M. Blanke, H. H. Niemann and J. H. Richter, 'Backlash estimation for industrial drive-train systems', *IFAC-PapersOnLine*, vol. 50, no. 1, pp. 3281 –3286, 2017, 20th IFAC World Congress.

[65] U. Angeringer and M. Horn, 'Sliding mode drive line control for an electrically driven vehicle', in *2011 IEEE International Conference on Control Applications (CCA)*, 2011, pp. 521–526.

[66] F. Walz, T. Schucht, J. Reger and S. Hohmann, 'Shaft torque and backlash estimation for longitudinal motion control of all-wheel-drive vehicles', in *2018 IEEE Conference on Control Technology and Applications (CCTA)*, 2018, pp. 1434–1440. DOI: 10.1109/CCTA.2018.8511096.

[67] J. Zhang, H. Zhang and X. Xiao, 'New identification method for backlash of gear transmission systems', in *2018 2nd IEEE Advanced Information Management,Communicates,Electronic and Automation Control Conference (IMCEC)*, 2018, pp. 378–382.

[68] C. Akoto and H Spangenberg, 'Modeling of backlash in drivetrains', in *Proceedings of the of the 4th CEAS conference*, Lingköping, Sweden, 2013.

[69] J. Vörös, 'Modeling and identification of systems with backlash', *Automatica*, vol. 46, no. 2, pp. 369–374, 2010.

[70] T. P. Goodman, 'Dynamic effects of backlash', *Machine Design*, vol. 35, no. 12, pp. 150–157, 1963.

[71] M. Skofitsch, R. Bauer, N. Dourdoumas and W. Rossegger, 'Model based torque ripple compensation of induction motors', in *Advances in Mechatronics*, Trauner Verlag, 2012.

[72] N. P. Quang, J.-A. Dittrich *et al.*, *Vector control of three-phase AC machines*. Springer, 2008, vol. 2.

[73] A. Y. Malkin and A. I. Isayev, *Rheology: concepts, methods, and applications*. Elsevier, 2017.

[74] A. Menne, 'Calculating Torsional Vibrations in Drives with Hydrodynamic Couplings', VDI Verlag GmbH, Tech. Rep., 2004, Accessed: 2019-06-13. [Online]. Available: https://d2euiryrvxi8z1.cloudfront.net/asset/445934742530/1617dc4e0397117ef92116fd53404bd3.

[75] B. E. Vik, 'Development and Verification of a Geislinger Flexible Coupling Bond Graph Model', Master's thesis, NTNU Trondheim, 2014.

[76] A. Beckenkamp, 'Modeling and Simulation of a flexible Damper during Ice in Propeller Impacts', Master's thesis, NTNU Trondheim, 2015.

[77] P. Jaschke and H. Waller, 'Different techniques of the modelling of hydrodynamic couplings', in *Process Modelling*, B. Scholz-Reiter, H.-D. Stahlmann and A. Nethe, Eds., Springer, Berlin, Heidelberg, 1999, pp. 329–344.

[78] A. Menne, 'Identifikation der dynamischen Eigenschaften von hydrodynamischen Wandlern', (in German), PhD thesis, Ruhr University Bochum, 1993.

[79] U. Folchert, 'Identifikation der dynamischen Eigenschaften hydrodynamischer Kupplungen', (in German), PhD thesis, Ruhr University Bochum, 1994.

[80] J. Steinhausen, 'Die Beschreibung der Dynamik von Antriebssträngen durch Black-Box-Modelle hydrodynamischer Kupplungen', (in German), PhD thesis, Ruhr University Bochum, 1998.

[81] K. Kranawetter, R. Seeber, R. Bauer and M. Horn, 'Control-oriented modelling of the transient behaviour of hydrodynamic couplings: A state-space approach', in *2018 Annual American Control Conference (ACC)*, IEEE, 2018, pp. 2940–2945.

[82] *Geislinger coupling*, Accessed: 2019-06-13, Geislinger GmbH., 2002. [Online]. Available: http://web.archive.org/web/20040716195746/http://www.geislinger.com/pdf/COUPLING_2003.pdf.

[83] P. Mayr, G. Pirker, A. Wimmer and M. Krenn, 'Simulation-based control of transient sce operation', in *WCX17: SAE World Congress Experience*, SAE International, 2017. DOI: 10.4271/2017-01-0544.

[84] *Geislinger coupling*, Accessed: 2019-06-13, Geislinger GmbH., 2016. [Online]. Available: http://web.archive.org/web/20170915144319/http://www.geislinger.com/assets/geislinger.at/downloads/Coupling_17.8.pdf.

[85] H. E. Merritt, *Hydraulic Control Systems*. John Wiley & Sons, 1967.

[86] H. Watter, *Hydraulik und Pneumatik*, 2nd ed. Springer Vieweg, 2007, (in German).

[87] J. Spurk and N. Aksel, *Fluid Mechanics*, 2nd ed. Springer, 2008.

[88] E. Galvagno, M. Velardocchia, A. Vigliani and A. Tota, 'Experimental analysis and model validation of a dual mass flywheel for passenger cars', in *SAE 2015 World Congress & Exhibition*, SAE International, 2015. DOI: 10.4271/2015-01-1121.

[89] R. Bauer, M. Lang, B. Pressl, W. Rossegger and F. Voit, *Method for damping vibrations*, US Patent App. 14/382,490, 2015.

[90] L. von Wangenheim, 'On the barkhausen and nyquist stability criteria', *Analog Integrated Circuits and Signal Processing*, vol. 66, no. 1, pp. 139–141, 2011.

[91] V. Singh, 'Discussion on barkhausen and nyquist stability criteria', *Analog Integrated Circuits and Signal Processing*, vol. 62, no. 3, pp. 327–332, 2010.

[92] F. He, R. Ribas, C. Lahuec and M. Jézéquel, 'Discussion on the general oscillation startup condition and the barkhausen criterion', *Analog Integrated Circuits and Signal Processing*, vol. 59, no. 2, pp. 215–221, 2009.

[93] R. Mancini, *Analyzing feedback loops containing secondary amplifiers*, 2003.

[94] W. Bahn, J.-M. Yoon, N.-K. Hahm, S.-S. Lee, S.-H. Lee and D.-I. Cho, 'Application of adaptive notch filter for resonance suppression in industrial servo systems', in *2014 14th International Conference on Control, Automation and Systems (ICCAS 2014)*, IEEE, 2014, pp. 976–979.

[95] W. Bahn, T.-I. Kim, S.-H. Lee *et al.*, 'Resonant frequency estimation for adaptive notch filters in industrial servo systems', *Mechatronics*, vol. 41, pp. 45–57, 2017.

[96] J. F. Chicharo and T.-S. Ng, 'Gradient-based adaptive IIR notch filtering for frequency estimation', *IEEE transactions on acoustics, speech, and signal processing*, vol. 38, no. 5, pp. 769–777, 1990.

[97] J. Levin and P. Ioannou, 'Multirate adaptive notch filter with an adaptive bandwidth controller for disk drives', in *2008 American Control Conference*, IEEE, 2008, pp. 4407–4412.

[98] T.-I. Kim, W. Bahn, J.-M. Yoon *et al.*, 'Online tuning method for notch filter depth in industrial servo systems', in *2016 35th Chinese Control Conference (CCC)*, IEEE, 2016, pp. 9514–9518.

[99] T.-I. Kim, J.-S. Han, J.-H. Park *et al.*, 'Application of discrete derivative method with a new frequency mapping technique for adaptive-notch-filter based vibration control in industrial servo systems', in *2017 IEEE Conference on Control Technology and Applications (CCTA)*, IEEE, 2017, pp. 414–419.

[100] M. Mojiri and A. R. Bakhshai, 'An adaptive notch filter for frequency estimation of a periodic signal', *IEEE Transactions on Automatic Control*, vol. 49, no. 2, pp. 314–318, 2004.

[101] P. A. Regalia, 'A complex adaptive notch filter', *IEEE Signal Processing Letters*, vol. 17, no. 11, pp. 937–940, 2010.

[102] Y. Sugiura, 'A fast and accurate adaptive notch filter using a monotonically increasing gradient', in *2014 22nd European Signal Processing Conference (EUSIPCO)*, IEEE, 2014, pp. 1756–1760.

[103] L. Tan, J. Jiang and L. Wang, 'Adaptive harmonic IIR notch filters for frequency estimation and tracking', in *Adaptive Filtering*, IntechOpen, 2011.

[104] J. Travassos-Romano and M Bellanger, 'Fast least squares adaptive notch filtering', *IEEE Transactions on Acoustics, Speech, and Signal Processing*, vol. 36, no. 9, pp. 1536–1540, 1988.

[105] S. N. Vukosavic and M. R. Stojic, 'Suppression of torsional oscillations in a high-performance speed servo drive', *IEEE Transactions on Industrial Electronics*, vol. 45, no. 1, pp. 108–117, 1998.

[106] J.-M. Yoon, W. Bahn, T.-I. Kim, J.-S. Han, S.-H. Lee and D.-i. D. Cho, 'Discrete derivative method for adaptive notch filter-based frequency estimators', *International Journal of Control, Automation and Systems*, vol. 15, no. 2, pp. 668–679, 2017.

[107] M. Aldag and J. Horn, 'Damping of resonance peaks using adaptive notch filters in gearless servo drives', in *2017 22nd International Conference on Methods and Models in Automation and Robotics (MMAR)*, IEEE, 2017, pp. 164–169.

[108] S Bosch, D Lebsanft and H Steinhart, 'Self-adaptive resonance frequency tracking for digital notch-filter-based active damping in lcl-filter-based active power filters', in *2017 19th European Conference on Power Electronics and Applications (EPE'17 ECCE Europe)*, IEEE, 2017, P–1.

[109] K. Ohno and T. Hara, 'Adaptive resonant mode compensation for hard disk drives', *IEEE Transactions on Industrial Electronics*, vol. 53, no. 2, pp. 624–630, 2006.

[110] S.-M. Yang and S.-C. Wang, 'The detection of resonance frequency in motion control systems', *IEEE Transactions on Industry Applications*, vol. 50, no. 5, pp. 3423–3427, 2014.

[111] F. Kong, S. Chen, S. Chen, L. Wang and X. Huo, 'Online identification of resonance using extremum seeking control', in *2016 12th World Congress on Intelligent Control and Automation (WCICA)*, IEEE, 2016, pp. 1152–1157.

[112] Y. Chen, M. Yang, J. Long, K. Hu, D. Xu and F. Blaabjerg, 'Analysis of oscillation frequency deviation in elastic coupling digital drive system and robust notch filter strategy', *IEEE Transactions on Industrial Electronics*, vol. 66, no. 1, pp. 90–101, 2019.

[113] H. Wang, D.-H. Lee, Z.-G. Lee and J.-W. Ahn, 'Vibration rejection scheme of servo drive system with adaptive notch filter', in *2006 37th IEEE Power Electronics Specialists Conference*, IEEE, 2006, pp. 1–6.

[114] J. Kang, S. Chen and X. Di, 'Online detection and suppression of mechanical resonance for servo system', in *2012 Third International Conference on Intelligent Control and Information Processing*, IEEE, 2012, pp. 16–21.

[115] D.-H. Lee, J. Lee and J.-W. Ahn, 'Mechanical vibration reduction control of two-mass permanent magnet synchronous motor using adaptive notch filter with fast fourier transform analysis', *IET electric power applications*, vol. 6, no. 7, pp. 455–461, 2012.

[116] T.-a. Shen, H.-n. Li, Q.-x. Zhang and M. Li, 'A novel adaptive frequency estimation algorithm based on interpolation fft and improved adaptive notch filter', *Measurement Science Review*, vol. 17, no. 1, pp. 48–52, 2017.

[117] M. Mismar and I. Zabalawi, 'Complex coefficient fir digital filters', *Circuits, Systems and Signal Processing*, vol. 13, no. 5, pp. 591–600, 1994.

[118] Y. Sugita and N. Aikawa, 'A design method of minimum phase fir filters with complex coefficients', in *2003 IEEE International Conference on Acoustics, Speech, and Signal Processing, 2003. Proceedings.(ICASSP'03).*, IEEE, vol. 6, 2003, pp. VI–5.

[119] O. Troeng, B. Bernhardsson and C. Rivetta, 'Complex-coefficient systems in control', in *2017 American Control Conference (ACC)*, IEEE, 2017, pp. 1721–1727.

[120] G. Moschytz and M. Hofbauer, *Adaptive Filter*. Springer, 2000, (in German).

[121] S. S. Haykin, *Adaptive filter theory*. Pearson Education India, 2008.

[122] M. Bodson and S. C. Douglas, 'Adaptive algorithms for the rejection of sinusoidal disturbances with unknown frequency', *Automatica*, vol. 33, no. 12, pp. 2213–2221, 1997.

[123] E. Aboutanios and B. Mulgrew, 'Iterative frequency estimation by interpolation on fourier coefficients', *IEEE Transactions on Signal Processing*, vol. 53, no. 4, pp. 1237–1242, 2005.

[124] M Gasior and J. Gonzalez, 'Improving fft frequency measurement resolution by parabolic and gaussian spectrum interpolation', in *AIP Conference Proceedings*, AIP, vol. 732, 2004, pp. 276–285.

[125] Q. Song, J. Liu, C. Yang and S. Qiao, 'Study on discrete spectrum correction technology of rlc measuring instrument', *Information Technology Journal*, vol. 12, no. 5, pp. 1045–1049, 2013.

[126] A. V. Oppenheim, *Discrete-time signal processing*. Pearson Education India, 1999.

[127] R. Bauer, 'Entwurf und Realisierung adaptiver Steuerungen und Regelungen', (in German), PhD thesis, 2003.

[128] D. Kang, C. Dangdang and L. Weihua, 'An approach to discrete spectrum correction based on energy centroid', in *Key Engineering Materials*, Trans Tech Publ, vol. 321, 2006, pp. 1270–1273.

[129] T. Grandke, 'Interpolation algorithms for discrete fourier transforms of weighted signals', *IEEE transactions on instrumentation and measurement*, vol. 32, no. 2, pp. 350–355, 1983.

[130] V. K. Jain, W. L. Collins and D. C. Davis, 'High-accuracy analog measurements via interpolated FFT', *IEEE Transactions on Instrumentation and Measurement*, vol. 28, no. 2, pp. 113–122, 1979.

[131] T Kuraishi, M Kawada and K Isaka, 'The phase compensation of recursive interpolated d/fft', in *2008 International Symposium on Electrical Insulating Materials (ISEIM 2008)*, IEEE, 2008, pp. 625–628.

[132] F. J. Harris, 'On the use of windows for harmonic analysis with the discrete fourier transform', *Proceedings of the IEEE*, vol. 66, no. 1, pp. 51–83, 1978.

[133] K. Kranawetter, 'Energieoptimale Positionsregelung einer Asynchronmaschine', (in German), Master's thesis, Institute for Automation and Control, Graz University of Technology, 2014.

[134] K. Kranawetter, R. Seeber, P. Mayr, G. Pirker, R. Bauer and M. Horn, 'Charge air and fuel gas pressure control on a hil-system for the development of transient large bore gas engines', in *2018 IEEE Conference on Control Technology and Applications (CCTA)*, IEEE, 2018, pp. 1441–1447.

[135] D. R. Mulvaney, Ed., *Green Energy: An A-to-Z Guide*. Sage, 2011.

[136] T. M. Letcher, Ed., *Future Energy: Improved, Sustainable and Clean Options for our Planet*. Elsevier, 2010.

[137] 'Powering Europe: Wind energy and the electricity grid', European Wind Energy Association, Tech. Rep., 2010, Accessed: 2019-06-13. [Online]. Available: https://windeurope.org/fileadmin/ewea_documents/documents/publications/reports/Grids_Report_2010.pdf.

[138] CIMAC working group 'gas engines', 'Transient response behaviour of gas engines', CIMAC, Tech. Rep., 2011, Accessed: 2019-06-13. [Online]. Available: http://www.cimac.com/cms/upload/workinggroups/WG17/CIMAC_PPaper_TransResp_21042011_FINAL.pdf.

[139] G. Merker and R. Teichmann, *Grundlagen Verbrennungsmotoren*. Springer Heidelberg, 2014, (in German).

[140] J. Zelenka, P. Mayr, G. Pirker and A. Wimmer, 'HiL Operation Of Single Cylinder Research Engines To Optimize The Behavior Of Large Gas Engines', in *Proceedings of the ASME 2017 Internal Combustion Fall Technical Conference*, ICEF, 2017.

[141] *GE's Jenbacher Gas Engines*, Accessed: 2018-01-30, 2018. [Online]. Available: http://www.clarke-energy.com/gas-engines/.

[142] G. A. Karim, *Dual-Fuel Diesel Engines*, 1st ed. CRC Press, Mar. 2015.

[143] Honeywell RMG, *RMG 330 gas pressure regulator*, Brochure, Accessed: 2019-06-13, 2018. [Online]. Available: http://sds-service.com/files/9814/0087/1306/RMG_330_00_GB_2011_02.pdf.

[144] H. Pucher and K. Zinner, *Aufladung von Verbrennungsmotoren: Grundlagen, Berechnungen, Ausführungen*. Springer-Verlag, 2012.

[145] P. Mayr, G. Pirker, A. Wimmer and M. Krenn, 'Simulation-based Control of Transient SCE Operation', in *SAE Technical Paper 2017-01-0544*, WCX17: SAE World Congress Experience, 2017.

[146] R. Pischinger, M. Klell and T. Sams, *Thermodynamik der Verbrennungskraftmaschine*. Springer-Verlag, 2009.

[147] L. Guzzella and C. Onder, *Introduction to Modeling and Control of Internal Combustion Engine Systems*, 2nd ed. Springer Heidelberg, 2010.

[148] R. Hanus, M. Kinnaert and J.-L. Henrotte, 'Conditioning technique, a general anti-windup and bumpless transfer method', *Automatica*, vol. 23, no. 6, pp. 729–739, 1987.

[149] AirCom, *Proportional pressure regulator AirTonic*, Brochure, Accessed: 2019-06-13, 2018. [Online]. Available: https://www.aircom.net/uploads/aircomdocs/Katalog/GB/Kapitel%2010/K-2017-10-8-10-GB.pdf.